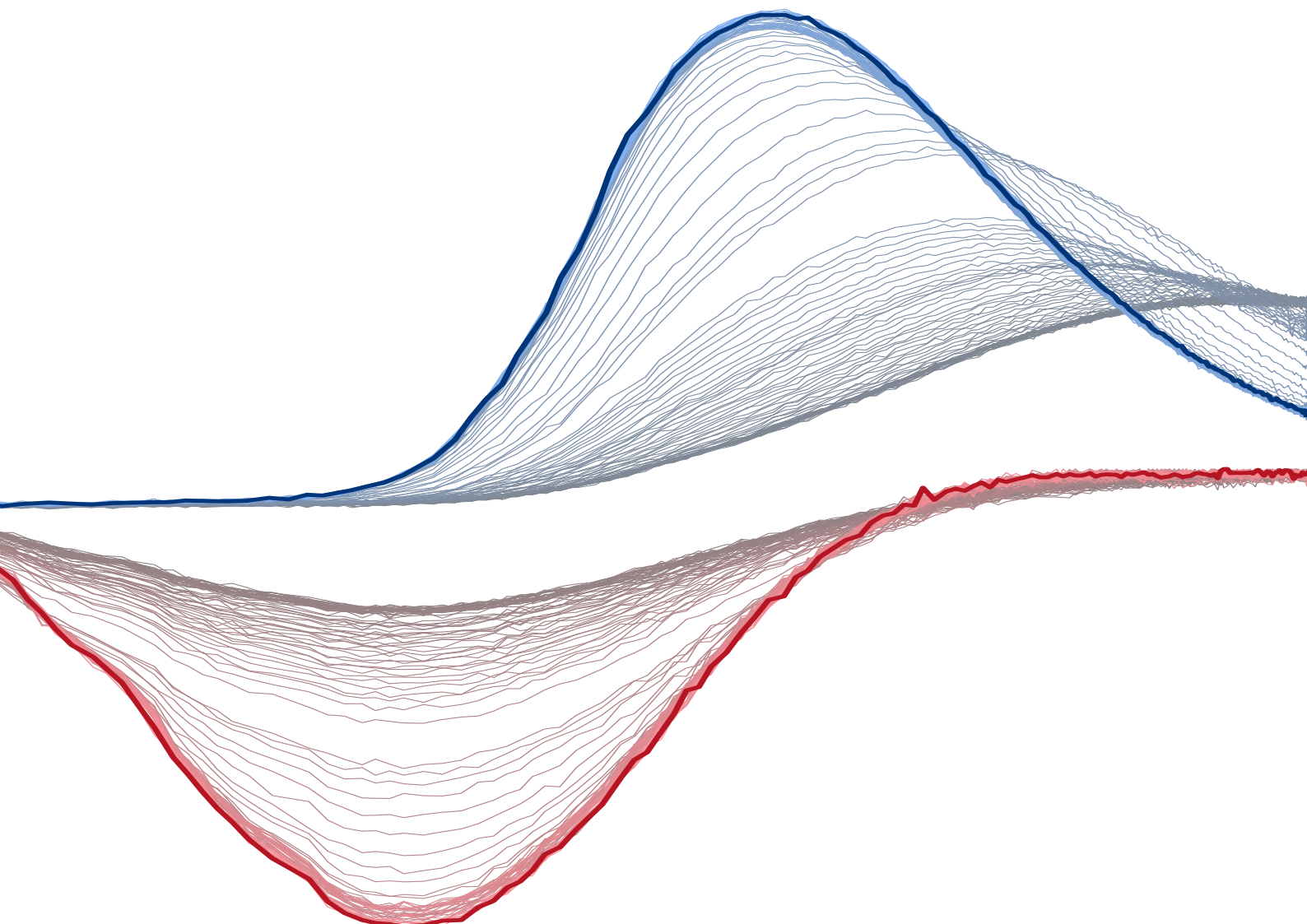


# Refining Argon Trap Trace Analysis – Crucial Features and Characterization Tools for Reliable Routine Measurements



**Julian Frederick Robertz**

Issued March 2023



Dissertation  
submitted to the  
Combined Faculty of Mathematics, Engineering and Natural Sciences  
of Heidelberg University, Germany  
for the degree of  
Doctor of Natural Sciences

Put forward by  
**Julian Frederick Robertz**  
born in Solingen, Germany

Oral exam: May 24, 2023



# Refining Argon Trap Trace Analysis – Crucial Features and Characterization Tools for Reliable Routine Measurements

Referees: Prof. Dr. Markus K. Oberthaler  
Prof. Dr. Selim Jochim



## Refining Argon Trap Trace Analysis – Crucial Features and Characterization Tools for Reliable Routine Measurements

Argon Trap Trace Analysis resolves  $^{39}\text{Ar}$  concentrations at the  $10^{-16}$  level. Perfect selectivity is achieved by exploiting the isotopic shift and a high number of photon scattering processes for detection. However, good measurement precision requires high count rates of  $^{39}\text{Ar}$  atoms. Therefore, this work presents crucial features and characterization tools for reliable routine measurements.

A new instrument for absolute quantization of the metastable  $^{40}\text{Ar}$  flux is developed and put into operation. The magneto-optical trap loading rate is evaluated and established as a standard characterization tool. It is part of the new collimator alignment procedure that resulted in a factor of 1.5 higher  $^{39}\text{Ar}$  count rate. Other improved alignment procedures are presented. In addition, a new laboratory control and monitoring system for stable day-to-day measurements is developed and installed.

The second part focuses on the study of sources of metastable atoms. Two radio frequency (RF) antennas and two cooling devices are presented and their main features are analyzed. A new LN<sub>2</sub>-dewar for cooling reduces the amount of liquid nitrogen consumed by a factor of 3 to 5. In combination with the established RF antenna, increasing the source pressure to  $2.0 \times 10^{-5}$  mbar leads to 50 % higher metastable flux, while the atoms slow down longitudinally.

## Weiterentwicklung der Argon Trap Trace Analysis – Entscheidende Merkmale und Charakterisierungsinstrumente für zuverlässige Routinemessungen

Die Argon Trap Trace Analysis löst  $^{39}\text{Ar}$  -Konzentrationen auf dem  $10^{-16}$ -Niveau auf. Perfekte Selektivität wird erreicht, indem die Isotopenverschiebung und eine hohe Anzahl von Photonenstreuprozessen für den Nachweis ausgenutzt werden. Für eine gute Messgenauigkeit sind jedoch hohe Zählraten von  $^{39}\text{Ar}$  -Atomen erforderlich. Daher werden in dieser Arbeit entscheidende Merkmale und Charakterisierungswerzeuge für zuverlässige Routinemessungen vorgestellt.

Ein neues Instrument zur absoluten Quantifizierung des metastabilen  $^{40}\text{Ar}$  -Flusses wird entwickelt und in Betrieb genommen. Die Beladungsrate der magneto-optischen Falle wird evaluiert und als Standardinstrument zur Charakterisierung etabliert. Sie ist Teil des neuen Verfahrens zur Ausrichtung des Kollimators, das zu einer um den Faktor 1,5 höheren  $^{39}\text{Ar}$  -Zählrate führte. Weitere verbesserte Ausrichtungsverfahren werden vorgestellt. Darüber hinaus wird ein neues Laborsteuerungs- und Überwachungssystem für stabile tagtägliche Messungen entwickelt und installiert.

Der zweite Teil befasst sich mit der Untersuchung von Quellen für metastabile Atome. Es werden zwei Hochfrequenzantennen (HF-Antennen) und zwei Kühlvorrichtungen vorgestellt und ihre Hauptmerkmale analysiert. Ein neuer LN<sub>2</sub>-Dewar zur Kühlung reduziert die Menge des verbrauchten flüssigen Stickstoffs um den Faktor 3 bis 5. In Kombination mit der etablierten HF-Antenne führt eine Erhöhung des Quelldrucks auf  $2.0 \times 10^{-5}$  mbar zu einem 50 % höheren metastabilen Fluss, während die Atome in Längsrichtung langsamer werden.



# Preface

*How can it be that a particle, for example a photon, knows about the second slit when it has passed the first one?*

This question fascinated me after I saw the double-slit experiment in high school. From the particle point of view, it's hard to understand how this is supposed to work. Because for me, up until that point in high school, particles were blind, without intelligence, and basically like very fine sand. On the other hand, it is trivial to understand the resulting signal when it is explained in terms of waves. But a particle is not a wave, is it? This experiment taught me that quantum mechanical objects are both. Particles are waves and waves are particles. This is what is known as wave-particle duality.

Laser light perfectly combines the pure nature of particles and waves. Therefore, ever since the double-slit experiment at school, I have developed a strong interest in quantum optics. On the other hand, I also have a passion for craft, technology and engineering. I read about the Argon Trap Trace Analysis (ArTTA) experiment when I was looking for possible PhD positions in Heidelberg. It was the word *glacier* that piqued my interest. Since mountaineering, especially high altitude touring on glaciers, is one of my passions, I applied directly for a position to combine the different fields of interest. Thus, during the PhD I learned a lot about glaciers and other environmental systems. Some of the projects to which my work contributed are presented in the appendix.

The ArTTA experiment provides a platform to apply all of these skills and gain further knowledge. Maintenance of lasers, setup of optics, manipulation of atoms with light, design of electrical circuits, software programming, constructing devices, manufacturing components, assembling vacuum parts, working within a group as well as teaching and leading new group members are some of the required expertise and abilities. I am grateful that I had the opportunity to improve many of my skills and dive into new areas. However, it was quite difficult to work half of the PhD alone on one of the devices without a partner, consequently with little support and sharing while the rest of the group relied on assistance. But I have learned more about myself as a result.

When I started as a graduate student, my task was to develop ArTTA towards reliable routine measurements. The consequent results are presented mainly at the beginning of this thesis. The theoretical description of the processes occurring in a new device for absolute flux measurements was one of those fascinating deep insights into quantum mechanics. At the end of this work, the focus is put on the source of argon atoms.

Many thanks already at this point to all who have contributed in any way to this thesis.

*Julian Robertz*

*Heidelberg, March 2023*



# Contents

<b>List of Abbreviations</b>	<b>v</b>
<b>1 Introduction</b>	<b>1</b>
1.1 A brief History of $^{39}\text{Ar}$ Atom Trap Trace Analysis . . . . .	3
<b>2 Fundamentals</b>	<b>5</b>
2.1 Argon Isotopes and their Level Structure . . . . .	5
2.1.1 $^{39}\text{Ar}$ Hyperfine Structure and its Consequences . . . . .	8
2.2 Radiative Transitions of Atoms . . . . .	9
2.2.1 Density Matrix and Quantum Optical Master Equation . . . . .	9
2.2.2 Scattering Rate . . . . .	11
2.2.3 Zeeman Effect . . . . .	13
2.2.4 Transition Strengths . . . . .	14
2.3 Laser Cooling and Magneto-Optical Trapping . . . . .	16
2.4 Argon Plasma and Metastable Atom Production . . . . .	19
2.5 AC Electronics . . . . .	21
2.5.1 Fundamental Linear Electrical Components and Terminology . . . . .	22
2.5.2 Circuit Algebra and Resonances . . . . .	23
2.5.3 Telegrapher's Equations and Electrical Waves . . . . .	25
2.5.4 S-Parameter Analysis, Reflections and Reciprocity . . . . .	26
<b>3 ArTTA Technology</b>	<b>29</b>
3.1 Overview of the ArTTA Apparatuses . . . . .	29
3.2 Tools for Metastable Flux Quantification . . . . .	32
3.2.1 MOT Loading Rate . . . . .	33
3.3 Consequences of a Widened Collimator and its Fundamental Alignment . . . . .	36
3.4 Alignment Procedure for Collimator and 2D-MOT . . . . .	41
3.5 Laboratory Control and Monitoring System . . . . .	45
3.5.1 Communication in a Decentralized System . . . . .	46
3.5.2 Design of a Data Transmitter and a Laser Switch Control . . . . .	46
3.5.3 Universal Monitoring Software ATTAsystem . . . . .	47
<b>4 Setup of a New Device for Absolute Metastable <math>^{40}\text{Ar}</math> Flux Measurements</b>	<b>53</b>
4.1 Working Principle . . . . .	53
4.2 Design and Characterization of the Image Objective . . . . .	54
4.3 Dynamical Decay Model . . . . .	56
4.3.1 Experimental Parameter . . . . .	58

4.3.2	Correction Factor . . . . .	60
4.3.3	Comparison of Experimental and DDM Results . . . . .	62
4.4	Conversion of the Image Data into the Equivalent Metastable $^{39}\text{Ar}$ Flux . . . . .	67
4.5	Application within the ArTTA Technology . . . . .	68
4.5.1	Metastable Flux Measurement of Other Isotopes . . . . .	69
<b>5</b>	<b>Velocity Distribution of the Metastable Atoms and its Consequences</b>	<b>71</b>
5.1	Measurement Setup and Impact of the Measurement itself . . . . .	71
5.2	Analysis of Velocity Distributions . . . . .	74
5.3	Transverse Diffusion during Longitudinal Deceleration . . . . .	78
5.3.1	Induced Losses by a Finite MOT Interaction Range . . . . .	81
<b>6</b>	<b>Evaluation of RF Driven Plasma Metastable Atom Sources</b>	<b>83</b>
6.1	Different Types of RF Antennas . . . . .	83
6.1.1	Open Resonator . . . . .	83
6.1.2	Helical Resonator . . . . .	86
6.2	Different Types of Liquid Nitrogen Cooling . . . . .	89
6.2.1	$\text{LN}_2$ -Can . . . . .	90
6.2.2	$\text{LN}_2$ -Dewar . . . . .	90
6.3	RF Electronic Analysis . . . . .	92
6.4	Spatial Dependence of Metastable Argon Production . . . . .	96
6.5	Study of the Metastable Atom Sources . . . . .	97
6.5.1	RF Power Dependence – first Comparison of $\text{LN}_2$ -Can and $\text{LN}_2$ -Dewar	99
6.5.2	Pressure Dependence . . . . .	100
6.5.3	Influence of the RF Frequency and the Plasma Mode . . . . .	102
6.6	Impact on ArTTA Performance – Conclusion . . . . .	103
<b>7</b>	<b>Conclusion and Outlook</b>	<b>107</b>
7.1	Second ArTTA Facility . . . . .	107
7.2	Metastable Atom Source . . . . .	109
7.3	ArTTA Technology . . . . .	110
<b>A</b>	<b>Appendix</b>	<b>113</b>
A.1	Radiation Pattern of Different Optical Transitions . . . . .	113
A.2	S-Parameter Calculation of a Two-Port Network . . . . .	114
A.3	Atmosphere to Ultrahigh Vacuum Fiber . . . . .	115
A.4	DDM: Supplementary Information . . . . .	116
A.5	Metastable Atom Sources: Supplementary Information . . . . .	116
<b>B</b>	<b>Environmental <math>^{39}\text{Ar}</math> Dating Projects</b>	<b>119</b>
<b>Acknowledgements</b>		<b>125</b>
<b>Bibliography</b>		<b>127</b>

# List of Abbreviations

<b>AMS</b>	Accelerator Mass Spectrometry
<b>AC</b>	alternating current
<b>A/D</b>	analog-to-digital converter
<b>AlN</b>	aluminum nitride
<b>Al<sub>2</sub>O<sub>3</sub></b>	aluminum(III) oxide
<b>AOM</b>	acousto-optic modulator
<b>APD</b>	avalanche photo diode
<b>ArTTA</b>	Argon Trap Trace Analysis (name of the facilities in Heidelberg, Germany)
<b>asl</b>	above sea level
<b>ATTA</b>	Atom Trap Trace Analysis (name of the measurement technique)
<b>CAD</b>	computer-aided design
<b>DC</b>	direct current
<b>DDM</b>	dynamical decay model
<b>DRC</b>	Democratic Republic of the Congo
<b>EOM</b>	electro-optic modulator
<b>GUI</b>	graphical user interface
<b>HR</b>	helical resonator
<b>I<sup>2</sup>C</b>	Inter-Integrated Circuit
<b>IoT</b>	Internet of Things
<b>ISWR</b>	current standing wave ratio
<b>JSON</b>	JavaScript Object Notation
<b>LAN</b>	local area network
<b>LN<sub>2</sub></b>	liquid nitrogen

<b>LLC</b>	Low-Level Counting
<b>MATLAB</b>	MATrix LABoratory
<b>MBD</b>	Maxwell-Boltzmann distribution
<b>MOT</b>	magneto-optical trap
<b>MW</b>	microwave
<b>OR</b>	open resonator
<b>OBE</b>	optical Bloch equation
<b>PEEK</b>	polyether ether ketone
<b>REST</b>	representational state transfer
<b>RF</b>	radio frequency
<b>RGA</b>	residual gas analyzer
<b>RP</b>	repumper transition
<b>RS-232</b>	Recommended Standard 232
<b>RWA</b>	rotating wave approximation
<b>SWR</b>	standing wave ratio
<b>TMP</b>	turbo-molecular pump
<b>TTL</b>	transistor-transistor logic
<b>USB</b>	Universal Serial Bus
<b>VCO</b>	voltage controlled oscillator
<b>VNA</b>	vector network analyzer
<b>VSWR</b>	voltage standing wave ratio
<b>ZSL</b>	Zeeman slower

# 1 Introduction

Natural science has evolved over a long period of time. While answering a question usually raises new questions, new measurement tools and ways to answer these questions are developed. However, the central core of natural science has remained the same. We still seek to describe, understand and predict our near and far environment and its phenomena using the methods of the natural sciences, based on empirical findings from experiments and observations.

The quantum technological Argon Trap Trace Analysis (ArTTA) belongs to both, experiment and observation. Its application focuses on understanding hydrological cycles and thus crucial aspects for our society such as climate change or water resources. Its use is therefore the observation of information given by the environment. The method itself and its refinement are based on experimentation, hypothesis generation and testing.

Understanding hydrological cycles and their associated processes requires knowledge of the appropriate time scales. The time information is derived from tracers, which can be of natural or anthropogenic origin. For example, pollen from a plant that was only present in the area from a certain point in time may indicate a time limit of the surrounding glacier ice. However, common tracers in hydrology are mostly rare isotopes [Car+17; Spr+19]. Figure 1.1 illustrates some of them, sorted by their dating range.

The probably most known dating tracer is carbon 14,  $^{14}\text{C}$ . As the name ArTTA supposes, ArTTA deals with the noble gas radioisotope argon 39,  $^{39}\text{Ar}$ . Its half-life is  $T_{1/2} = 268(8)$  y [SSK65; Che18]. Therefore, the dating range is between 50 y and 1300 y, depending on sample size, required precision, and other factors. This closes the gap between  $^{85}\text{Kr}$  and  $^{14}\text{C}$ ,

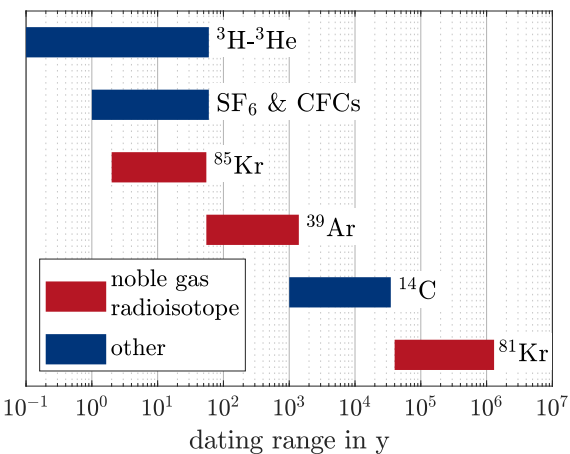
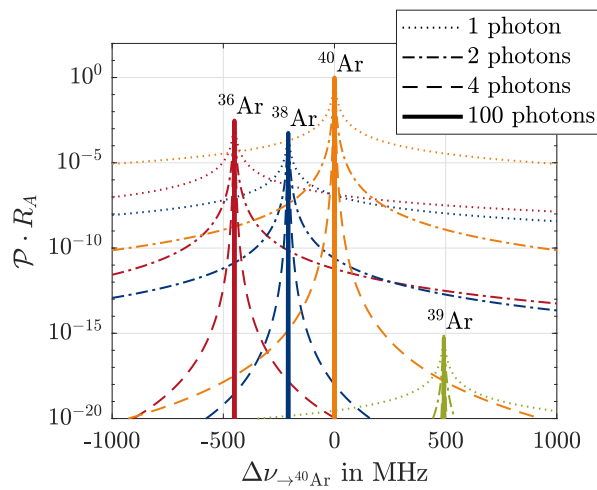


**Figure 1.1:** The imaged tracers are widely used in hydrology and other research fields for age determination. The dating range does not have sharp edges as the accuracy continuously decreases for shorter and longer periods. Therefore, the bars can be seen as a guide to the eye.

**Figure 1.2:** Illustration of the working principle of the ATTA for argon. On the  $y$ -axis the excitation probability  $\mathcal{P}$  is plotted scaled with the natural abundance  $R_A$  of the respective isotope.  $\Delta_{\rightarrow^{40}\text{Ar}}$  is the laser frequency relative to the  ${}^{40}\text{Ar}$  cooling transition. Even at the physical limit  $s_0 \rightarrow 0$ , the detection of  ${}^{39}\text{Ar}$  is impossible by orders of magnitude if only one photon is used (dotted line). Increasing the number of scattered photons before obtaining a signal to four, allows the detection of  ${}^{39}\text{Ar}$  at atmospheric concentration in an ideal experiment (dashed line).



which is not covered by another suitable tracer.  ${}^{39}\text{Ar}$  is mainly generated in the atmosphere by neutron spallation processes of  ${}^{40}\text{Ar}$ :  ${}^{40}\text{Ar}(n,2n){}^{39}\text{Ar}$  [LO68]. Although  ${}^{40}\text{Ar}$  is quite abundant in the atmosphere ( $\sim 1\%$ ),  ${}^{39}\text{Ar}$  is very rare with a natural relative abundance of  ${}^{39}\text{Ar}/\text{Ar} = 8.1(3) \times 10^{-16}$  [Col+04]. This corresponds to a 1-cent coin from the year 39 in a train filled with 1-cent coins from the years 36, 38 and 40, extending 18 times around the world. Reliable detection of many of them requires ultrasensitive measurement methods. Three have been successfully deployed so far: Low-Level Counting (LLC), Accelerator Mass Spectrometry (AMS) and Atom Trap Trace Analysis (ATTA).

ATTA is the basic method of ArTTA. The latter designation refers to the activities of the research group in Heidelberg, Germany, where this work was carried out. ATTA is not restricted to argon. It is also used for measuring  ${}^{41}\text{Ca}$ ,  ${}^{81}\text{Kr}$  and  ${}^{85}\text{Kr}$  [Moo+04; Che+99]. Usage of ATTA for other research fields than environmental physics is also thinkable. For example are scientists of astrophysics currently interested in the concentration determination of  ${}^{39}\text{Ar}$  and  ${}^{42}\text{Ar}$ , which are both suitable for ATTA [Cal+22].

The working principle is introduced in the following, while an overview of the realized apparatuses is given in section 3.1. LLC counts the decay of the  ${}^{39}\text{Ar}$  atoms. As the decay rate of atmospheric argon is  $140 \text{ h}^{-1} \text{ mol}^{-1}$ , a large amount of argon gas is needed besides a strong suppression of background radiation.

AMS counts directly the  ${}^{39}\text{Ar}$  atoms and discriminates them from other isotopes by their different mass. The interfering isobar  ${}^{39}\text{K}$  is separated by the gas-filled magnet technique from the peak of  ${}^{39}\text{Ar}$  [Col+04].

ATTA also counts the  ${}^{39}\text{Ar}$  atoms directly. However, it uses the isotopic shift of the electron states to distinguish between the different argon isotopes. The electron is excited to another state by laser light. How likely this excitation depends on the detuning of the laser light with respect to the transition frequency of the atom. Figure 1.2 illustrates this probability  $\mathcal{P}$  scaled by the natural relative abundance  $R_A$ . However, the probability of exciting a  ${}^{40}\text{Ar}$  atom is orders of magnitude more likely even at the physical limit of very weak light fields. By increasing the number of interacting photons before obtaining a signal, only  ${}^{39}\text{Ar}$  atoms can be addressed and detected. The remaining task is to obtain a high and reliable count rate of  ${}^{39}\text{Ar}$  atoms for routine measurements. The present work

focuses on some aspects of this task and describes crucial features.

Chapter 2 explains fundamental concepts and provides the knowledge on which this thesis is based. The ArTTA technology is presented in more detail in chapter 3. Emphasis is placed on characterization tools as well as a laboratory control and monitoring system. A new device for measuring the absolute metastable  $^{40}\text{Ar}$  flux is one of these tools and is introduced in chapter 4. Chapter 5 prepares and analyzes the measurement of velocity distributions for the discussion of the metastable atom sources in chapter 6. The thesis concludes with a summary and conclusion of the results and gives an outlook on further possibilities for improvements in chapter 7. Additionally, appendix B provides a timeline of the  $^{39}\text{Ar}$  dating measurements to which this work has contributed. Some of the environmental projects and their main results are presented.

## 1.1 A brief History of $^{39}\text{Ar}$ Atom Trap Trace Analysis

The history of  $^{39}\text{Ar}$  Atom Trap Trace Analysis evolved from two separate paths. The first one starts in 1968 with the determination of the  $^{39}\text{Ar}$  activity in atmospheric argon by LLC [LO68]. At that time, Loosli and Oeschger have already discussed the possibility of using  $^{39}\text{Ar}$  as a tracer, especially in oceanography and glaciology.  $^{39}\text{Ar}$ -LLC dating is as an applicable method presented in 1983 and issues like underground production addressed [Loo83].

The second path starts a couple of years later. Chen et al. present 1999 a new method called Atom Trap Trace Analysis (ATTa) for measuring the radiogenic tracers  $^{85}\text{Kr}$  and  $^{81}\text{Kr}$  [Che+99]. The first application of  $^{81}\text{Kr}$ -ATTa dating succeeded 2003 [Du+03].

These paths connected in Heidelberg, Germany, with a hyperfine spectroscopy of  $^{39}\text{Ar}$  in 2009 [Wel+09]. First estimations of the  $^{39}\text{Ar}$  count rate of atmospheric samples predicted a value of  $6\text{ }^{39}\text{Ar h}^{-1}$  [Wel+10], which reduces the measurement time to about one day. Shortly after, the first measurement of  $^{39}\text{Ar}$  in an atmospheric sample was reported [Jia+11]. However, the count rate at this time was too low for environmental sample measurements. The final realization and first application of  $^{39}\text{Ar}$ -ATTa succeeded in 2014 [Rit+14]. The achieved count rate of  $3.58(10)\text{ }^{39}\text{Ar h}^{-1}$  agreed with the predictions. Furthermore, the proportionality of  $^{39}\text{Ar}$ -ATTa was successfully confirmed by comparison with LLC results and artificial samples with known  $^{39}\text{Ar}$  concentration. The measured groundwater revealed  $^{39}\text{Ar}$  ages between  $44(71)\text{ y}$  and more than  $644\text{ y}$ . The latter was obtained from a borehole in the Hessian Ried about 30 km northwest of the city of Heidelberg, Germany. It is tapped to the lower aquifer in the sediments of the Upper Rhine Graben [Rit+14].

In the following years, several additional techniques have been evolved. As the argon atoms leave the effusive source under a wide solid angle, efficient collimation is crucial. The bichromatic force on argon was studied, achieving three times stronger forces than the scattering force [Fen+17]. A gain of about 1.7 per dimension was estimated. The challenge of including optical repumping due to hyperfine splitting of  $^{39}\text{Ar}$  remains to be addressed. Another idea focused on the enrichment of  $^{39}\text{Ar}$  in the sample. The argon isotopes are separated using a high mass resolution spectrometer system and collected on an aluminum target [Jia+20]. Most of the highly abundant  $^{40}\text{Ar}$  is cut off before extracting and measuring the remaining argon. The enrichment factor is roughly estimated to be more than 100.

However, many issues have to be addressed before this method can reliably be applied to environmental samples.

The last approach presented here, concentrates on an enhanced metastable argon flux. As argon is a noble gas, the atoms have to be excited to a metastable state before they are addressable by standard lasers. First promising studies using optical enhanced discharge excitation achieved an increase of 87 % in a spectroscopy cell [Frö15; Han14]. The latest work accomplished a twofold increase of the  $^{39}\text{Ar}$  loading rate [Chu+22]. This will lead soon to significant improvements, as according to the authors, nothing stands in the way of application.

All in all, the  $^{39}\text{Ar}$ -ATTA has not reached its physical detection limit yet, which is given by the statistical fluctuations of  $^{39}\text{Ar}$  atoms within a sample. The latest report on the performance concludes a determinable  $^{39}\text{Ar}$  age range of 250 y to 1300 y with a better precision than 20 % for 1 mL STP of argon gas [Ton+21].

While the  $^{39}\text{Ar}$ -ATTA method evolved, its application was extended to further environmental systems. The study of ocean ventilation, particularly the centennial dynamics of the deep ocean, is greatly facilitated by the use of  $^{39}\text{Ar}$ -ATTA. While  $^{39}\text{Ar}$  dating was already applied to the deep ocean using LLC in 1985 [Sch+85], routine measurements have been hindered by the large sample size of around 1000 L. Near these sampling locations, the first study using  $^{39}\text{Ar}$ -ATTA obtained comparable results [Ebs+18]. Due to the smaller sample size of 20 L, more samples could be taken and dated. Since then, several other projects have been performed, e.g. on the ventilation of the Yap-Mariana Junction [Gu+22]. An ongoing project of the ArTTA group focuses on the ventilation of the Arctic Ocean.

The field of glaciology was addressed by demonstrating  $^{39}\text{Ar}$  dating of ice blocks from European Alps weighing only a few kilograms [Fen+19]. This opens the door to new possibilities, as other dating methods for Alpine glaciers in this age range have not been available. The application further evolved to the measurement of ice cores, demonstrated at the Tibetan Plateau [Rit+22]. In addition,  $^{85}\text{Kr}$ -ATTA was used to quantify and correct modern air contamination. Initial parts of an ongoing project to fully develop the application of ArTTA dating to alpine glaciers are presented in appendix B.

Another water-related environmental research area is limnology. A study of the meromictic Lake Kivu on the border between Rwanda and Democratic Republic of the Congo (DRC) yielded  $^{39}\text{Ar}$  concentrations well above atmospheric [Sch21]. The origin of these large values is suspected to be geogenically produced  $^{39}\text{Ar}$  introduced by groundwater. Further details can be found in appendix B and the final results will soon be published.

Last but not least, additional projects in the course of groundwater hydrology have been performed. One example is multi-tracer groundwater dating in southern Oman. The results suggest a composition of the groundwater with a very young component below 30 y and a very old component beyond 1000 y [Räd+22].

All in all, the technological development of  $^{39}\text{Ar}$ -ATTA as well as its application holds unique ideas, ingenious possibilities and fascinating insights. In the past as well as in the future.

## 2 Fundamentals

This chapter provides the theoretical background for the main processes of the ATTA technology and the investigations carried out in this work. It starts with the argon isotopes and their level structure. Subsequently, the operating principle of ATTA is discussed in more detail.

The interaction between atoms and light as well as magnetic fields is discussed on a general level. Thereby, specific aspects for ArTTA are paid attention to. The first half ends with a basic discussion of laser cooling techniques relevant for ArTTA.

After covering the field of laser cooling, the second part begins with basics about low temperature plasmas. They are used to make argon atoms available for laser cooling. The chapter ends with an introduction into alternating current (AC) electronics. A focus is set on useful tools, which provide the opportunity to study the argon plasma source in greater detail.

### 2.1 Argon Isotopes and their Level Structure

Many argon isotopes are known, starting with  $^{30}\text{Ar}$  and going up to  $^{53}\text{Ar}$  [IAE22]. However, only a few of them occur naturally. In particular, these include the three stable isotopes  $^{36}\text{Ar}$ ,  $^{38}\text{Ar}$  and  $^{40}\text{Ar}$ . Of interest to this work, in addition to the stable isotopes, is the rare and radioactive isotope  $^{39}\text{Ar}$  with a natural abundance of  $8.1(3) \times 10^{-16}$  [Col+04]. Other naturally existing isotopes, like  $^{37}\text{Ar}$ , have even lower concentrations. Table 2.1 gives an overview over of some characteristic parameters relevant to ArTTA. Their level structure is discussed in the following, based on [Rin21].

Since argon is a noble gas, it has completely filled electronic shells in the ground state. Each shell has its principal quantum number  $n = \{1, 2, \dots\}$ . The possible orbital angular momenta depending on this are  $l = \{0, 1, \dots, n - 1\} = \{\text{s}, \text{p}, \text{d}, \dots\}$ . Each of these momenta has  $m_l = \{-m_l, -m_l + 1, \dots, m_l\}$  magnetic sublevels. Finally, each electron has a spin of  $s = 1/2$ . Because of their therefore fermionic nature, each state can only be occupied once. This is the well-known Pauli exclusion principle. Accordingly the 18 electrons are in the configuration

$$[\text{Ar}] \equiv 1s^2 2s^2 2p^6 3s^2 3p^6 = [\text{Ne}] 3s^2 3p^6$$

using tuple notation  $nl^e$ , where  $e$  denotes the amount of electrons being in  $nl$ .

The energy difference between the ground state and the next higher addressable level

with photons is  $11.6 \text{ eV} = 107 \text{ nm}$ . This wavelength is, at the moment, not accessible with standard optics and laser technology. Therefore, laser cooling from the ground state is technically not possible. Instead, a metastable state is used as a baseline for laser cooling. It has a lifetime of  $38^{+8}_{-5} \text{ s}$  [KS93] being long enough for efficiently cooling, trapping and counting the atoms. The atoms are transferred into that state using a radio frequency (RF) discharge, which is discussed in subsection 2.4.

The electron being in the metastable state is in the 4s shell. As the orbital radius scales with  $n^2$ , the non-excited electrons form the so-called “body”. All spins  $\vec{s}_i$  of these electrons couple with each other to  $\vec{S}_{\text{body}} = \sum_i \vec{s}_i = 1/2 \cdot \hat{S}_{\text{body}}$  and the orbit angular momenta  $\vec{l}_i$  to  $\vec{L}_{\text{body}} = \sum_i \vec{l}_i = 1 \cdot \hat{L}_{\text{body}}$ , respectively<sup>1</sup>. The LS-coupling results in the total angular momentum of the body  $\vec{J}_{\text{body}} = \vec{S}_{\text{body}} + \vec{L}_{\text{body}} = \{1/2, 3/2\} \hat{J}_{\text{body}}$ . For the metastable state used in the ArTTA apparatus is  $J_{\text{body}} = 3/2$ .

After having coupled the different angular momenta of the body, the momenta of the excited electron are coupled to the body in the following steps. The orbital angular momentum of the excited electron  $\vec{l}$  couples with the total body angular momentum  $\vec{J}_{\text{body}}$  to  $\vec{K} = \{|J_{\text{body}} - l|, |J_{\text{body}} - l| + 1, \dots, J_{\text{body}} + l\} \hat{K}$ . Finally, the spin  $\vec{s}$  of the excited electron couples with  $\vec{K}$  to the resulting total angular momentum  $\vec{J} = \{|K - s|, K + s\} \hat{J}$ . The state of a noble gas isotope with vanishing nuclear spin can be noted using the shortened Racah notation  $nl[K]_J$ .

Figure 2.1 shows a part of the argon fine spectrum relevant for ArTTA<sup>2</sup>. The metastable 4s[3/2]<sub>2</sub> state is shown in blue. It is metastable as a decay to a lower state is highly suppressed due to  $\Delta J = -2$ . For dipole transition the selection rules request  $\Delta J = \{-1, 0, 1\}$  [MS99; Fox06].

From this metastable state the closed transition to the 4p[5/2]<sub>3</sub> state is used for cooling and trapping. For the corresponding wavelength of  $\lambda = 811.754 \text{ nm}$ , standard lasers and optics are available. On the other hand, the quench transition allows to de-excite the metastable

<sup>1</sup> $\hat{x} = \vec{x}/|\vec{x}|$  and  $|\vec{x}| = x$ .

<sup>2</sup>An extended part can be found for example in [Rit13].

**Table 2.1:** Characteristic parameters of the argon isotopes of interest for ArTTA.

The isotopic shift of the cooling transition for the fine splitting is given relative to  ${}^{40}\text{Ar}$ ,  $\Delta\nu_{\rightarrow{}^{40}\text{Ar}}^{(\text{FS})}$ . For  ${}^{39}\text{Ar}$  one has to add the hyperfine shift getting  $\Delta\nu_{\rightarrow{}^{40}\text{Ar}} = 492 \text{ MHz}$  (see figure 2.2). Note that the natural abundance of  ${}^{39}\text{Ar}$  is under change of about 17 % in the past 2500 years due to its cosmogenic production [Gu+21] and the abundance of  ${}^{40}\text{Ar}$  is marginally increasing [Ben+08]. Data taken from [IAE22; Wel11; Lee+06; Col+04; DPS99].

isotope	mass in u	nat. abundance in mole fraction	$T_{1/2}$	$\Delta\nu_{\rightarrow{}^{40}\text{Ar}}^{(\text{FS})}$ in MHz	nuclear spin $I$	discovery
${}^{36}\text{Ar}$	35.968	0.3336(4) %	stable	-450.1(9)	0	1920
${}^{37}\text{Ar}$	36.967	-	35.011(19) d	-	3/2	1941
${}^{38}\text{Ar}$	37.963	0.0629(1) %	stable	-208.1(15)	0	1934
${}^{39}\text{Ar}$	38.964	$8.1(3) \times 10^{-16}$	268(8) y	-94.6(4)	7/2	1950
${}^{40}\text{Ar}$	39.962	99.6035(4) %	stable	0.0	0	1920

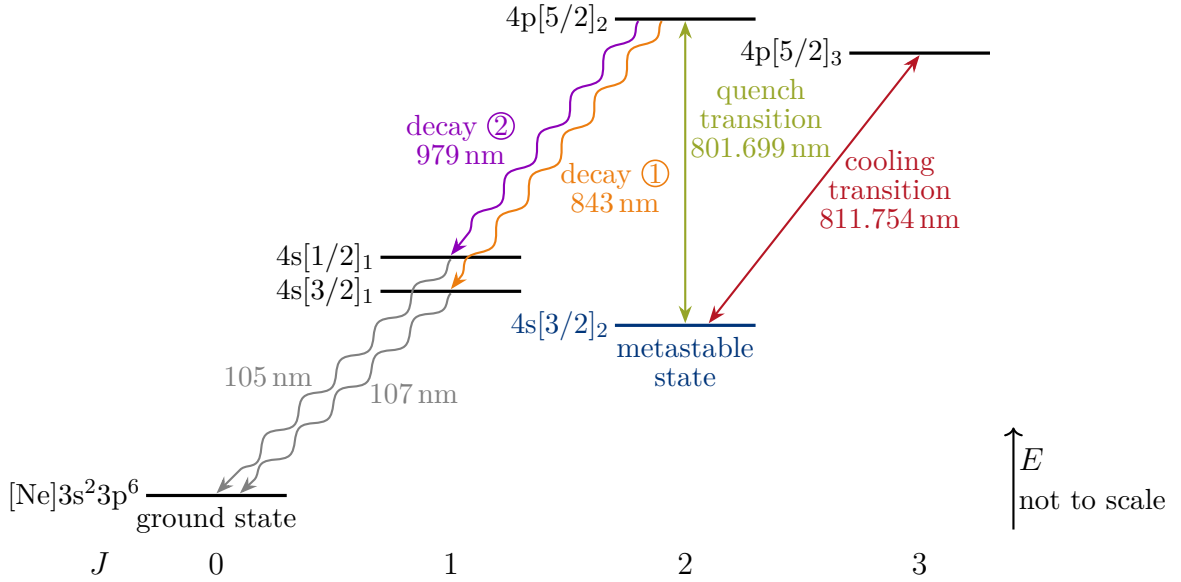


**Figure 2.1:** Part of the argon energy spectrum relevant for ArTTA. The states are named according to the  $nl[K]_J$  notation. The atoms are excited to the metastable state  $4p[5/2]_2$  using a RF discharge. From this state, a closed cooling transition to the state  $4p[5/2]_3$  exists. The quench transition to the state  $4p[5/2]_2$  is used for de-exciting the metastable atoms. Two loss channels exist from  $4p[5/2]_2$ , decay ① and ②, to the interstates  $4s[3/2]_1$  and  $4s[1/2]_1$  before they decay to the ground state. Adapted from [Rin21], data taken from [Kra+22].

atoms via some interstates to the ground state. It also provides an absolute measurement of the metastable flux. The development of a new device to perform these measurements is presented in chapter 4. An absolute measurement is possible, since each atom that transitions to the ground state emits exactly one photon at the detection wavelength.

To distinguish different argon isotopes, one makes use of the isotopic shift. It is caused by a change in nuclear mass and volume, which leads to a shift in energy levels. In the case of  $^{39}\text{Ar}$ , a non-vanishing nuclear spin additionally leads to a hyperfine splitting of the energy levels. Table 2.1 lists the isotopic shifts of the cooling transition compared to  $^{40}\text{Ar}$ . In contrast to the natural linewidth of the selfsame, being  $\gamma = 5.87 \cdot 2\pi$  MHz [MS99], the isotopic shift is large. Nevertheless, the spontaneous scattering rate (2.7) is a proxy to the abundance detection limit. Lets assume having an argon sample with  $^{40}\text{Ar}$  and another argon isotope. One wants to determine the abundance of the latter. A laser beam tuned to the cooling transition of the second is send through the sample. One can define the detection limit as the point where the scattering probability of a photon at the abundant  $^{40}\text{Ar}$  is equal to that at the rare isotope. The minimal limit of the abundance  $A$  is therefore given by

$$A = \lim_{s_0 \rightarrow 0} \frac{1 + s_0}{1 + s_0 + 4\delta^2/\gamma^2}, \quad \text{for } 4\frac{\delta^2}{\gamma^2} \gg 1 + s_0,$$

with  $\delta = 2\pi \cdot \Delta\nu_{\rightarrow 40\text{Ar}}$  being the detuning caused by the isotopic shift. The limits compared to  $^{40}\text{Ar}$  are 36 ppm, 200 ppm and 43 ppm for  $^{39}\text{Ar}$ ,  $^{38}\text{Ar}$  and  $^{36}\text{Ar}$ , respectively. Note that

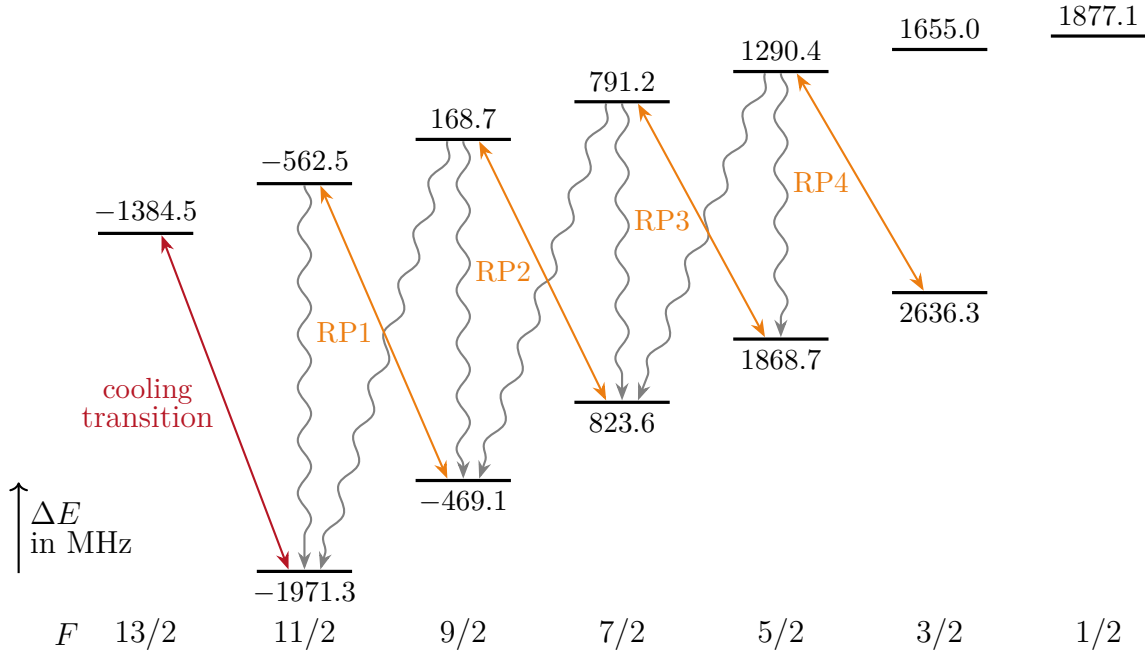


**Figure 2.2:** Hyperfine splitting of the metastable  $4s[3/2]_2$  and the excited state  $4p[5/2]_3$  of the cooling transition. The energy shift  $\Delta E$  towards the unsplit state is given in MHz at each hyperfine state. The vertical distances between the different metastable or excited states are to scale. The cooling transition as well as the four repumper transitions (RPs) and their decay paths are shown. Data taken from [Wel11].

the hyperfine splitting of  $^{39}\text{Ar}$ , discussed in the following, is considered. By looking again at table 2.1 and comparing the limits with the natural abundances, it becomes clear that especially for the abundance measurement of  $^{39}\text{Ar}$  a highly sensitive method is required going far beyond the capability of standard spectroscopy: the Atom Trap Trace Analysis. Here, multiple photons have to interact with an atom before a signal is evaluated. Consequently one has to rise, in first order, the limit  $A$  to the power of the amount of necessary scattering events required for a suitable selectivity. This is the working principle of the ATTA technology, illustrated in figure 1.2.

### 2.1.1 $^{39}\text{Ar}$ Hyperfine Structure and its Consequences

$^{39}\text{Ar}$  has a non-zero nuclear spin of  $I = 7/2$ . Therefore, one has to couple  $\vec{J}$  with  $\vec{I}$  additionally to the total angular momentum  $\vec{F} = \{|I - J|, |I - J| + 1, \dots, I + J\}\hat{F}$ . The resulting hyperfine splitting for the cooling transition is shown in figure 2.2. The selection rule  $\Delta F = \{-1, 0, 1\}$  implies that two closed transitions exist that can be used for laser cooling. The transition  $F = 11/2 \rightarrow 13/2$  is chosen, because the energy difference to the adjacent transition is larger. Nevertheless, off-resonant excitation occurs during the laser cooling process requiring repumper transitions (RPs). They shovel the  $^{39}\text{Ar}$  atoms from the other  $4s[3/2]_2$  hyperfine states to the one with  $F = 11/2$ . Especially after the RF discharge excitation into the metastable state, all hyperfine levels are occupied requiring all RPs in order to address all atoms [Rit13]. However, the 4<sup>th</sup>RP is not used, as the

increase in complexity and effort within the laser setup does not account for the count rate gain.

Only within the Zeeman slower (ZSL) RPs are not necessary. Shortly after the atoms entered the ZSL magnetic field they reach the stretched state  $|m_F| = 11/2$ . From this state only the transition to  $F = 13/2$ ,  $|m_F| = 13/2$  is allowed due to the  $\sigma$ -polarization of the laser beam and its direction parallel to the magnetic field (see also subsection 2.2.4). Therefore off-resonant excitation to  $F = 11/2$  is forbidden.

Another consequence of the hyperfine splitting are reduced forces within the 2D- and 3D-magneto-optical trap (MOT). The net force on the atoms is dependent on the respective detuning  $\delta^\pm$  of the two counter propagating laser beams. The detuning difference of the Zeeman shifted energy levels (2.12) is

$$\delta_Z^+ - \delta_Z^- = (13/2g - 9/2g) \frac{\mu_B B}{\hbar} = 1.231 \frac{\mu_B B}{\hbar},$$

with  $g = 0.6155$  being the Landé factor of the  $F = 13/2$  state (see table 2.2). In contrast, the difference for even mass number isotopes is more than twice as big with  $\delta_Z^+ - \delta_Z^- = 2.6670(2)\mu_B B/\hbar$  [Rit13]. As all stable isotopes have no hyperfine structure, effects of the reduced forces are not present during standard alignment measurements of the apparatus. They first occur when switching to  $^{39}\text{Ar}$ , making considerations of them, as well as testing of the RPs, tedious.

## 2.2 Radiative Transitions of Atoms

Radiative transitions in atoms enable the possibility to manipulate them with light and to gain information by looking at their radiative response. The interaction of (argon) atoms with laser beams strongly depends on their wavelength, polarization and intensity. This behavior is mathematically described in the upcoming subsections giving the basis for further considerations.

### 2.2.1 Density Matrix and Quantum Optical Master Equation

All information about a system in its quantum mechanical description is stored in its wavefunction  $\Psi$  as long as it is in a pure state. However, looking at statistical mixtures<sup>3</sup>, it is not longer possible to describe a system by a single wavefunction. This problem can be overcome using the concept of the density matrix model. The basics are discussed in the following. A more detailed description can be found in [MS99; BP07].

Starting with a system in a pure state described by the wavefunction  $\Psi$ , the density operator is defined as

$$\rho = |\Psi\rangle\langle\Psi|.$$

Using the basis  $\{\phi_n\}$  of the Hilbert space, the density operator can be written as a  $n \times n$

---

<sup>3</sup>Statistical mixtures occur in systems with multiple, uncorrelated subsystems. A common example is the description of a single atom interacting with light, where spontaneous emission is taken into account.

density matrix

$$\rho = \sum_{i,j} |\phi_i\rangle \langle \phi_i| \Psi \rangle \langle \Psi| \phi_j \rangle \langle \phi_j| = \sum_{i,j} \rho_{ij} |\phi_i\rangle \langle \phi_j|, \quad (2.1)$$

with  $|\Psi\rangle = \sum_i c_i |\phi_i\rangle$  and  $\rho_{ij} = c_i c_j^*$ . Note that global phase is not included in the density matrix. Looking at statistical mixtures of several states  $\{\Psi_m\}$  with probability  $p_i$  of state  $i$ , the density operator takes the form [MS99]

$$\rho = \sum_i p_i |\Psi_i\rangle \langle \Psi_i|.$$

The diagonal elements  $\rho_{ii} = |c_i|^2$  of the density matrix give the probability to find the system in the corresponding basis state. Consequently the trace of the density matrix of a normalized system is  $\text{tr}(\rho) = 1$ . The off-diagonal elements  $\rho_{ij} = c_i c_j^*$  are called coherences. They include the phase difference between  $c_i$  and  $c_j$  and the strength of correlation. From equation (2.1) one can see that for a pure state  $\rho_{ij}\rho_{ji} = \rho_{ii}\rho_{jj}$ . This equality no longer holds for statistical mixtures. This leads to the fundamental correlation  $\rho_{ij}\rho_{ji} \leq \rho_{ii}\rho_{jj}$  [MS99].

The description of a quantum mechanical system via the density matrix allows to discuss the interaction of a simple two-level system with light. As a result, the optical Bloch equations (OBEs) are obtained. The density matrix  $\rho$  of a two-level system with ground state  $|g\rangle$  and excited state  $|e\rangle$  is

$$\rho = \begin{pmatrix} \rho_{ee} & \rho_{eg} \\ \rho_{ge} & \rho_{gg} \end{pmatrix}.$$

The energy difference of the ground and excited state is defined as  $\Delta E = \hbar\omega_a$ . The angular frequency of the laser light is  $\omega_L$ . The detuning  $\delta = \omega_L - \omega_a$  of the laser light is assumed to be small compared to the resonance frequency,  $|\delta| \ll \omega_a$ . Together with the requirement  $|\Omega| \ll \omega_L$ , describing a weak coupling, the rotating wave approximation (RWA) can be applied<sup>4</sup>.

$$\Omega \equiv -\frac{E_0}{\hbar} e \langle e | \vec{r} | g \rangle = \frac{E_0}{\hbar} \mu_{eg} \quad (2.2)$$

is the Rabi frequency of the transition using the electric dipole approximation [MS99].  $E_0$  is the laser light field amplitude and  $\mu_{eg}$  the transition dipole matrix element [Fox06]. In the following the interaction picture is used<sup>5</sup>, denoted by the suffix  $I$ . With that the interaction Hamiltonian  $\mathcal{H}_I$  can be expressed as

$$\mathcal{H}_I = \frac{\hbar\Omega}{2} \begin{pmatrix} 0 & e^{-i\delta t} \\ e^{i\delta t} & 0 \end{pmatrix}. \quad (2.3)$$

---

<sup>4</sup>The RWA neglects terms in the Hamiltonian oscillating with frequency  $\omega_L + \omega_a$ .

<sup>5</sup>In quantum mechanics three pictures are used: the Schrödinger, the Heisenberg and the interaction picture. In the Schrödinger picture, the density matrix is time dependent and the operators are mostly constant in time. Expressing the time dependency with the operators one receives the Heisenberg picture. The general case is the interaction picture where only the time dependence of one part of the Hamiltonian  $\mathcal{H} = \mathcal{H}_0 + \mathcal{H}_1$  is transferred. A general discussion can be found in [BP07].

The time evolution of the, up to now, closed system is described by the Liouville-von Neumann equation [BP07]

$$\frac{d\rho_I}{dt} = -\frac{i}{\hbar} [\mathcal{H}_I, \rho_I].$$

The Liouville-von Neumann equation is derived from the time dependent Schrödinger equation. The two-level system performs Rabi oscillations between the ground and the excited state, while remaining in a pure state. Opening and coupling the system to the environment involves the process of spontaneous photon emission which is the basis for many laser cooling techniques. The quantum optical master equation, also known as Lindblad equation [BP07],

$$\frac{d\rho_I}{dt} = -\frac{i}{\hbar} [\mathcal{H}_I, \rho_I] + \mathcal{D}(\rho_I) \quad (2.4)$$

allows to include spontaneous emission of photons. Therefore, the coherence of the pure state decays with a rate of  $\gamma/2$  and the system evolves into a statistical mixture. The dissipator  $\mathcal{D}(\rho_I)$  of the two-level systems thus reads<sup>6</sup>

$$\mathcal{D}(\rho_I) = \gamma \left( \sigma \rho_I \sigma^\dagger - \frac{1}{2} \{ \sigma^\dagger \sigma, \rho_I \} \right) = \gamma \begin{pmatrix} -\rho_{I,ee} & -\rho_{I,eg}/2 \\ -\rho_{I,ge}/2 & \rho_{I,ee} \end{pmatrix}. \quad (2.5)$$

Here,  $\sigma$  is the annihilation and  $\sigma^\dagger$  the creation operator for the excited state of the two-level system. Inserting (2.3) and (2.5) in the Lindblad equation (2.4) results in a set of four coupled differential equations, the optical Bloch equations (OBEs). Figure 2.3 shows a numerical solution of the OBES for an exemplary parameter set. The steady-state of the OBES is analyzed in the subsequent subsection.

### 2.2.2 Scattering Rate

Einstein developed a phenomenological description for stimulated absorption, stimulated emission and spontaneous emission [Fox06]. He linked those three types of transitions together, forming the optical rate equation

$$\frac{dN_e}{dt} = \underbrace{B_{ge} N_g u(\omega)}_{\text{stim. abs.}} - \underbrace{B_{eg} N_e u(\omega)}_{\text{stim. em.}} - \underbrace{A_{eg} N_e}_{\text{spon. em.}}. \quad (2.6)$$

$N_i$  describes the amount of atoms in the ground, respectively excited state. The spectral energy density of the electromagnetic field with angular frequency  $\omega$  is given by  $u(\omega)$ .  $A_{eg}$ ,  $B_{ge}$  and  $B_{eg}$  are the Einstein coefficients. These are correlated to each other according to

$$g_g B_{ge} = g_e B_{eg},$$

$$A_{eg} = \frac{\hbar \omega^3}{\pi^2 c^3} B_{eg},$$

---

<sup>6</sup>Stimulated emission and absorption by the thermal background radiation is neglected as the contribution is comparably small.

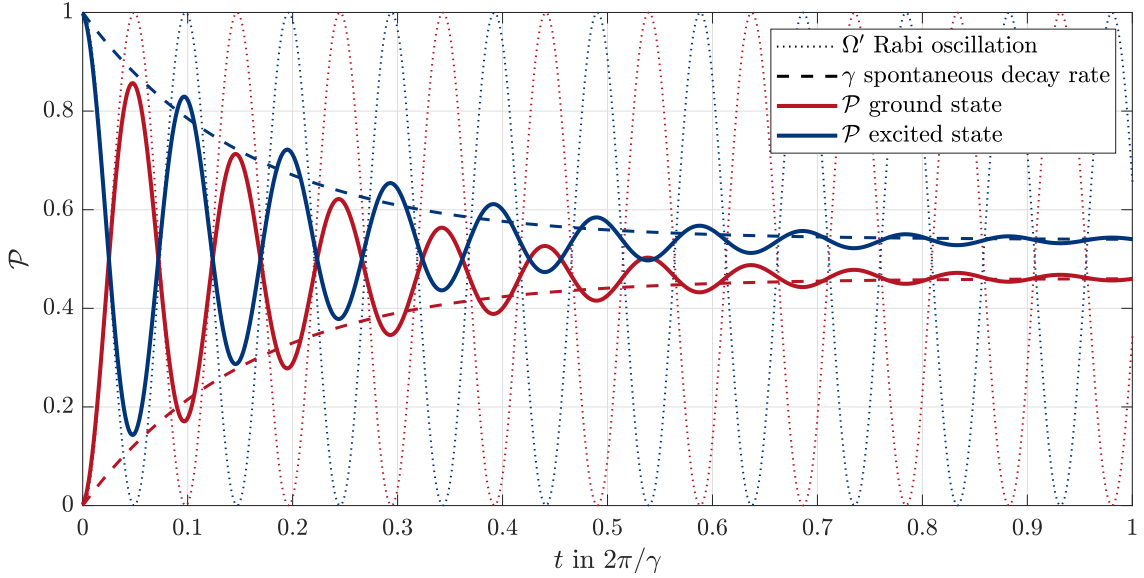


**Figure 2.3:** Solution of the OBEs for a two-level system. The atom is in the ground state at  $t = 0$ . For  $t > 0$  a light field of strength  $\Omega = 10\gamma$  and detuning  $\delta = 2\gamma$  interacts with the atom.  $\gamma$  is the spontaneous decay rate of the atom. The probability to find the atom in the ground (blue), respectively excited (red) state is given by  $\mathcal{P}$  (solid lines). The dashed lines illustrate the decay of the coherence due to spontaneous emission. The dotted lines represent the Rabi oscillations at frequency  $\Omega' = \sqrt{\Omega^2 + \delta^2}$  without spontaneous emission.

where  $g_i$  is the degeneracy of the energy level  $i$ .  $A_{eg}$  is the already known decay rate  $\gamma = A_{eg}$ . Therefore transitions that have a high absorption probability also have a high emission probability [Fox06]. However, some aspects of the scattering rate are first covered by a quantum mechanical description.

The preceding subsection ended with the OBEs. By solving them for the steady-state condition one derives the scattering rate [MS99]

$$\gamma_s = \frac{\gamma}{2} \frac{s_0}{1 + s_0 + 4\delta^2/\gamma^2}. \quad (2.7)$$

The spontaneous decay rate  $\gamma$  of the excited state is a physical constant of the corresponding transition.  $\delta = \omega_L - \omega_a$  is the previously introduced detuning of the laser light with respect to the transition angular frequency  $\omega_a$ . The dimensionless on-resonance saturation parameter

$$s_0 \equiv 2 \frac{|\Omega|^2}{\gamma^2} = \frac{I}{I_s} \quad (2.8)$$

is defined to be one for the scattering rate being half its maximum [MS99].  $I$  is the current intensity and

$$I_s \equiv \pi\gamma hc/3\lambda^3 \quad (2.9)$$

is the transition dependent saturation intensity for a relative transition strength of one

(see the following subsection for details about the relative transition strength).

As the scattering rate  $\gamma_s$  is proportional to the light force  $\vec{F}$ , it is worth analyzing the impact of the two free parameter  $s_0$  and  $\delta$ . For a weak coupling  $s_0 \ll 1$  the scattering rate increases linearly with  $s_0$ , correspondingly is  $\gamma_s \propto s_0$ . The scattering rate has its maximum for  $\delta = 0$  becoming  $\gamma_s \approx \gamma s_0/2$ . As the scattering rate decreases with increasing absolute detuning, one can define a frequency range of interaction, the linewidth which is equal to the decay rate  $\gamma$ . At very high intensities  $s_0 \gg 1$  the scattering rate saturates at  $\gamma_s = \gamma/2$  and the linewidth is broadened to  $\gamma' = \gamma\sqrt{1+s_0}$  [MS99]. Therefore the atom is less sensitive to the detuning  $\delta$ .

Coming back to the light induced force on the atom  $\vec{F}$ . Each photon has a momentum  $\vec{p} = \hbar\vec{k}$ . Here,  $\vec{k}$  is the wave vector of the laser light. This momentum is transferred to the atom during the absorption of the photon. In case of stimulated emission the same momentum is transferred back to a photon, resulting in an unchanged momentum of the atom. If the atom decays via spontaneous emission, the photon is radiated in a random direction. Therefore, the overall recoil vanishes for many spontaneously emitted photons. Consequently, the rate of spontaneous emission determines the strength of the force while the wave vector is responsible for its direction:

$$\vec{F} = \gamma_s \hbar \vec{k}. \quad (2.10)$$

Since the force results in a change of the atom velocity  $\vec{v}$ , the Doppler effect has to be considered. In the atom's rest frame the angular frequency of the laser light shifts by [Fox06]

$$\delta_D = -\vec{k} \cdot \vec{v}. \quad (2.11)$$

For a given velocity one can set the laser frequency appropriately. However, changing the atom velocity over a wide range is mandatory in many applications. This requires additional compensation approaches. Therefore, the Zeeman effect is introduced in the following.

### 2.2.3 Zeeman Effect

The preceding discussion ended with the Doppler shift (2.11) and the request for another effect changing the detuning of a transition. With the help of a magnetic field the atom's internal structure can be changed and thus the detuning: the Zeeman effect.

In section 2.1 the atomic level structure of argon with quantum numbers  $L$ ,  $S$  and  $J$  was introduced. Each of those states has  $2J + 1$  degenerate magnetic sublevels  $m_J = \{-J, -J + 1, \dots, J\}$ . Applying a magnetic field leads to a shift of the  $m_J$  sublevels with respect to their energy, which is called the Zeeman effect [Fox06]. For the following discussion the quantization axis<sup>7</sup> is chosen along the  $z$ -axis and  $\vec{B} = B\hat{z}$ .

The energy of an atom's state  $|Jm_J\rangle$ , respectively  $|Fm_F\rangle$ , in a magnetic field  $B$  is shifted

---

<sup>7</sup>The quantization axis defines the orientation of the mathematical description of the system. In most cases it is set along the  $z$ -axis.

by

$$\Delta E_Z = m_{J,F} g_{J,F} \mu_B B, \quad (2.12)$$

with the Bohr magneton  $\mu_B$  and the Landé  $g$ -factor [Fox06]

$$g_J = 1 + \frac{J(J+1) + S(S+1) - L(L+1)}{2J(J+1)}, \quad \text{respectively} \quad (2.13)$$

$$g_F \approx g_J \frac{F(F+1) + J(J+1) - I(I+1)}{2F(F+1)}. \quad (2.14)$$

Thus the degenerate sublevels  $m_{J,F}$  are split into a manifold of magnetic sublevels. The separation of them increases linearly with the magnetic field. The most important Landé factors for the ArTTA technology are listed in table 2.2. Note that the Zeeman regime discussed here is only valid for weak magnetic fields. At higher field strengths one has to consider the Paschen-Back effect.

With equation (2.12) the Zeeman detuning  $\delta_Z$  of a transition from  $|Jm_J\rangle$  to  $|J'm_{J'}\rangle$  is simply the difference between the two energy shifts  $\Delta E_Z$ :

$$\delta_Z = (m_J g_J - m_{J'} g_{J'}) \frac{\mu_B B}{\hbar}. \quad (2.15)$$

The different Landé  $g$ -factors of  $^{39}\text{Ar}$  result in lower forces within the 2D- and 3D-MOT, as discussed in subsection 2.1.1. A more detailed discussion is found in [Rit13].

## 2.2.4 Transition Strengths

Coming back to the discussion of the level structure of argon derived by coupling the different angular momenta in section 2.1. This coupling resulted in the fine and hyperfine structure. The coupled states have multiple magnetic sublevels  $m_J$ , respectively  $m_F$ , as discussed in the preceding part. In the following, transition characteristics depending on the magnetic sublevel are discussed.

The transition strength varies for different ground states  $|Jm_J\rangle$  and excited states  $|J'm_{J'}\rangle$ .

**Table 2.2:** Landé  $g$ -factors for the main states used. Calculated values are obtained using the generalized Landé equation instead of the common equation (2.13). In the latter the Landé  $g$ -factor of the electron is set to  $g_{e^-} = -2$ . The measured values are used for calculating the values of  $^{39}\text{Ar}$ . Measured values are taken from [SGH81; Bra99].

state		$^{36}\text{Ar}, ^{38}\text{Ar}, ^{40}\text{Ar}$		$^{39}\text{Ar}$
		calculated	measured	calculated
metastable	$4s[3/2]_2$	1.5012	1.5008(2)	0.5457 ( $F = 11/2$ )
excited (cooler)	$4p[5/2]_3$	1.3341	1.3335(1)	0.6155 ( $F = 13/2$ )
excited (quench)	$4p[5/2]_2$	1.1671	1.11 221(33)	-

The relative transition strength  $\Xi_{m_J, m_{J'}}^{J, J'}$  is defined as the transition strength divided by the maximum  $\alpha$  of the selfsame with same  $J$  and  $J'$ . Thus it is proportional to the absolute square of the transition dipole moment  $\mu_{eg}$  [MS99]:

$$\Xi_{m_J, m_{J'}}^{J, J'} \equiv \left| \frac{\mu_{eg}}{\alpha} \right|^2 = (2J+1) \begin{pmatrix} J & 1 & J' \\ m_J & \Delta m & -m_{J'} \end{pmatrix}^2. \quad (2.16)$$

$\Delta m = m_{J'} - m_J$  is the change of the magnetic sublevel. The matrix with parentheses denotes the Wigner 3j-symbol and is a direct consequence of the momenta coupling. The maximum value is given by

$$|\alpha|^2 \equiv \sum_{L, L'} | -e \langle \alpha' L' | | \vec{r} | | \alpha L \rangle |^2 (2J'+1) \left\{ \begin{matrix} L' & J' & S \\ J & L & 1 \end{matrix} \right\}^2, \quad (2.17)$$

with the Wigner 6j-symbol as matrix with braces.  $\langle \alpha' L' | | \vec{r} | | \alpha L \rangle$  is the radial term of the dipole moment being equal for all transitions from  $J$  to  $J'$ .

In the case of atoms with hyperfine splitting, the coupling of  $\vec{J}$  with the nuclear spin  $\vec{I}$  to the total angular momentum  $\vec{F}$  has to be added. The relative transition strength  $\Xi_{m_F, m_{F'}}^{J, J', F, F'}$  now reads [MS99]

$$\begin{aligned} \Xi_{m_F, m_{F'}}^{J, J', F, F'} &\equiv \left| \frac{\mu_{eg}}{\alpha} \right|^2 \\ &= (2J+1)(2F+1)(2F'+1) \left\{ \begin{matrix} J' & F' & I \\ F & J & 1 \end{matrix} \right\}^2 \left( \begin{matrix} F & 1 & F' \\ m_F & \Delta m & -m_{F'} \end{matrix} \right)^2. \end{aligned} \quad (2.18)$$

The radial term is still independent of the magnetic substates and  $\alpha$  is given by equation (2.17).

The quadratic dependence of the transition strength on  $\mu_{eg}$  also implies that the transition strength is quadratically dependent on the Rabi frequency (compare equation (2.2)). Correspondingly the Rabi frequency  $\Omega_{m, m'}$  for a transition from the magnetic sublevel  $m$  to  $m'$  scales with the square root of the relative transition strength  $\Xi_{m, m'}$ :

$$\Omega_{m, m'} = \sqrt{\Xi_{m, m'}} \Omega_\alpha.$$

$\Omega_\alpha = \alpha E_0 / \hbar$  is the maximum Rabi frequency. The suffix  $J$ , respectively  $F$ , is neglected, as it is valid for both.

## Selection Rules and Polarization

So far the relative transition strength of the magnetic sublevels and their splitting to individual energy levels in a magnetic field was discussed. However, how one can drive a specific subset of the possible transitions and, more general, which changes of quantum numbers are possible under single photon interactions is part of the following overview. A summary with some more explanations can be found in [Fox06].

The selection rules for electric-dipole transitions of many-electron atoms are [Fox06]:

- $\Delta l = \{-1, 1\}$  for the changing electron

- $\Delta m = \{-1, 0, 1\}$
- $\Delta L = \{-1, 0, 1\}$ ,  $L = 0 \nrightarrow 0$
- $\Delta J = \{-1, 0, 1\}$ ,  $J = 0 \nrightarrow 0$ , respectively  $F$
- $\Delta S = 0$ .

These rules are a result of momentum conservation and the interaction of the photon with the angular momentum  $l$  but not with the spin  $s$ . Let us define the  $z$ -axis again as the quantization axis. Is a photon positive circular polarized along the  $z$ -axis<sup>8</sup>, it is referred to as  $\sigma^+$  polarized. As this photon carries an angular momenta of  $+\hbar$  along the  $z$ -axis, it drives transitions with  $\Delta m = +1$ . The same accounts for a  $\sigma^-$  polarized photon but with minus signs. The third set of transitions with  $\Delta m = 0$  is driven by  $\pi$  polarized light, which is linearly polarized along the  $z$ -axis. Thus, once the magnetic sublevels are not degenerate, one can select which set of transition shall be driven by choosing the appropriate polarization:  $\sigma^+$ ,  $\pi$ , respectively  $\sigma^-$ .

The polarization of the spontaneously emitted photons also depend on the transition of the selfsame. Looking into the negative or positive direction of the  $z$ -axis one will never observe photons from a  $\pi \hat{=} \Delta m = 0$  transition. The electron oscillates as a Hertzian dipole along the  $z$ -axis. Consequently, no radiation is emitted in the oscillation direction. Following this argument, one will observe linearly polarized light along the  $z$ -axis by looking from the  $x, y$ -plane. On the other hand the electron rotates around the  $z$ -axis for  $\sigma^\pm \hat{=} \Delta m = \pm 1$  transitions. Consequently one will observe light which is perpendicular polarized to the  $z$ -axis by looking from the  $x, y$ -plane. Therefore it also depends on the propagation direction of the laser beam towards the  $z$ -axis which set of transitions can be driven. More information about the radiation direction probability is given in appendix A.1.

## 2.3 Laser Cooling and Magneto-Optical Trapping

In the preceding section the basic information about radiative transitions and how one addresses and manipulates them are given. This is now applied within the frame of standard laser cooling techniques and magneto-optical trapping of atoms. The discussion is restricted to basics, as one finds general discussion in [MS99; Fox06] and many other books. Detailed discussions in the context of ArTTA are additionally found in [Rin21; Ebs18; Rit13; Wel11] and further.

### Zeeman Slower

Zeeman slowers (ZSLs) are used for decelerating fast, mostly thermal atoms. For the ArTTA apparatuses an increasing magnetic field slower is used. Therefore, an atom starts at position  $z = 0$  with a magnetic field  $\vec{B} = 0\hat{z}$ . The initial velocity  $v_i$  is in positive  $z$ -direction. A laser beam pointing in negative  $z$ -direction has a detuning  $\delta_L = -kv_c$ ,

---

<sup>8</sup>If the propagation direction is along the  $z$ -axis and one is looking into the light source, the electric field vector rotates counterclockwise. The light is then left circularly polarized [Fox06].

equal to the Doppler shift (2.11) of the fastest atoms one wants to decelerate. For the ArTTA apparatuses is  $\delta_L = -746 \cdot 2\pi$  MHz. It corresponds to a maximal capture velocity of  $v_c \approx 610 \text{ m s}^{-1}$  [Ebs18].

During the flight of the atoms through the ZSL the effective detuning is given by

$$\delta = \delta_L + \delta_D(v(z)) + \delta_Z(B(z)).$$

Thus the position dependent Zeeman detuning  $\delta_Z$  (2.15) has to compensate the decreasing Doppler shift such that  $\delta \approx 0$  for all atoms in the deceleration process. With the light induced force (2.10), the maximum deceleration is given by

$$a_{\max} = \frac{F_{\max}}{m} = \frac{\hbar k \gamma}{2m}.$$

Here the saturation parameter is set to  $s_0 \rightarrow \infty$ . However, the maximum deceleration  $a_{\max}$  is not achievable. Already small imperfections in the magnetic field and finite laser power result in lower forces. Therefore, atoms get a slightly too fast and leave the deceleration process. A so-called fudge factor  $\xi$  is introduced, to overcome this problem, being  $\xi = 0.44$  for the ArTTA machines [Rin21]. The deceleration present in the ZSL is thus reduced to  $a = \xi a_{\max}$ , resulting on the other hand in a approximately five times longer ZSL than at the physical limit. This also has negative consequences, which have to be balanced. Two are increased transverse spreading. On the one hand due to finite initial transverse velocities, on the other hand due to transverse heating caused by the deceleration. Both are increased because of the longer travel time through the ZSL. Section 5.3 broaches this issue.

The final velocity  $v_f$  of the ZSL is, with the maximum magnetic field  $B_{\max} \approx 470 \text{ G}$ , about  $v_f \approx 70 \text{ m s}^{-1}$  [Ebs18]. This is well above the capture velocity of the MOT. However, a second ZSL, the so-called “booster”, is used for further decreasing the atom velocity. In order to keep transverse spreading minimal, the booster uses the increasing field of the MOT coils. Therefore the final deceleration takes place under the presence of the MOT laser beams cooling the atoms in transverse direction.

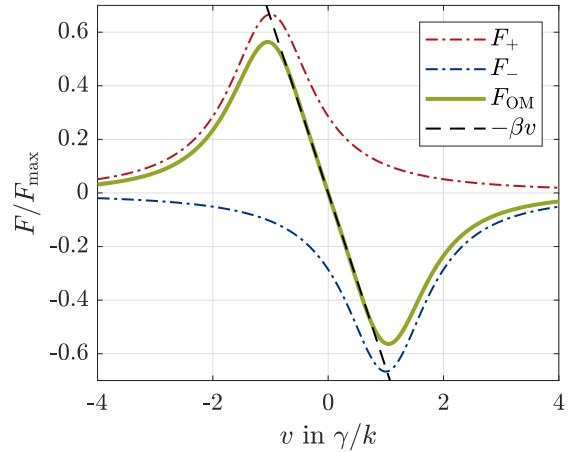
## Optical Molasses

So far the interaction of atoms with a single laser beam has been discussed. For low laser intensities this is now expanded to two counter propagating laser beams in the absent of a magnetic field.

In the case of low laser intensities the process of stimulated emission can be neglected. Therefore each laser beam excites an atom individually, followed by spontaneous emission. For an atom at rest the effective detuning  $\delta_{\pm} = \pm \delta_L$  of the laser beams is, in absolute terms, equal. Consequently the net force  $\vec{F}$  is zero. This is no longer the case for an atom with velocity  $v$  in the direction of the + laser beam. The effective detuning gets  $\delta_{\pm} = \delta_L \mp kv$ . The net force results with (2.10) in

$$\vec{F}_{\text{OM}} = \vec{F}_+ + \vec{F}_- \stackrel{v \lesssim \gamma/k}{\approx} \frac{8\hbar k^2 \delta_L s_0 \vec{v}}{\gamma(1 + s_0 + 4\delta_L^2/\gamma^2)^2} \equiv -\beta \vec{v}, \quad (2.19)$$

**Figure 2.4:** Velocity dependent damping forces for an one-dimensional optical molasses.  $\beta$  is the damping coefficient for small velocities  $v$ .  $F_{\pm}$  are the forces of the laser beams traveling in  $\pm$  direction.  $F_{\text{OM}}$  is the resulting net force on the atom. The saturation parameter is set to  $s_0 = 2$  and the laser detuning to  $\delta_L = -\gamma$ .  $F_{\text{max}} = \hbar k \gamma / 2$  is the maximum force. The figure is adapted from [MS99].



where terms of order  $(kv/\gamma)^4$  and higher have been neglected [MS99]. For  $\delta_L < 0$  is  $\beta > 0$  and the net force opposes the velocity. The atom is damped viscous giving the optical molasses its name. Figure 2.4 shows a graph of the forces.

All in all optical molasses can cool atoms down to the Doppler cooling temperature limit  $T_D = \hbar\gamma/2k_B$ , with  $k_B$  being the Boltzmann constant [MS99]. In the ArTTA machines the end of the collimator nearly forms an optical molasses (see also section 3.3). Therefore the metastable atoms are leaving the source chamber in a collimated beam. However, an optical molasses does not confine or trap atoms as an spatial dependent term is missing. This is the main difference compared to a MOT.

## Magneto-Optical Trap

A magneto-optical trap (MOT) uses the cooling force of an optical molasses and combines it with a position dependent restoring force. This is achieved using an inhomogeneous magnetic quadrupole field  $\vec{B}(\vec{r})$ . In one dimension the magnetic field close to the center is given by  $B(z) = \mathcal{B}z$ , with gradient  $\mathcal{B}$ . For the following discussion is  $\mathcal{B} > 0$  assumed. The easiest case is a transition from  $J = 0$  to  $J = 1$ . The magnetic sublevels  $m_J$  of the excited state have thus a position dependent energy, as depicted in figure 2.5.

In the 1-D case two laser beams travel in  $\pm z$ -direction with  $\sigma^{\pm}$  polarization. The  $\sigma^+$  beam thus couples with the  $m_J = 0 \rightarrow 1$  transition and, respectively, the  $\sigma^-$  beam with  $m_J = 0 \rightarrow -1$ . For an atom with velocity  $\vec{v} = v\hat{z}$  the effective detuning is

$$\delta_{\pm} = \delta_L \mp kv \pm (g_g|m_g| - g_e|m_e|) \frac{\mu_B B}{\hbar},$$

with the Landé  $g$ -factor of the ground  $g_g$ , respectively excited state  $g_e$ . The resulting net force of the MOT is again given by the sum of the single forces:  $\vec{F}_{\text{MOT}} = \vec{F}_+ + \vec{F}_-$ . For small Doppler and Zeeman detunings compared to the laser detuning, one can expand the net force resulting in

$$\vec{F} = -\beta\vec{v} - \kappa\vec{r}, \quad \text{with} \quad \kappa = \underbrace{(g_e|m_e| - g_g|m_g|)\mu_B}_{=\mu'} \frac{\mathcal{B}}{\hbar k} \beta$$

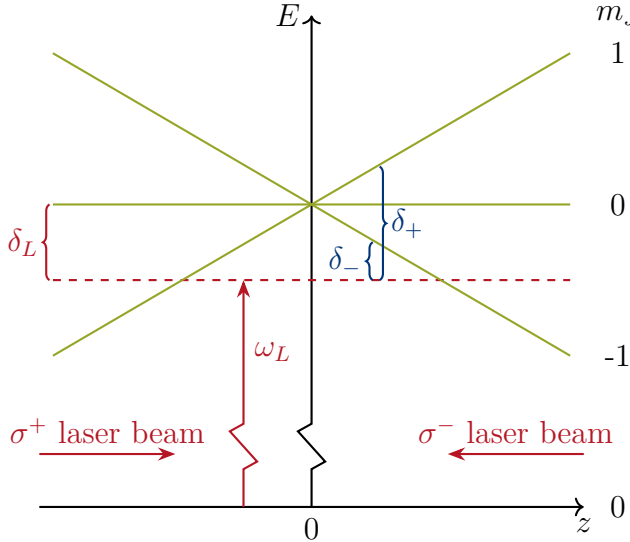


**Figure 2.5:** Illustration of the MOT concept in one dimension for an atom at rest with a transition from  $J = 0$  to  $J = 1$ . The magnetic field  $B(z)$  is proportional to the position  $z$  and therefore also the energy of the magnetic sublevels  $m_J = \{-1, 0, 1\}$  (green lines). The  $\sigma^\pm$  laser beams travel in  $\pm z$ -direction and have a detuning of  $\delta_L < 0$ . The effective detunings  $\delta_\pm$  determine the net force  $\vec{F}_{\text{MOT}}$  of the MOT. The figure is adapted from [MS99].

being the spring constant and the damping coefficient  $\beta$  as defined in (2.19) [MS99].  $\mu'$  is the effective magnetic moment.

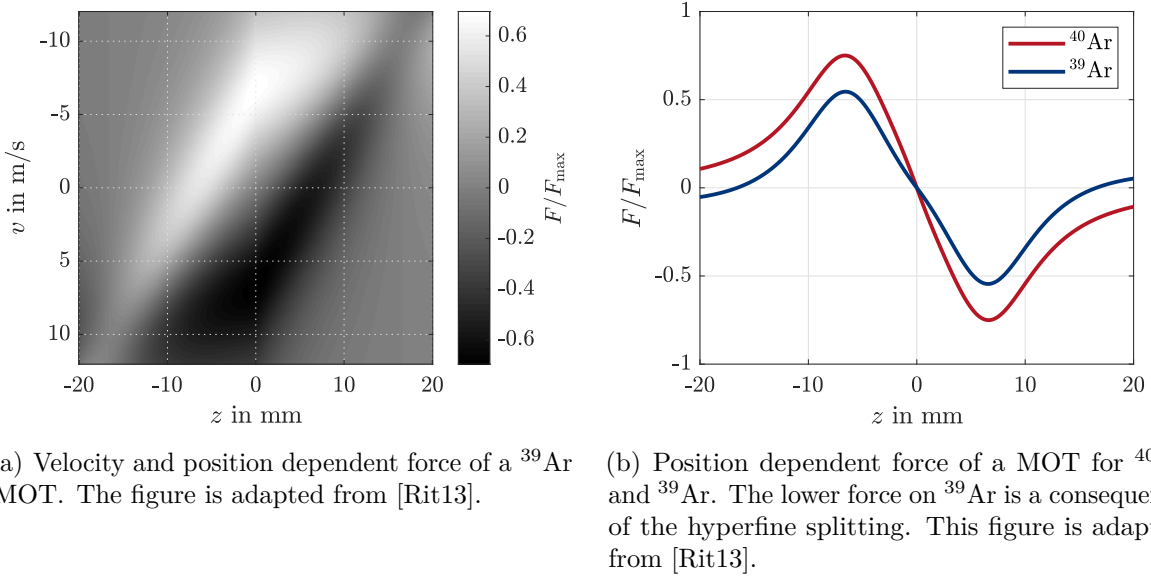
For a transition from a ground state with  $J > 0$  the considerations have to be complemented. Now several magnetic sublevels exist in the ground state. Is the atom mainly interacting with the  $\sigma^+$  laser beam, it is pumped in the stretched state  $m_J = J$ . Therefore the effective magnetic moment of the  $\sigma^-$  laser beam is now given by  $\mu'_- = (g_g J - g_e(J-1))\mu_B$ . Once the atom is interacting mainly with the  $\sigma^-$  laser beam, it is pumped to the opposite stretched state  $m_J = -J$ . The effective magnetic moment of the selfsame now reads  $\mu'_+ = -(g_g J - g_e(J+1))\mu_B$ . Therefore the absolute value of the effective magnetic moment of the laser beam changes by  $2g_e\mu_B$ . Correspondingly the strength of the Zeeman shift depends on the current  $m_J$  of the ground state.

The force of a MOT is exemplarily shown for the argon cooling transition in figure 2.6. It is assumed that the atom instantaneously changes the stretched state, when it passes  $B = 0$ . In reality one has to define the trajectory through the MOT and solve the full set of dynamical equations.  $^{39}\text{Ar}$  has twelve magnetic sublevel ground states, even mass number isotopes five. Accordingly the  $^{39}\text{Ar}$  atoms need more time to change the stretch state further decreasing the MOT force.

Figure 2.6(b) illustrates the reduced force on  $^{39}\text{Ar}$  atoms compared to the even mass number isotopes (remember the discussion in subsection 2.1.1). It is caused by a lower detuning difference of the two opposing laser beams, as a consequence of the hyperfine splitting. Aligning the apparatus is therefore tedious having only measurements with  $^{39}\text{Ar}$  underlying the lower forces.

## 2.4 Argon Plasma and Metastable Atom Production

Plasma physics in general and the generation of metastable argon using plasmas in particular are a separate field of research. In the following, the basic processes involved in electron-induced argon excitations are discussed along with their main features. However, a detailed modeling of the plasmas used in this work would go beyond the scope of this



(a) Velocity and position dependent force of a  $^{39}\text{Ar}$  MOT. The figure is adapted from [Rit13].

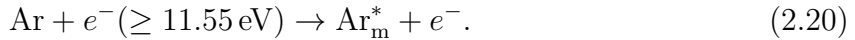
(b) Position dependent force of a MOT for  $^{40}\text{Ar}$  and  $^{39}\text{Ar}$ . The lower force on  $^{39}\text{Ar}$  is a consequence of the hyperfine splitting. This figure is adapted from [Rit13].

**Figure 2.6:** MOT force for the argon cooling transition. The saturation parameter is set to  $s_0 = 5$ , the laser detuning to  $\delta_L = -8 \cdot 2\pi$  MHz and the magnetic field gradient to  $\mathcal{B} = 0.9 \text{ G mm}^{-1}$ . The atom is assumed to be in the stretched state  $m_J = \pm J$  for a position  $z = \mp|z|$ . This reduced examination results in forces pushing the  $^{39}\text{Ar}$  atoms away from the center for outer regions.

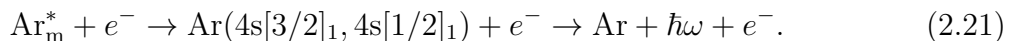
thesis. Many individual aspects have to be taken into account, which alone already have the scope of a research project.

A plasma contains a significant amount of free charged particles and is one of four fundamental states of matter. In the context of ATTA are weakly ionized plasma discharges used. They are inductively driven by a RF. Collisions of charged particles with neutral atoms are as well important as losses at the surface [LL05]. Furthermore, the plasma is sustained by ionization of neutral atoms and the electrons are not in equilibrium with the ions.

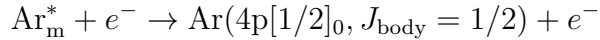
The main metastable argon  $\text{Ar}_m^*$  production mechanism is the electron-impact excitation from the ground state [Bel+09; BG95; FLR85]:



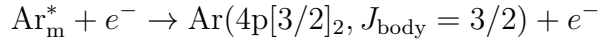
11.55 eV is the energy difference of ground and metastable state. The electron-induced excitation cross-section of equation (2.20) has its maximum around 25 eV [Loc+16]. In addition, several intermediate states, that decay to the metastable state by radiation, contribute to the set of metastable argon atoms. Their cross-sections are around the peak comparable to that of equation (2.20) [Loc+16]. However, there are also various loss mechanisms. A major metastable loss mechanism in low-pressure plasmas, as present in ATTA, is electron-induced quenching to a nearby non metastable state, followed by radiative decay to the ground state [Bel+09; BG95]:



Especially moderate- and low-energy electrons are responsible for these processes [Hay+09; BG95]. Note that the cross-section at 3 eV of <sup>9</sup>

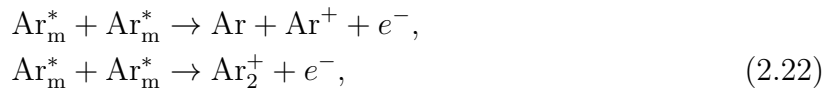


is of the same order as the maximum of (2.20) [Loc+16]. However, the cross-section of



is even around two orders of magnitude larger. Fortunately, 71 % subsequently decay back to the metastable state, while the remainder de-excite to the ground state<sup>10</sup>.

Diffusion followed by wall collision and relaxation is another relevant loss channel within the plasma source tube [BG95; FLR85]. In contrast, losses due to metastable pooling, also named metastable-metastable collisions



occur especially within the MOT, as the densities there can be appropriately high. The corresponding rate constant is  $\Gamma_{mm} = 6.4 \times 10^{-16} \text{ m}^3 \text{ s}^{-1}$  [BG95; FLR85; FR83]. These are the main processes. For example, a more complete set is given in [BG95; FLR85].

The electron energy distribution within a weakly ionized plasma is often in first order Maxwellian [LL05]. Therefore, the process of metastable argon atom production is not describable by a simple rate equation for one electron energy. Even more, in cases of non-Maxwellian electron energy distributions they have to be described using the kinetic theory of discharges, which is introduced in [LL05], for example. There is special software for solving these problems (see for example <https://us.lxcat.net/download/>).

A detailed discussion of calculations and experimental data for various argon electron-impact excitation cross-sections can be found in [ZWB14]. Generally, reactions between various species and many more is provided by *Quantemol-DB* (<https://www.quantemoldb.com/>) [Ten+22]. Thereby, each state of argon or other elements and molecules is a separate species. Another plasma data exchange project for low-temperature plasma is *LXCat*, which can be addressed at <https://us.lxcat.net/home/>.

## 2.5 AC Electronics

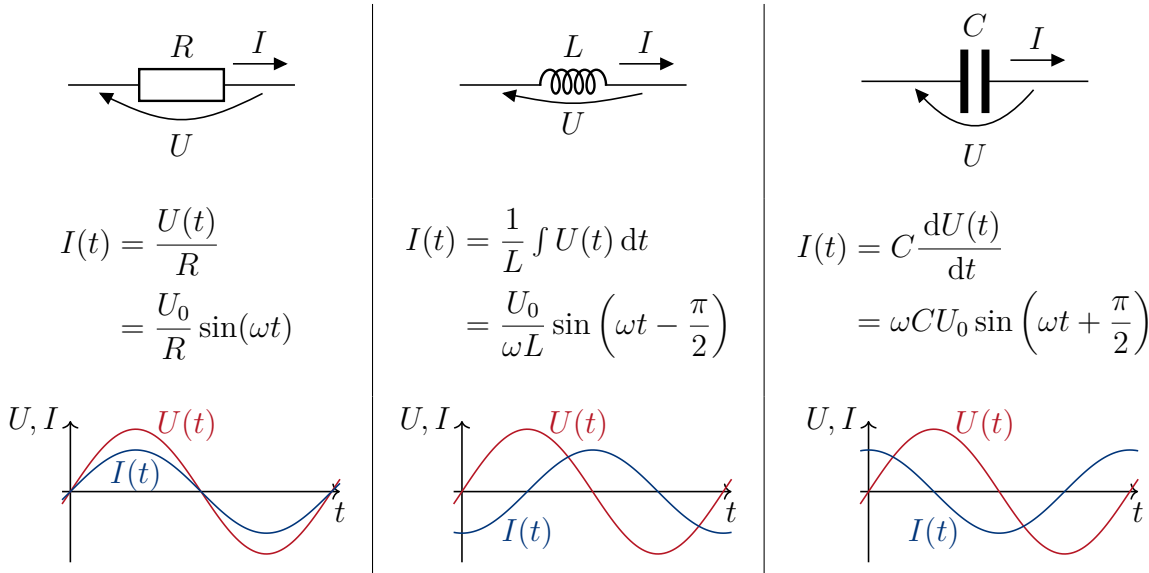
This section gives a rough overview over fundamental linear electrical components and their responses applying sinusoidal voltages or currents. It is assumed that the reader is familiar with the basics of direct current (DC) electronics. The algebra of circuits is recapitulated and extended to sinusoidal voltages. The discussion of a transmission line provides the basis for describing networks with the propagation of waves. The S-parameter will be introduced as one of the basic measurement techniques in AC circuit analysis. All this provides the background for analyzing the radio frequency (RF) properties of the

---

<sup>9</sup> $J_{\text{body}}$  is given here because otherwise the state notation is not unique.

<sup>10</sup>The loss probability of 29 % is calculated using the A Einstein coefficients given in [Wie+89].

**Table 2.3:** Response of the current applying a sinusoidal voltage  $U(t) = U_0 \sin(\omega t)$  across the components. The technical direction of electric current is marked. This figure is adapted from [CG02].



plasma sources in chapter 6. The interested reader will find more details and further discussions in [Hag09] or many other books.

### 2.5.1 Fundamental Linear Electrical Components and Terminology

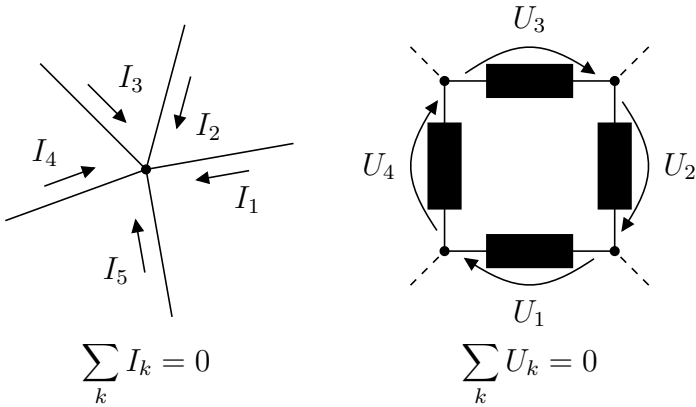
The three fundamental linear electrical components are resistors, capacitors and inductors. They are specified by their resistance  $R$ , capacitance  $C$  and inductance  $L$ , respectively. These quantify the relationship between the voltage  $U$  across their terminals and the current  $I$  through them as described in table 2.3 [CG02]. In this discussion all elements are assumed to be ideal, meaning a resistor has no capacitance or inductance and the other ways around. Also their parameters are assumed to be independent from voltage, current and frequency. This is in general not the case for real elements.

While power is dissipated in a resistor, capacitors and inductors store energy in form of electric or magnetic fields, respectively [CG02]. As a result, the current lags the voltage having an inductances and it leads the voltage in the case of a capacitances. This becomes apparent applying a sinusoidal voltage

$$U(t) = U_0 \sin(\omega t) \quad (2.23)$$

across the components. The resulting current is illustrated in table 2.3. It can clearly be seen that the responses have the same frequency as the generator. This is the case for all circuits made out of linear elements once a steady-state is reached [Hag09].

In general, circuits are described by Kirchhoff's laws in combination with the equations given in table 2.3. Instead of solving the resulting differential equations the formulation in complex quantities allows a simplified treatment of single frequency components. The real



(a) The sum over all currents flowing into a junction is zero.

(b) The sum of potential differences around a closed loop is zero.

voltage in (2.23) is therefore replaced by

$$U(t) = U_0 e^{i\omega t} = U_0 (\cos(\omega t) + i \sin(\omega t)).$$

In the following, the real part represents the physical quantities. With this complex voltage the response of the ideal components in table 2.3 also becomes complex:

$$I(t) = \frac{U_0}{R} e^{i\omega t}, \quad I(t) = \frac{U_0}{\omega L} e^{i(\omega t - \frac{\pi}{2})} \quad \text{and} \quad I(t) = \omega C U_0 e^{i(\omega t + \frac{\pi}{2})}, \quad (2.24)$$

respectively. Reordering these equations and introducing the impedance  $Z$  results in the general equation

$$I(t) = \frac{U(t)}{Z} \quad \text{with} \quad Z_R = R, \quad Z_L = i\omega L \quad \text{and} \quad Z_C = \frac{1}{i\omega C}, \quad (2.25)$$

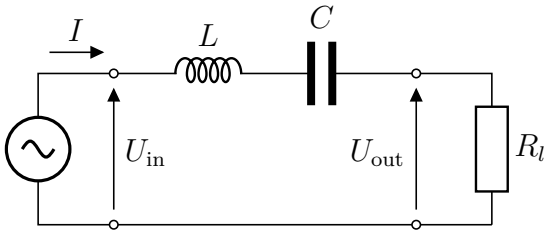
respectively. In contrast to the resistance  $R$ , the last two induce a phase shift of  $\pm 90^\circ$  in the current. The imaginary part of the impedance is called reactance  $X$ . The set of terms is completed by the reciprocal term of impedance  $Z$  named admittance  $Y = Z^{-1}$ . The real and imaginary parts of the admittance are called conductance  $G$  and susceptance  $B$ , respectively [Hag09].

## 2.5.2 Circuit Algebra and Resonances

Kirchhoff's<sup>11</sup> current and voltage law forms the basis of circuit analysis. It states that the sum of currents through conductors meeting at a point must be zero (see figure 2.7(a)). On the other hand the sum of potential differences (voltages) around any closed loop is zero (see figure 2.7(b)) [Kir45]. These two laws result in the known rules for the total resistance of resistors in series or in parallel. Kirchhoff's law is also valid for complex

<sup>11</sup>Remark: Gustav R. Kirchhoff is the eponym of the Kirchhoff Institute for Physics (KIP) where this thesis is worked out. The logo of the KIP is based on a graph in “Ueber den Durchgang eines elektrischen Stromes durch eine Ebene, insbesondere durch eine kreisförmige” [Kir45].

**Figure 2.8:** Circuit of a simple bandpass filter with a capacitor and inductor in series.



voltages and currents rewriting the rules for resistances with impedances and admittances:

$$Z = \sum_k Z_k \quad (\text{series}), \quad \text{and} \quad Y = \sum_k Y_k \quad (\text{parallel}). \quad (2.26)$$

This allows analyzing the circuit of an inductor and a capacitor in series (see figure 2.8). All currents have to be equal  $I = I_L = I_C = I_{R_l}$  and the voltages add up to  $U_{\text{in}} = U_L + U_C + U_{\text{out}}$ . With (2.26) and (2.25) the impedance of the LC part reads [Hag09]

$$Z_{LC} = Z_L + Z_C = i\omega L + \frac{1}{i\omega C} = i\frac{L}{\omega} \left( \omega^2 - \frac{1}{LC} \right). \quad (2.27)$$

The final output voltage  $U_{\text{out}}$  across the load resistance  $R_l$  is

$$U_{\text{out}} = U_{\text{in}} - Z_{LC}I = \frac{U_{\text{in}}}{1 + Z_{LC}/R_l}, \quad \text{with} \quad I = \frac{U_{\text{out}}}{R_l}. \quad (2.28)$$

This voltage has its maximum for  $Z_{LC}$  equal to zero, which occurs at the resonance frequency

$$\omega_0 = \frac{1}{\sqrt{LC}}. \quad (2.29)$$

Accordingly, at the resonance frequency the impedance of the LC part vanishes. This is, from the DC perspective, remarkable, as a capacitor is an open circuit for a DC voltage. For lower and higher frequencies the output voltage monotonically decreases.

In general Crecraft and Gergely define a physical resonance as

“the process of [maximum] energy transfer between two forms of stored energy  
(here storage in the inductor and the capacitor)” [CG02].

This directly requires a vanishing impedance (2.27) and results in a maximum voltage (2.28). When the impedance (2.27) becomes zero, the reactance also changes its sign meaning that the current changes from lagging to leading the voltage or vice versa:

$$U(t) = \underbrace{|Z(\omega)| e^{i\varphi(\omega)}}_{=Z(\omega)} I(t).$$

This sign change of the phase  $\varphi$ , crossing the resonance, is known, as this circuit corresponds to a harmonic oscillator.

Besides the resonance frequency  $\omega_0$  of a resonator the bandwidth  $\Delta\omega$  is another characteristic measure of a RLC circuit. It is defined as the full width half maximum of the transferred power. The ratio of the resonance frequency  $\omega_0$  to the bandwidth  $\Delta\omega$  is related

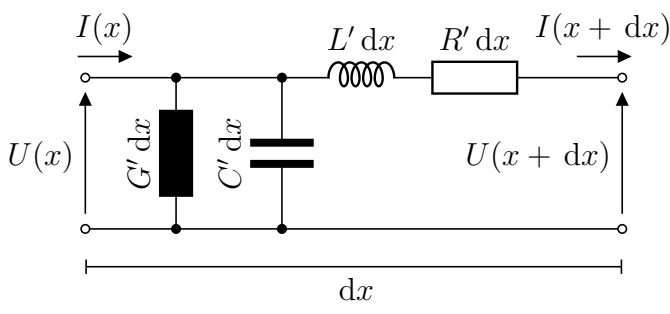


**Figure 2.9:** Equivalent circuit for an arbitrary transmission line of length  $dx$ . In order to derive the telegrapher's equations (2.31, 2.32) the length has to go to zero. The prime symbol ' notes the definition per unit length. For a lossless line is  $G' = 0$  and  $R' = 0$ . This figure is adapted from [Wil13].

to the widely used quality factor  $Q$  in circuit analysis, which will be used in this thesis. The quality factor  $Q$  is defined as the ratio of energy stored versus that dissipated during one resonant cycle [CG02]. In order to describe a realistic result of the LC resonator in figure 2.8, an additional resistor  $R_{LC}$  is added in series to the inductor and the capacitor, because in reality the inductor is lossy. The unloaded resonator has then a Q-factor

$$Q_u = \omega_0 \frac{E_{LC}}{P_{R_{LC}}} = \sqrt{\frac{L}{C}} \frac{1}{R_{LC}}, \quad (2.30)$$

with the stored energy  $E_{LC} = 1/2CU_0^2 = 1/2LI_0^2$  and the dissipated power  $P_{R_{LC}} = 1/2R_{LC}I_0^2$ . For a loaded resonator the resistances of the load  $R_l$  and the source  $R_s$  have to be added. Combining all three resistances to the overall resistance  $R$  leads to the loaded Q-factor  $Q_l = Q_u R_{LC} R^{-1}$ . Therefore, the Q-factor of the loaded resonator is smaller and the bandwidth  $\Delta\omega$  larger as of the unloaded one. Hence, when applying a LC resonator as bandpass filter, its bandwidth also depends on the load.

### 2.5.3 Telegrapher's Equations and Electrical Waves

In the preceding subsections the electrical signal is treated as location-independent, which is considered more in detail in the following. The telegrapher's equations describe the time and spatial-dependent voltage and current on an electrical transmission line which can be derived from the equivalent circuit in figure 2.9 [Wil13]:

$$\frac{\partial U(x, t)}{\partial x} = -L'(x) \frac{\partial I(x, t)}{\partial t} - R'(x)I(x, t) \quad (2.31)$$

$$\frac{\partial I(x, t)}{\partial x} = -G'(x)U(x, t) - C'(x) \frac{\partial U(x, t)}{\partial t}. \quad (2.32)$$

$R'$ ,  $L'$ ,  $C'$  and  $G'$  are the resistance, inductance, capacitance and conductance per unit length, respectively, and are in general location-dependent. In the following they will be assumed to be constant what is also the case for standard transmission lines. Combining (2.31) and (2.32) to develop two independent differential equations one arrives at the

inhomogeneous wave equations [Wil13]:

$$\begin{aligned}\frac{\partial^2 U(x, t)}{\partial x^2} - L'C' \frac{\partial^2 U(x, t)}{\partial t^2} &= (L'G' + R'C') \frac{\partial U(x, t)}{\partial t} + R'G'U(x, t) \\ \frac{\partial^2 I(x, t)}{\partial x^2} - L'C' \frac{\partial^2 I(x, t)}{\partial t^2} &= (L'G' + R'C') \frac{\partial I(x, t)}{\partial t} + R'G'I(x, t).\end{aligned}$$

In the case of a lossless ( $R' = 0, G' = 0$ ) transmission line the solutions are plane waves without damping

$$\begin{aligned}U(x, t) &= U_0 \exp(i(\omega t - kx)) \\ I(x, t) &= I_0 \exp(i(\omega t - kx))\end{aligned}\quad \text{with } k = \pm \omega \sqrt{L'C'} = \pm \frac{2\pi}{\lambda} = \pm \frac{\omega}{v_\varphi} \quad (2.33)$$

propagating in positive and negative direction.  $k$  is the wave-vector,  $\lambda$  the wavelength and

$$v_\varphi = \frac{1}{\sqrt{L'C'}} \quad (2.34)$$

the phase velocity. Therefore, the voltage or current at any position at the transmission line is a superposition of waves traveling in forward and backward direction with the introduced frequencies.

Inserting the solutions (2.33) in the telegraph equation (2.31) and using the definition of the impedance  $Z$  (2.25) results finally in the characteristic impedance of the transmission line

$$Z = \frac{U(x, t)}{I(x, t)} = \sqrt{\frac{L'}{C'}}. \quad (2.35)$$

The negative solution is neglected in this case as it is common to define the characteristic impedance only for waves traveling in positive direction. The discussion of RF and microwave (MW) electronics in the following will be based on the wave nature of signal propagation in transmission lines.

#### 2.5.4 S-Parameter Analysis, Reflections and Reciprocity

In the preceding subsection, the voltage and current propagation through transmission lines is described using plane waves. Different lumped elements<sup>12</sup> are used for an equivalent circuit of the selfsame. The above considerations and the resulting wave picture is now applied to arbitrary circuits.

As is known for waves, these are (partially) reflected and transmitted depending on the location-dependent potential of the system. In the case of electrical systems this potential is described by the impedance  $Z$ . The reference point is normally defined as the reference impedance  $Z_0$ . This allows to introduce the S-parameter now.

The term S-parameter stands for scattering parameter and is a set of transmission and reflection coefficients of electrical waves going into and through a circuit element with

---

<sup>12</sup>Lumped elements have an electrical length of zero. Therefore, no phase is accumulated due to a finite travel time.

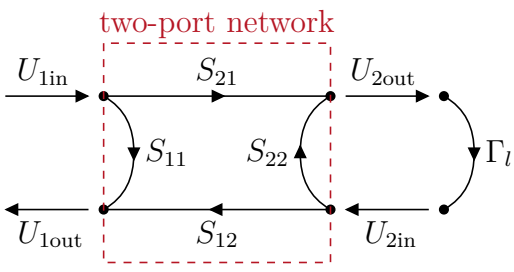


**Figure 2.10:** Signal flow within a two-port network expressed by the S-parameter. Note that the directionality of the waves is pictured. Therefore both bullets at each side correspond to the same physical wire.  $\Gamma_l$  is the reflection coefficient of a load connected to port 2. This figure is adapted from [Hag09].

a certain number of ports. It has become a standard tool for linear circuit analysis in RF and MW electronics. Measurements can be performed by using a vector network analyzer (VNA). A full set of S parameters over the whole frequency range of interest fully characterizes a circuit [Hag09].

An  $n$ -port device has  $n^2$  S parameters. Hagen defines them as follows (see figure 2.10):

“For any properly terminated  $n$ -port device,  $S_{ij}$  is the ratio of the (complex) amplitude of the wave exiting port  $i$  to the (complex) amplitude of a wave incident port  $j$ . Note that, when  $i = j$ , the S parameter is a reflection coefficient and, when  $i \neq j$ , the S parameter is a transmission coefficient.” [Hag09]

Proper termination by the impedance  $Z_0$  is required. Otherwise a part of the electrical wave is reflected leading to distorted measurements. A  $50\Omega$  impedance is the standard termination. However, sometimes  $75\Omega$  systems are also found. Its assumed that all ports are designed for  $50\Omega$  termination in the following.

Appendix A.2 explains how one calculates the S-parameter from a circuit constructed from given impedances. In the following the effects of an arbitrary two-port network, as illustrated in figure 2.10, is analyzed. It is distinguished between incoming and outgoing waves at each port. The amplitudes depend on each other described by the S-parameter as follows:

$$\begin{pmatrix} U_1 \\ U_2 \end{pmatrix}_{\text{out}} = S \begin{pmatrix} U_1 \\ U_2 \end{pmatrix}_{\text{in}}. \quad (2.36)$$

A part of the outgoing wave from port 2 is reflected by the connected load with impedance  $Z_l$ . The load is an one-port network completely described by<sup>13</sup>  $S_{11}^{(l)} = \Gamma_l$ . The reflection coefficient  $\Gamma_l$  (A.4) of an impedance  $Z_l$  is given by

$$\Gamma_l = \frac{Z_l - Z_0}{Z_l + Z_0} \Leftrightarrow Z_l = Z_0 \frac{1 + \Gamma_l}{1 - \Gamma_l}, \quad (2.37)$$

with  $Z_0 = 50\Omega$  being the reference impedance [Hag09]. Therefore the incoming amplitude at port 2 becomes  $U_{2\text{in}} = \Gamma_l U_{2\text{out}}$ . Inserting in (2.36) results in the reflection coefficient of port 1 for the loaded two-port network:

$$\Gamma_{1l} = \frac{U_{1\text{out}}}{U_{1\text{in}}} = S_{11} + \frac{S_{12}\Gamma_l S_{21}}{1 - S_{22}\Gamma_l}.$$

<sup>13</sup>Different S-parameter will be distinguished in the following by uppercase characters in brackets.

This system is now a one-port network with  $S_{11}^{(1l)} = \Gamma_{1l}$  as complex reflection coefficient for incoming waves. Therefore knowing the S-parameter of a network allows to determine the response under a specific load without knowing the inner details. For calculating a cascade<sup>14</sup> of devices one converts the S-parameter into an ABCD-parameter, which is an equivalent parameter set. The result of a cascade is then the multiplication of the single ABCD-parameter matrices [Gre15], like in optical lens systems the ray transfer matrices.

Let us now consider the one-port network to be connected to a lossless transmission line with impedance  $Z_0$ . The S-parameter of the transmission line with length  $x$  and wave-vector  $k$  (2.33) is

$$S^{(t)} = \begin{pmatrix} 0 & e^{-ikx} \\ e^{-ikx} & 0 \end{pmatrix}.$$

Therefore, the norm of the reflection coefficient does not change as one would expect. But the phase of the resulting reflection coefficient  $\Gamma'_{1l}$  of the one-port network with transmission line does:

$$\Gamma'_{1l} = S_{12}^{(t)} \Gamma_{1l} S_{21}^{(t)} = \Gamma_{1l} e^{-i2kx}. \quad (2.38)$$

Both, the incoming and the outgoing wave, must each travel the distance  $x$ . Therefore a phase of  $-i2kx$  is overall accumulated. Connecting a short ( $Z_l = 0, \Gamma_l = -1$ ) and a transmission line of length  $x = \pi/2k = \lambda/4$  to a port is therefore equal to directly leaving a port open ( $Z_l = \infty, \Gamma_l = 1$ ). In both cases a standing wave on the transmission line is the result. In general, the incoming wave is partly reflected and the standing wave quantified with the voltage standing wave ratio (VSWR)

$$\text{VSWR} = \frac{|U_{\text{in}}| + |U_{\text{out}}|}{||U_{\text{in}}| - |U_{\text{out}}||},$$

which is infinity for total reflection [Hag09]. In contrast, a vanishing reflection results in a VSWR of 1. This corresponds to a perfect impedance match. Note that the VSWR is also often called standing wave ratio (SWR) and is for (nearly) ideal systems the same as the current standing wave ratio (ISWR). The diagonal elements of the S-parameter become zero in the case of a network with perfect impedance match.

One distinguishes between reciprocal and non-reciprocal networks in circuit analysis. The former is built from passive isotropic materials, such as cables or the three fundamental components of subsection 2.5.1. The reciprocity theorem states, that if a voltage source is inserted into branch  $n$  and causes a current  $I$  through branch  $m$ , the same current  $I$  will flow through branch  $n$  when the voltage source is connected to branch  $m$  [Hag09]. As a consequence, the S matrix has to be symmetric,  $S_{ij} = S_{ji}$ , independent of the circuits symmetry. For amplifiers this is obviously not the case as they have a large gain in forward but not in backward direction. Other typical examples for non-reciprocal elements are isolators and circulators which, are made out of anisotropic materials.

---

<sup>14</sup>A cascade is a series of two-port elements, for example, an attenuator followed by a low-pass filter.

# 3 ArTTA Technology

Argon Trap Trace Analysis (ArTTA) is a ultrasensitive kind of spectroscopy, based on the isotopic shift and application of quantum optics. ArTTA resolves  $^{39}\text{Ar}$  abundances at the level of  $10^{-16}$  and lower. The working principle is introduced in chapter 1. In the following a more detailed perspective of the ArTTA technology is given. An overview of the measurement setup is drawn in the first section. In the following, a focus is placed on the various options for quantifying the metastable flux. With the gained knowledge the fundamental alignment of the collimator is recapped. As the gain in metastable flux is on the order of two magnitudes, the consequences of widening the mirror distance is investigated. The quantum optical part ends with a detailed instruction for the alignment procedure for collimator and 2D-MOT, based on the newest knowledge.

Last but not least, a new monitoring system is introduced. The design of a custom-made laser switch control and data transmitter for self-made sensors is presented as well as the network for data exchange is discussed. Finally the basis for an universal software package is investigated and the solution of the monitoring task presented.

## 3.1 Overview of the ArTTA Apparatuses

Two ArTTA apparatuses are located in Heidelberg. Both setups are generally comparable but differ in details. A detailed description of the second setup is found in [Rin21; Fen18], while the first machine is mainly based on the work of [Ebs18; Rit13; Wel11]. An overview and further developments within the scope of this work are described below.

Figure 3.1 shows a schematic view of the main vacuum system and the quantum optical tools. Three inlets for argon gas are shown at the bottom left above the output. One port is connected to samples, while the others are connected by default to a reference gas container and a  $^{39}\text{Ar}$  depleted sample. The latter is also called “dead”, as it does not contain radioactive  $^{39}\text{Ar}$ . The expansion to three inlets is based on a redesign of the prevacuum by Schmidt for the first machine [Sch21]. This redesign is slightly adapted for the second one.

The argon gas volume is measured with the inlet pressure gauge, knowing the volume of the vacuum part. From the reservoir, the gas is transferred to the metastable plasma source. The pressure within the source chamber is adjusted using the dosing valve in front of the source. The set pressure within the source chamber is  $p_{\text{source}} \approx 1 \times 10^{-5}$  mbar. The liquid nitrogen ( $\text{LN}_2$ ) cooling of the metastable plasma source serves as a first cooling step

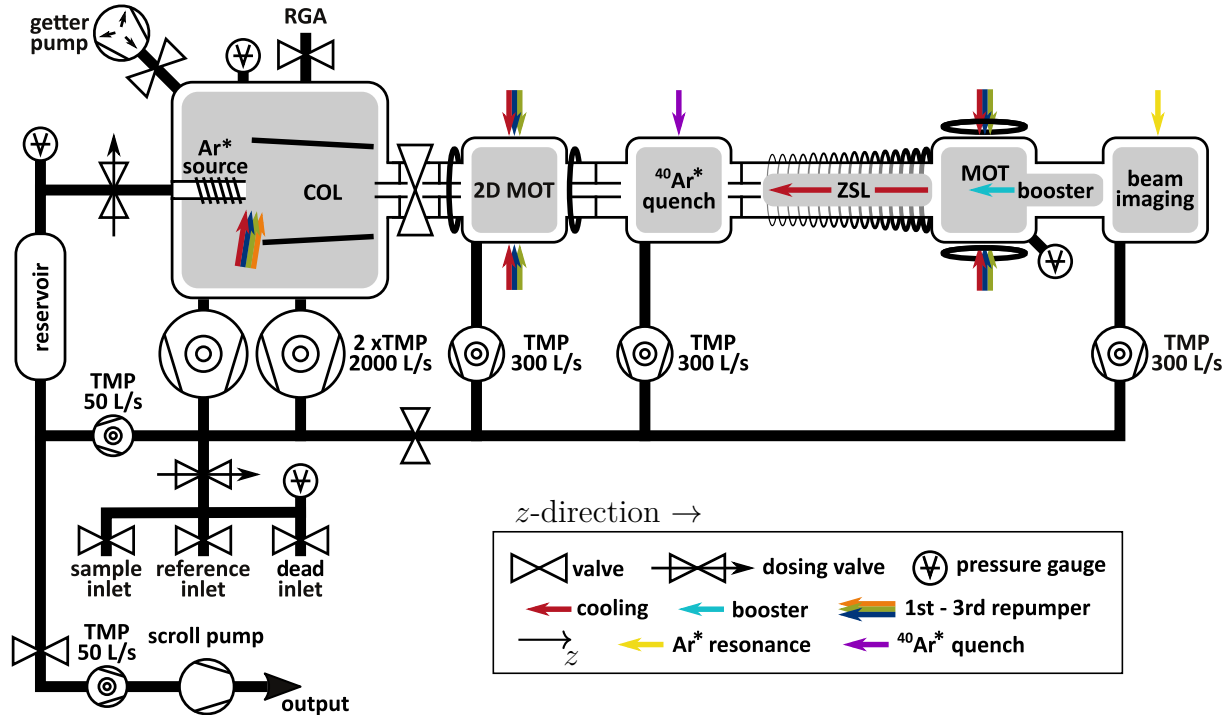


**Figure 3.1:** Schematic view of the ArTTA apparatuses. Three inlets are illustrated at the lower left. From there, the argon gas enters the apparatus, is pumped into the reservoir and reaches the metastable argon plasma source. Due to the high pressure difference needed between source and MOT, the source chamber is pumped with two turbo-molecular pumps (TMPs). After transverse deceleration within the collimator (COL), the atoms pass a differential pumping stage. The 2D-MOT focuses the atoms. The  $^{40}\text{Ar}$  quench de-excites metastable  $^{40}\text{Ar}$  for monitoring purposes and background signal reduction in the MOT. The ZSL decelerates the atoms longitudinally before they are finally slowed down by the booster within the MOT region. There, they are trapped and detected by their fluorescence. The beam imaging is for aligning purposes. All pumped gas is transferred back to the reservoir and the cycle begins again. This figure is adapted from [Rin21] and originally created from [Fen18].

for the argon atoms. A detailed description and evaluation of different sources is given in chapter 6.

The output of the plasma source is a broad velocity distribution in both longitudinal and transverse directions. Many  $^{39}\text{Ar}$  atoms shall be trapped at the end of the apparatus. Therefore, the collimator (COL) slows them down in transverse direction. Details are discussed in the following section 3.3. The collimated beam enters through a differential pumping stage the 2D-MOT. Two pairs of laser beams in horizontal and vertical direction focus the metastable atom beam towards the MOT. In the following quench chamber  $^{40}\text{Ar}$  atoms are de-excited. This is done for metastable flux monitoring and background signal reduction in the MOT.  $^{40}\text{Ar}$  atoms never will be trapped during  $^{39}\text{Ar}$  measurements. However, they still have a finite probability scattering photons from the laser beams. Due to their high abundance they increase the background signal significantly. Details and further developments of the metastable flux measurement using de-excitation are presented

in chapter 4.

The third and last differential pump stage is installed at the outlet of the quench chamber. The following ZSL is build with an increasing magnetic field. It decelerates atoms from up to  $v_c \approx 610 \text{ m s}^{-1}$  down to  $v_f \approx 70 \text{ m s}^{-1}$  [Ebs18]. This velocity is still to high for capturing atoms with the MOT. However, due to their higher longitudinal velocity, the lateral propagation of the atoms is reduced. As soon as they reach the MOT, they are slowed down further by a second ZSL, called a booster. The atoms are simultaneously cooled transversally by the MOT laser beams and finally trapped. Their fluorescence signal is detected using an avalanche photo diode (APD). The latter is able to detect single photons, whereof the signature of  $^{39}\text{Ar}$  atoms is extracted [Ebs18]. A cloud of atoms is measured with a camera, for example measuring the MOT loading rate.

The last chamber is used for visualizing a cross-section of the metastable atom beam. It helps aligning collimator and 2D-MOT. Therefore, a non-detuned laser beam is send in gravity direction through the chamber. The laser beam has a line-shape with an angle of  $45^\circ$  with respect to the longitudinal axis. Looking from the side shows the transverse beam profile, which is visualized with a camera.

All laser frequencies required for the various quantum optical tools are generated in a separate setup next to the vacuum system. The latest version of this setup is described in [Rin21]. The light is transferred via standard polarization maintaining optical fibers to the vacuum system. The two collimator fibers are self assembled as they end within the vacuum (see appendix A.3). Further details about specific issues of the quantum optical tools in the case of argon are found in subsection 2.3 as well as in the literature mentioned at the beginning.

Some final comments regarding the vacuum system itself. As earlier mentioned, the pressure in the source chamber is, with  $p_{\text{source}} \approx 1 \times 10^{-5} \text{ mbar}$ , high compared to other quantum optical experiments. In fact, the metastable plasma source needs such high pressures to work well. Once the atoms are in the metastable state, preferably no collision with other atoms should take place. Therefore, the source chamber is pumped with two TMP with a total pumping speed of  $4000 \text{ L s}^{-1}$ . The three differential pumping stages in combination with three further TMP reduce the pressure down to  $p_{\text{MOT}} \approx 3 \times 10^{-8} \text{ mbar}$  in the MOT chamber. However, the local pressure at the position of the MOT itself is higher, due to the atom beam coming directly from the source (compare subsection 3.2.1).

Two further instruments are worth mentioning. A residual gas analyzer (RGA) is connected to the source chamber. It measures concentrations of various gases and is part of standard observations for the experimenter. The getter pump is also connected to the source chamber at the second machine. At the first it is located directly in front of the upper  $50 \text{ L s}^{-1}$  TMP. During 20 h and longer measurements some unwanted gases accumulate within the machine. The getter pump assimilates all none noble gases and therefore keeps the argon gas sample clean.

## 3.2 Tools for Metastable Flux Quantification

A proper alignment of the ArTTA apparatus is mandatory for  $^{39}\text{Ar}$  measurements. Various instruments exist to quantify the metastable flux under specific conditions at different locations. In the following, a summary of two of them is given. Further, a detailed review of the MOT loading rate is given, motivating to use it as a standard tool to determine the current state of the apparatus.

At this point, it is already referred to table 3.1. It gives an overview of the advantages and disadvantages of the different tools described in this section and their application for alignment purposes, described in section 3.4.

### Absolute Metastable $^{40}\text{Ar}$ Flux

The absolute metastable  $^{40}\text{Ar}$  flux is determined in the quench chamber. Metastable  $^{40}\text{Ar}$  atoms are de-excited using the quench transition (see figure 2.1 with the argon level scheme). A part of the thereby emitted photons is detected and evaluated. This tool is able to measure absolute numbers, as each decaying atom emits exactly one detectable photon. Chapter 4 delivers a detailed discussion and evaluation. However, measuring  $^{36}\text{Ar}$  would be beneficial and may therefore be a standard in the future.

### Beam Imaging

The beam imaging is located at the very end of the beam line behind the MOT chamber. The atoms are illuminated with a sheet of light under an angle of  $45^\circ$  with respect to their direction of traveling. Looking perpendicular to the laser beam and the atom direction allows to see a cross-section of the atom beam. The laser light is tuned to the cooling transition of the isotope of interest. The principle setup is based on [Ebs12]. In this work, an extension to  $^{36}\text{Ar}$  and  $^{38}\text{Ar}$  was motivated and a possible implementation was worked out. Therefore, a remaining beam of the 2<sup>nd</sup> RP is used for the beam imaging, as it can be freely tuned to the right frequency when measuring. The implementation is presented [Mei22]. Remember that measuring one of the even mass number isotopes does not require RPs and the corresponding part of the laser system can easily be tuned to another frequency. Additional improvements are achieved using the existing acousto-optic modulator (AOM) in the laser path for intensity stabilization. Further, the stray light of the laser beam itself is reduced by approximately 30 % dumping the laser beam far away from the chamber.

All in all, the beam imaging enables to, in a first order, spatially resolve the metastable density of the atom beam. However, slow atoms contribute stronger to the signal  $S$ , as  $S_i \propto 1/v_i$ , leading to over, respectively under representations. The impact of the remaining MOT magnetic field has not been considered yet, what should be subject of further improvements. Therefore, this tool has its advantages in the spatial resolution but is not able to resolve the overall flux with sufficient quality.

### 3.2.1 MOT Loading Rate

The MOT loading rate has already been discussed in the context of ArTTA in the past [Rin16; Rit13; Ebs12; Kau11]. However, until today, the loading rate has not been implemented as a standard analysis tool. First, a brief summary of the theoretical foundations is given. Afterwards, the different regimes and consequences are discussed in combination with experimental results. The upcoming section 3.4, the MOT loading rate is established as a standard tool during alignment of the ArTTA apparatus.

The rate equation of the trapped atom number  $N$  is given by [Wei+99]

$$\frac{dN}{dt} = L - \frac{N}{\alpha} - \frac{1}{\beta'} \int_V n^2(r, t) d^3r. \quad (3.1)$$

$L$  is the loading rate,  $\alpha$  the mean lifetime due to single particle losses and  $\beta'$  the volume mean lifetime due to collisions between trapped atoms. Single particle losses are collisions with background gas or, especially in the case of a hyperfine splitting, losses out of the cooling cycle. Two particle losses are caused by metastable-metastable induced ionization (2.22) and therefore  $1/\beta' = \Gamma_{mm}$ .  $n(r, t)$  is the spatial atom density. It can be replaced by a three-dimensional Gaussian distribution of width  $w$  in the low density limit. Equation (3.1) can thus be rewritten as [Wei+99]

$$\frac{dN}{dt} = L - \frac{N}{\alpha} - \frac{N^2}{\beta'(2\pi)^{3/2}w^3}, \quad \text{with } n(r, t) = n_0(t) \exp\left(-\frac{r^2}{w^2}\right). \quad (3.2)$$

The two particle losses mean lifetime  $\beta = \beta'(2\pi)^{3/2}w^3$  is introduced for the low density regime. The steady-state solution,  $\dot{N} = 0$ , reads [Rit13]

$$N_\infty = \frac{\sqrt{\beta^2 + 4L\alpha^2\beta} - \beta}{2\alpha} \stackrel{\beta \gg N}{=} L\alpha.$$

The latter holds for small atom numbers. Therefore, the final atom number is proportional to the capture rate in this regime. However, this is rarely the case. The solution for the differential equation (3.2) with the condition  $N(0) = 0$  yields

$$N(t) = \frac{\sqrt{\beta}}{2\alpha} \left[ \kappa \tanh \left( \frac{\kappa t}{2\alpha\sqrt{\beta}} + \operatorname{atanh} \left( \frac{\sqrt{\beta}}{\kappa} \right) \right) - \sqrt{\beta} \right], \quad (3.3)$$

with  $\kappa = \sqrt{4\alpha^2 L + \beta}$ .

The MOT first loads linearly and saturates towards  $N_\infty$ . On the other hand, the solution of (3.2) for  $R = 0$  and  $N(t) = N_0$  is

$$N(t) = \frac{\beta N_0}{(\alpha N_0 + \beta)e^{t/\alpha} - \alpha N_0}. \quad (3.4)$$

Thus, if the density is low and the mean lifetime  $\beta$  is relatively large, a loaded MOT loses exponentially its atoms.<sup>1</sup>

---

<sup>1</sup>Remark: Both formula (3.3) and (3.4) in [Rit13; Kau11] have a typing error.

The atom number can be obtained from the emitted fluorescence  $F$  of the trapped atoms. The atom number  $N$  is proportional to the fluorescence  $F$ , as long as the density is not in a regime where a spontaneously emitted photon is likely absorbed by another atom. The loading rate  $L$  is measured by switching the MOT laser beams on and detecting the fluorescence over time. Fitting the linear slope at the beginning gives the loading rate  $L$ , except for an unknown conversion factor. Another approach, using the metastable nature, would be to de-excite the atoms at the center of the MOT. The single photon per atom, emitted during the decay to the ground state, is detected, as done for the metastable  $^{40}\text{Ar}$  flux quantification [Jia+12]. Thus the density of the MOT stays low and the scaling factor between fluorescence and atom number is easier to determine. Section 4.5 discusses the advantages in the context of ArTTA and the possibility of an absolute measurement.

Lasers are usually switched on and off on fast time scales ( $\mu\text{s}$ ) using AOMs or EOMs. However, the current design of the laser systems of both ArTTA apparatuses do not provide AOMs for this purpose without switching off the light of the 2D-MOT. Therefore, a homemade bow-tie shutter [Zha+15] is used in both experiments with a 10% to 90% raise time of 0.6 ms. The MOT is loaded for the loading time  $\tau_{\text{LR}}$  before an image is taken. Afterwards, the MOT laser beams are switched off for 200 ms to empty the MOT. This procedure is repeated. Either with a fixed time  $\tau_{\text{LR}}$ , if one wants to measure changes, for example during alignment. Or  $\tau_{\text{LR}}$  is varied in order to look for the time regime of the linear increase. However, one has to take care that the selected exposure time of the camera is small compared to the evolution time of the MOT. Otherwise one integrates over the evolution. In general, a complete scan of the fluorescence evolution should be measured first, before a second measurement of the linear part allows for a more precise analysis.

In the following, equation (3.3) and (3.4) are experimentally verified for the low density regime with small atom numbers. Additionally, the influence the atom beam from the source has on the MOT lifetime is evaluated. Figure 3.2 shows the measurement results compared to the theoretical course. Due to the slow evolution time, it is possible to measure all points in time within one run. Ten runs have been performed per set and combined to the plotted mean values with standard deviation as error bars. For the decay measurements in the right subplot, the loading rate is set to zero by de-exciting the  $^{40}\text{Ar}$  atoms in the quench chamber.

The lifetime of the MOT in the low density regime is mainly determined by collisions with background atoms. Losses due to off-resonant excitation to other states do not occur for  $^{40}\text{Ar}$  as happens for  $^{39}\text{Ar}$ . However, these collisions have two contributions. One is the location independent background gas and the other the atoms of the atom beam coming directly from the source. The latter is nearly completely removed closing the valve behind the source chamber up to a point, where even with collimator and 2D-MOT turned on just a very small  $^{40}\text{Ar}$  MOT remains (blue data points in figure 3.2). These measurements are compared to the influence of the atom beam. To do so, the same MOT size is achieved by tuning the collimator to a state where it diffuses the metastable atoms and by decreasing the source efficiency. The 2D-MOT is turned off and the valve is completely open. The background pressure in the MOT stayed nearly constant at  $p_{\text{MOT}} \simeq 2.5 \times 10^{-8} \text{ mbar}$ .

Equation (3.3) is fitted to the measurement results in the left subplot and (3.4) to the selfsame of the right subplot. For the MOT decay, an offset is added, as the signal does not go to zero. For the loading, a time offset is added to account for the non constant loading

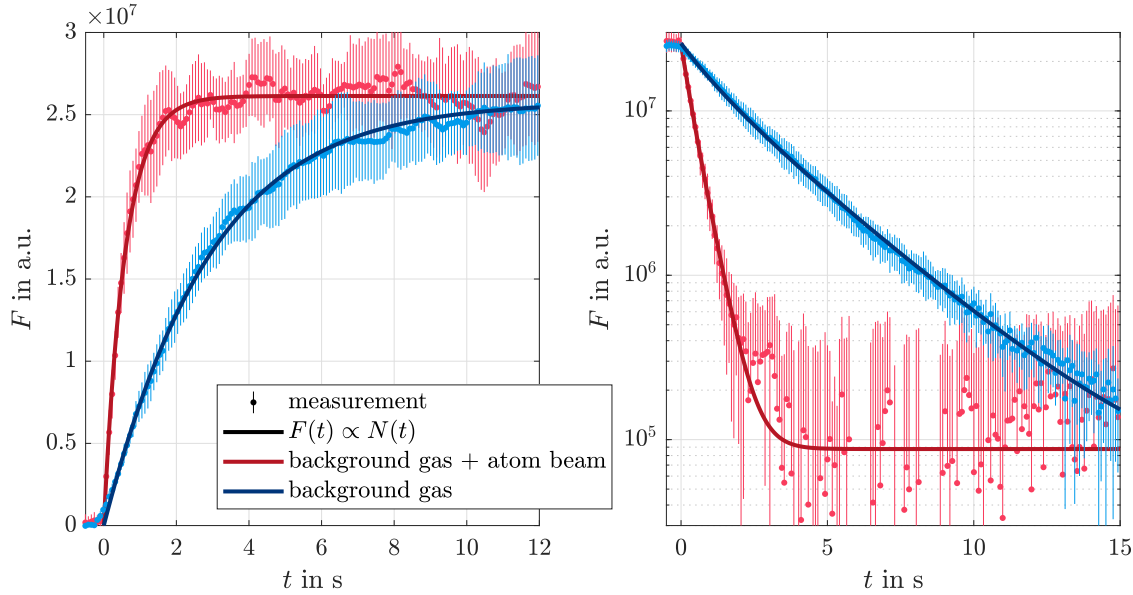


**Figure 3.2:** Measurement of the time-dependent MOT fluorescence  $F$  in the low density, small atom number regime. The fluorescence is in this regime proportional to the atom number  $N$ . The subplot on the left shows the loading of the MOT, described by equation (3.3). On the right is the exponential decay of the atom number measured, described by (3.4). The measurements in blue are performed with only the background pressure of  $p_{\text{MOT}} \simeq 2.5 \times 10^{-8}$  mbar. Results in red are additionally under the influence of the local atomic beam. Note that error bars are not illustrated when they end at a negative fluorescence due to the logarithmic scale.

rate at the beginning [Rit13]. The fitted mean lifetime  $\alpha$  of the measurements with only background gas for loading and decay are  $3.4(5)$  s and  $3.00(9)$  s, respectively. The values obtained for the measurements with background gas and atom beam are  $0.58(5)$  s and  $0.47(5)$  s, respectively. The values agree within their uncertainty in both cases. The mean lifetime for background gas and atom beam is also in the range of the lifetimes obtained for  $^{39}\text{Ar}$  atoms, where the mean value is typically around 0.3 s.

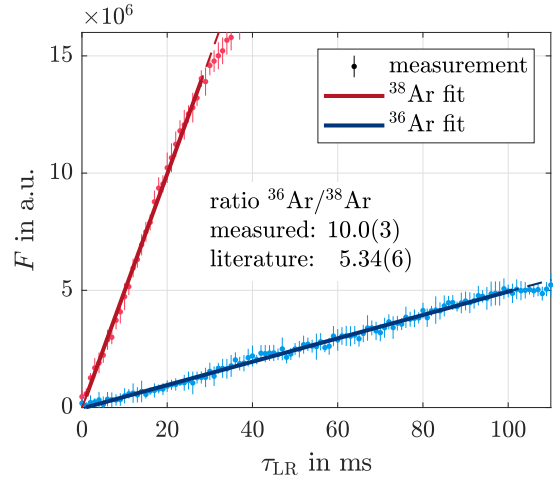
The mean lifetime  $\alpha$  for background gas and atom beam is a combination of two exponential decays with  $\alpha_{\text{bg}}$  and  $\alpha_{\text{ab}}$ , respectively. Therefore, the mean lifetime caused by the atom beam is

$$\alpha_{\text{ab}} = \frac{\alpha_{\text{bg}}\alpha}{\alpha_{\text{bg}} - \alpha} = 0.63(12) \text{ s}, \quad \text{with } \alpha_{\text{bg}} = 3.06(22) \text{ s}, \alpha = 0.53(8) \text{ s}$$

of the single measurements. Hence, the lower limit of the loss rate from the source to the MOT for an atom at rest is  $1/\alpha$ . This rate increases towards the source, as the background pressure and atom beam density also increase. However, atoms need about 20 ms to travel the distance from the 2D-MOT to the MOT [Ebs12]. Consequently, losses of  $^{39}\text{Ar}$  atoms due to collisions are, with this consideration, not completely neglectable.

The determination of the MOT loading rate is mainly limited by two factors. First of all, the scaling factor between measured fluorescence and number of trapped atoms is not constant. Changes of detuning, magnetic field, laser intensity or polarization have an

**Figure 3.3:** Measurement of the abundance ratio of  $^{36}\text{Ar}$  to  $^{38}\text{Ar}$  using the MOT loading rate. Two lines are fitted at the experimental data. The ratio of the slopes is  $10.0(3)$ . However, the literature value is  $5.34(6)$  (compare table 2.1), which is confirmed with the RGA. The difference can be explained by (slightly) different detunings of the MOT laser beams, as this changes the scattering and loading rate. Therefore, such kind of measurements are mainly able to quantify differences in the metastable flux on a short timescale and of the same isotope.



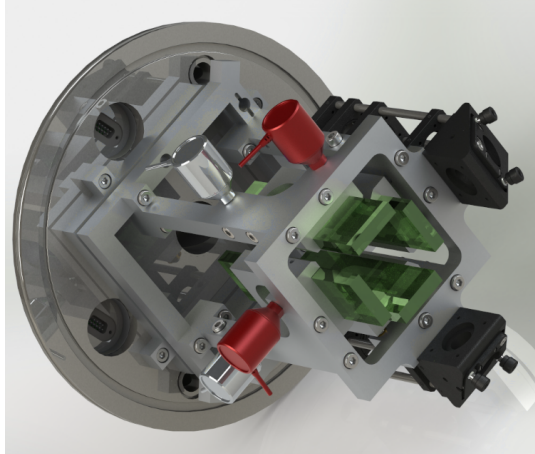
impact on the scattering rate as well as the loading rate. Changing one of these parameters while using the loading rate to discriminate the metastable argon flux, can lead to wrong results. An example is shown in figure 3.3.

Secondly, the mean lifetime  $\beta$  depends on the atom density, which is in general neither constant nor scales with the atom number  $N$ . In fact the density above a critical limit remains nearly unchanged and the MOT expands [Wei+99]. However, as one wants to measure at densities, where  $\beta$  is neglectable, measurements of very high loading rates are biased. This is almost always the case for  $^{40}\text{Ar}$ , as here the density of the incoming atoms on the way to the center of the MOT is already too high.  $^{38}\text{Ar}$  has the lowest abundance of the stable argon isotopes and is therefore mostly used. Nevertheless, collisions of trapped atoms can become rapidly relevant when using the collimator and the 2D-MOT. As the fluorescence at a specific time is still monotonically increasing with the loading rate, measurements of the selfsame can be used for alignment purposes. However, as a linear proportionality cannot always be assumed, absolute numbers have to be treated carefully.

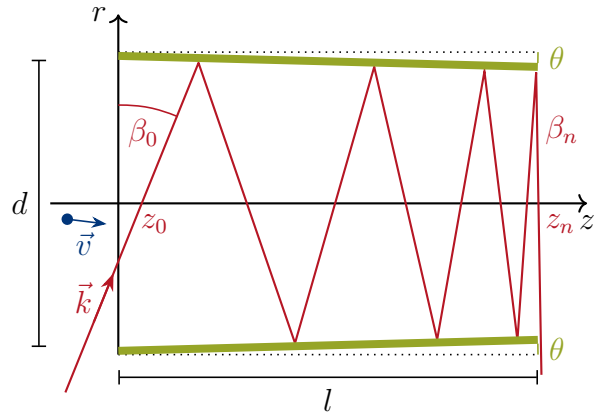
All in all, this tool allows to estimate the influence of most apparatus parameters on the  $^{39}\text{Ar}$  count rate, although the fluorescence does not always scale linearly with the loading rate. Therefore, it complements the previously existing toolkit with another important proxy.

### 3.3 Consequences of a Widened Collimator and its Fundamental Alignment

The collimator design is based on work from Ritterbusch [Rit09; Rit13], with slight changes made by Ebser [Ebs18]. Figure 3.4(a) shows the latest version of the collimator in the first ArTTA apparatus. The distance between the mirrors has been increased by Feng [Fen18] for the second machine. He assumed that this reduces the degradation of the mirrors due to sputtering by the plasma. A quantitative investigation of the resulting effects and a discussion on the collimation performance is carried out in the following.



(a) CAD image of the tight collimator setup. The laser beams are shaped within the black cage systems before threading them between the mirror pairs (green). One mirror of each pair is adjustable within the vacuum using two stepper motors (silver, red). The setup can be tilted as a whole with respect to the vacuum flange at the back. This figure is adapted from [Ebs18].



(b) Geometrical scheme of a collimator with tilted mirrors. On the left, an exemplary atom is drawn in blue. A decrease of the entrance angle  $\beta_0$  allows to reduce the tilting of the mirrors  $\theta$  and results in a higher laser beam density within the collimator. The width of the laser beam and the distance between the mirrors  $d$  define the minimum achievable angle for  $\beta_0$ . This figure is adapted from [Rit09].

**Figure 3.4:** Computer-aided design (CAD) image and geometrical scheme of the collimator.

The collimator is used to decelerate the metastable atoms in transverse direction directly after the plasma source. Figure 3.4(b) shows a scheme of the geometry. Fast deceleration of the radial velocity  $v_r$  is important, as the atoms have to pass the first differential pumping stage with an inner radius of  $r_t = 9\text{ mm}$  [Ebs18]. In order to keep the effective detuning with decreasing  $v_r$  small, the angles  $\beta_i$  of the laser beams  $i$  decrease with increasing distance from the source. If the number of reflections within the collimator is very high, the distance between the intersection points  $z_i$  becomes small and one receives [Rit13]

$$\beta(z) = \sqrt{\beta_0^2 - \frac{4\theta}{d}z} \approx \beta_0 \sqrt{1 - \frac{z}{l}}, \quad \text{with } \theta = \theta_{\text{opt}} \approx \frac{\beta_0^2 d}{4l}. \quad (3.5)$$

$\theta_{\text{opt}}$  is the optimum mirror angle [Rit09; Rit13]. It is the maximum angle  $\theta$ , where the laser beam still leaves the mirror pair at its end and does not reverse.

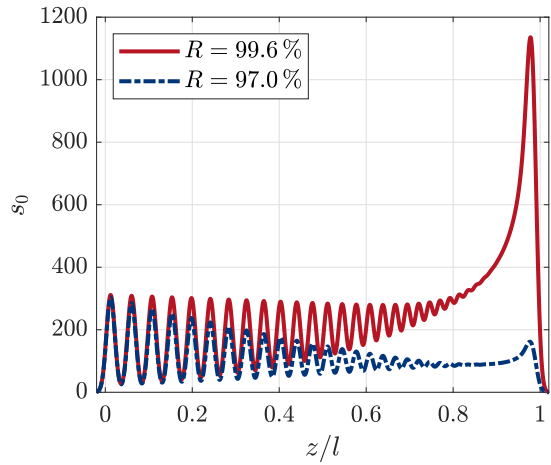
With the Doppler shift (2.11) and the laser detuning  $\delta_L$ , the effective detuning  $\delta$  reads [Rit09]:

$$\delta = \delta_L - k(v_z \sin \beta - v_r \cos \beta) \stackrel{\beta \approx 0}{\approx} \delta_L - k(v_z \beta(z) - v_r(z)). \quad (3.6)$$

Here,  $v_z$  is the longitudinal velocity. It is assumed to be constant due to small angles of  $\beta$ .

However, looking at all metastable atoms, the longitudinal velocity varies greatly (compare chapter 5). Therefore, the intensity of the laser beams have to be high resulting in a power broadened linewidth  $\gamma' = \gamma \sqrt{1 + s_0}$  [MS99]. Figure 3.5 shows the saturation parameter of the e.g. upward directed laser beams for example, for typical experimental parameters.

**Figure 3.5:** Graph of the saturation parameter  $s_0$  (2.8) on the experiment  $z$ -axis for all e.g. upward directed laser beams.  $R$  is the mirror reflectivity. Towards the end, the rays overlap more and more, hence  $s_0$  increases (strongly). If the reflectivity gets to low, the mirrors have to be replaced. Interference effects and edge clipping of the laser beam at the end are not considered. Laser power, radial beam radius, beam radius in  $z$ -direction and incident angle are  $P = 0.2 \text{ W}$ ,  $w_r = 9.8 \text{ mm}$ ,  $w_z = 2.9 \text{ mm}$  and  $\beta_0 = 1.3\beta_{\min}$ , respectively.



The reflectivity of the mirrors  $R$  is once set to the minimum manufacturer specification,  $R = 99.6\%$ , and once to a degraded value of  $R = 97.0\%$ . Note that the degradation in the experiment is location dependent and gets even lower near the plasma source. However, a high reflectivity is necessary, as the laser beam is reflected approximately 80 times. Nevertheless, the laser intensity does not depend on the distance  $d$  between the mirrors, keeping  $\beta_0 d = \text{const.}$  and  $\beta_0 \approx 0$ . That holds with the restriction that the opacity of the metastable atoms has to be neglectable. The latter is definitely not the case when the laser is tuned to the  ${}^{40}\text{Ar}$  cooling transition as shown below.

However, the location dependence of the saturation parameter changes with the angle of incidence  $\beta_0$ . The minimum achievable angle [Rit09]

$$\beta_{\min} = \arctan\left(\frac{w_z}{d}\right) \quad (3.7)$$

is reached, when the incident laser beam tightly passes the lower mirror, while the first reflection hits it just completely. This angle can be reduced by increasing the distance  $d$  between the mirrors. Theoretical considerations and simulations of Ritterbusch in [Rit09; Rit13] clearly showed an improved performance for  $\beta_0$ . Therefore the optimum angle of incidence is  $\beta_0 = \beta_{\min}$ . The distance is increased from  $d = 60 \text{ mm}$  to  $d = 81 \text{ mm}$  in [Fen18]. Therefore, the minimum angle decreased, with the beam radius  $w_z = 2.9 \text{ mm}$  in  $z$ -direction, from  $\beta_{\min} = 2.8^\circ$  to  $\beta_{\min} = 2.1^\circ$ .

In the experiment, the angle  $\beta_0$  is measured performing the following steps. First,  $\beta = 0^\circ$  is aligned perpendicular to the mirror surface by overlapping the incoming and reflected beam. Now, the angle is increased up to the point, where the physical definition of  $\beta_{\min}$  is reached.  $\beta_0$  is increased by  $2 \cdot 7.6 \text{ mrad}$  per turn of the screw [Tho21]. The minimal achievable angle of the widened collimator in the experiment is determined to be  $\beta_{\min} = 2.6^\circ$ . This angle is slightly higher as than the one obtained by equation (3.7), due to a small uncoated strip at the beginning of the mirror.

Summing up the theoretical considerations and simulations in [Rit09; Rit13], the optimum setup combines the laser angle  $\beta_{\min}$  (3.7) and the mirror angle  $\theta_{\text{opt}}$  (3.5). However, an effect of the mirror distance  $d$ , apart from the influence on  $\beta_{\min}$  and  $\theta_{\text{opt}}$ , is not directly

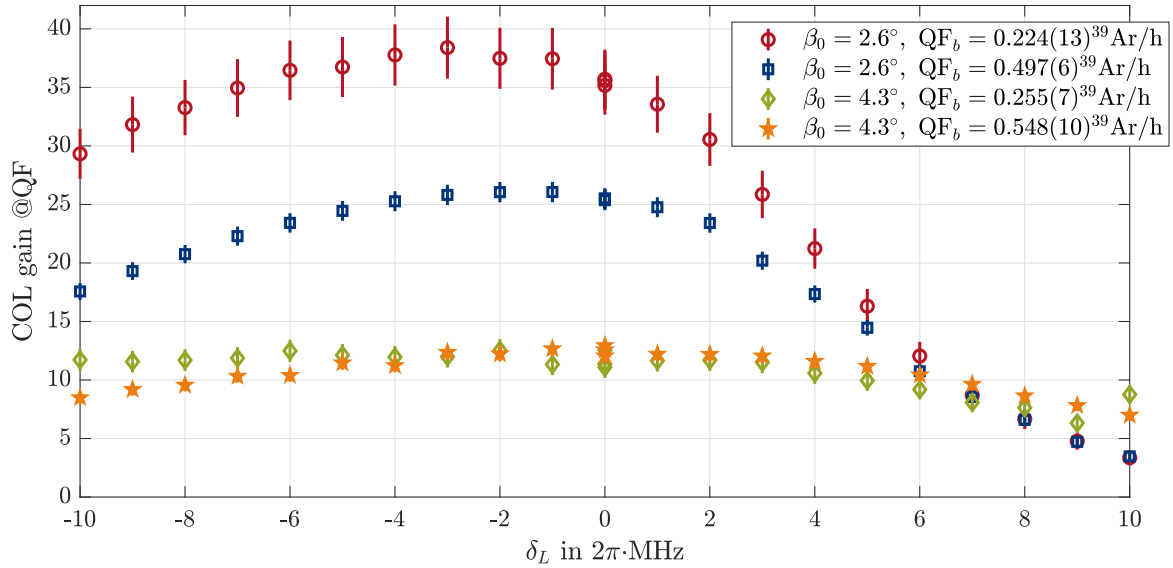


**Figure 3.6:** Measurements of the collimator gain at the  ${}^{40}\text{Ar}$  metastable flux in the quench chamber depending on the laser detuning  $\delta_L$ . Two laser angles  $\beta_0$  are realized as well as two different metastable densities. The maximum gain is up to three times higher for the smaller angle  $\beta_0 = 2.6^\circ$  as for the larger  $\beta_0 = 4.3^\circ$ . The dependence on the laser detuning increases with decreased  $\beta_0$ . Note that the effect of different plasma densities is dominant measuring  ${}^{40}\text{Ar}$  (see figure 3.8). Error bars represent the  $1\sigma$ -error caused by statistical fluctuations.

reported. Nevertheless, a larger distance besides reduced degradation is preferable, as the following consideration suggest. The laser angle (3.5) decreases down to  $\beta(l) = 0^\circ$ . Therefore, the collimator forms an optical molasses at its end. The force of the latter only cools atoms for a laser detuning  $\delta_L < 0$ . However, the optimal laser detuning is larger for a larger  $\beta_0$ , as the atoms have to follow the laser beam more and more (3.5). This is also confirmed by [Rit09; Rit13]. For the tight collimator the optimum detuning is  $\delta_L > 0$ . Thus, increasing the mirror distance  $d$  allows to decrease the laser detuning  $\delta_L$  and to therefore reach even negative detunings. In this case, the optical molasses at the end of the collimator cools the atoms instead of heating them.

The previously made considerations are proven by the following measurements. They are performed with the widened collimator with  $d = 81$  mm. The collimator gain at the  ${}^{40}\text{Ar}$  metastable flux QF in the quench chamber is shown in figure 3.6. For measurements under the same laser angle  $\beta_0$ , only the specified parameters were changed. The mirror angle  $\theta_{\text{opt}}$  is used for both laser angles  $\beta_0$ .

The measured quench flux QF is divided by the bare flux  $QF_b$ . The latter is determined without any laser light in the collimator. Two laser angles  $\beta_0$  are realized as well as two different metastable densities. The maximum gain is up to three times higher for the smaller angle  $\beta_0 = 2.6^\circ$  as for the larger  $\beta_0 = 4.3^\circ$ . On one side, the gaps between the laser beams increase with  $\beta_0$ , resulting in a decrease of the force acting on the atoms. On the other hand, assuming a constant laser intensity and analytically deriving the optimal initial laser angle results in  $\beta_0 = 0^\circ$  for a saturation parameter  $s_0 \geq 60$  [Rit13]. Both

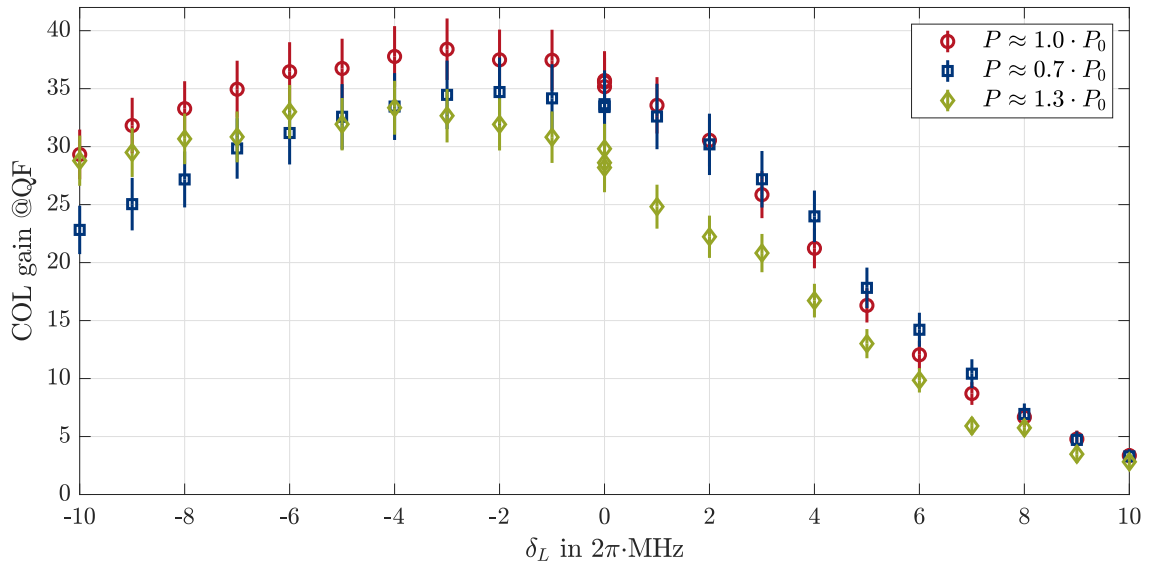


**Figure 3.7:** Measurements of the collimator gain at the  $^{40}\text{Ar}$  metastable flux in the quench chamber depending on the laser detuning  $\delta_L$  and the laser power  $P$ . The dependence on the detuning shows different characteristics. The highest laser intensity obtains better results than the lowest for laser detunings below the optimum  $\delta_L \approx 3 \cdot 2\pi \text{ MHz}$  and vice versa. Note that there is an optimum laser intensity, as the opposing laser beams gain in influence with greater power broadening. The bare quench flux is  $\text{QF}_b \approx 0.25 \text{ }^{39}\text{Ar h}^{-1}$  for all measurements. The error bars represent the  $1\sigma$ -error caused by statistical fluctuations.

points result in a higher gain of the collimator for a lower angle of incidence.

Another characteristic difference between the two laser angles is the dependence of the collimator gain on the detuning. It increases with decreased  $\beta_0$ . While for the larger laser angle a wide plateau at maximum gain is measured, the optimum laser detuning of the smaller  $\beta_0$  is more defined. When  $\beta_0$  is large, the Doppler detuning of the longitudinal velocity is also larger, compare equation (3.6). Therefore, the laser has to be more blue detuned in order to compensate the Doppler effect. However, the optical molasses at the end of the collimator needs a red detuning,  $\delta_L < 0$  to prevent heating of the atoms. Both effects compete against each other, resulting in a less prominent optimum detuning. This can be verified by looking at the measurements with different metastable densities, quantified by the bare quench flux  $\text{QF}_b$ . Due to the opacity of the highly abundant  $^{40}\text{Ar}$ , the laser intensity decreases in  $z$ -direction. Therefore, especially the laser power at the end of the collimator is reduced, where the optical molasses is formed. Consequently, the gain of the  $\beta_0 = 4.3^\circ$ ,  $\text{QF}_b = 0.55 \text{ }^{39}\text{Ar h}^{-1}$  measurement is higher for blue detunings compared to the one with  $\text{QF}_b = 0.25 \text{ }^{39}\text{Ar h}^{-1}$ . The negative consequences of the optical molasses are lower, due to the decrease in laser intensity. On the other hand, at red detunings, the gain difference is reversed, as the optical molasses has a positive gain.

Comparable considerations can be made for  $\beta_0 = 2.6^\circ$ . For  $\delta_l \sim 8 \cdot 2\pi \text{ MHz}$  no differences between different metastable densities are visible. The detuning is comparably large for this laser angle, resulting in even lower values as for  $\beta_0 = 4.3^\circ$ . With decreasing detuning the gain increases. Less opacity even further increases the gain, as the power broadening

stays higher and more laser intensity is left within the optical molasses. Therefore, the optimum tends to a slightly lower detuning.

The mirror distance  $d$  cannot be changed without replacing the whole collimator setup. However, the collimator setup of the first ArTTA apparatus still has a collimator with a mirror distance of  $d = 60$  mm. Typical gain values at the quench flux of this machine are around 20. These values are up to 20 % lower than the comparable measurement with  $\beta_0 = 2.6^\circ$ ,  $QF_b = 0.497 \text{ } ^{39}\text{Ar h}^{-1}$ . Therefore, theory and simulations as well as measurements indicate that widening the collimator increases the  $^{39}\text{Ar}$  count rate.

In addition to the previous measurements, the input laser power  $P$  is varied. The measurement results are shown in figure 3.7. All three measurements have their optimum at  $\delta_L \approx 3 \cdot 2\pi$  MHz. The results of higher laser power tend towards lower detunings, as the opposing laser beams gain in influence with greater power broadening. Consequently, the gain at the lower intensity is higher at detunings above the optimum. However, the main statement of this measurement is the existence of an optimal laser intensity for a given set of parameter. Therefore, a profound optimization, walking all available parameters, is necessary to reach the global maximum. Even then, a reduced laser power can be the optimum, as the laser angle cannot go below  $\beta_{\min}$ .

In general these measurements clearly demonstrate the large influence of the  $^{40}\text{Ar}$  metastable density on the optimal alignment of the collimator. The consequences drawn from this are discussed in the following section.

## 3.4 Alignment Procedure for Collimator and 2D-MOT

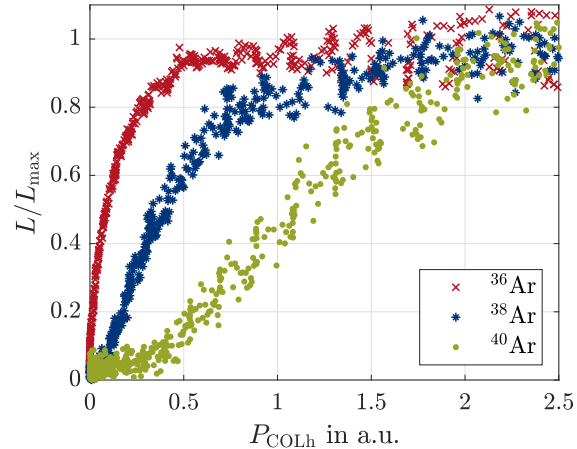
This section serves as a handbook for experimenters to align the collimator and 2D-MOT. It starts from the very beginning and comments on why which tool for metastable flux quantification should be used in which alignment step. Table 3.1, at the end of this section, gives an overview of the optimization toolkit with its advantages and disadvantages.

### Collimator

Lets start with a short summary of the fundamental alignment, discussed in the previous section (see figure 3.4(b) for geometrical definitions used in the following). In general the laser beam center has to cross the center axis from the source to the differential pumping stage. The laser angle  $\beta_0$  must be reduced until the laser beam just not yet clips. The mirror angle  $\theta$  has to be set to its highest possible value before the laser beam reverses its direction. The lateral tilt has to be zero. The laser power should be maximal and the laser detuning  $\delta_L = 0 \cdot 2\pi$  MHz, if not further investigated for a specific alignment. All this is done for both axis of the collimator separately. Note that some parameters can only be changed when the vacuum setup is open.

From this point on, the effect on the atoms is observed for further alignment. For the next step, aligning the output direction of the collimator, the beam imaging with  $^{40}\text{Ar}$  atoms is used, as it is the only tool available which has a spatial resolution. Therefore, the whole collimator setup is tilted inside the vacuum with two manual actuators from outside. It is worth looking separately at each axis of the collimator and at both together.

**Figure 3.8:** Measurement of the collimator power saturation for the three stable isotopes  $^{36}\text{Ar}$ ,  $^{38}\text{Ar}$  and  $^{40}\text{Ar}$ , respectively. Only the horizontal collimator axis is used. The power saturates faster the larger the isotopic shift with respect to  $^{40}\text{Ar}$ . The loading rate  $L$  is measured after a fixed loading time and normalized to the mean maximum value  $L_{\max}$  of the corresponding isotope. The booster is switched off for  $^{40}\text{Ar}$ . Otherwise the loading rate is too high for reliable measurements.



Now all lasers are switched to the  $^{36}\text{Ar}$  frequencies, as the laser power within the collimator is comparably absorbed than measuring  $^{39}\text{Ar}$  (see discussion below). The collimator laser detuning is set to the highest signal at the beam imaging using both collimator axes. Further, the laser power is tuned to the optimum signal. Both parameters have to be walked in order to obtain maximum gain (see discussion in section 3.3).

The next part is the mirror angle  $\theta$  and lateral tilt alignment. Both are optimized based on the beam imaging for each collimator axis alone. It could be necessary to walk both parameters against each other. After both axes are optimized, one should check the output direction, now using  $^{36}\text{Ar}$ . One has to iterate all steps performed with  $^{36}\text{Ar}$  to get the maximum. Finally one continues aligning the 2D-MOT (see next segment).

$^{36}\text{Ar}$  is used for the final optimization, as it still results in useful signals at the beam imaging, while the metastable atom opacity in the collimator is the lowest and comparable to  $^{39}\text{Ar}$ . In the following, this statement is substantiated using the loading rate to determine the metastable flux.

Figure 3.8 shows the isotope dependent power saturation of the collimator.  $^{36}\text{Ar}$  is already more or less saturated, where the loading rate of  $^{40}\text{Ar}$  starts to increase. Coming back to table 2.1 shows, that the isotopic shift towards  $^{40}\text{Ar}$  is the largest for  $^{36}\text{Ar}$ . The effect of the approximately five times higher abundance compared to  $^{38}\text{Ar}$  is in contrast neglectable. The absorption of light in a solid, liquid or gas is described by the Beer-Lambert law [Bee52]

$$I(x) = I_0 \exp(-\varepsilon cx),$$

with the material concentration  $c$  and the absorption coefficient  $\varepsilon$ . However, the absorption coefficient is highly inhomogeneous, as it is proportional to the scattering rate (2.7). The latter is dependent on the intensity and especially on the detuning  $\delta$ . Modifying (3.6), for a  $^{40}\text{Ar}$  atom flying with velocity  $v$  in the plane of the corresponding collimator axis, results in

$$\delta_{\pm} = 2\pi\Delta\nu_{\rightarrow 40\text{Ar}} + \delta_L - kv(\beta \cos \alpha \pm \sin \alpha). \quad (3.8)$$

The  $\pm$  sign represents the two possible directions of the laser beams.  $\alpha$  is the direction angle of the atom with respect to the  $z$ -axis and  $\Delta\nu_{\rightarrow 40\text{Ar}}$  the isotopic shift compared to  $^{40}\text{Ar}$ . The detuning caused by the Doppler shift has to be large in order to compensate

the isotopic shift. This is the case for great angles  $\alpha$ , as  $\beta$  is always small. Lets assume  $\alpha = 45^\circ$ , which is a possible angle for the first collimator laser beams. Equation (3.8) then reads

$$\delta_{\pm} = 2\pi\Delta\nu_{\rightarrow 40\text{Ar}} + \delta_L - \frac{kv}{\sqrt{2}}(\beta \pm 1) \stackrel{\beta \approx 0}{\approx} 2\pi\Delta\nu_{\rightarrow 40\text{Ar}} + \delta_L \mp \frac{kv}{\sqrt{2}}. \quad (3.9)$$

The resulting Doppler shift is approximately  $1 \cdot 2\pi \text{ MHz}$  per  $1 \text{ m s}^{-1}$ . Thereby, looking at typical velocities (see chapter 5),  ${}^{40}\text{Ar}$  atoms can become resonant for laser frequencies of  ${}^{36}\text{Ar}$  and  ${}^{38}\text{Ar}$ . However, the maximum angle  $\alpha$  decreases with increasing distance from the source. Additionally, only a small fraction of the metastable  ${}^{40}\text{Ar}$  is in the velocity regime required to compensate the isotopic shift of  ${}^{36}\text{Ar}$  as well as  ${}^{39}\text{Ar}$ . Therefore, the collimator saturates the faster the larger the absolute isotopic shift towards  ${}^{40}\text{Ar}$  is. This is validated by the measurement in figure 3.8. Finally, the difference in intensity loss between  ${}^{36}\text{Ar}$  and  ${}^{39}\text{Ar}$  is small, as the opposite sign of the isotopic shift is canceled by the selfsame of the Doppler shift in equation (3.9).

Meienburg [Mei22] showed, that the measured collimator gain with the  ${}^{40}\text{Ar}$  beam imaging does not correlate with the  ${}^{39}\text{Ar}$  count rate. Based on the findings above, the collimator has been optimized to the  ${}^{38}\text{Ar}$  loading rate. The obtained improvement of the  ${}^{39}\text{Ar}$  count rate is 47(5) % compared to using the  ${}^{40}\text{Ar}$  beam imaging for aligning. However, using either  ${}^{36}\text{Ar}$  or  ${}^{38}\text{Ar}$  loading rate for collimator alignment, showed equal  ${}^{39}\text{Ar}$  count rates within the errors [Mei22].

## 2D-MOT

After aligning the collimator for a maximal  ${}^{36}\text{Ar}$  metastable flux, the 2D-MOT is positioned based on the  ${}^{38}\text{Ar}$  loading rate. The collimator is in the following always on.  ${}^{38}\text{Ar}$  is used, as the loading rate with collimator and 2D-MOT for  ${}^{36}\text{Ar}$  is too high for proper measurements (compare section 3.2.1). Using the loading rate has the advantage that it takes the deceleration of the ZSL and the capturing of the MOT into account. As the ZSL changes the atom flight times depending on their longitudinal velocity, it also changes the radial beam density.

Again, first the fundamental alignment. The polarization of both laser beams has to be circular with the rotation direction according to the magnetic field (see section 2.3). The center of both beams should cross the point of zero magnetic field, which has to be on the center axis of the differential pumping stages. The laser beams have to be perpendicular to each other as well as to the atom beam. The retro reflections of the beams shall overlap with the incoming ones.

The first alignment on the atoms should be done using  ${}^{36}\text{Ar}$  beam imaging. If no typical value for the 2D-MOT coil current is known, 0 A is used as a starting value. In this case, the 2D-MOT acts as an optical molasses<sup>2</sup>. The following steps are done by having only one axis of the 2D-MOT switched on. Varying the angle  $\beta$  of the laser beam with respect to the  $z$ -axis, changes the effective detuning. This angle has to be tuned such, that the atom beam still hits the center of the beam imaging. Thereby, the retro reflected beam should overlap. Otherwise both beams have a finite Doppler shift. Turning both 2D-MOT

---

<sup>2</sup>The laser detuning is not assumed to be an open parameter, as it is currently the same for 2D-MOT and MOT.

axes on and increasing the coil current should compress the atom beam observed on the beam imaging. Maybe slight readjustments of the laser beam orientation have to be done.

For the detailed alignment, an appropriate loading time  $\tau_{LR}$  for the  $^{38}\text{Ar}$  loading rate is selected. First, the magnetic field strength is optimized using both axes. As a next step, the angle  $\beta$  of incoming and retro reflected beams are walked against each other, while the other axis is switched off. After having aligned both axes, the magnetic field is revisited and if necessary again optimized. Now, both axes are turned on and these steps iterated until an optimum is reached. If huge improvements have been made, one should consider choosing a new appropriate loading time  $\tau_{LR}$ .

**Table 3.1:** Overview of the different tools for metastable flux quantification with respect to their advantage and disadvantage during alignment. For details it is referred to section 3.2 and 3.4.

<b>Metastable <math>^{40}\text{Ar}</math></b>			
Tool	(Quench) Flux	Beam Imaging	MOT Loading Rate
<b>Overall Advantages</b>	<ul style="list-style-type: none"> <li>absolute signal of the atoms within the quench chamber</li> </ul>	<ul style="list-style-type: none"> <li>spatial resolution of the atom beam behind the MOT chamber</li> <li>usable for <math>^{36}\text{Ar}</math>, <math>^{38}\text{Ar}</math> (limited) and <math>^{40}\text{Ar}</math></li> </ul>	<ul style="list-style-type: none"> <li>only tool including all cooling stages except RPs</li> <li>usable for <math>^{36}\text{Ar}</math> (limited), <math>^{38}\text{Ar}</math> and <math>^{40}\text{Ar}</math> (limited)</li> </ul>
<b>Overall Disadvantages</b>	<ul style="list-style-type: none"> <li>only <math>^{40}\text{Ar}</math> (<math>^{36}\text{Ar}</math> maybe feasible)</li> </ul>	<ul style="list-style-type: none"> <li>velocity dependent</li> <li>effect of MOT magnetic field unknown</li> </ul>	<ul style="list-style-type: none"> <li>limited by collisions of trapped atoms</li> </ul>
<b>Advantages for Collimator</b>	<ul style="list-style-type: none"> <li>close to it <math>\Rightarrow</math> quantifies the amount of atoms transferred to the 2D-MOT</li> </ul>		<ul style="list-style-type: none"> <li>gives an appropriate gain value using <math>^{38}\text{Ar}</math></li> </ul>
<b>Disadvantages for Collimator</b>	<ul style="list-style-type: none"> <li><math>^{40}\text{Ar}</math> is too opaque</li> </ul>		
<b>Advantages for 2D-MOT</b>			<ul style="list-style-type: none"> <li>includes effects caused by ZSL and MOT</li> </ul>
<b>Disadvantages for 2D-MOT</b>	<ul style="list-style-type: none"> <li>too close to enable investigations</li> </ul>	<ul style="list-style-type: none"> <li>does not account for ZSL and MOT effects</li> </ul>	

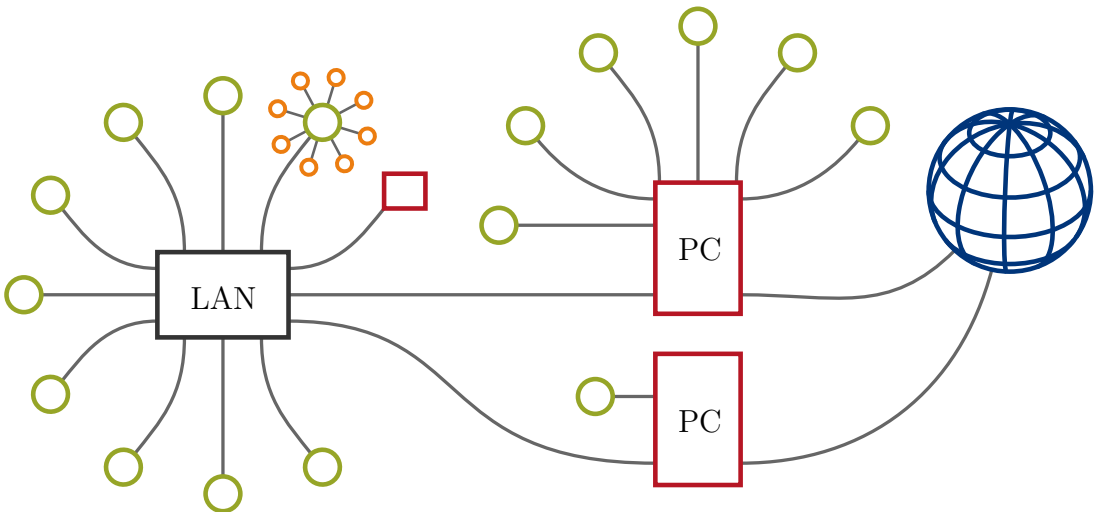


**Figure 3.9:** Schematic drawing of the laboratory network. The lower PC is only used for recording the APD signal. Above is the monitoring PC. Devices (green circles) without an Ethernet interface are directly connected to the latter, mostly using Recommended Standard 232 (RS-232) or Universal Serial Bus (USB) interfaces. Both PCs are connected to the internet (blue sphere) as well as to the local area network (LAN). Devices with Ethernet interface are also connected to the LAN. Homemade sensors (orange circles) are read out from a custom-made data transmitter. The small red box is an optional Raspberry Pi for monitoring 24/7 data.

## 3.5 Laboratory Control and Monitoring System

Setting up a second laboratory and replacing of outdated and undocumented equipment from the first apparatus raised the question of a new system. The general task is to provide the experimenter a platform to properly operate the laboratory. The two main sub-tasks are (automatic) controlling of some parameters and monitoring of various metrics. It is the goal of the latter to help detecting changes of the count rate performance by looking at the monitored data and directly localize its origin. All in all, the laboratory control and monitoring system shall help the experimenter to keep the ArTTA apparatus running and perform reliable measurements. For the former are additional functionalities implemented and described in the following.

The first section explains the communication network of the different devices and draws a short outline for 24/7 recording. The so-called monitoring box, an interface for homemade sensors, is introduced in the second section together with a newly developed laser switch control. Finally, the main parts of the universal software for monitoring and their interplay are summarized. A focus is thereby drawn on relevant aspects during programming and for further developments. Some aspects are reported in detail as this work is partly part of the documentation.

### 3.5.1 Communication in a Decentralized System

Technology has evolved since the first ArTTA system and Internet of Things (IoT) becomes more and more a standard than a vision. Therefore, the concepts are transferred to the laboratory, where possible. A LAN is set up with all devices having an Ethernet interface, being part of it. Figure 3.9 shows a schematic drawing of the network. Different devices measuring and/or controlling various parameters are symbolized by a green circle. The green circle surrounded by small orange circles is a custom-made data transmitter for homemade sensors (orange circles). The latter are the orange circles. The design of the custom-made sensor is explained in the following subsection. The small red box is an optional Raspberry Pi for monitoring 24/7 data. All devices without an Ethernet interface are directly connected to the monitoring PC, being the upper one in figure 3.9. These connections are mainly based on RS-232 and USB interfaces. The second PC is only used for reading out the APD signal as well as the MOT camera. Both PCs are connected to the internet and can be addressed from outside the laboratory.

The optional Raspberry Pi is used for monitoring 24/7 data, as some metrics are also of interest looking for long-term drifts and correlations. Here are especially named room temperature, humidity, laser output power and others. The working principle is explained in [Oxe20]. However, this part has been developed up to a demonstration level, but not been finished yet, due to limited time and personnel turnover in the electronic workshop.

The advantage of a LAN is on one side the possibility to communicate between arbitrary devices. Therefore, both PCs are able to control and read the status of the laser shutter, switching off and on the different laser beams in the experiment, for example. On the other side, the Ethernet interface is more robust compared to RS-232 and USB connecting many devices. From time to time connection problems occurred in the past, which often require a restart of the corresponding PC. Also exchanging a PC is less laborious, as less special drivers are necessary and IP addresses do not change.

### 3.5.2 Design of a Data Transmitter and a Laser Switch Control

The custom-made data transmitter is based on an Arduino Yún Rev 2. The latter provides twelve 10-bit analog-to-digital converter (A/D), 0 V..5 V, as well as an Ethernet and Inter-Integrated Circuit ( $I^2C$ ) interface. Therefore, up to twelve analogue sensors can be connected using DE-9-sub connectors. Besides the signal wire,  $\pm 12$  V, +5 V and ground are at hand. Homemade sensors can use these as supply voltages. Table 3.2 displays the

**Table 3.2:** Pin assignment of the DE-9-sub and the RJ45 connectors of the custom-made data transmitter described in subsection 3.5.2. GND means ground, AS analog signal, SDA serial data, SCL serial clock and nc stands for not connected. Note that the RJ45 connector only has eight pins.

pin	1	2	3	4	5	6	7	8	9
DE-9-sub	GND	AS	+12 V	SDA	SCL	+5 V	-12 V	nc	nc
RJ45	SDA	GND	SCL	nc	GND	GND	+5 V	GND	

pin assignment.

Two I<sup>2</sup>C multiplexer create 16 I<sup>2</sup>C networks. Each DE-9-sub connector is equipped with one of these. The remaining networks are linked to RJ45 connectors, as some homemade sensors already exist for this connector type. The advantage of multiple I<sup>2</sup>C networks is not so much the increased number of devices that can be connected, but rather the improved stability. If one device perturbs a network, only this network fails and the other ones still work. Table 3.2 displays again the pin assignment.

The Arduino continuously reads the A/D and I<sup>2</sup>C out. The measured signal  $S$  is slightly lowpass filtered to the output

$$S_i = \frac{S_{i-1} + S}{2}.$$

The output signal  $S_i$  is then written to a key-value list for the corresponding key. The list itself can be fetched sending a representational state transfer (REST) request<sup>3</sup> via the LAN. The Arduino sends a JavaScript Object Notation (JSON) formatted file with the key-value list and some additional information back. The request as well as further processing of the answer file is done using MATLAB (see the following subsection).

The current version and documentation of the data transmitter circuit, the Arduino code as well as circuits for self-made sensors can be found on GitLab under <https://git.kip.uni-heidelberg.de/atta/monitoringbox> (access permission required).

The laser switch control is also based on an Arduino Yún Rev 2. It provides 18 ports switching between 0 V and +12 V, delivering up to 1.5 A. Six of these 18 ports additionally output a standard transistor-transistor logic (TTL) signal. The status of the various ports can be fetched requesting again the key-value list of the corresponding Arduino. The status of a single port or a port group is also changed using REST. These commands are typically not directly used by the experimenter. They are either sent by MATLAB or JavaScript. The latter is embedded in a web-based GUI, shown in figure 3.10, and can therefore be used from any device within the LAN with an internet explorer. Last but not least, one can also implement some sequences in the laser switch control. They perform time-dependent switches, as necessary for the MOT loading rate, for example. A detailed documentation and the current version is found on GitLab under [https://git.kip.uni-heidelberg.de/atta/shutter\\_control](https://git.kip.uni-heidelberg.de/atta/shutter_control) (access permission required).

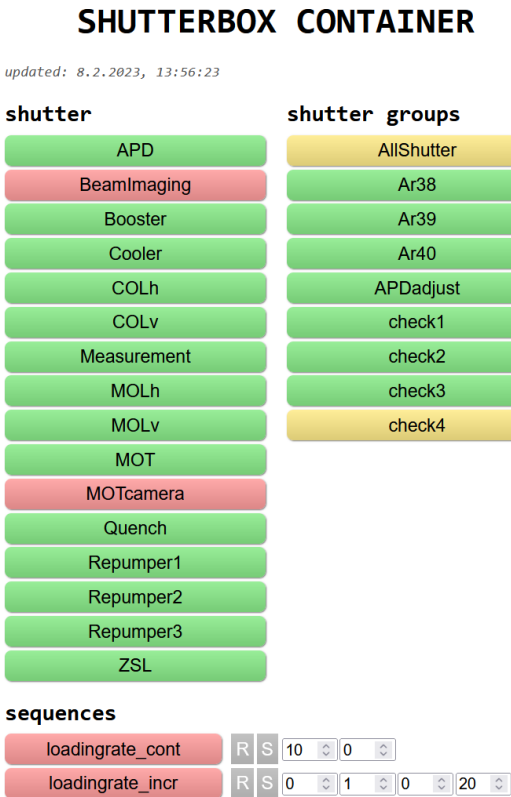
### 3.5.3 Universal Monitoring Software ATTAsystem

ATTAsystem is the name of a universal software package written in MATrix LABoratory (MATLAB). Up to now, its use case is restricted to monitoring and comparable tasks. The software provides the basis for including additional functionalities, built up on the given infrastructure. However, it is known, that universal software projects are never finished, especially under limited time and/or money resources. This is only one point, why it is important to already use them on the way. The current status of the software is

---

<sup>3</sup>Sending a REST request simply means calling a specific URL, which tells the device what to do. Credentials are often required. E.g. `http://root:arduino@192.0.2.42/data/get` logs into the Arduino as `root` with the password `arduino` and requests the key-value list, assuming the Arduino is at the specified IP address.

**Figure 3.10:** Image of the web-based graphical user interface (GUI) for the laser switch control. The color of the buttons represents the current status. Green stands for open, red closed and yellow means undefined. The latter occurs mainly at groups, when not all ports of the group have the same status. Sequences perform a specific time-dependent sequence of enabling and disabling different ports. Some parameters of the sequence can also be changed using the GUI. As writing a new status to the key-value list needs an undefined amount of time, the Arduino omits this during time critical sequences. As all buttons are generated from the key-value list of the Arduino, the GUI automatically adds or removes buttons, if new objects are defined on the Arduino.



reported in the following. The main focus is on the basic idea and strategy.

GitLab is used for version controlling during the past and ongoing development. This helps documenting the software, finding old versions and introducing new functionalities, while simultaneously using a proofed version. The current version and documentation of the software is found under <https://git.kip.uni-heidelberg.de/atta/attasystem> (access permission required).

## Basic Idea and Strategy

As the necessity of a new monitoring system stems from building a second ArTTA apparatus, it is the goal to build one software for both. It is one thing to copy software to another device. But it is another thing to build a software being able to operate on two different laboratories. However, with the increased effort comes the gain to only care for one software and compatibility in all further steps. Consequently the basic idea is to have one software package running and operating arbitrary many comparable ArTTA machines<sup>4</sup>. The basic strategy to let this become happen is summarized in the following requirements:

- **Easy to Use**

The software should be easy and quick to use for the experimenter. Logical or repeating steps have to be done by the software. This increases acceptance of the software and saves time in the laboratory.

- **Settings Separated from Functionalities**

Laboratory specific settings have to be stored separately from the functionality

<sup>4</sup>In general are also KrypTTA apparatuses, measuring <sup>81</sup>Kr, respectively <sup>85</sup>Kr, comparable.

description, as the former has to be exchanged. All functionalities have to work in all laboratories. Otherwise several software version will exist soon.

- **Single Functionalities into Single Functions**

Comparable and especially equal functionalities have to be done by the same part of the code, a separate function or script. This improves readability and helps finding as well as adapting a functionality.

- **Shared Information**

Each information shall only exist once. This allows, as at the point before, a change of an information to become active every where without the necessity to exchange that information at multiple places.

- **Traceability**

Each used version of the software has to be distinctly identifiable within a created and saved data set as well as traceable. Therefore, the version number of the software is stored with the data and a tool like GitLab used for version control.

- **Comment your Code**

Comments are necessary for yourself and everyone else to understand the code without executing it step by step in the brain. Otherwise it is extremely hard to make any changes. This goes along with a proper documentation.

## Device and Data Classes

As MATLAB supports object-oriented programming, the advantage of class<sup>5</sup> definitions is used for devices and some special data types. Each device has its own class containing all necessary properties and methods to communicate with and operate the device. Therefore, the user just calls the method `obj.getData` in order to get whatever data the device in `obj` measures. Additional methods or general properties can be added to a class and are instantaneously available for all objects, respectively devices, of this class.

Device and data class definitions are each stored in their own folder. Every class file starts with a standardized documentation of all defined properties and methods. Extensive testing of input parameter as well as proper handling of typical errors serve for stable operation.

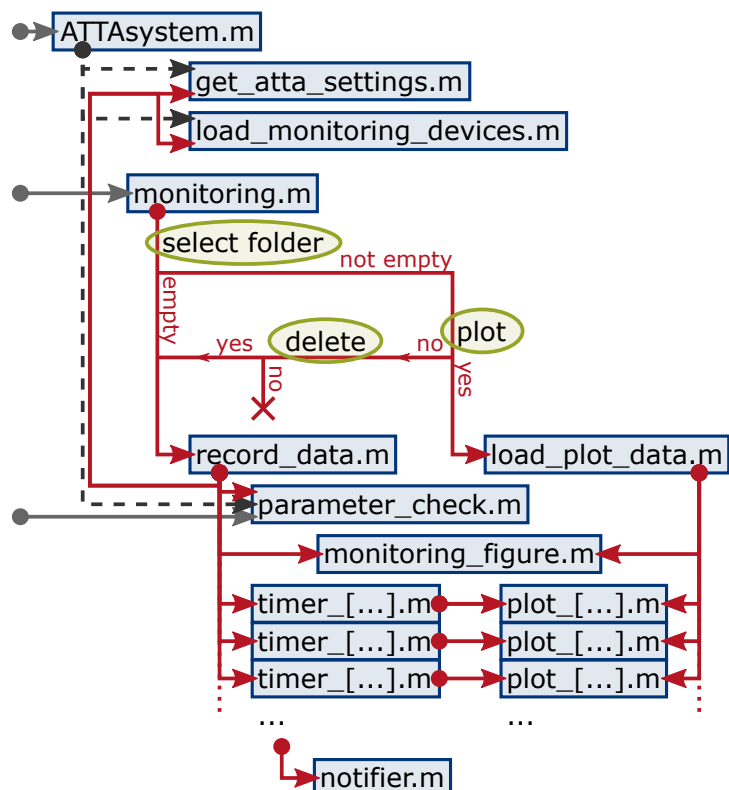
## Settings and Scripts

As required from the basic strategy, specific settings are stored separately in their own folder. Each laboratory has its own file containing two variables, `devices` and `parameter`. In the former are all information stored about which devices exist, where to find them and, if applicable, which settings to apply. The latter contains reference parameters for the apparatus, e.g. laser beating frequencies. An additional file provides a list of experimenters with addresses in order to send notifications, if a measured value is out of the defined parameter range.

---

<sup>5</sup>Each object is of a specific class. The class defines which properties an object has and which methods can operate on the object and especially how. E.g. one can define the class `integer` and `string`, both owning the method `sum`. Depending on the class, `obj.sum`; does either `result = a+b;` or `result = strcat(a,b);`.

**Figure 3.11:** Scheme of the monitoring part of the ATTAsystem software. Each blue box represents the corresponding MATLAB file. Green ellipses are prompted user input. The user can start at any gray dot on the left. Following the arrows shows in which order which file is executed. Note that `parameter_check` only works, if all necessary devices have been loaded to the global variable space. Therefore, it is best practice to run `ATTAsystem` once after booting MATLAB. The actual monitoring is started calling `monitoring`. The same script is also used for loading and plotting recorded data. In principle, this is possible on any PC.



“Stand-alone” functionalities are stored in the folder `script`. This only serves to keep the amount of files manageable in some way.

## Monitoring

Figure 3.11 shows a scheme of the current ATTAsystem software. Additional functionalities will be added in the future. Three different MATLAB files are typically called by the experimenter. `ATTAsystem` is the root script. It makes all other files available on the command line, if not already done automatically by MATLAB at the end of booting<sup>6</sup>. This saves time, as all functions can be executed without looking for and opening them. `ATTAsystem` loads parameters and settings as well as initializes the devices. Occurring problems are printed to the command line. Additionally, the user is asked, whether a parameter check shall be done or not. The latter can also be called directly from the command line. The parameter check compares the laser power of each frequency in each beam of the vacuum system with a reference range. This lasts less than half a minute. Short enough to implement it as a standard check. The result is printed to the command line and stored in the output variable of the function `parameter_check`.

The monitoring itself is started calling `monitoring`. A folder named `monitoring` is created in the selected measurement folder. If such a folder already exists, MATLAB asks whether the existing data shall be plotted or not. As can be seen in figure 3.11, the same functionalities are used for plotting existing data as during recording. This has been required by the statements noted above. Note that the folder `monitoring` is a reserved folder and at the

<sup>6</sup>If the necessary custom-made *matlab functions* package is configured properly, all files of ATTAsystem are already part of the search path.

beginning of recording no files are accepted in it. A file called *info.mat* is created at the beginning of data recording. It contains, beside the different software version numbers, the result of the parameter check, all settings and further information. For each recorded device a separated data file is created. It is a simple text file and the data stored as a tab stop separated table. The header lists all variable names and units. Each row is a data point, starting with a timestamp. Therefore the files can also be read by other programs or even humans. Note that computer running a Microsoft operation system are fairly bad in time synchronization. The clocks easily differ by multiple tens of seconds from day to day as well as computer to computer. A network time protocol (NTP) can be installed<sup>7</sup> as a solution. Approximately each ten seconds a data point is taken per device. Devices are read out one after another. Occurring problems during monitoring are directly communicated to the contact information of the user by the function **notifier**.

In the following, more detailed information is given on how the monitoring task is solved in the software. Reference is not always made to the requirements mentioned above and instead they are generally referred to again.

- Global information, as the device objects or a log variable, are stored in the global workspace. Thus all functions and even humans can on the one hand access and use them but on the other hand also manipulate them. However, this is exactly what part of the functionalities have to do.
- Distinction of cases is used when handling differences between laboratories. Especially the advantage of defining classes for each device come into play here. Each device has to be initialized using the correct class. Afterwards it does not matter which kind of, e.g., pressure gauge is stored in **obj**. As long as the methods are called the same way, **obj.getData** will always return the same kind and format of data. Therefore, after mastering the first step, all devices of the same type can be considered the same.
- Missing or unavailable devices are left out. In general typical errors, like a missing response, are caught and the experimenter informed.
- Informing users about errors or noticeable problems is done by the **notifier**. Other functions call **notifier** with specific status codes, e.g. '**MONITORING:BL1:frequency:Range**'. This code tells the **notifier**, that the laser beating frequency *BL1* is out of range. If this status is new, the status code is printed to the command line, the log file and send together with a more detailed message via mail<sup>8</sup> to the user. '**MONITORING:BL1:frequency:Ok**' resets this kind of issue.
- Reduced failure of the complete monitoring system is achieved using one MATLAB timer per device. An uncaught error therefore only stops the recording from one device and not all. Additionally, each data point is directly written to the corresponding data file on the hard drive.

All in all, the focus is set on a software which is easy and quick to handle. Some functionalities, like the parameter check, are completely new. They offer additional possibilities increasing reliability. Documentation and version control of all software and circuit files is done on GitLab. This enables subsequent students the possibility to copy, comprehend and further develop all parts. However, the users can run the software by themselves without extensive knowledge.

---

<sup>7</sup>E.g., the software on <https://www.meinbergglobal.com/english/sw/ntp.htm>.

<sup>8</sup>Telegram messages are also possible since February 2023 thanks to Wachs.



# 4 Setup of a New Device for Absolute Metastable $^{40}\text{Ar}$ Flux Measurements

A high count rate is essential for precise  $^{39}\text{Ar}$  dating. The count rate depends on many parameters. However, the determination of the current count rate itself takes several hours depending on the required precision. Therefore, additional tools for analyzing and aligning the apparatus are necessary, which have to be good proxies for the  $^{39}\text{Ar}$  count rate. A new device, which measures the metastable  $^{40}\text{Ar}$  flux in absolute terms, makes it possible to quantify an equivalent metastable  $^{39}\text{Ar}$  flux between source and MOT. It is located in the quench chamber (see also figure 3.1).

The working principle is explained in the first section, followed by a detailed characterization of the image objective. The dynamical decay process is modeled from a theoretical perspective in order to include effects caused by the magnetic field in connection with the laser light polarization. Finally, the equivalent metastable  $^{39}\text{Ar}$  flux is derived. An expansion of the quantum technology to other isotopes and its application within the ArTTA is discussed.

The precursor of the new device was investigated by Ringena in [Rin21]. It allows the determination of a relative metastable  $^{40}\text{Ar}$  flux. The sensitivity is already increased compared to the implementation in the first ArTTA machine [Rit13]. In these earlier stages, the metastable  $^{40}\text{Ar}$  flux was mainly used for performance monitoring of the RF discharge source, which remains one of the applications of the new design.

## 4.1 Working Principle

Measuring the absolute metastable  $^{40}\text{Ar}$  flux is done by selectively quenching the  $^{40}\text{Ar}$  atoms to the ground state and counting a specific part of the thereby emitted photons. Let us recall again the figure 2.1 with the involved part of the argon energy spectrum. The  $^{40}\text{Ar}$  atoms in the metastable state  $4\text{s}[3/2]_2$  get excited to the state  $4\text{p}[5/2]_2$  using the quench transition with a wavelength of 801.699 nm. Two loss channels exist from this excited state, decay ① and ②. They result in two interstates before they further decay to the ground state. Therefore each decayed metastable  $^{40}\text{Ar}$  atom emits exactly one photon with a wavelength of either  $\lambda_{①} = 843 \text{ nm}$  or  $\lambda_{②} = 979 \text{ nm}$  depending on the decay path. The emitted photons from decay ① and ② are transmitted through an objective onto a detector.

**Figure 4.1:** Illustration of the working principle of the absolute metastable  $^{40}\text{Ar}$  flux measurement. The atoms fly from left to right. The quench laser beam (green) comes out of the drawing plane. The left half of the Gaussian shaped beam is blocked (D shape). Therefore, most of the fluorescence light comes from a thin disc-shaped volume. A part of this light is projected with an objective onto a detector. The objective is not to scale. A color filter blocks light from the quench as well as the cooling transition.

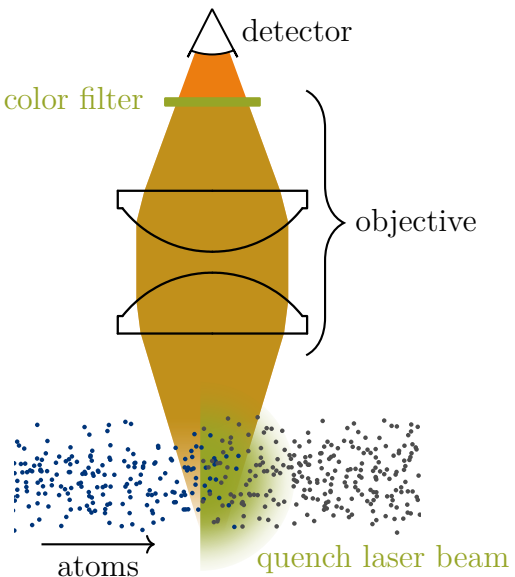


Figure 4.1 sketches the setup. The metastable  $^{40}\text{Ar}$  atoms fly from left to right. The quench laser beam comes out of the plane. It has a steep intensity drop towards the atom source. Therefore, most of the  $^{40}\text{Ar}$  atoms are quenched within a small volume. A low original volume of the spontaneously emitted photons increases the transmission efficiency of the lens to the detector. The laser intensity has to be high enough to quench the atoms before they leave the laser beam again. However, also an upper limit exists. Too high laser intensities considerably increase considerably the amount of de-excitation outside of the volume. As a result the detected signal erroneously drops.

The design of the objective is a crucial part of the setup and therefore covered in detail in the following subsection 4.2. The long-pass color filter within the objective blocks stray light from the quench and cooling transition, as they have a shorter wavelength than the decay ① and ② photons. Finally the detector measures the amount of decay photons per unit time with a specific efficiency. Knowing all efficiencies and conversion factors allows to determine the amount of metastable  $^{40}\text{Ar}$  atoms per unit time (see subsection 4.4).

This working principle is of course not restricted to  $^{40}\text{Ar}$ . Generally all metastable isotopes with a corresponding energy spectrum can be measured with this scheme, especially also krypton atoms. However, this method is restricted, as all methods are, to a signal-to-noise ratio larger or equal to one. Therefore, measurements of the metastable  $^{36}\text{Ar}$  flux are restricted to cases of enhanced flux (compare subsection 4.5.1).

## 4.2 Design and Characterization of the Image Objective

The design and characterization of the image objective is an important part deriving an absolute flux measurement. In general it has to fulfill three requirements:

- The transmission efficiency must be independent of the spatial origin of the decay photons so that it does not depend on the spatial density of the atomic beam.
- It should collect as many decay photons as possible.
- Stray light must be blocked, especially photons of the quench and cooling transition

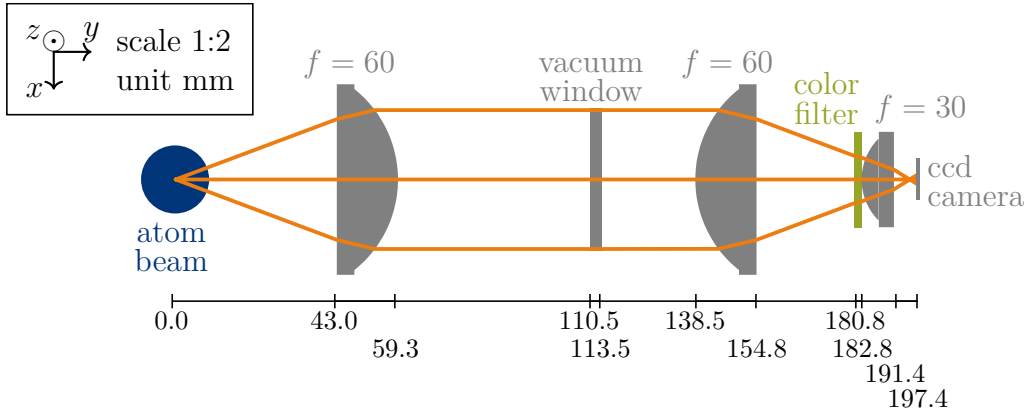


**Figure 4.2:** Graph of the quench objective looking into the atom beam (blue circle on the right). Three exemplary light rays in orange are shown. Both  $f = 60$  mm lenses are of the *LA1401-AB* type from *Thorlabs*. The  $f = 30$  mm lens is from the same manufacturer and is of the type *LA1805-AB*. The clear aperture of the vacuum window is  $d = 38$  mm. The long-pass color filter *LP02-830RU-25* from *Semrock* has an optical density of  $\text{OD} \gtrsim 6$  for wavelengths  $\lambda = 675 \text{ nm..}812 \text{ nm}$  and angles of incident  $\alpha \leq 20^\circ$  [Sem]. The camera *Mako-G 223B NIR* is from *Allied Vision*.

wavelengths.

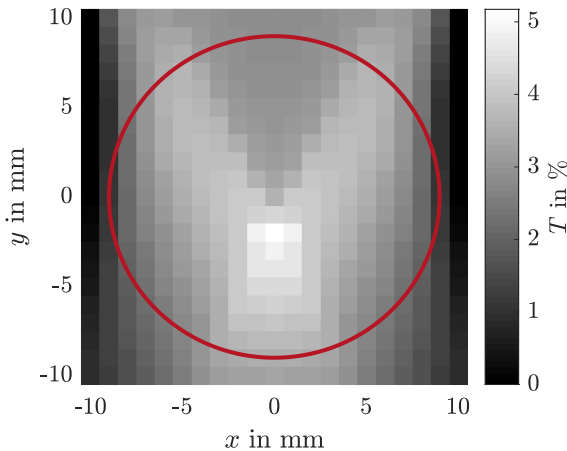
As it usually is, some of the requirements are mutually exclusive. Therefore, a compromise has to be made between the first and second point. The last point, blocking stray light, is solved using a long-pass color filter. A *LP02-830RU-25* filter from *Semrock* is used. Its transmission efficiency at  $\lambda = 843 \text{ nm}$  and at an incident angle of  $\alpha = 0^\circ$  is a factor five better compared to earlier used filters [Rin21]. The optical density of the filter in the blocking band is  $\text{OD} \gtrsim 6$  for  $\lambda = 675 \text{ nm..}812 \text{ nm}$  and  $\alpha \leq 20^\circ$  [Sem]. As the characteristic of such thin-film filters shifts to shorter wavelengths with increasing incident angle, their position within the objective has to be chosen carefully.

A graph of the final objective is shown in figure 4.2. A  $f = 60$  mm biconvex lens collimates the spontaneously emitted light. After passing a vacuum window, an equal lens focuses the photons towards the color filter. The incident angles at the color filter do not exceed  $24^\circ$  due to geometrical restrictions. This still corresponds to an optical density of approximately seven for the quench transition. However, the incident angle is typically below  $20^\circ$ . A final lens with a focal length of  $f = 30$  mm is placed behind the color filter, which increases the transmission efficiency of the objective.

Design and characterization of the objective is done using the ray tracing software *OSLO 6.3*. A detailed analysis is given in [Sch22]. In addition to this work, Schwenzer has also taken experimental data of a second setup for the first ArTTA machine being in good agreement to the modeled results.

As a first characterization step, the transmission efficiency of the objective is determined. The original volume of the spontaneously emitted photons is assumed to be a thin disk (compare the blue circle in figure 4.2). The diameter of this disk is given by the diameter of differential pumping stage being 18 mm. The thickness is assumed to be approximately one millimeter from the results of the dynamical decay model in the following section.

**Figure 4.3:** Spatial dependency of the transmittance  $T$  modeled with a point-like source in *OSLO 6.3*. Objective and camera are placed above the graph. The atoms are flying out of the paper plane within the red circle. Mean and standard deviation of the region of interest are  $T = 3.36(64)\%$ .



A light source emitting photons randomly within this volume in random directions is programmed into OSLO. The transmittance of the objective from this light source onto the camera is  $T = 3.35\%$ .

The spatial dependency of the transmission efficiency is instead analyzed using a point like light source. Figure 4.3 graphs the results of the transmittance placing this light source once at each grid position. The highest value is slightly below the center with 5.12 %. The very left and right edge have the lowest transmittance with 1.11 %. All in all, the mean and standard deviation of the region of interest is  $T = 3.4(6)\%$ . Compared to the objective presented in [Rin21], the transmittance is reduced by 30 %. However, this is compensated for by the transmission through the color filter, which is five times higher. On the other hand, the spatial dependency is reduced by a factor of approximately two. Therefore, a good trade off between overall transmittance and spatial dependency is achieved. This enables qualitative measurements of the metastable  $^{40}\text{Ar}$  flux using the collimator and/or the 2D-MOT, as they produce an inhomogeneous atom beam density.

Compendious, the objective fulfills the above stated requirements. The overall transmittance is increased by a factor 3.5 and the spatial dependency reduced by a factor of approximately two compared to the precursor. The new long-pass color filter now blocks unwanted stray light down to the noise level of the camera.

### 4.3 Dynamical Decay Model

In the following, a theoretical model is derived describing the decay process under the presence of a magnetic field. The absolute metastable  $^{40}\text{Ar}$  measurement takes place at the quench chamber, located between the 2D-MOT and the ZSL. Both use magnetic fields for operation. The remaining field within the quench chamber is not negligible and affects the measurement. As the metastable atoms are in a state with  $J = 2$  and get excited to  $J' = 2$ , transitions from  $m_J = 0$  to  $m_{J'} = 0$  are forbidden by the selection rules. Additionally, the spatial radiation possibility towards the objective depends on the polarization of the emitted photon. Thus, the orientation of the electromagnetic wave with respect to the magnetic field plays a crucial role. The dynamical decay model (DDM) is derived to account for the magnetic field and the polarization during the decay process.

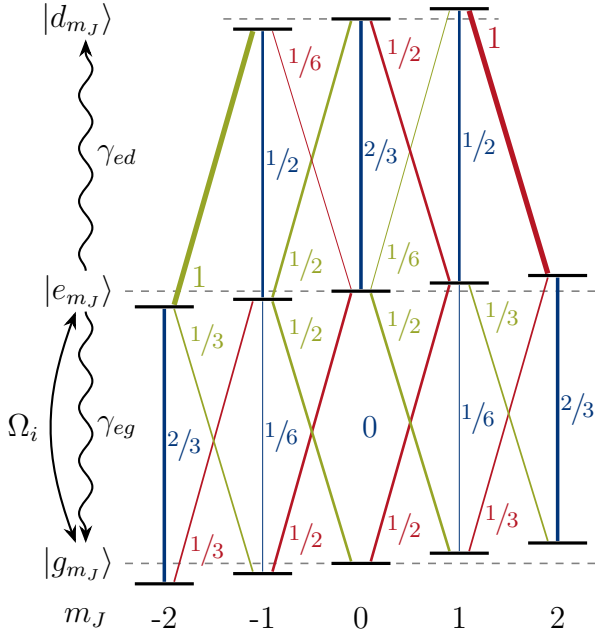


**Figure 4.4:** Illustration of the DDM. The atoms start in the metastable states  $|g_{m_J}\rangle$ . The transitions to the excited states  $|e_{m_J}\rangle$  are driven with the Rabi frequency  $\Omega_i$  depending on the polarization (green  $\sigma^+$ , blue  $\pi$ , red  $\sigma^-$ ). The atoms decay back to the metastable states or to the decayed states  $|d_{m_J}\rangle$ . Note that the energy levels of the latter are below the selfsame of the  $|g_{m_J}\rangle$ . For readability  $|d_{m_J}\rangle$  is drawn at the top. The line width of the transitions scales with the relative transition strengths noted close to them. The sublevels are detuned by the Zeeman effect.

A correction factor is derived from the DDM to parameterize the observed effects.

The DDM for the quench process is derived in close analogy to the interaction of a two-level system with light (compare subsection 2.2.1). Again, the interaction picture is used and the suffix  $_I$  is neglected for readability.

Remember the relevant part of the energy spectrum in figure 2.1. The atoms start in the metastable state  $4s[3/2]_2$  with the magnetic sublevels  $m_J = \{-2, \dots, 2\}$ . For clearness these states are denoted with  $g$ , as  $m$  is already used for the magnetic sublevel:  $\{|g_{-2}\rangle, \dots, |g_2\rangle\}$ . Starting in these states, the atoms get excited to the state  $4p[5/2]_2$ , again with five magnetic sublevels:  $\{|e_{-2}\rangle, \dots, |e_2\rangle\}$ . These states additionally couple with the two decay interstates  $4s[3/2]_1$  and  $4s[1/2]_1$ . The transitions to the decay interstates are identical up to the decay rate<sup>1</sup>. Therefore, one can combine these two states to the decayed state, which has three magnetic sublevels:  $\{|d_{-1}\rangle, \dots, |d_1\rangle\}$ . Figure 4.4 shows a sketch of the system. All in all, the Hilbert space has  $n = 13$  dimensions.

Let us define the  $13 \times 13$  density matrix (2.1) as

$$\rho \equiv \sum_{i,j} \rho_{ij} |i\rangle \langle j|,$$

with the basis vectors  $|i\rangle = |j\rangle^\dagger$  of the orthonormal basis  $\{|g_{m_J}\rangle, |e_{m_J}\rangle, |d_{m_J}\rangle\}$ . At  $t = 0$  the system is assumed to be in a statistical mixture of equal occupied magnetic sublevels in the metastable state:

$$\rho(t=0) = \sum_i \frac{1}{5} |g_i\rangle \langle g_i|. \quad (4.1)$$

A uniform population is assumed since the atoms have not been manipulated since

<sup>1</sup>The wavelength of the emitted photons is also different, but at the moment not significant. It is considered below in equation (4.14).

excitation to the metastable state within the plasma source [Rit13].

The interaction Hamiltonian  $\mathcal{H}_I$  of the atoms with the laser light is given by

$$\begin{aligned} \mathcal{H}_I = & \frac{\hbar}{2} \left( \Omega_{\sigma^+} \sum_{i=-2}^1 \sqrt{\Xi_{i,i+1}^{2,2}} \exp(i\delta_{i,i+1}t) |g_i\rangle \langle e_{i+1}| \right. \\ & + \Omega_\pi \sum_{i=-2}^2 \sqrt{\Xi_{i,i}^{2,2}} \exp(i\delta_{i,i}t) |g_i\rangle \langle e_i| \\ & \left. + \Omega_{\sigma^-} \sum_{i=-1}^2 \sqrt{\Xi_{i,i-1}^{2,2}} \exp(i\delta_{i,i-1}t) |g_i\rangle \langle e_{i-1}| \right) + \text{h. c.} \end{aligned} \quad (4.2)$$

The three summands define the  $\sigma^+$ ,  $\pi$  and  $\sigma_-$  transitions with Rabi frequency  $\Omega_i$ , respectively.  $\Xi_{m_J, m_{J'}}^{J, J'}$  is the relative transition strength (2.16). The detuning  $\delta_{i,j}$  is given by the Zeeman detuning  $\delta_Z$  (2.15) with the measured Landé  $g$ -factors in table 2.2.

The dissipator for the spontaneous emission from the excited states  $|e_{m_J}\rangle$  into the metastable states  $|g_{m_J}\rangle$  is

$$\mathcal{D}_{eg}(\rho) = \gamma_{eg} \sum_{i,j} \Xi_{i,j}^{2,2} \left( \sigma_{ij} \rho \sigma_{ij}^\dagger - \frac{1}{2} \{ \sigma_{ij}^\dagger \sigma_{ij}, \rho \} \right), \quad \text{with } \sigma_{ij} = |g_j\rangle \langle e_i| \quad (4.3)$$

and the decay rate  $\gamma_{eg} = 9.28(74)$  MHz [Wie+89]. Accordingly, the dissipator for the spontaneous emission into the decayed states  $|d_{m_J}\rangle$  is quite similar:

$$\mathcal{D}_{ed}(\rho) = \gamma_{ed} \sum_{i,j} \Xi_{i,j}^{2,1} \left( \sigma_{ij} \rho \sigma_{ij}^\dagger - \frac{1}{2} \{ \sigma_{ij}^\dagger \sigma_{ij}, \rho \} \right), \quad \text{with } \sigma_{ij} = |d_j\rangle \langle e_i|. \quad (4.4)$$

Here, the decay rate  $\gamma_{ed} = A_{\textcircled{1}} + A_{\textcircled{2}} = 22.97$  MHz is the sum of the Einstein coefficients of decay  $\textcircled{1}$  and  $\textcircled{2}$  [Wie+89].

Inserting (4.2), (4.3) and (4.4) into the Lindblad Equation (2.4) results in the equation of motion for the DDM:

$$\frac{d\rho}{dt} = -\frac{i}{\hbar} [\mathcal{H}_I, \rho] + \mathcal{D}_{eg}(\rho) + \mathcal{D}_{ed}(\rho). \quad (4.5)$$

This equation is solved numerically for the starting condition (4.1).

### 4.3.1 Experimental Parameter

Before the DDM can be solved, some experimental parameters have to be determined. The following values were measured at the second facility. One is the magnetic field direction and strength at the cross-section of the atoms and the quench laser beam. For the orientation of the laboratory coordinate system it is referred to figure 4.2. The magnetic field is measured to be  $\vec{B} \approx (0.03, 0.32, -3.6)^T$  G at a ZSL solenoid current of

$I_{\text{ZSL}} = 11.43 \text{ A}$  and a 2D-MOT solenoid current<sup>2</sup> of  $I_{\text{2D-MOT}} = 1.00 \text{ A}$ . The orientation of the quantization axis for the DDM  $\hat{z}_{\text{ddm}}$  is chosen such that  $\vec{B} = B\hat{z}_{\text{ddm}}$ . The angles

$$\sin \theta = \frac{B_y}{B} \quad \text{and} \quad \sin \phi = \frac{B_x}{\sqrt{B_x^2 + B_z^2}} \quad (4.6)$$

describe the orientation of  $\hat{z}_{\text{ddm}}$  with respect to  $\hat{z}_{\text{lab}}$ . Therefore, a vector is first rotated by the angle  $\theta$  around the  $x$ -axis and by then the angle  $\phi$  around the  $y$ -axis of the laboratory.

The Rabi frequencies are retrieved from the measured laser power  $P = 15.8 \text{ mW}$ . The laser beam has a Gaussian intensity profile with a radius of  $w \approx 10 \text{ mm}$ . According to the equations for Gaussian beams [Mes10], the maximum intensity is  $I_{\text{max}} \approx 27 \text{ mW/cm}^2$  and the mean intensity over the whole laser-atom cross-section  $\tilde{I} \approx 4.7 \text{ mW/cm}^2$ . The saturation intensity (2.9) is  $I_s = 0.375 \text{ mW/cm}^2$ . With equation (2.8), the Rabi frequency is  $\Omega_{\text{max}} \approx 6.0\gamma_{eg}$ , respectively  $\tilde{\Omega} \approx 2.5\gamma_{eg}$ . Note that these Rabi frequencies only correspond to the actual Rabi frequency of the atom if the relative transition strength is one and the entire laser intensity drives the transition. The dependence on the actual Rabi frequency is derived below.

First, the linear polarized light is split into the  $\sigma^+$ ,  $\pi$  and  $\sigma^-$  polarizations of the DDM<sup>3</sup>. The laser beam is traveling in negative  $x$ -direction and the angle between the linear polarization and the  $z$ -axis is defined as  $\alpha$ . Thus the direction of the electric field  $\hat{E}$  in the laboratory frame is given by

$$\hat{E}_{\text{lab}} = \begin{pmatrix} 0 \\ \sin \alpha \\ \cos \alpha \end{pmatrix}_{\text{lab}}.$$

Rotating  $\hat{E}_{\text{lab}}$  into the coordinate system of the DDM using the angles  $\theta$  and  $\phi$ , defined in (4.6), results in

$$\hat{E}_{\text{ddm}} = \begin{pmatrix} -\cos(\alpha - \theta) \sin \phi \\ \sin(\alpha - \theta) \\ \cos(\alpha - \theta) \cos \phi \end{pmatrix}_{\text{ddm}}.$$

The  $z_{\text{ddm}}$  component of the electric field drives the  $\pi$  transitions, while the other two drive  $\sigma^\pm$  transitions in equal parts. Using the proportionality of the electric field and the Rabi frequency results in the Rabi frequencies of the different polarizations

$$\Omega_\pi = \cos(\alpha - \theta) \cos \phi \Omega \quad \text{and} \quad (4.7)$$

$$\Omega_{\sigma^+} = \Omega_{\sigma^-} = \sqrt{\frac{\sin^2(\alpha - \theta) \cos^2 \phi + \sin^2 \phi}{2}} \Omega. \quad (4.8)$$

The factor  $1/\sqrt{2}$  results from splitting the linear polarized light in left and right circular polarization. Note that these are still the Rabi frequencies for a relative transition strength

---

<sup>2</sup>The current of the 2D-MOT solenoid is defined positive, when the magnetic field of the selfsame in the quench chamber points in the same direction as the magnetic field of the ZSL solenoid. A negative current consequently result in two opposing magnetic fields.

<sup>3</sup>Basic information about the polarization dependencies of the transitions is found in the discussion about selection rules and polarization in subsection 2.2.4.

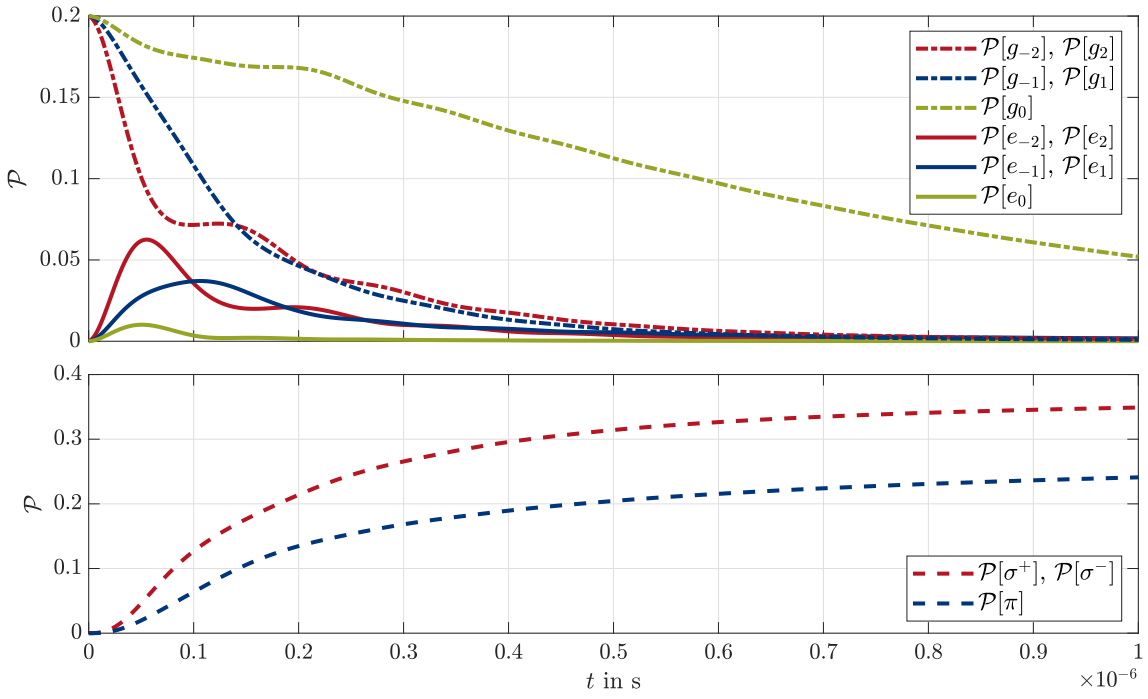


**Figure 4.5:** Exemplary solution of the Lindblad equation (4.5) for the DDM. The upper subplot shows the time-dependent occupation of the magnetic sublevels. The dot-dash lines represent the ground states and the solid lines the excited states. Note that the occupation of the  $\{m_J, -m_J\}$  states is identical and therefore only plotted once. The decay polarization probability is shown at the bottom subplot. The polarization angle is  $\alpha = 27^\circ + \theta$ , the magnetic field  $\vec{B} \approx (0.03, 0.32, -3.6)^\top \text{G}$  and the Rabi frequencies are  $\Omega_\pi = 5.36\gamma_{eg}$  and  $\Omega_{\sigma^\pm} = 1.93\gamma_{eg}$ .

equal to one. However, the latter is already included in the Hamiltonian (4.2). The equations (4.7) and (4.8) already show the symmetry of the results in relation to the polarization. The results are mirror-symmetric at  $0^\circ$  and  $90^\circ$ .

The last experimental parameter is the interaction time  $T_I$  of the atoms with the laser light. It is given by the width of the quench laser beam at the radial position of the atom and the atom's velocity. As both vary from atom to atom, an estimated value of  $T_I = 15 \mu\text{s}$  is used. For example, this corresponds to a velocity of  $v_z = 400 \text{ m s}^{-1}$  and a width of 6.0 mm.

### 4.3.2 Correction Factor

The next step towards the correction factor for the fluorescence signal is solving the Lindblad equation (4.5) of the DDM for different experimental parameters. This is done numerically using MATLAB. An exemplary time-dependent solution is shown in figure 4.5. For readability the probability of being in the basis state  $|i\rangle$  is denoted with  $\mathcal{P}[i] = \langle i|\rho|i\rangle = \rho_{ii}$ . The upper subplot illustrates the magnetic sublevel occupation of the

ground and excited state,  $\mathcal{P}[g_{m_J}]$ ,  $\mathcal{P}[e_{m_J}]$ , respectively. In the beginning, some strongly damped Rabi oscillations and a redistribution of the atoms towards the  $m_J = 0$  and  $m_J = \pm 2$  ground states are visible. These redistributions during the decay process make it necessary to solve the equation of motion (4.5) to describe the fluorescence signal.

The lower subplot of figure 4.5 shows the time-dependent probability that an atom decays with the polarization  $\mathcal{P}[\sigma^+]$ ,  $\mathcal{P}[\pi]$  and  $\mathcal{P}[\sigma^-]$ . These probabilities are derived looking at the decay rate from the excited state  $|e_i\rangle$  to the decayed state  $|d_j\rangle$ :

$$\Gamma_{e_i d_j}(\tau) = \gamma_{ed} \Xi_{i,j}^{2,1} \mathcal{P}[e_i](\tau).$$

Adding all transitions with the same polarization and integrating over time results in the desired probabilities:

$$\begin{aligned} \mathcal{P}[\sigma^+](t) &= \gamma_{ed} \int_0^t \sum_{i=-1}^1 \Xi_{i+1,i}^{2,1} \mathcal{P}[e_{i+1}](\tau) d\tau, \\ \mathcal{P}[\pi](t) &= \gamma_{ed} \int_0^t \sum_{i=-1}^1 \Xi_{i,i}^{2,1} \mathcal{P}[e_i](\tau) d\tau, \\ \mathcal{P}[\sigma^-](t) &= \gamma_{ed} \int_0^t \sum_{i=-1}^1 \Xi_{i-1,i}^{2,1} \mathcal{P}[e_{i-1}](\tau) d\tau. \end{aligned} \quad (4.9)$$

Note that

$$\mathcal{P}[\sigma^+] = \mathcal{P}[d_1], \quad \mathcal{P}[\pi] = \mathcal{P}[d_0] \quad \text{and} \quad \mathcal{P}[\sigma^-] = \mathcal{P}[d_{-1}] \quad (4.10)$$

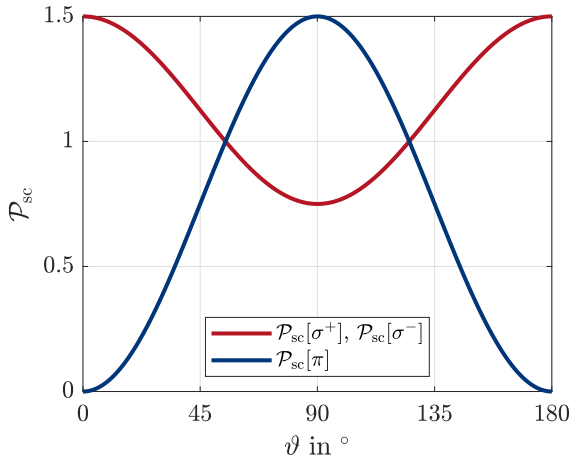
for symmetry reasons. This can be shown when multiplying (4.5) from left with  $\langle d_0 |$  and from right with  $|d_0 \rangle$ :

$$\begin{aligned} \dot{\mathcal{P}}[d_0] &= -\frac{i}{\hbar} \underbrace{\langle d_0 | [\mathcal{H}, \rho] | d_0 \rangle}_{=0} + \underbrace{\langle d_0 | \mathcal{D}_{eg}(\rho) | d_0 \rangle}_{=0} + \langle d_0 | \mathcal{D}_{ed}(\rho) | d_0 \rangle \\ &= \gamma_{ed} \sum_{i=-1}^1 \Xi_{i,0}^{2,1} \mathcal{P}[e_i]. \end{aligned} \quad (4.11)$$

The symmetry of the relative transition strength shows  $\Xi_{i,0}^{2,1} = \Xi_{i,i}^{2,1}$  (compare figure 4.4). Using this relation and integrating (4.11) over time results in equation (4.9). The proof of the others follows accordingly. In general, the equalities in (4.10) account for all decay transitions from  $J = 2$  to  $J = 1$ , as no argon specific assumptions have been made.

Coming back to the derivation of the correction factor. The decay of the metastable  ${}^{40}\text{Ar}$  is a continuously ongoing process as new atoms arrive all the time. Therefore, the dynamics themselves are not observable. However, the fluorescence signal is the sum of all detected decay photons at interaction time  $T_I$ . Remember from the discussion of the selection rules and polarization in subsection 2.2.4 that no photons are radiated in the direction of the quantization axis from  $\pi$  transitions. Therefore, the probabilities (4.9) have to be weighted with the radiation pattern. Figure 4.6 shows the radiation pattern as relative scattering probability  $\mathcal{P}_{sc}$ . The latter depends on the angle of observation  $\vartheta$ , defined with respect to

**Figure 4.6:** Graph of the scattering probability  $\mathcal{P}_{\text{sc}}$  in direction  $\vartheta$ .  $\vartheta$  is defined with respect to the quantization axis.  $\mathcal{P}_{\text{sc}}$  is normalized to a uniform scattering distribution. Thus, a value of  $\mathcal{P}_{\text{sc}}(\vartheta) = 1.5$  corresponds to 1.5 times more observed atoms per solid angle under the angle  $\vartheta$  than having for a direction independent radiation pattern.



the quantization axis.  $\mathcal{P}_{\text{sc}}$  is normalized to a uniform scattering distribution and is given by<sup>4</sup> [LM81]

$$\mathcal{P}_{\text{sc}}[\pi](\vartheta) = \frac{3}{2} \sin^2 \vartheta \quad \text{and} \quad \mathcal{P}_{\text{sc}}[\sigma^\pm](\vartheta) = \frac{3}{4}(2 - \sin^2 \vartheta). \quad (4.12)$$

In the experiment, the decay photons are detected in  $y$ -direction of the laboratory. With the angles of the quantization axis (4.6), the angle  $\vartheta$  is given by  $\cos \vartheta = \cos \phi \sin \theta$ . Finally, the correction factor  $C$  of the fluorescence signal is the sum of all decayed photons (4.9) multiplied with their relative scattering probability (4.12) at time  $T_I$ . This reads:

$$C = \mathcal{P}_{\text{sc}}[\sigma^\pm](\vartheta) (\mathcal{P}[\sigma^+](T_I) + \mathcal{P}[\sigma^-](T_I)) + \mathcal{P}_{\text{sc}}[\pi](\vartheta) \mathcal{P}[\pi](T_I). \quad (4.13)$$

The dependency of this factor on different experimental parameter as well as the comparison with measurement results is discussed in the following subsection.

### 4.3.3 Comparison of Experimental and DDM Results

In the following, the results of the DDM are compared with two measurements at different magnet field strengths.

#### Magnetic Field caused by the ZSL

Let us start with the comparison of results obtained at lower magnetic fields. To do so, 2D-MOT current is chosen to be  $I_{\text{2D-MOT}} = 0.0 \text{ A}$  and the measured magnetic field within the quench chamber  $\vec{B} \approx (-0.14, 0.44, -1.8)^T \text{ G}$ . With (4.6), this results in  $\theta \approx 14^\circ$  and  $\phi \approx -4^\circ$ .

Figure 4.7 shows the decay time  $T_d$  of the DDM. It is defined as the length of interaction time in which a certain fraction of atoms has decayed. The latter is given by  $\mathcal{P}[d] = \sum_i \mathcal{P}[d_i]$ . The results are plotted for the mean and maximum Rabi frequency,  $\tilde{\Omega} = 2.5\gamma_{eg}$  and  $\Omega_{\text{max}} = 6.0\gamma_{eg}$ . Most of the atoms decay within the first 5  $\mu\text{s}$ , for  $\Omega_{\text{max}}$  even within the first 2  $\mu\text{s}$ . A slight increase is visible towards  $\alpha - \theta = \pm 90^\circ$ , where the coupling of  $\pi$  transitions

<sup>4</sup>See also table 5.1 in section 5.3.

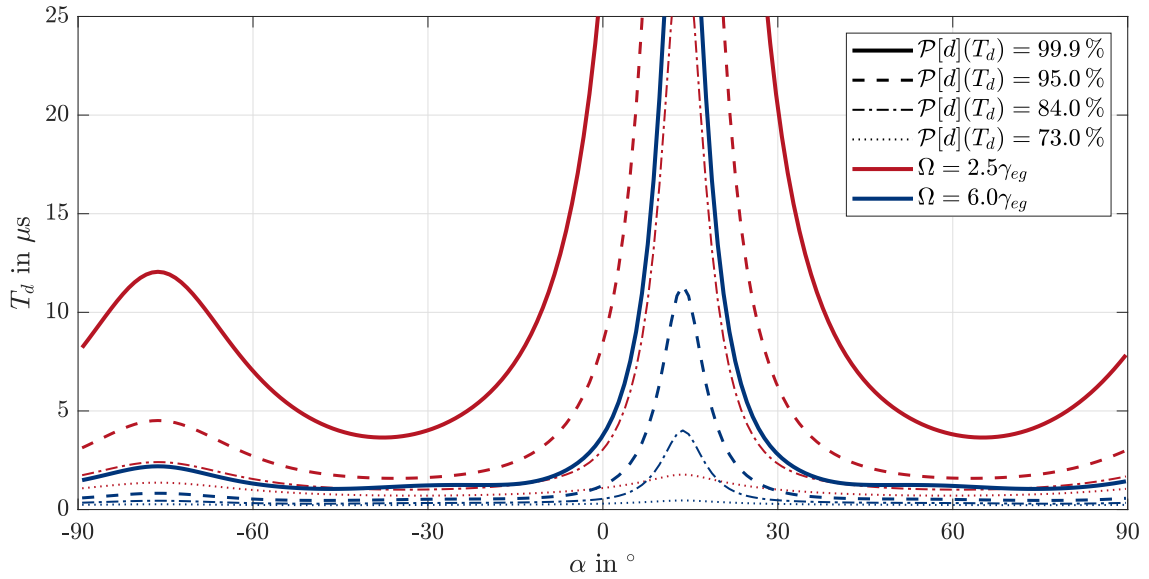


**Figure 4.7:** Plot of the decay time  $T_d$  until 99.9 %, 95.0 %, 84.0 % and 73.0 % of the atoms decayed. Most of the atoms decay within the first 5  $\mu\text{s}$ . However, for laser polarizations  $\alpha - \theta \sim 0^\circ$  the coupling of the  $m_J = 0$  ground state gets very weak and the decay time strongly increases for these final atoms. Further, the stretched state is only weakly coupled with  $\sigma^\pm$  excitations for  $\alpha - \theta = 90^\circ$ . The magnetic field is set to  $\vec{B} = (-0.14, 0.44, -1.8)^\top \text{G}$ .

gets weaker and actually becomes zero. As the Zeeman shift of the  $\sigma^\pm$  transitions of the stretched state is the largest and their relative transition strength only  $1/3$ , the overall coupling of these states to the excited states gets strongly suppressed. However, a larger effect is visible for laser polarizations  $\alpha - \theta \sim 0^\circ$ , where the decay time increases drastically. For example is  $T_d(99.9\%) = 37.5 \mu\text{s}$  for  $\Omega = \Omega_{\max}$ . The coupling of  $\sigma^\pm$  transitions gets minimal for these polarizations. As the  $\pi$  excitation  $m_J = 0 \rightarrow 0$ ,  $J = 2 \rightarrow 2$  is forbidden, only very small Rabi frequencies  $\Omega_{\sigma^\pm} \approx \phi\Omega/\sqrt{2}$ , with  $\phi \approx 0$ , couple the corresponding ground state. Consequently, the interaction time  $T_I$  is too short in order to de-excite all atoms.

The amount of non-decayed  ${}^{40}\text{Ar}$  is verified by looking at the corresponding loading rate. A comparably long loading time of  $\tau_{\text{LR}} = 40 \text{ ms}$  is selected. Thus, combined with a long exposure time, a high sensitivity for even small loading rates  $L$  is achieved. The measured loading rate  $L$  is shown in the lower subplot of figure 4.8 (green circles). They are compared with the amount of atoms in the decayed states  $\mathcal{P}[d]$  after an interaction time of  $T_I = 15 \mu\text{s}$ . Therefore, if all atoms are de-excited, the loading rate has to be zero:  $L = 0 \stackrel{?}{=} \mathcal{P}[d] = 1$ . The further actual scaling between them is unknown. However, with decreasing decay probability  $\mathcal{P}[d]$  the loading rate has to increase. This is actually the case. Where the DDM derives  $\mathcal{P}[d] = 1$ , there the loading rate clearly shows, that all  ${}^{40}\text{Ar}$  atoms decay up to a small, presumably fast moving, amount. Both show a decreased amount of decayed  ${}^{40}\text{Ar}$  atoms for polarizations  $\alpha - \theta \sim 0^\circ$ . The position of the minimum depends on the magnetic field direction. The latter is measured for the DDM directly within the quench chamber. The polarization of the laser beam is measured behind the quench chamber with a polarization analyzer. However, the small deviation of the minimum position is thought

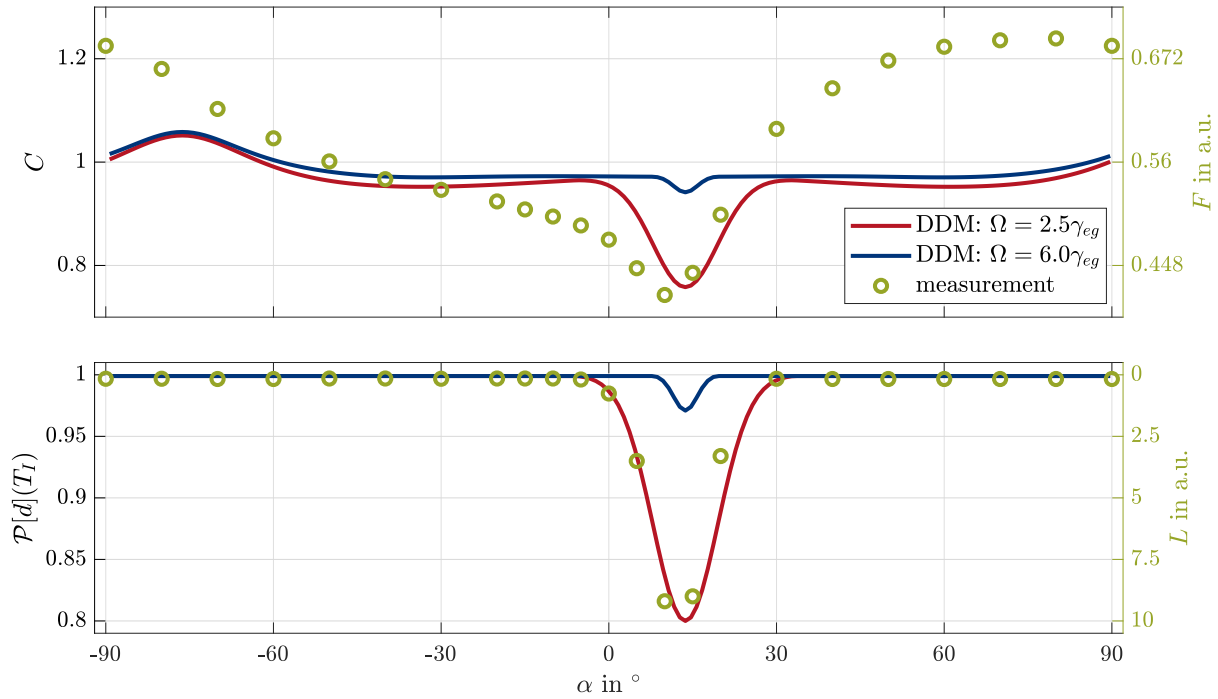


**Figure 4.8:** Comparison of DDM and experimental results with  $I_{\text{ZSL}} = 11.43 \text{ A}$  and  $I_{\text{2D-MOT}} = 0.0 \text{ A}$ . The upper subplot shows the correction factor  $C$  compared to the measured fluorescence  $F$ . The lower subplot illustrates the decay probability  $\mathcal{P}[d]$  of an atom and the loading rate  $L$  of the MOT. The  $y$ -axis of the loading rate is inverted since only non-decayed atoms can be trapped. While the results in the lower subplot agree, they suggest that the deviation of the selfsame in the upper subplot is an effect not covered by the DDM.

to mainly depend on measurement errors of the magnetic field. Due to the necessity of opening the vacuum, a resulting hysteresis between magnetic field and loading rate measurement can be assumed.

Comparing the width of the dip with the results of the DDM for  $\Omega = 2.5\gamma_{eg}$  shows a good agreement. This validates, that the assumed interaction time  $T_I = 15 \mu\text{s}$  as well as the mean Rabi frequency  $\tilde{\Omega}$  in general deliver convincing results. However, it should be noted that the actual experiment is a combination of different interaction times, Rabi frequencies, and other factors.

The upper subplot of figure 4.8 displays the theoretical derived correction factor  $C$ . This value is compared to the fluorescence  $F$  of the atoms, which is measured with the new  ${}^{40}\text{Ar}$  absolute flux measurement tool objective and camera. Both  $y$ -axis have the same zero point. The linear scaling between them is fixed to  $F = 0.56C$  for all measurements. As it is the case in the lower subplot, the dip is visible in the fluorescence signal and the correction factor. Depth as well as width of the dip approximately agree. However, the dependence of the fluorescence on the polarization is larger as the selfsame of the correction factor. A possible explanation is the finite perfection of polarization. Therefore, a difference between  $\Omega_{\sigma+}$  and  $\Omega_{\sigma-}$  is introduced. The ratio of them is arbitrarily set to  $\Omega_{\sigma+}/\Omega_{\sigma-} = 1.5$ , while

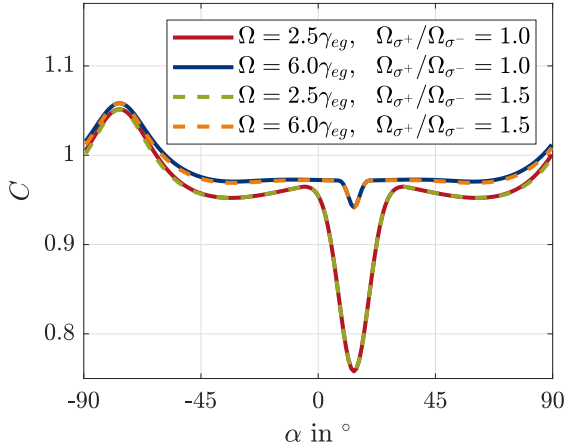


**Figure 4.9:** Graph of the correction factor  $C$  depending on the laser polarization  $\alpha$ . Once for perfect linear polarization,  $\Omega_{\sigma+}/\Omega_{\sigma-} = 1.0$  and once for elliptical polarized light with  $\Omega_{\sigma+}/\Omega_{\sigma-} = 1.5$ .  $\Omega_\pi$  is still given by (4.7). No significant difference occurs. The interaction time is  $T_I = 15 \mu\text{s}$  and the magnetic field is  $\vec{B} \approx (-0.14, 0.44, -1.8)^\top \text{G}$ .

$\Omega_\pi$  is still given by (4.7). This corresponds to an increasing polarization ellipticity with decreasing  $\Omega_\pi$ . The correction factor obtained in this way is shown in figure 4.9. However, only minor differences are visible compared to the original correction factor. The main difference, which is not visible in figure 4.9, is a longer decay time  $T_d$  at polarization angles  $\alpha - \theta \sim 90^\circ$ . However, this can only result in a smaller but not larger correction factor. Furthermore, in the experiment, only the part of the light that travels along the direction of the quantization axis can couple to  $\sigma^+$ ,  $\sigma^-$  transitions. This part is small, due to a small angle  $\phi$ . Therefore, the finite perfection of polarization is unlikely the reason for the measured effect.

Effects from a non-vanishing Doppler shift are also evaluated. Indeed, a detuning of the laser frequency increases the correction factor from  $C = 1.06$  to  $C = 1.07$  for a Doppler shift introduced detuning of  $\delta_D = 5\gamma_{eg}$ <sup>5</sup> at  $\alpha - \theta = 90^\circ$ . However, this is neglectable compared to the measured discrepancy. Therefore, no significant offset of the correction factor due to made assumptions has been found. Further measurements with magnetic fields in this regime and other with even lower magnetic fields also showed a strong fluorescence increase towards  $\alpha - \theta \sim 90^\circ$ . All have in common, that the Zeeman shift is in the same order or even lower as the light shift of the dressed atom [MS99]. All in all, this results in the hypothesis that the derived DDM does not cover the limit of a weak magnetic field compared to the light field.

## Magnetic Field caused by ZSL and 2D-MOT

Under standard conditions holds  $I_{\text{2D-MOT}} \neq 0.0 \text{ A}$ . If  $I_{\text{2D-MOT}} > 0$  is selected, the resulting magnetic field is stronger. The results of these experimental parameters, also mentioned in subsection 4.3.1, are discussed in the following. A short recap: The 2D-MOT current is  $I_{\text{2D-MOT}} = 1.00 \text{ A}$  and the resulting magnetic field  $\vec{B} \approx (0.03, 0.32 - 3.6)^\top \text{G}$  is approximately two times stronger than the field with  $I_{\text{2D-MOT}} = 0.0 \text{ A}$ .  $\theta$  is approximately  $5^\circ$  and  $\phi \approx 0.5^\circ$ . Note that additional graphs can be found in appendix A.4.

The increased Zeeman shift also increases the decay times  $T_d$ <sup>6</sup>. This is reflected in the loading rate measurement obtained under the new conditions. The lower subplot in figure

<sup>5</sup>A Doppler shift of  $\delta = 5\gamma_{eg}$  corresponds to a velocity of  $6 \text{ m s}^{-1}$  in direction of the laser beam. This in turn corresponds to an angle of approximately  $1^\circ$  with an overall velocity of  $400 \text{ m s}^{-1}$ .

<sup>6</sup>See figure A.3 in the supplementary appendix A.4.

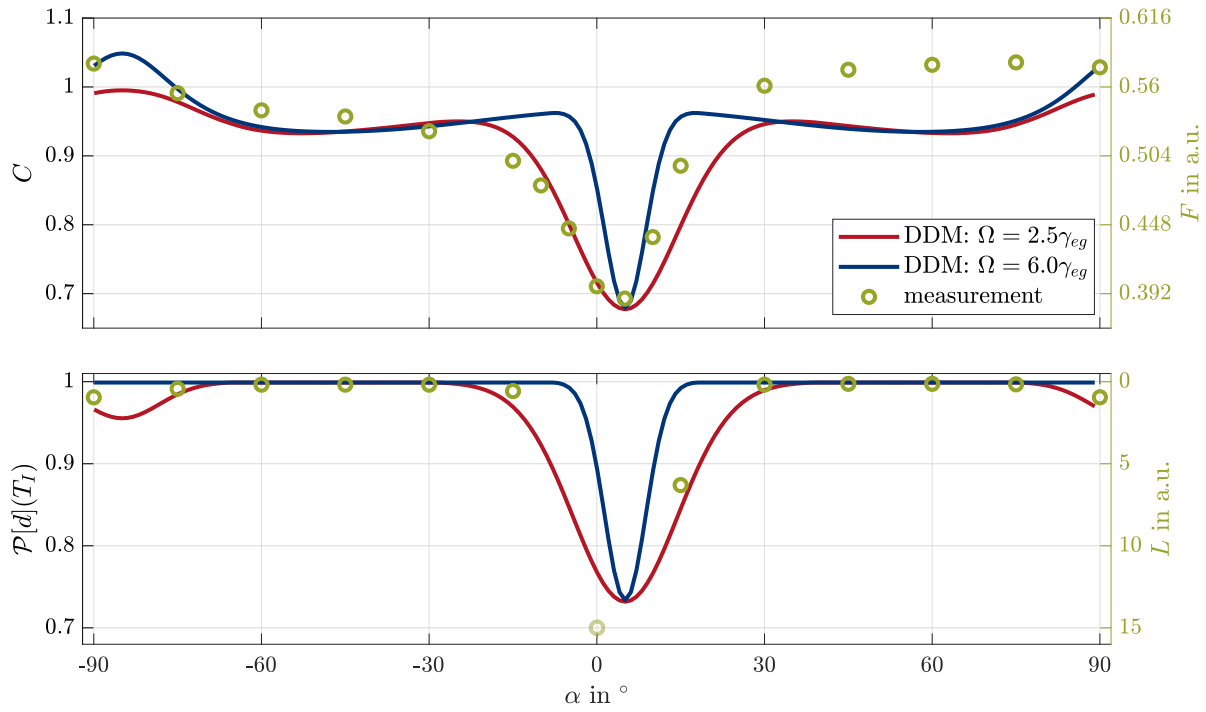


**Figure 4.10:** Comparison of the DDM and experimental results with  $I_{\text{ZSL}} = 11.43 \text{ A}$  and  $I_{\text{2D-MOT}} = 1.00 \text{ A}$ . The upper subplot shows the correction factor  $C$  compared to the measured fluorescence  $F$ . The lower subplot illustrates the decay probability  $\mathcal{P}[d]$  of an atom and the loading rate  $L$  of the MOT. The scaling between the two  $y$ -axes of each subplot is the same as in figure 4.8. The theoretical and measured results basically agree in both subplots. Note that the measuring point  $L(\alpha = 0^\circ)$  is outside the measuring range due to too many atoms and is therefore displayed transparently.

4.10 shows the comparison of decay probability  $\mathcal{P}[d]$  and loading rate  $L$  for this setup. The scaling between the two  $y$ -axis is the same as in figure 4.8. Beside the dip at  $\alpha - \theta \sim 0^\circ$ , an additional increase of the loading rate is visible at  $\alpha - \theta \sim 90^\circ$ . This is in agreement with the DDM.

Again, the upper subplot of figure 4.10 shows the comparison of the correction factor  $C$  and the measured fluorescence  $F$ . The theoretically derived dip around  $\alpha - \theta \sim 0^\circ$  basically agrees with the measured values. This time, the slightly imperfect symmetry of the latter can be explained in terms of finite polarization perfection. The polarization perfection changes with the polarization angle  $\alpha$ , which breaks symmetry considerations. This argument can be extended to the discrepancies on the right. However, measurement and DDM agree quite well on the left side of the dip. The fluorescence maximum is on the scale of the correction factor.

All in all, the DDM is able to explain the observed MOT loading rates. For weak magnetic fields, a stronger increase of the fluorescence is measurable, as theoretically derived. However, the DDM describes the measured fluorescence in general quite well for regimes with a maximum Zeeman shift well above the Rabi frequency. As a consequence, the magnetic field orientation of the 2D-MOT should be chosen in a way that it strengthens

the field of the ZSL inside the quench chamber. As a nice side-effect, it slightly increases the ZSL's capture limit. Negative effects on the  $^{39}\text{Ar}$  count rate are unlikely. The laser polarization should be linear with  $\alpha \approx 45^\circ$ . Circular polarization is not preferable, as any angle  $\phi \neq 0^\circ$  results in not coupling one of the stretched states.

For precise absolute measurements of the  $^{40}\text{Ar}$  metastable flux, it is necessary to measure the polarization dependent correction factor  $C$ . Since the factor depends on the actual solenoid currents, it must be determined each after adjustment. Without the need for precise measurements,  $C = 1$  is applicable. The resulting error can be estimated from the above measurements.

## 4.4 Conversion of the Image Data into the Equivalent Metastable $^{39}\text{Ar}$ Flux

Before converting the absolute metastable  $^{40}\text{Ar}$  flux into an equivalent absolute metastable  $^{39}\text{Ar}$  flux, the former has to be calculated from the image data. A detailed discussion can be found in [Sch22]. However, a short summary focusing on the main aspects is given in the following.

As discussed in subsection 4.1, two possible decay paths exist to the ground state, decay ① and ②. From the rate equation (2.6) one finds the selection probability

$$P_{\textcircled{1}} = \frac{A_{\textcircled{1}}}{A_{\textcircled{1}} + A_{\textcircled{2}}} = 93.6(6)\% \quad \text{and} \quad P_{\textcircled{2}} = \frac{A_{\textcircled{2}}}{A_{\textcircled{1}} + A_{\textcircled{2}}} = 6.4(6)\%.$$

$A_{\textcircled{1}} = 21.5(11)$  MHz and  $A_{\textcircled{2}} = 1.47(12)$  MHz are the Einstein coefficients for decay ① and ②, respectively [Wie+89]. Next, the correction factor  $C$ , derived in the previous section, has to be applied. Note that the correction factor depends on the actual magnetic field and therefore cannot be given in general terms. However, in first approximation  $C = 1$  is applicable. The resulting amount of photons is collected by the objective. Besides the geometrical transmittance  $T_{\text{geo}} = 3.4(6)\%$ , discussed in section 4.2, a transmission factor through the lenses, window and filter of  $T_{\text{opt}} \approx 86\%$  is added [Sch22]<sup>7</sup>. The arriving photons are detected with the camera. The ratio of incoming photons to triggered electrons is given by the quantum efficiency  $\text{QE}_{\textcircled{1}} \approx 40\%$ , respectively  $\text{QE}_{\textcircled{2}} \approx 10\%$  [All22]. As the camera sends digital numbers DN to the computer, the number of triggered electrons is converted with the digital gain  $G = 2.4^{-1} \text{DN}(\text{e}^-)^{-1}$  at 12 bit resolution [All19]. Therefore, the amount of quenched  $^{40}\text{Ar}$  atoms is resolved from the summed pixel values  $S$  as

$$N_{^{40}\text{Ar}} = \frac{S}{GT_{\text{geo}}T_{\text{opt}}C} \left( \frac{P_{\textcircled{1}}}{\text{QE}_{\textcircled{1}}} + \frac{P_{\textcircled{2}}}{\text{QE}_{\textcircled{2}}} \right). \quad (4.14)$$

Dividing the amount of quenched  $^{40}\text{Ar}$  atoms  $N_{^{40}\text{Ar}}$  by the exposure time  $\tau$  of the image results in the metastable  $^{40}\text{Ar}$  flux

$$\text{QF} = \frac{N_{^{40}\text{Ar}}}{\tau}.$$

---

<sup>7</sup>Other than in [Sch22] no protective glass in front of the ccd sensor is considered, as it not exist [All19].

This metastable  $^{40}\text{Ar}$  flux is also named quench flux in the following. To compare the measured values with the  $^{39}\text{Ar}$  count rate, the quench flux is normally given as an equivalent metastable  $^{39}\text{Ar}$  flux using the unit  $^{39}\text{Ar h}^{-1}$ . Therefore, the abundance ratio of  $^{39}\text{Ar}$  to  $^{40}\text{Ar}$  of  $8.1(3) \times 10^{-16}$  from table 2.1 is multiplied.

The measurement error is mainly caused by systematic errors. Statistical errors from photon statistics can be neglected due to a large amount ( $> 1 \times 10^7$ ) of detected photons. The temporal dark noise of the CCD chip is reduced by water cooling of the camera. Nevertheless, it plays a role for very weak signals, as discussed in the following subsection 4.5.1. It restricts the resolution limit to  $0.007\text{ }^{39}\text{Ar h}^{-1}$ .

Contributions to the systematic error come mainly from the spatial dependent sensitivity of the objective. This is estimated to 19 % from the ratio of standard deviation to mean. Deviations from the theoretical assumed objective alignment are below 1 mm. Therefore, the effects on the objective transmittance are estimated to be 10 %. The quantum efficiency is also assumed to be correct within 10 %. However, the error of the correction factor depends on current settings and how precise it is determined. If the advices at the end of subsection 4.3.3 have been taken into account, a default error of 10 % is appropriate. Using Gaussian error propagation the overall measurement error is 26 % for the absolute value. The inaccuracy of the isotopic abundance, see table 2.1, does not have an relevant impact. However, the errors of relative values are much smaller as those systematic errors does not fluctuate. They can be derived from the statistical fluctuations of repeated measurements. In addition to absolute measurements, this also enables precise relative measurements that provide information about the ArTTA machines.

## 4.5 Application within the ArTTA Technology

Several applications of the (absolute) metastable  $^{40}\text{Ar}$  flux measurement exist within the ArTTA technology. The most important is the monitoring of the source performance. The improved accuracy compared to the design from [Ebs18] allows to detect output changes of the metastable source during a measurement, as Ringena [Rin21] showed. She demonstrated the correlation of a plasma mode jump and changes of the  $^{39}\text{Ar}$  count rate. The latter was mainly influenced by a contaminated component from which the plasma released  $^{39}\text{Ar}$ .

In the course of this thesis, the source is purposefully decreased and the effect on the  $^{39}\text{Ar}$  count rate  $r$  is measured. The quench flux QF reduced to  $\text{QF}_2/\text{QF}_1 = 60(11)\%$ , while the  $^{39}\text{Ar}$  count rate decreased to  $r_2/r_1 = 81(5)\%$ . Note that for the quench flux error fluctuations during the whole count rate determination are considered. The larger reduction of the quench flux compared to the count rate indicates a nonlinearity within the apparatus. One explanation could be that the lower metastable density within the collimator is less optical dense resulting in a higher laser intensity. The actual explanation is not part of this work, as further analyzes are necessary.

Another application focuses on the absolute number of metastable atoms per time. Comparing the quench flux with the actual count rate gives information about possible optimizations. Tuning the collimator laser to the  $^{40}\text{Ar}$  cooling transition typically shows values in the range of  $\text{QF} \gtrsim 10\text{ }^{39}\text{Ar h}^{-1}$  while the  $^{39}\text{Ar}$  count rate is in the range of  $r \sim 3\text{ }^{39}\text{Ar h}^{-1}$ . Assuming that the collimator works for  $^{39}\text{Ar}$  at least as good as for

$^{40}\text{Ar}$  this points to high losses of metastable  $^{39}\text{Ar}$  atoms behind the quench chamber. So the absolute metastable  $^{40}\text{Ar}$  flux measurement can provide important information for optimizations. These will be addressed in the future.

Research on metastable plasma sources is another field of application. It allows the discrimination of the metastable flux under a specific solid angle. The gain of absolute measurements is the comparability between different setups, as it is in all fields. Some research and results on metastable plasma sources undertaken with this new device is presented in chapter 6.

One possible application in the future might be the alignment of the collimator. The exercise of the collimator is decelerating metastable atoms in transversal direction as fast as possible. Preferably many of them have to pass the differential pumping stage and reach the 2D-MOT. It is not the task to bring metastable atoms the whole way to the MOT. Therefore, measuring the amount of metastable atoms within or close to the 2D-MOT chamber is preferable during the alignment of the collimator. In principle this is already possible using  $^{40}\text{Ar}$ . As mentioned in subsection 3.4, the optical density within the collimator at the cooling frequency of  $^{40}\text{Ar}$  is too high and the intensity rapidly drops. This is less the case for other isotopes (compare figure 3.8), especially for  $^{36}\text{Ar}$ . The possibilities measuring  $^{36}\text{Ar}$  is discussed in the following subsection.

Inserting this device at other positions is also thinkable. Especially an absolute metastable  $^{36}\text{Ar}$  or  $^{38}\text{Ar}$  flux measurement within the MOT will help aligning and optimizing the ArTTA apparatuses as well as detecting most of the drifts during  $^{39}\text{Ar}$  measurements. Therefore, a quench laser beam going in vertical direction is focused onto the center of the MOT. The  $^{36}\text{Ar}$ , respectively  $^{38}\text{Ar}$  atoms in the MOT are continuously quenched and the thereby radiated quench photons detected. The signal directly corresponds to the MOT loading rate. Consequently it contains all parameter except the RPs of  $^{39}\text{Ar}$ . This will help to understand, among other things, the differences caused by hyperfine splitting. Additionally the atom density in the MOT stays low, as de-excited atoms are now longer trapped. Switching in appropriate time-steps from  $^{39}\text{Ar}$  to  $^{36}\text{Ar}$ , respectively  $^{38}\text{Ar}$  allows to quantize drifts of the apparatus performance. Thus, they can be taken into account in the analysis. [Ton+21; Jia+12]. However, to the author's knowledge, an absolute measurement has not yet been proven.

#### 4.5.1 Metastable Flux Measurement of Other Isotopes

Measuring the metastable flux of other argon isotopes is of interest, as stated above. Especially measurements of  $^{36}\text{Ar}$  for the collimator alignment.  $^{38}\text{Ar}$  is generally also thinkable. However, looking at the signal-to-noise ratio it becomes clear, that with the present camera a sufficient detection of  $^{38}\text{Ar}$  is not possible. The temporal dark noise of the camera is  $2.9 \times 10^6 \text{e}^-$  for a typical exposure time of  $\tau = 100 \text{ ms}$  [All22]. In contrast, the signal are  $2.5 \times 10^5 \text{e}^-$  for  $^{38}\text{Ar}$  having a quench flux of  $\text{QF} = 1.0 \text{ }^{39}\text{Ar h}^{-1}$ . Therefore, the signal-to-noise ratio is too low for a meaningful measurement.  $^{36}\text{Ar}$  is five times more abundant than  $^{38}\text{Ar}$ . The corresponding signal of  $1.3 \times 10^6 \text{e}^-$  is still too low. However, the additional use of the collimator amplifies this signal further, resulting in signal-to-noise ratios greater than one that allow measurement.

The quench flux measurement works the same way with  $^{36}\text{Ar}$  as with  $^{40}\text{Ar}$ . Only the quench transition has to be tuned to the quench resonance frequency of  $^{36}\text{Ar}$ . Therefore, a second quench laser stabilized with an offset beat lock onto the master quench laser is used. The necessary frequency of the offset beat lock is measured quenching an  $^{36}\text{Ar}$  MOT with a very weak laser beam. The resonance frequency of  $^{36}\text{Ar}$  compared to  $^{40}\text{Ar}$  is approximately  $-463\text{ MHz}$ .

Tuning the laser to the  $^{36}\text{Ar}$  quench transition, a small signal of the bare metastable  $^{36}\text{Ar}$  flux of  $\text{QF} = 1.8(14)\text{ }^{39}\text{Ar h}^{-1}$  is detectable<sup>8</sup>. Using the collimator to enhance the flux a signal of  $\text{QF} = 8.6(12)\text{ }^{39}\text{Ar h}^{-1}$  is measured. A further reduction of the measurement limit can be achieved in particular by cooling the camera to lower temperatures. Another possibility are optimized exposure times and averaging over multiple images during the post processing. The obtained results show that quench flux measurements of  $^{36}\text{Ar}$  in addition with the collimator are possible, enabling a measurement tool in close position to the latter. Also measuring the bare flux is thinkable with further improvements. Finally, it should be mentioned that krypton isotopes have a comparable structure and therefore they are also measurable.

All in all, monitoring the performance of the metastable plasma source is currently the main application of the absolute metastable  $^{40}\text{Ar}$  flux within the ArTTA technology. However, the observed  $^{40}\text{Ar}$  metastable flux with collimator triggered the question of possible optimizations of the ZSL. This finding is based on the new potential of absolute measurements. In addition, future research projects will benefit from this tool as it allows comparisons across an apperature as well as over long periods of time.

---

<sup>8</sup>Only statistical errors combining several single images are given.

# 5 Velocity Distribution of the Metastable Atoms and its Consequences

This chapter prepares the comparison and characterization of different metastable atom sources for the following chapter 6. There, among other things, the velocity distributions of the escaping atoms are analyzed in detail. For this purpose, the measurement setup for the determination is described below. The focus is subsequently on the effects of the measurement itself, which are to be considered in particular for longitudinal velocity distributions.

In the second section, the measured velocity distributions are analyzed, focusing on the deviations from the expected theoretical descriptions. A comparison with previous measurements reported in [Fen12; Ebs12; Rit09] is not made because various parameters, not documented in detail, have an impact on the distributions, as will be seen in 6.5. Nevertheless, it can already be said that the longitudinal velocity distributions are generally comparable to those in [Ebs12].

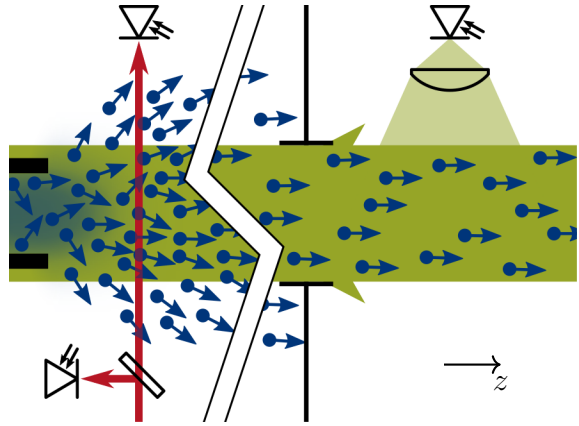
At the end of this chapter, the transverse diffusion during longitudinal deceleration is derived as a function of longitudinal velocity change. The results are combined into a simple model and discussed in the context of the obtained measured values. This leads to a motivation for a redesign of the ZSL and gives requirements for the MOT setup.

## 5.1 Measurement Setup and Impact of the Measurement itself

The measurement setup is generally comparable to those used in [Ebs12; Fen12; Rit09]. However, a short summary focusing on the main aspects is explained in the following. Subsequently, the influences of the measurement itself and necessary adjustments are considered in more detail.

A sketch of the measurement setup is shown in figure 5.1. The transverse velocity distribution is measured close to the source tube exit. A thin laser beam passes through the source chamber perpendicular to the atomic beam axis. The ratio between incoming and outgoing laser power is quantified resulting in an absorption profile. The longitudinal velocity distribution is determined detecting the atom fluorescence in the 2D-MOT chamber. All artificial magnetic fields are switched off. The booster laser beam is amplitude modulated using its AOM. This allows to detect the small fluorescence signal with a lock-in amplifier.

**Figure 5.1:** Sketch of the measurement setup. On the left, the end of the source tube is visible. The metastable atoms in blue leave the tube in a random direction. The transverse velocity distribution is measured close to the source tube exit (red laser beam). The atom direction in the 2D-MOT chamber is restricted to approximately  $\pm 2.5^\circ$  by the differential pumping stage after 0.24 m. There, the longitudinal velocity distribution is measured using the booster laser beam (green).



The laser frequency is scanned using an offset frequency lock. Therefore, offset-generating voltage controlled oscillator (VCO) is ramped with a frequency of about 0.1 Hz. All signals are measured with a four channel oscilloscope. The VCO tuning voltage is converted to the laser detuning  $\delta_L$  with a look-up table. The latter is determined scanning the VCO tuning voltage very slowly, while voltage as well as frequency are measured with the oscilloscope and a frequency counter, respectively.

The longitudinal velocity distribution is measured at the 2D-MOT chamber, since all atoms there fly almost straight ahead<sup>1</sup>. A differential pumping stage is located 0.24 m behind the source tube exit. It restricts possible directions of travel to a range within  $\pm 2.5^\circ$ . Therefore, all atoms with absolute velocity  $v$  have nearly the same Doppler shift (2.11) and thus contribute equally to the signal. However, the atoms fly half a meter towards the laser beam until the fluorescence is measured. During this time of flight they interact with the laser beam. Their velocity is changed by the scattering force (2.10) according to

$$\dot{v} = -\frac{\hbar k}{m} \gamma_s(v), \quad \text{with} \quad \gamma_s(v) = \frac{\gamma}{2} \frac{s_0}{1 + s_0 + 4(\delta_L - kv)^2/\gamma^2}.$$

$m = 40 \text{ u}$  is the  $^{40}\text{Ar}$  atom mass. This differential equation is solved for the initial velocity  $v_i$  until the atom traveled the distance between source exit and 2D-MOT chamber of  $\Delta z = 0.5 \text{ m}$ :

$$v(t=0) = v_i \quad \text{and} \quad \Delta(t=0) = 0, \quad \Delta z(T_i) = \int_0^{T_i} v(t, v_i) dt \stackrel{!}{=} 0.5 \text{ m}.$$

The detected fluorescence of the arrived atom is now proportional to its scattering rate, while it is inversely proportional to its final velocity  $v_f(v_i) = v(T_i, v_i)$ . The latter relation results from a shorter dwell time in front of the photodiode. The overall fluorescence is then proportional to the integral over the signal of each final velocity class:

$$F(\delta_L) \propto \int_0^{\infty} \frac{\gamma_s(v_f(v_i), \delta_L)}{v_f(v_i)} \rho(v_i) dv_i. \quad (5.1)$$

<sup>1</sup>All magnetic fields and laser beams not mentioned here are switched off.

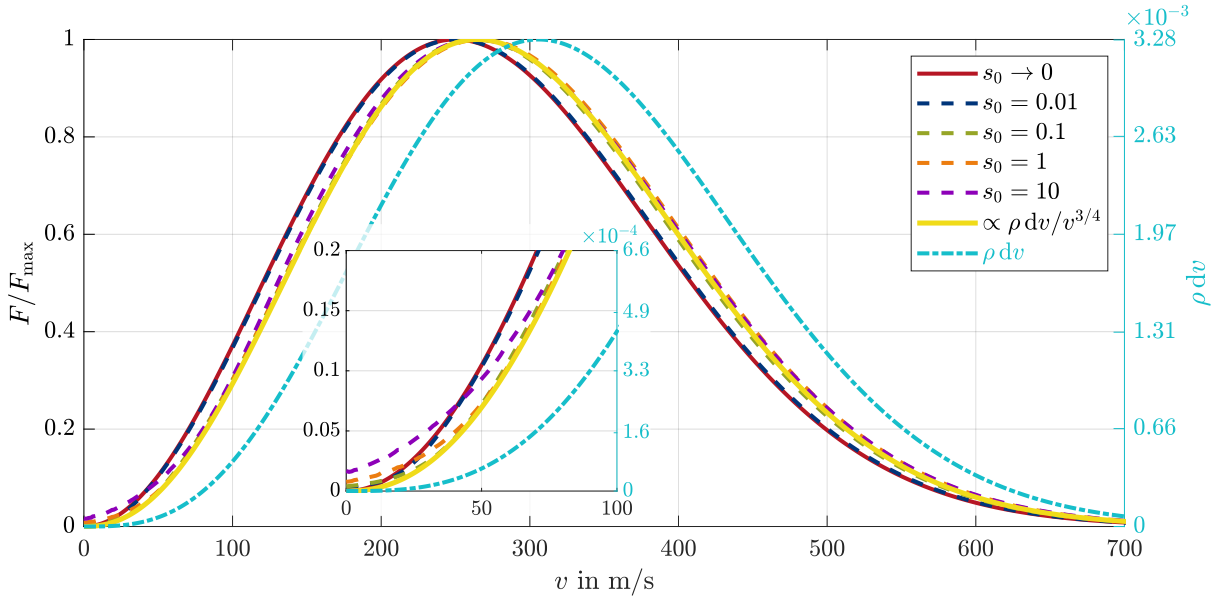


**Figure 5.2:** Graph of the thermal beam velocity distribution  $\rho dv$  (5.2) and the normalized measured fluorescence  $F/F_{\max}$  (5.1) depending on the velocity  $v = -k\delta_L$ . The temperature is  $T = 150$  K. The waveform of the measured signal is shifted to lower velocities due to the inverse proportionality to  $v$ .  $s_0 = 0.01$  still agrees quite well with the limit  $s_0 \rightarrow 0$  being proportional to  $\rho dv/v$ . However, the waveform is shifted slightly back towards higher velocities for saturation parameters  $s_0 = 0.1..10$ , neglecting velocities below  $80 \text{ m s}^{-1}$  (see inset). The fluorescence  $F$  measured with these saturation parameters is proportional to  $\rho dv/v^{3/4}$  in good agreement.

$\rho(v_i)$  is the velocity density of the initial velocity  $v_i$ .

Lets assume a longitudinal velocity distribution of a thermal atom beam [Ram85; AVV72]

$$\rho(v) dv = \frac{2v^3}{\alpha^4} \exp\left(-\frac{v^2}{\alpha^2}\right) dv, \quad \text{with } \alpha = \sqrt{\frac{2k_B T}{m}}. \quad (5.2)$$

$k_B$  is the Boltzmann constant and  $T$  the temperature. This distribution is proportional to a Maxwell-Boltzmann distribution (MBD) multiplied by the velocity  $v$ , as the escape rate from the source is proportional to  $v$  [Ram85; RDS74].  $\alpha$  is the most probable velocity of the corresponding MBD.

The resulting fluorescence (5.1) is displayed in figure 5.2 for different saturation parameter  $s_0$ . The measured fluorescence  $F$  is proportional to  $\rho(v) dv/v$  for  $s_0 \rightarrow 0$ . The waveform shifts to higher velocities when increasing the saturation parameter. However, it stays at velocities that are lower compared to the actual distribution  $\rho(v) dv$ . Due to the integral in equation (5.1) it is not possible to derive the actual velocity distribution from the measured fluorescence. Nevertheless, it was found that the measured fluorescence is approximately proportional to  $\rho dv/v^{3/4}$  (yellow solid line). This is true for a wide and typical range of the saturation parameter  $s_0 = 0.01..10$ . Correspondingly, this correlation is used in the following.

The transverse velocity distribution is derived from the absorption profile. The amount of

absorbed photons is equal to the amount of scattered photons. Opposite to the longitudinal measurement, the dwell time is inverse proportional to the velocity perpendicular to the laser beam  $v_{\perp}$ . The overall scattering rate  $\bar{\gamma}_s(\delta_L)$  is again proportional to the integral over all contributions from the various velocity classes:

$$\bar{\gamma}_s(\delta_L) \propto 2\pi \int_{-\infty}^{\infty} \int_0^{\infty} \frac{\gamma_s(v_{\parallel}, \delta_L)}{v_{\perp}} \rho(v_{\parallel}, v_{\perp}) v_{\perp} dv_{\perp} dv_{\parallel}. \quad (5.3)$$

Measuring close to the source exit is used as a condition here.  $v_{\parallel}$  is the velocity of interest parallel to the laser beam. The factor  $2\pi$  results from the integral over the polar angle  $\varphi$ . The origin of a MBD is a 3D Gaussian distribution

$$\rho(\vec{v}) d^3v = (\pi\alpha^2)^{-3/2} \exp\left(-\frac{|\vec{v}|^2}{\alpha^2}\right) d^3v.$$

Inserting in (5.3) and integrating over  $v_{\perp}$  results in

$$\bar{\gamma}_s(\delta_L) \propto \alpha^{-2} \int_{-\infty}^{\infty} \gamma_s(v_{\parallel}, \delta_L) \exp\left(-\frac{v_{\parallel}^2}{\alpha^2}\right) dv_{\parallel} \quad (5.4)$$

$$\approx \alpha^{-2} \frac{\pi s_0 \gamma^2}{4k\sqrt{1+s_0}} \exp\left(-\frac{\delta_L^2}{\alpha^2 k^2}\right) \quad \text{for } \gamma\sqrt{1+s_0} \ll \alpha k. \quad (5.5)$$

The function in the upper line is of the so-called Voigt function type [Olv+10]. In the last line, it is approximated for a small linewidth of the transition compared to the width of the Boltzmann distribution. Therefore, the exponential function in (5.4) is fixed for the maximum scattering rate at  $v_{\parallel} = \delta_L/k$  and the integral over the remaining scattering rate  $\gamma_s$  is solved. The result is displayed in (5.5). Consequently, the absorption profile is proportional to the Voigt profile, which becomes a Boltzmann distribution for a small linewidth compared to the width of the velocity distribution. The actual saturation parameter of the experiment is around one. Thus, the equation (5.5) holds for the following measurements.

Both transverse and longitudinal velocity distribution can be measured at once. However, this restricts the longitudinal measurements to a maximum velocity of around  $550 \text{ m s}^{-1}$  without performing greater changes of the existing laser system. Nevertheless, most of the atoms escaping the  $\text{LN}_2$  cooled source are within this range and it coincides with the velocity range of the current ZSL setup.

## 5.2 Analysis of Velocity Distributions

This section focuses on the evaluation of velocity distributions in a general focus. They are evaluated with respect to changes caused by various parameter in addition to further measurements in section 6.5. The results discussed in the following are obtained using the open resonator (OR) antenna for the plasma generation and the dewar for  $\text{LN}_2$  cooling (see subsections 6.1.1 and 6.2.2 for further details).

As discussed in the previous section, a determination of the actual longitudinal velocity

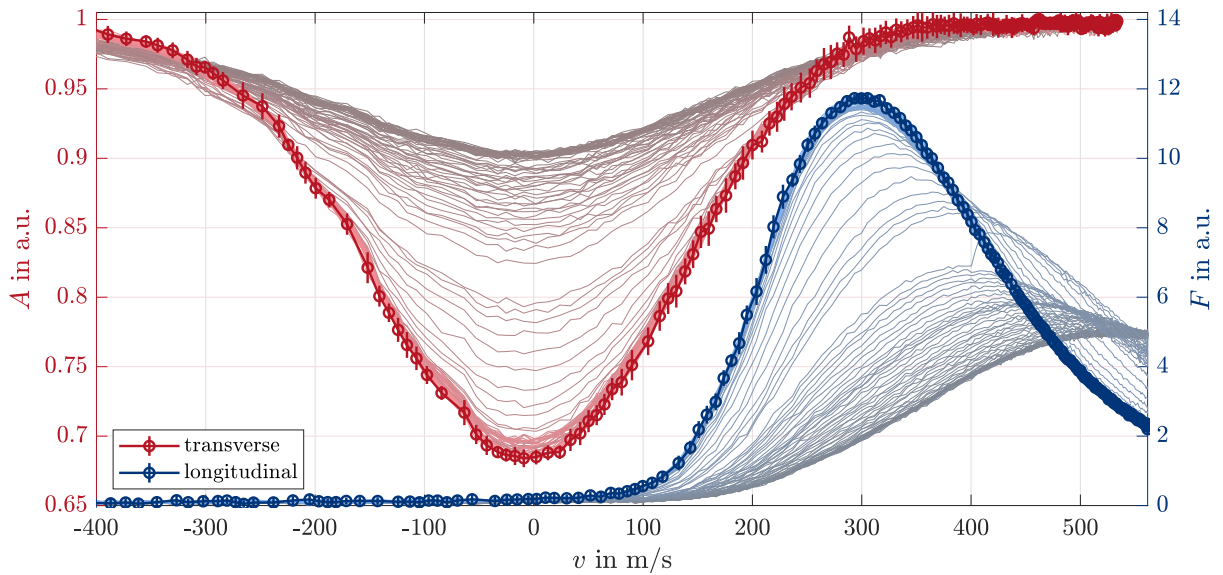


**Figure 5.3:** Observation of velocity distributions during the cooling down of the dewar with the OR antenna. The color saturation decreases towards the past. The measurements extend over 19 minutes, of which cooling down takes the first 14 minutes. The larger gap between the single measurements resulted from plasma mode hope, which is typical during cooling down.

distribution from the measured fluorescence is not possible without any assumptions. Therefore, the measured longitudinal fluorescence  $F$  and transverse absorption  $A$  itself is shown and discussed in the following. Nevertheless, the terminus “velocity distribution” is used. Note that  $A$  is defined as the relative amount of light passing the atoms. Thus, a value of  $A = 1$  corresponds to no absorption.

Figure 5.3 displays the transverse and longitudinal velocity distributions during cooling the metastable source down. The measurements start at ambient temperature. The latest measurement is plotted with error bars. The further back a measurement is, the lower the color saturation of the plot. The width of the longitudinal velocity density gets smaller with decreasing temperature and therefore the density itself increases. The decreasing width can also be the result of smaller transverse velocities. However, the overall absorption apparently increases. Referring back to equation (5.5), no increase of the overall absorption is expected changing the temperature and assuming a timely constant metastable atom flux. Apart from small changes in the latter, the finite distance to the source exit comes into consideration. Thus, the slower the atoms become in the longitudinal direction, the more light they absorb, resulting in a greater overall absorption.

Comparing the measured longitudinal velocity distribution to the theoretically obtained distribution from a thermal beam in figure 5.2 displays a depletion of slow velocities. This has also been observed with cesium atoms coming out of an capillary array [AG72] or thallium atoms out of a long exit channel [AVV72], which are generally comparable to the long tube used in this experiment. This can be understood looking at the consequences of collisions. Estermann, Simpson, and Stern [ESS47] derived a weakening function  $W$  considering collisions in the neighborhood of an oven slit. They assumed that every

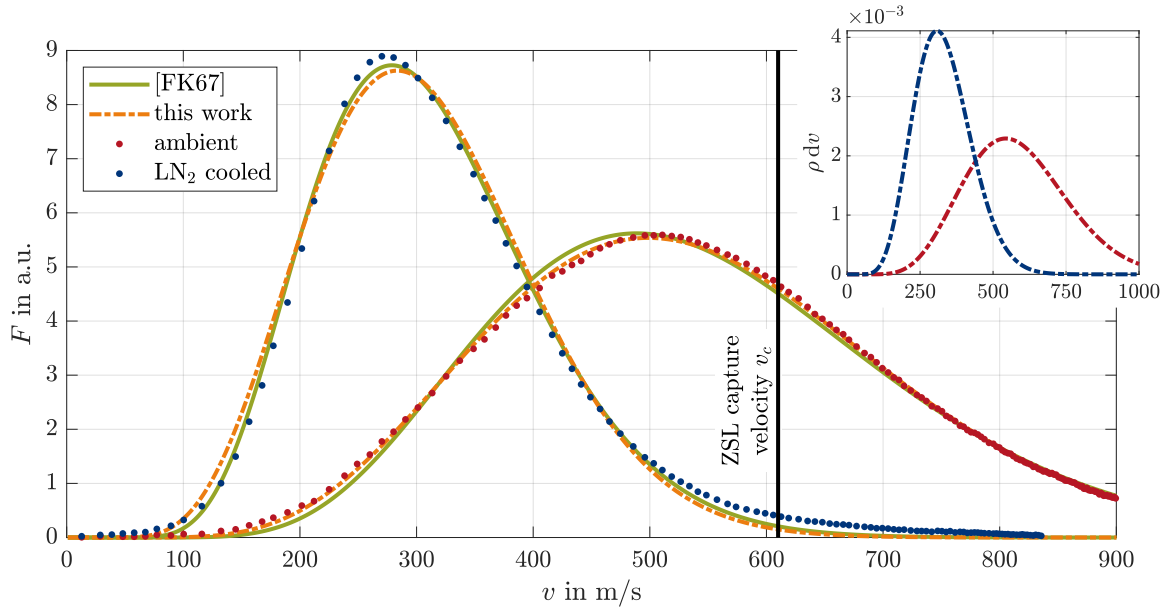


**Figure 5.4:** Comparison of the longitudinal velocity distribution of the cold (LN<sub>2</sub> cooled) and warm (ambient temperature) source. Measurements are plotted as dots with approximately the size of the measurement errors. The values are fitted with  $\rho dv/v^{3/4}$  according to the results in figure 5.2. Both theoretical descriptions [FK67] (5.6) and this work (5.7) are depicted. The obtained temperatures are 412 K and 345 K for the warm source and 131 K and 108 K for the LN<sub>2</sub> cooled source, respectively. The inset illustrates the normalized  $\rho dv$  using (5.7). Comparison of the normalization coefficients shows an approximately 10 % higher flux of the source at ambient temperatures, which is in contrast to results of [Rit13; Fen12].

collision throws the atom out of the beam. Some values of  $W$  as well as the definition can be found in [ESS47]. Combining the weakening function and the thermal velocity distribution (5.2) results in [FK67]

$$\rho dv = \frac{2v^3}{\alpha^4} \exp\left(-\frac{v^2}{\alpha^2} - \frac{pDW(v/\alpha)}{T}\right) dv. \quad (5.6)$$

$p$  is the pressure of the gas in the source and  $D$  is a constant that contains, among other things, the elastic scattering cross-section. Another approach, derived in this work, assumes a mean collision rate, although this rate is location dependent.  $\tau$  is the mean time until an atom is kicked out of the atom beam between the metastable atom source and the 2D-MOT chamber. The resulting velocity distribution is then given by

$$\rho dv = \frac{2v^3}{\alpha^4} \exp\left(-\frac{v^2}{\alpha^2} - \frac{l}{v\tau}\right) dv, \quad (5.7)$$

with the distance  $l = 0.5$  m between source and 2D-MOT chamber.

Figure 5.4 illustrates measurements of the longitudinal velocity distribution up to 900 m s<sup>-1</sup> covering also most of the distribution at ambient temperature (dots). The experimental results are compared with the theoretical distributions using the findings of figure 5.2 that

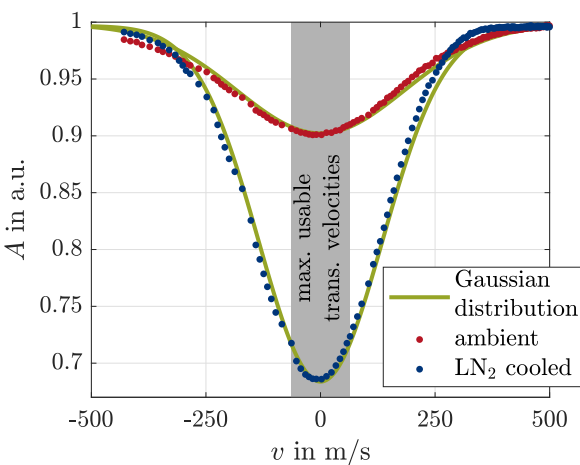


**Figure 5.5:** Graph of the transverse velocity distribution at ambient temperature as well as LN<sub>2</sub> cooled. Measurement results are displayed as dots of approximately the same size as measurement errors. Gaussian distributions, corresponding to equation (5.5), are adapted to the data. Assume that the atoms are decelerated to zero in the transverse direction with the physical maximum acceleration. The gray area then shows the region which comes to a transverse stop within the radius of the differential pumping stage of 9 mm.

$F$  is proportional to  $\rho dv/v^{3/4}$ . Both theoretical distributions (5.6) and (5.7) are fitted varying the temperature  $T$ , the parameter  $pD$  and  $\tau$ , respectively, as well as an overall scaling factor. All curves agree quite well with the experimental data. A closer look results in a better agreement of (5.6) with the LN<sub>2</sub> cooled source, while (5.7) agrees remarkably well with the distribution obtained from the source at ambient temperature.

Nevertheless, comparing the derived temperatures with each other displays larger deviations. They are  $T_{[FK67]} = 412\text{ K}$ , respectively  $T_{tw} = 345\text{ K}$  for the ambient measurement and  $T_{[FK67]} = 131\text{ K}$ , respectively  $T_{tw} = 108\text{ K}$  for the LN<sub>2</sub> cooled one. All temperature fit errors are below 1 K. The model of [FK67] results in higher temperatures as the mean lifetime model of this work. Therefore, a rough value for the temperature can be given, whereas precise measurements require a well substantiated model for the collisions.

Both models agree regarding an increase of slow atom losses for the warmer source. The fitted parameters  $pD$  from equation (5.6) are 1610 K and 596 K for the ambient measurement and the LN<sub>2</sub> cooled one, respectively. The model of this work (5.7) results in a mean time  $\tau$  of 0.83 ms and 1.33 ms, respectively. This result can be compared with the mean lifetime of the MOT measured in subsection 3.2.1. It is 0.53(8) s and thus about 400 times larger than the value between source exit and 2D-MOT of the LN<sub>2</sub> cooled source. It may be assumed that the collision rate decreases quadratically with increasing distance from the source. Then, the weighted average collision distance from the source for the velocity distribution measurements is 0.14 m with the MOT being at a distance of 2.7 m. This is generally consistent with the expectation that the weighted average is closer to the source.

Measurements of the transverse velocity distributions at ambient temperatures and with LN<sub>2</sub> cooling in figure 5.3 are averaged to the values displayed in figure 5.5. A Gaussian distribution, corresponding to equation (5.5), is adapted to the experimental data. The derived temperatures are 160 K and 87 K for ambient and LN<sub>2</sub> cooled, respectively. However, both values are too low, as the value for the ambient data clearly shows. This can be explained by the finite distance from the source exit omitting transversally fast atoms. Instead, the measurement results illustrate the velocity distribution in transverse direction at the beginning of the collimator. The latter pushes atoms to zero transverse velocity

in order to let them pass the differential pumping stage. Correspondingly, the gray area illustrates the physically maximum usable transverse velocity range for a differential pumping stage of radius  $r = 9 \text{ mm}$ <sup>2</sup>:

$$v_{\perp,\max} = \sqrt{2a_{\max}r} \approx 65 \text{ m s}^{-1}, \quad \text{with } a_{\max} = \gamma\hbar k/2m \approx 2.32 \times 10^5 \text{ m s}^{-2}.$$

However, the actual usable velocity range is smaller due to  $a < a_{\max}$  and assuming that this effect is larger than the deviation from a point source. Nevertheless, the current distance between the source exit and the beginning of the collimator results in a loss of potentially usable atoms, as no deceleration occurs over this distance. Motivated by these considerations, Kundy recently reported an increase of 35 % of the  $^{38}\text{Ar}$  loading rate using an additional optical molasses in one dimension between source and collimator [Kun23]<sup>3</sup>.

Overall, the necessity of  $\text{LN}_2$  cooling is already clear from the transverse velocity distributions and the maximum usable velocity range. However, a narrow, slow distribution is also advantageous in the longitudinal direction, since the transverse velocity distribution is broadened during longitudinal deceleration. This effect will be derived in detail in the following section, followed by a discussion of consequences and possible optimizations.

### 5.3 Transverse Diffusion during Longitudinal Deceleration

The large longitudinal velocities of the metastable atoms requires a deceleration before trapping. As discussed in subsection 2.3, ZSLs are able to overcome these velocity shifts. The operating force is again a result of the spontaneous emission of absorbed photons. As the emission happens randomly in all directions, the atom undergoes a random walk in momentum space. Consequently, the atoms diffuse in transverse direction [MS99].

An initial velocity of  $\vec{v}_i = (0, 0, \Delta v + v_{\parallel,f})^\top$  is assumed being the sum of the final velocity  $v_{\parallel,f}$  and the velocity shift  $\Delta v$ . Note that the atom is described by an Dirac delta distribution in the 2D momentum space perpendicular to the optical axis. Some photons with wave vector  $\vec{k} = (0, 0, -k)^\top$  are added to the system. During the first spontaneous emission the atom does a step of  $\hbar\vec{k}$  in a random direction in the momentum space. The probability distribution of this step

$$\varrho^{(1)}(\vec{p}) = \frac{1}{4\pi\hbar^2 k^2} \delta(\hbar k - |\vec{p}|) \quad (5.8)$$

is a 3D sphere with radius  $\hbar k$ , if no polarization effects have to be considered. As the momentum step in direction  $\vec{p}$  is as likely as in the opposite direction  $-\vec{p}$  and as each step is completely independent from the one before, the requirements for random walk are fulfilled. The diffusivity  $D_i$  in direction  $i = \{x, y, z\}$  is given by the variance of the

---

<sup>2</sup>Values are given for  $^{39}\text{Ar}$ .  $\gamma$  is again the natural linewidth of the cooling transition.

<sup>3</sup>The master thesis of Kundy will be issued around April 2023.

momentum projection in this direction [Ein05; LM81]

$$\begin{aligned}\text{Var}(p_i^{(1)}) &= \int_0^\infty \int_0^\pi \int_0^{2\pi} p_i^2 \varrho^{(1)}(\vec{p}) p^2 \sin \theta d\varphi d\theta dp \\ &= \frac{\hbar^2 k^2}{4\pi} \int_0^\pi \int_0^{2\pi} n_i^2 \sin \theta d\varphi d\theta \\ &= \frac{1}{3} \hbar^2 k^2 = \underbrace{\alpha_0 \alpha_p}_{=\alpha} \hbar^2 k^2 = 2D\tau,\end{aligned}\quad (5.9)$$

which for the distribution (5.8) direction is independent.  $\alpha_0 = 1/3$  is the projection factor,  $\alpha_p = 1$  the polarization factor and  $\hat{n} = (n_x, n_y, n_z)^\top$  the unit vector.  $\tau = \gamma_s^{-1}$  is the mean time for one scattering process. The scattering rate  $\gamma_s$  is assumed to be constant over the whole deceleration time.

Because of the independent random nature of the spontaneous emission, each step can be seen as the first one with the same conditions but a shifted coordinate system. Summing up and using the differential equation of diffusion [Ein05]

$$\frac{\partial \varrho}{\partial t} = D_i \frac{\partial^2 \varrho}{\partial p_i^2}$$

results in the momentum distribution<sup>4</sup>

$$\varrho(\vec{p}, t) = \sqrt{(4\pi t)^3 \prod_i D_i}^{-1} \exp\left(-\sum_i \frac{p_i^2}{4D_i t}\right)$$

after many scattering processes ( $t \gg \tau$ ). Note that this result is only correct if the momentum contribution in direction  $i$  is not correlated with the contributions in the other directions  $j \neq i$ . The consequential transverse momentum distribution is

$$\varrho_{\perp}(p_{\perp}, \varphi, t) = \frac{1}{4\pi t \sqrt{D_x D_y}} \exp\left(-\frac{p_x^2}{4D_x t} - \frac{p_y^2}{4D_y t}\right) = \frac{1}{4\pi D t} \exp\left(-\frac{p_{\perp}^2}{4D t}\right),$$

with  $D = D_x = D_y$ .

Equation (5.9) is transferred to many scattering processes by replacing  $\tau = 1/\gamma_s \rightarrow t = N/\gamma_s$ . Therefore, the variance and the standard deviation of the transverse momentum after  $N$  scattered photons are given by

$$\text{Var}(p_{\perp}) = 2Dt = \hbar^2 k^2 \alpha N \quad \text{and} \quad \text{SD}(p_{\perp}) = \hbar k \sqrt{\alpha N}. \quad (5.10)$$

Converting equation (5.10) into the standard deviation of the atom's transverse velocity

---

<sup>4</sup>The momentum distribution is a 3D normal distribution.

and integrating over time  $t = N/\gamma_s$  results in the spatial transverse standard deviation

$$\begin{aligned} \text{SD}(r) = \sigma_r(t) &\approx \frac{\sqrt{3}}{2} \int_0^t \frac{\sqrt{\text{Var}(p_{\perp}(t'))}}{m} dt' \\ &= \frac{\sqrt{3}\hbar k}{2m} \int_0^t \sqrt{\alpha\gamma_s t'} dt' \\ &= \frac{\hbar k}{\sqrt{3}m} \sqrt{\alpha\gamma_s t^3}. \end{aligned} \quad (5.11)$$

Note that the factor  $\sqrt{3}/2$  is derived from a Monte Carlo simulation. The amount of scattered photons needed to overcome the longitudinal velocity  $\Delta v$  is  $N = m\Delta v/(\hbar k)$ <sup>5</sup>. This leads to the needed time

$$t = \frac{1}{\gamma_s} \frac{m}{\hbar k} \Delta v = \frac{2}{\gamma\eta} \frac{m}{\hbar k} \Delta v,$$

with the natural linewidth  $\gamma$  of the used transition and the fudge factor<sup>6</sup>  $\eta$  of the ZSL. Insertion in equation (5.10) and (5.11) yields

$$\sigma_{v_{\perp}}(\Delta v) = \sqrt{\frac{\hbar k}{m} \alpha \Delta v} \quad \text{and} \quad \sigma_r(\Delta v) \approx \frac{2}{\gamma\eta} \sqrt{\frac{m}{3\hbar k} \alpha \Delta v^3}. \quad (5.12)$$

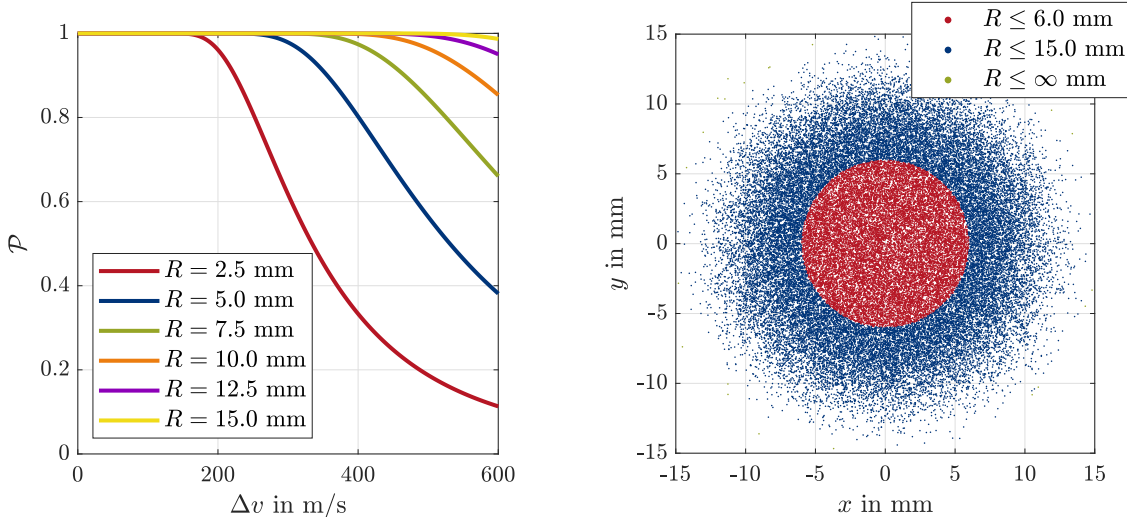
As already mentioned, the 3D momentum distribution in (5.8) is not valid for polarized spontaneous emission. However, table 5.1 lists the momentum distributions as well as the polarization factors for  $\pi$  and  $\sigma$  polarizations. A detailed derivation can be found in appendix A.1. Most ZSLs use  $\sigma$  polarization resulting in  $\alpha = 3/10$  with  $\alpha_p = 9/10$ .

**Table 5.1:** The table lists the polarization factor  $\alpha_p$  and the momentum distribution  $\varrho^{(1)}(\vec{p})$  of  $\pi_z$  and  $\sigma_{x,y}$  polarization [LM81]. The polarization factor is given for the  $x, y$ -plane. The momentum distribution is given for one spontaneously emitted photon.

polarization	$\alpha_p$	$\varrho^{(1)}(\vec{p}) \frac{4\pi\hbar^2 k^2}{\delta(\hbar k -  \vec{p} )}$
non-polarized	1	1
$\pi_z$ -polarized	$\frac{6}{5}$	$\frac{3}{2} \sin^2 \theta$
$\sigma_{x,y}$ -polarized	$\frac{9}{10}$	$\frac{3}{4} (2 - \sin^2 \theta)$

<sup>5</sup>This number is not exact due to the also in longitudinal direction happening random scattering. The deviations can be neglected for large, typical longitudinal velocities  $\Delta v$  that have to be overcome.

<sup>6</sup>In the case of a ZSL, the fudge factor describes the factor between the actual mean deceleration and the maximum physically possible deceleration.



(a) Passing probability (5.13) depending on the longitudinal velocity shift  $\Delta v$ . The atoms are initially located at  $R = 0$ . Results for various radii  $R$  are illustrated.

(b) Atom scattering plot of 50 000 atoms shifted by  $\Delta v = 306.0(18) \text{ m s}^{-1}$ . They are initially equally distributed over a circle with a radius of 10 mm.

**Figure 5.6:** Passing probability  $\mathcal{P}$  of a ZSL with a fudge factor of  $\eta = 0.44$  equal to the current ArTTA ZSLs [Rin21] depending on the longitudinal velocity shift. The initial transverse velocity is  $v_r = 0$ . The MOT interaction radius may be equated with the corresponding laser beam radii. Therefore, the region with  $R \leq 6 \text{ mm}$  and  $R \leq 15 \text{ mm}$  is distinguished in (b) corresponding to the laser beam radii of the second [Rin21] and first apparatus, respectively.

### 5.3.1 Induced Losses by a Finite MOT Interaction Range

The spreading of the atoms leads to losses caused by various effects. One is the finite size of the ZSL laser beam. Once the atom is in a region with insufficient laser intensity it is no longer decelerated fast enough and will be lost from the deceleration cycle. Another one is the capture range of the MOT.

It is assumed that the atoms enter the ZSL with a radial displacement of  $r = 0$  and a radial velocity of  $v_r = 0$ . Further, they have to pass an iris diaphragm at the end of the ZSL with radius  $R$ . The passing probability  $\mathcal{P}$  is then given by the integral over open area of the spatial 2D normal distribution of width  $\sigma_r$  (5.11):

$$\mathcal{P}(R, \Delta v) = \int_0^R \int_0^{2\pi} \frac{r}{2\pi\sigma_r^2} \exp\left(-\frac{r^2}{2\sigma_r^2(\Delta v)}\right) d\varphi dr = 1 - \exp\left(-\frac{R^2}{2\sigma_r^2(\Delta v)}\right). \quad (5.13)$$

Figure 5.6(a) illustrates the passing probability for typical longitudinal velocity shifts  $\Delta v$  and various radii  $R$  for  ${}^{39}\text{Ar}$ . The fudge factor is set to the current value of the ArTTA ZSLs being  $\eta = 0.44$  [Rin21]. For a radius of  $R = 10 \text{ mm}$ , the passing probability is still above 80 % for high longitudinal velocity shifts of  $600 \text{ m s}^{-1}$ . Nevertheless, this is only the case as long as the atoms originate from a point at  $r = 0$ . Therefore, figure 5.6(b) shows a scattering plot of 50 000 atoms shifted by  $\Delta v = 306.0(18) \text{ m s}^{-1}$ . They are initially equally

distributed over a circle with a radius of 10 mm corresponding to the exit cross-section of the differential pumping stage before the ZSL. 85 % of these atoms are still at a position  $r \leq R = 10$  mm. However, the laser beam radius of the second machine is around 6 mm [Rin21] resulting in a passing probability of 35 %. In contrast, 99.9 % of the atoms are within the MOT interaction radius equating it with the laser beam radii of around 15 mm of the first apparatus.

This simplified model already displays the importance of large MOT laser beams although they do not ensure capturing an atom. Further aspects, like finite initial radial velocities or time of flights without laser interaction, have to be considered towards the actual spatial atom distribution of the metastable atoms entering the MOT region. However, a detailed analytical and numerical derivation incorporating all aspects is not essential. Regarding the ZSL it gets clear, that the transverse diffusion as well as collisions with other atoms call for a small capture velocity and a large fudge factor in order to minimize concomitant losses. On the other hand, a large capture velocity and a sufficient small fudge factor decelerates all atoms neglecting diffusion and losses. As they all compete with each other, an optimum exist. Therefore, these findings serve as a motivation and give some theoretical models and descriptions at hand deriving a new ZSL design accounting for loss mechanisms. Furthermore, the necessity of sufficient large MOT laser beams in combination with a large MOT capture range is underlined. Albeit, the latter also accounts for the detectability and is given by the magnetic field gradient requiring again a tradeoff. The necessity accounts equally for the ZSL and booster laser beam radius.

# 6 Evaluation of RF Driven Plasma Metastable Atom Sources

Two different types of RF antennas as well as LN<sub>2</sub> cooling for metastable atom generation are introduced and evaluated in this chapter. It starts with a detailed description of them. Characteristic parameters as the thermal conductivity or equivalent circuits and resonance frequencies are derived and discussed. In the subsequent section 6.3, the influence of the plasma on the original RF properties is analyzed.

The second part of the chapter focuses on the metastable atoms. The measurement technique for the spatial origin of metastable atoms is described in 6.4 and first results are presented. In the following section, the influence of various source parameters on the origin of metastable atoms and their velocity distributions is reported. Explanations are discussed and possible improvements are deduced. Thereby, attention is paid to observed differences between both LN<sub>2</sub> cooling methods. The chapter ends with a summary and conclusion towards the impact on the ArTTA performance.

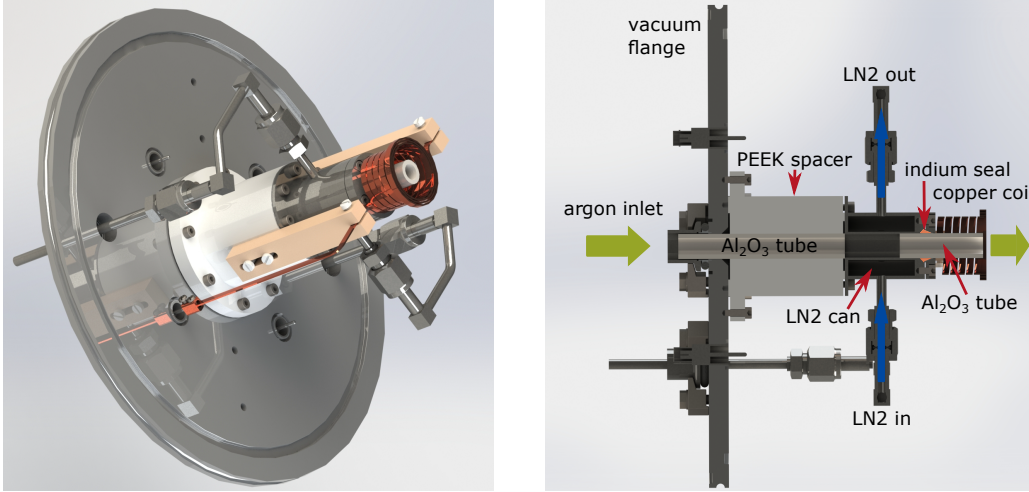
## 6.1 Different Types of RF Antennas

Two RF antennas of different types are analyzed and compared in the following. The first antenna is called open resonator (OR) and was mainly implemented by Ritterbusch in [Rit09; Rit13]. The dimensions and characteristics are discussed in the first section. The other antenna is a helical resonator (HR). HRs are also used in various other applications like ion traps [Siv+12; Den+14; Ped+18], RF filters, precision measurements and metamaterial research [Mar+21] or plasma generation [Mar+21; LLF90; Nia+94].

### 6.1.1 Open Resonator

The open resonator (OR) belongs to the type of monopole antenna. The most important characteristics of this type are described before the more complex form of the OR is explained in detail below. The actual resonant frequency is measured and the influence of the conductor shape is discussed.

The simplest form of a monopole antenna is ground plane and a straight rod-shaped conductor that is perpendicular to the plane. The end of the conductor is left open and reflects back the RF signal. A resonance occurs when the conductor has a length of an



(a) Isometric CAD illustration of the source flange with OR and  $\text{LN}_2$ -can cooling. This image is taken from [Ebs18].

(b) Cross-section of the CAD illustration on the left. This figure is adapted from [Ebs18].

**Figure 6.1:** CAD model of the OR with  $\text{LN}_2$ -can cooling. The coil has  $N = 8.5$  turns where the last four are stacked above each other. Note that for the current setup the flange size has been increased to ISO-K 320 and the spacer has been made out of polyether ether ketone (PEEK).

odd number of quarter wavelengths  $\lambda$ . As the length of the conductor is  $l = 1.10(5)$  m, the resonance frequency yields

$$f_0 = \frac{c}{4l} = 68(3) \text{ MHz}, \quad (6.1)$$

with  $c$  being the speed of light in vacuum. Nevertheless, one can also drive such antennas also out of resonance. For example, in a  $5/8\lambda$  monopole antenna, the maximum power is transmitted or received perpendicular to the antenna axis [Sch02]. The OR is typically driven with an electrical<sup>1</sup> length of approximately one half [Ebs18] which corresponds to a RF frequency of  $f \approx 150$  MHz.

A CAD model of the OR mounted on the source flange with  $\text{LN}_2$ -can cooling is depicted in figure 6.1. The source chamber, especially the source flange, functions as a ground plane. The perpendicular conductor is an isolated copper wire ( $4.0 \text{ mm} \times 1.0 \text{ mm}$ ) with a length of  $l = 1.10(5)$  m. At the end, a coil with  $N = 8.5$  turns is formed whereof the last four are stacked above each other. Therefore, the field strength and thus the plasma in this region is increased [Ebs18]. The inner diameter of the coil is  $d = 33(3)$  mm and the length is  $b = 30(3)$  mm. An aluminum(III) oxide ( $\text{Al}_2\text{O}_3$ ) tube is used for shielding the conductors from the argon plasma.

The actual resonance frequency is determined measuring the reflectance  $|S_{11}|^2$  of the OR using a vector network analyzer (VNA) with a reference impedance  $Z_0$  of  $50 \Omega$ . The measurement results are plotted in figure 6.2. The incoming power reflected from the OR at the resonant frequency is minimal, which is why the latter shows up as a dip in

<sup>1</sup>Electrical length is the ratio of the physical length of a device to the wavelength of the signal frequency [Sch02].

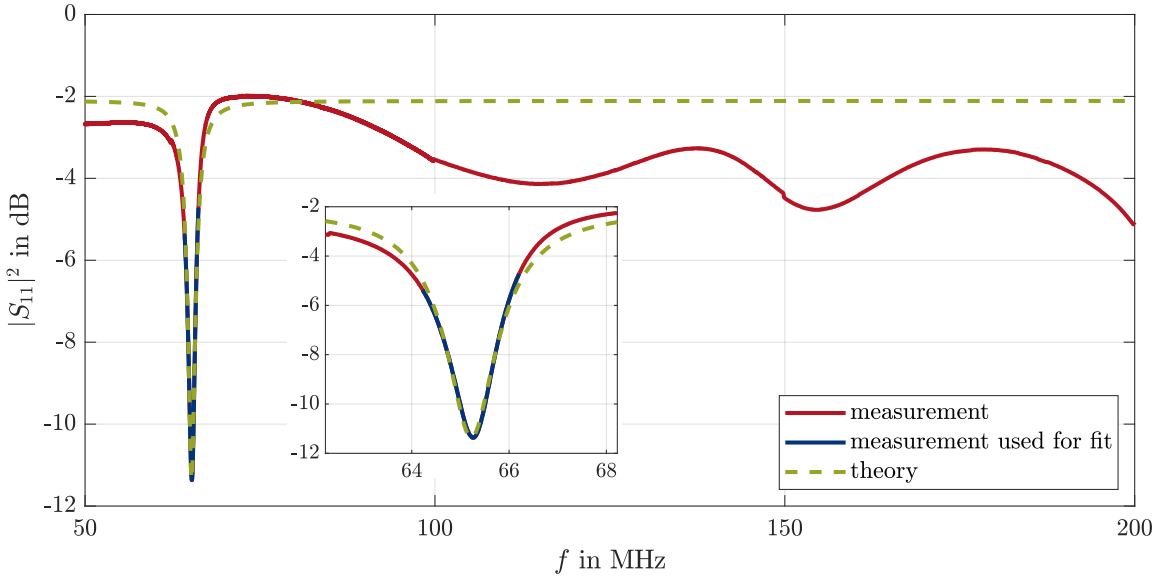


**Figure 6.2:** Measurement of the reflectance  $|S_{11}|^2$  of the OR using a VNA. The resonance is fitted by the theoretical behavior of a lumped LCR series circuit (6.2). The obtained resonance frequency is  $f_0 = 65.22(16)$  MHz, while the quality factor is resolved to be  $Q = 43.3(17)$ . The inset shows a magnification of the resonance.

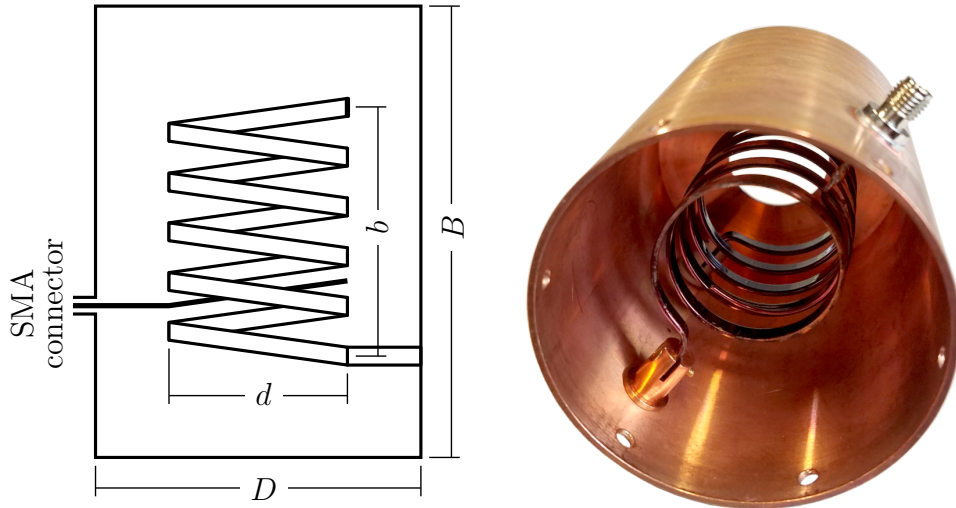
the VNA signal. The OR can be considered as a lumped LCR series circuit to a first approximation. From the discussion of such a circuit in subsection 2.5.2 and using the reflection equation (2.37), the theoretical description of the reflectance reads

$$|S_{11}|^2 = \left| \frac{Z_r - Z_0}{Z_r + Z_0} \right|^2, \quad \text{with} \quad Z_r = R_r + i \frac{L_r}{\omega} (\omega^2 - \omega_0^2). \quad (6.2)$$

This relation is fitted to the measured values within a span of 2.0 MHz around the minimum. An overall offset is added to take care of losses within the measurement setup. The results of the fit assuming a lumped LCR series circuit are  $f_0 = 65.22(16)$  MHz,  $L_r = 10.9(3)$   $\mu\text{H}$  and  $R_r = 102.6(22)$   $\Omega$ . Therefore, the Q-factor (2.30), which refers to the bandwidth, is  $Q = 43.3(17)$ . Deviations from the theoretical behavior, especially far away from the resonance frequency, may be explained by the more complex antenna geometry, which is not captured by the single lumped LCR model. Nevertheless, the measured resonance frequency itself agrees within the error with the quarter wavelength condition for resonance (6.1).

Once again back to the reflectance equation (6.2) for the OR and the consequences of the coil at the end of the conductor. Coiling the wire increases the inductance  $L_r$ . As one sees from the imaginary part of the resonator impedance  $Z_r$ , this results in a reduced width of the resonance. This is also expressed in the Q-factor  $Q = L_r \omega_0 / R_r$ . The inductance of the coil at the end of the antenna is [Whe28]

$$L_c \approx \frac{\mu_0 \mu_r N^2 d^2 \pi}{4b + 0.45d} = 1.7 \mu\text{H}.$$



(a) Sketch of an HR with the defining dimensions. The driving coil is connected to the SMA connector, while the main coil is connected to the shielding.

(b) Picture of the inside of the HR used in the experiment. The SMA connector for the input signal is at the top right. The shielding is grounded and the front shield removed.

**Figure 6.3:** HRs offer a high Q-factor by having a comparably compact size.

The HR in (b) has an inner diameter of the shielding of  $D = 62.0$  mm and inside a length of  $B = 87.0$  mm, for example.

$N$ ,  $b$  and  $d$  are the number of turns, the length and the diameter given above, respectively. The relative permeability  $\mu_r$  is assumed to be one. Comparing this value with the fitted inductance  $L_r = 10.9(3)$   $\mu\text{H}$ , the Q-factor is increased by the coil in the order of 20 % compared to a straight rod. Therefore, coiling the wire has a relevant influence on the width of the resonance, while it is necessary to obtain high fields within the plasma region. However, the remaining reflectance at resonance is given by the deviation of  $R_r$  from  $Z_0$  yielding  $|S_{11}|^2 = 0.119(7)$ . Thus, at least 12 % of the RF input power is reflected if no additional impedance matching network is used.

### 6.1.2 Helical Resonator

Helical resonators (HRs) are widely used in RF and MW technology. They come with a large quality factor  $Q_u \sim 1000$  and in small sizes compared to equivalent circuits [MS59]. In the following, the operating principle of the HR is explained and the resonant frequency is derived from it. Subsequently, an equivalent circuit with lumped elements is developed. Missing parameters of its elements are obtained from a measurement of the reflectance.

Macalpine and Schildknecht [MS59] give a set of useful equations and hints constructing a HR. A sketch of the HR used is shown in Figure 6.3(a) with all relevant dimensions. Coil and shielding act like a transmission line with comparably high characteristic impedance. One end is open and the other short-circuited, creating a resonator for the propagating waves.

Figure 6.3(b) shows the inside of the HR used in the experiment. It consists of the outer

cylindrical shielding, the main coil and a driving coil for the RF input. The latter is connected to the SMA connector and is inductively coupled with the main coil. The shield is grounded and conductively connected to the main coil on the side facing the drive coil. The other side of the coil is fixed isolated. All following dimensions are labeled according to the sketch in figure 6.3(a).

All conductive parts are made out of copper. The main coil is made out of a rectangular ( $4.0\text{ mm} \times 1.0\text{ mm}$ ) wire and has  $N = 5$  turns of winding with an axial length of  $b = 50.8\text{ mm}$  and a mean diameter of  $d = 33\text{ mm}$ . The driving coil for the RF input has half a winding and a wire diameter of  $1.0\text{ mm}$ . It is oriented such that at resonance the impedance of the HR matches with  $Z_0 = 50\Omega$ . The orientation determines the impedance matching, as it influences the coupling between both coils. The inner diameter of the shielding is  $D = 62.0\text{ mm}$  and the inside length  $B = 87.0\text{ mm}$ . To shield the argon plasma inside the resonator from the conductors, an  $\text{Al}_2\text{O}_3$  tube is inserted into the HR.

The resonance frequency  $f_0$  of the HR can be derived using the semi-empirical equations from Macalpine and Schildknecht [MS59]. For this, the drive coil is neglected since its influence is small, as will be seen later. Inserting the dimensions of the HR yields for the inductance of a long shielded solenoid per unit length [Ter43]

$$L'_r \approx \mu_0 \mu_r N^2 \frac{\pi d^2}{4b^2} \left( 1 - \frac{d^2}{D^2} \frac{b}{B} \frac{1}{K} \right) = 8.12 \mu\text{H m}^{-1},$$

with an empirical factor  $K \approx 0.75$ , which in general depends on  $b/B$ . The shielding and the main coil form a capacitor. For the capacitance per unit length  $C'_r$  one derives

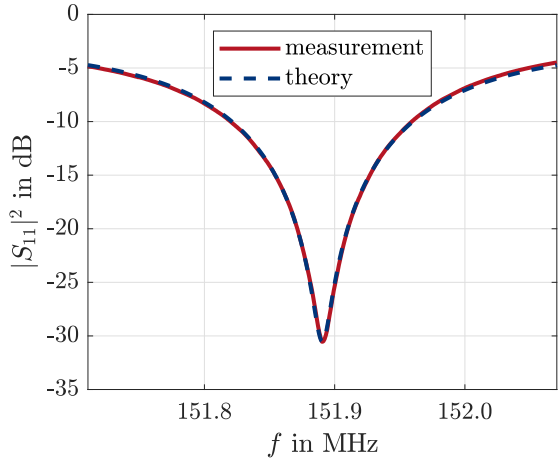
$$C'_r \approx 1.22 \frac{2\pi \varepsilon_0 \varepsilon_r}{\ln\left(\frac{D}{d}\right)} = 108 \text{ pF m}^{-1}.$$

For the calculation of these values, which are valid for an air filled HR, i.e. without plasma, the relative permeability  $\mu_r$  and permittivity  $\varepsilon_r$  are assumed to be one. The factor 1.22 in the capacitance describes the deviation from a coaxial cylinder and is derived from empirical measurements [MS59]. As already stated, the HR acts like a transmission line. Therefore, the characteristic impedance (2.35) of the HR is  $Z_{0r} = 274\Omega$ . The finite velocity of the electromagnetic wave has to be taken into account. The phase velocity (2.34) is  $v_\varphi = (L'_r C'_r)^{-1/2} = 0.113c = 33.8 \times 10^6 \text{ m s}^{-1}$ ,  $c$  being the speed of light in vacuum. For the resonance condition, a phase of  $2\pi$  must be accumulated during one round trip in the HR. A phase shift of  $\pi$  comes from the reflection at the grounded end of the coil (see equation (2.37)). The open end does not imprint any phase shift. Therefore, the other phase shift of  $\pi$  has to be a result of the finite traveling time leading to the condition for the axial coil length  $b = 0.94\lambda/4$ , with 0.94 being an empirical factor [MS59]. This results in the resonance frequency

$$f_0 = \frac{0.94}{4b\sqrt{L'_r C'_r}} = 157 \text{ MHz} \quad (6.3)$$

using the definition of the wavelength  $\lambda = v/f_0$  and the phase velocity  $v_\varphi$  (2.34). The actual resonance frequency of  $f_0 = 151.891\text{ MHz}$  measured outside the vacuum and without an additional pick-up coil agrees well with the theoretical value (see figure 6.4). Already small changes of the setup, e.g. applying a vacuum or not, shift slightly this frequency. Therefore,

**Figure 6.4:** Measurement of the reflectance  $|S_{11}|^2$  of the HR using a VNA. The theoretical behavior is given in equation (6.5). The actual resonance frequency of 151.891 MHz agrees well with the theoretically derived value of 157 MHz. The Q-factor (2.30), which is an expression for the relative width of the resonance, is calculated to be  $Q = 514(6)$ .



the difference to the predicted resonance frequency may be explained by deviations from the physical dimensions given above. Furthermore, the permittivity of the  $\text{Al}_2\text{O}_3$  tube of  $\varepsilon_r^{(\text{Al}_2\text{O}_3)} = 9.6$  @100 MHz is neglected in the previous calculation [Met].

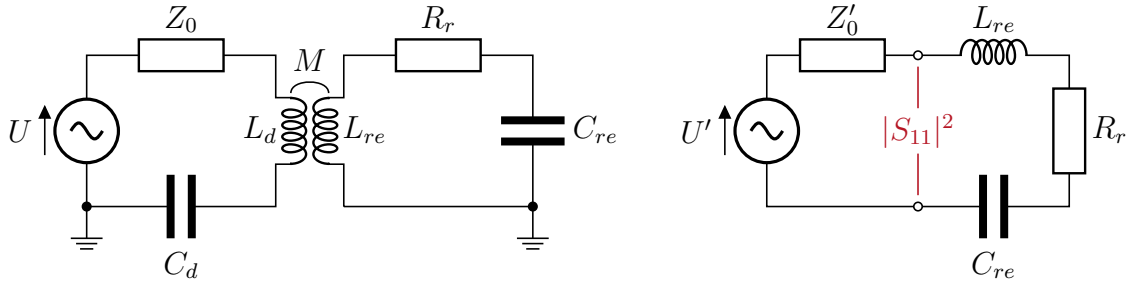
Subsequently, an equivalent circuit for the HR is now derived, from which further parameters are obtained. Let us recall the resonance frequency  $\omega_0 = 1/\sqrt{LC}$  of a lumped LC circuit (2.29). Comparing this with equation (6.3) for the HR, we obtain the effective inductance

$$L_{re} = \frac{2L'_r b}{0.94\pi} = 280 \text{ nH} \quad \text{and capacitance} \quad C_{re} = \frac{2C'_r b}{0.94\pi} = 3.7 \text{ pF} \quad (6.4)$$

for an equivalent circuit with lumped elements. Since the HR is inductively coupled, the equivalent circuit consists of two parts [Ter43]. One is the driving part and the other is the resonant part, as shown in figure 6.5(a). The coupling between these two parts is expressed with the mutual inductance  $M = k\sqrt{L_d L_r}$ ,  $k$  being the coupling coefficient.

In the following, the series resistance  $R_r$  of the equivalent circuit in figure 6.5(b) and its deviation from the reference impedance  $Z'_0$  is derived. At the end, the characterization is completed with the Q-factor  $Q$ . The LCR circuit is driven by a voltage source with amplitude  $U' = -i\omega M U/Z_d$  and internal impedance  $Z'_0 = (\omega M)^2/Z_d$ .  $Z_d$  is the series impedance of the driving part considered by itself, i.e. without the coupling to the HR [Ter43]. Therefore, the driving circuit transforms the amplitude and reference impedance of the RF source. As mentioned earlier, the transformation, i.e. the mutual coupling and therefore  $M$ , is tuned to match the impedance of the HR at resonance, so there is minimal back reflection. Note that a non vanishing reactance of the driving part shifts the resonance frequency compared to the resonant part considered by itself. This is because the total reactance disappears at resonance and consequently the HR itself must then have a reactance opposite to the driving part. However, this effect is small and  $Z_d$  is therefore assumed to be real. The resistance of the resonator  $R_r$  is now derived from the reflectance measurement in figure 6.4. Using the reflection equation (2.37) results at the reflectance

$$|S_{11}|^2 = \left| \frac{Z_r - Z'_0}{Z_r + Z'_0} \right|^2 = \left| \frac{\Delta_R + iX}{2\bar{R} + iX} \right|^2, \quad \text{with} \quad Z_r = R_r + i \underbrace{\frac{L_{re}}{\omega} (\omega^2 - \omega_0^2)}_{=iX} \quad (6.5)$$



(a) Equivalent circuit for the HR setup. RF source and driving coil are at the left. The resonator is at the right.  $L_{re}$  and  $C_{re}$  are calculated using (6.4) as 280 nH and 3.7 pF, respectively.  $R_r$  is derived using figure 6.5(b) resulting in 276(11) mΩ. The driving coil  $L_d$  and mutual inductance  $M$  is tuned to match the impedance.

(b) Equivalent circuit for the resonator part of the HR, i.e. the right side in figure 6.5(a). The amplitude of the voltage source  $U'$  is given by  $-i\omega MU/Z_d$  and the internal impedance by  $Z'_0 = (\omega M)^2/Z_d$  [Ter43]. The reflectance  $|S_{11}|^2$  is defined in equation (6.5) and measured in figure 6.4.

**Figure 6.5:** The HR can be described using equivalent circuits with lumped elements.

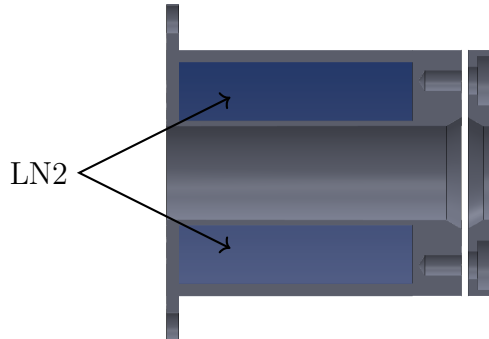
being the series impedance of the resonant part when considered by itself. Because of the absolute value function in (6.5),  $R_r$  and  $Z'_0$  cannot be uniquely derived from  $|S_{11}|^2$ . Therefore,  $\Delta_R = |R_r - Z'_0|$  and  $\bar{R} = (R_r + Z'_0)/2$  are introduced as uniquely determinable values.  $|S_{11}|^2$  is fitted to the reflection measurement in Figure 6.4, varying  $\bar{R}$  and  $\Delta_R$  as well as an overall offset caused by losses in the measurement setup. The results are  $\bar{R} = 268(3)$  mΩ and  $\Delta_R = 21.0(9)$  mΩ. Therefore, the reflected power without plasma at resonance is less than 1%. For comparison, at OR it is 12%. Furthermore, the losses within the resonator due to its resistance are 350 to 400 times smaller in the case of the HR. The Q-factor (2.30), which is an expression for the relative width of the resonance, is finally calculated to be  $Q = 514(6)$ . This Q-factor is around ten times larger than that of the OR and the resonance width is therefore narrower. As a consequence, the plasma can only be ignited within a small RF frequency range. However, how the antennas perform with plasma is discussed in section 6.3.

## 6.2 Different Types of Liquid Nitrogen Cooling

Liquid nitrogen ( $\text{LN}_2$ ) cooling of the metastable atom source is essential for efficient  $^{39}\text{Ar}$  count rates. The atoms become slower, which allows for a shorter length of the ZSL, which in turn results in less diffusive losses (see section 5.3). One effect is fewer collisions with other atoms and the other is a reduced radial distance when reaching the MOT.

Two devices for  $\text{LN}_2$  cooling are presented. The first is the  $\text{LN}_2$ -can which is used for a while in the ArTTA setups. The  $\text{LN}_2$  uptake rate of approximately  $150 \text{ L d}^{-1}$  is quite high and plasma flushing of the source without periodically  $\text{LN}_2$  cooling is not possible. This motivated to design a new device, the  $\text{LN}_2$ -dewar.

**Figure 6.6:** CAD cross-section of the LN<sub>2</sub>-can. The argon gas is flowing from left to right through the central tube surrounded by the LN<sub>2</sub>. The Al<sub>2</sub>O<sub>3</sub> source tube is thermally connected using an indium press fitting. Therefore, the plate on the right is clamped onto the can pressing the indium between the tapered surfaces and the Al<sub>2</sub>O<sub>3</sub> tube.



### 6.2.1 LN<sub>2</sub>-Can

The LN<sub>2</sub>-can is a hollow cylinder made out of stainless steel with a tube for the argon gas along the axial axis. A CAD cross-section with mounted OR and source flange is shown in figure 6.1(b) and a magnification of the can itself in figure 6.6. The LN<sub>2</sub> inserts the can from the bottom. Gaseous and liquid nitrogen is leaving the can at the top. Therefore, the horizontal tube on the center axis is surrounded by LN<sub>2</sub>. The Al<sub>2</sub>O<sub>3</sub> source tube entering on the right is thermally connected using an indium press fitting. As indium has a comparably low melting point of (157 °C), the source cannot be run without cooling for a longer time.

The thermal resistance  $\rho_{\text{can}}$  from the LN<sub>2</sub> to the Al<sub>2</sub>O<sub>3</sub> tube among the stainless steel and the indium is estimated to be approximately 1.2 K W<sup>-1</sup> from the thermal conductivities and the geometrical dimensions. As the indium<sup>2</sup> part is only responsible for about 0.06 K W<sup>-1</sup>, the stainless steel<sup>3</sup> part generates most of the resistance. Building the can out of copper would decrease the thermal resistance of the metal part by a factor of 65 resulting in a better cooling of the Al<sub>2</sub>O<sub>3</sub> tube. However, the tube<sup>4</sup> itself has a thermal resistance per unit length of  $\rho_{\text{Al}_2\text{O}_3}/l \approx 110 \text{ K W}^{-1} \text{ m}^{-1}$ , with an outer diameter of  $15.0^{+0.7}_{-0.7} \text{ mm}$  and an inner diameter of  $10.0^{+0.5}_{-0.5} \text{ mm}$ . Thus, the thermal resistance of the tube dominates already after a length of around 1 cm. Besides a larger cross-section of the tube is the use of tubes made out of aluminum nitride (AlN) a possible solution. The thermal conductivity of AlN depends strongly on its purity and ranges between 300 W m<sup>-1</sup> K<sup>-1</sup> and above 1000 W m<sup>-1</sup> K for very pure crystals at a temperature of 100 K [Che+20]. These values are three to ten times higher as those of Al<sub>2</sub>O<sub>3</sub>.

### 6.2.2 LN<sub>2</sub>-Dewar

The LN<sub>2</sub>-dewar has a L shape and is made out of stainless steel. A CAD cross-section is shown in figure 6.7. The LN<sub>2</sub> reservoir and bath are surrounded by an isolating prevacuum and all connections to the outer part are elongated for decreased thermal energy transfer. The volume of the reservoir at the top is chosen such that it contains enough LN<sub>2</sub> for at least one hour. Therefore, the 250 L storage tank can be disconnected and refilled directly.

<sup>2</sup>The thermal conductivity of indium at  $T = 73 \text{ K}$  is  $\kappa_{\text{In}} = 109 \text{ W m}^{-1} \text{ K}^{-1}$  [PWT62].

<sup>3</sup>The thermal conductivity of stainless steel 304 at  $T = 77 \text{ K}$  is  $\kappa_{304} = 7.92 \text{ W m}^{-1} \text{ K}^{-1}$  [Nat].

<sup>4</sup>The thermal conductivity of Al<sub>2</sub>O<sub>3</sub> at  $T \approx 80 \text{ K}$  is  $\kappa_{\text{Al}_2\text{O}_3} = 90 \text{ W m}^{-1} \text{ K}^{-1}$  [NSH85].

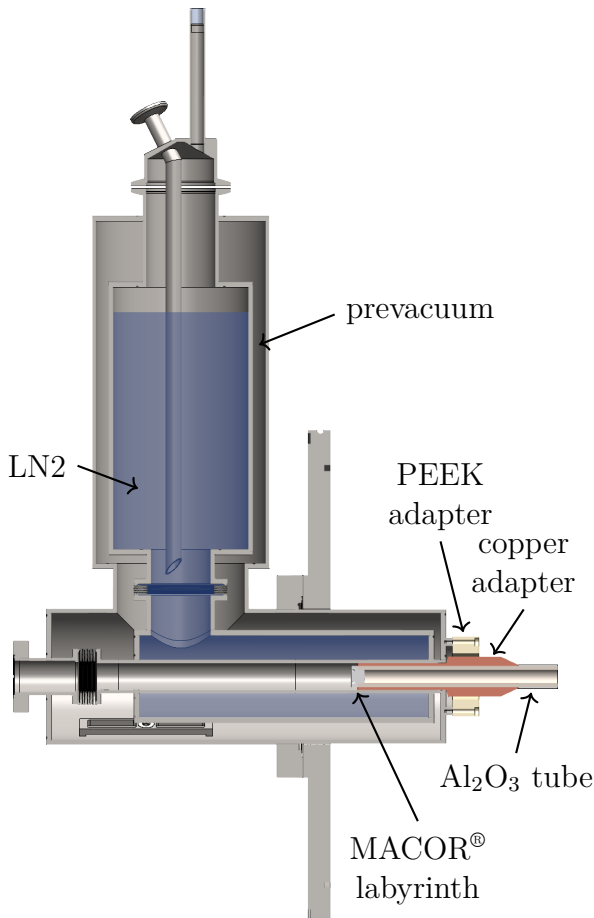


**Figure 6.7:** CAD cross-section of the LN<sub>2</sub>-dewar. It is made out of stainless steel 304. The argon gas is flowing from left to right through the central tube surrounded by the LN<sub>2</sub>. The Al<sub>2</sub>O<sub>3</sub> source tube outer diameter is precisely round sanded. The gap between the Al<sub>2</sub>O<sub>3</sub> tube and the copper adapter is filled with Apiezon N grease. As well is the gap between the copper adapter and the dewar. Sputtered metal is captured at the MACOR® labyrinth at the entrance to the Al<sub>2</sub>O<sub>3</sub> source tube. The copper and PEEK adapter shown are used for the OR antenna. The HR antenna is directly mounted and the copper adapter ends with the dewar.

For the LN<sub>2</sub>-can, an additional transportation tank for storage refilling is necessary costing time, money and LN<sub>2</sub>. The dewar is automatically replenished by a system developed as part of this work. A microcontroller detects via some temperature sensors the LN<sub>2</sub> level and operates a magnetic valve between storage tank and dewar. As the refilling LN<sub>2</sub> flux does not have to be tuned to a very small amount compared to the constant flux for the can, the cool down of the dewar is much faster. It takes approximately 14 minutes (compare figure 5.3) instead of around one hour.

The amount of LN<sub>2</sub> uptake is decreased by a factor of around five compared to the LN<sub>2</sub>-can. This reduction is achieved having a LN<sub>2</sub> bath instead of a steady flow. Therefore, only gaseous nitrogen is leaving the dewar at the top through an outlet pipe (not visible in the cross-section).

The thermal resistance  $\rho_{\text{dewar}}$  from the LN<sub>2</sub> to the Al<sub>2</sub>O<sub>3</sub> tube is calculated to be approximately  $0.15 \text{ K W}^{-1}$ . This is a reduction of around 90 % compared to the LN<sub>2</sub>-can. Again the thermal resistance of the stainless steel part with  $0.11 \text{ K W}^{-1}$  has the largest impact. The thermal contact between the different parts is achieved by reducing the gaps to a practical minimum and filling them with Apiezon N grease<sup>5</sup>. However, the gap between stainless steel and copper part increases when cooling the dewar down, while the gap towards Al<sub>2</sub>O<sub>3</sub> decreases. Table 6.1 lists all relevant diameters. The Al<sub>2</sub>O<sub>3</sub> tube itself has a thermal resistance per unit length of  $\rho_{\text{Al}_2\text{O}_3}/l \approx 130 \text{ K W}^{-1} \text{ m}^{-1}$ , which is slightly higher

<sup>5</sup>The thermal conductivity of Apiezon N grease at  $T = 77 \text{ K}$  is  $\kappa_{\text{Apiezon N}} = 0.12 \text{ W m}^{-1} \text{ K}^{-1}$  [MI 18].

**Table 6.1:** Table with the dimension and tolerances of the dewar parts involved in the thermal energy transport. All dimensions in mm and at ambient temperatures.

	outer diameter	inner diameter
stainless steel tube	25.0	$20.000^{+0.021}_{-0.000}$
copper adapter	$20.000^{+0.000}_{-0.021}$	$16.000^{+0.018}_{-0.000}$
$\text{Al}_2\text{O}_3$ tube	$16.00^{+0.01}_{-0.05}$	$12.0^{+0.6}_{-0.6}$

as the value in the case of the  $\text{LN}_2$ -can. Using the OR antenna, the copper<sup>6</sup> adapter is elongated and strengthened towards the source exit for better cooling as shown in figure 6.7.

A MACOR® labyrinth is placed in front of the  $\text{Al}_2\text{O}_3$  tube. Material sputtered from the stainless steel is captured by the labyrinth, as it otherwise has to fly around the corner. This prevents the tube from becoming conductive over time. The  $\text{LN}_2$ -can also has bare stainless steel areas exposed to the plasma. As no labyrinth or another shielding is used, the  $\text{Al}_2\text{O}_3$  tube has to be exchanged from time to time. Otherwise, the conductive coating, being a Faraday cage, prohibits an ignition of the plasma. Other solutions, like an  $\text{Al}_2\text{O}_3$  tube extension, e.g. out of glass, through the whole dewar to a point without plasma, are also thinkable.

### 6.3 RF Electronic Analysis

The interaction of the plasma with the two antennas OR and HR is analyzed electronically below. Figure 6.8 illustrates the measurement setup. A VCO (left) generates the RF frequency  $f_{\text{RF}}$  for plasma generation. This signal is amplified by about 52 dB up to a power of  $P_{\text{max}} \approx 49 \text{ dBm} \approx 80 \text{ W}$  [Mina]. The RF signal is fed into the resonator antenna via a circulator and a directional coupler. The probe signal from a VNA is threaded onto the resonator antenna using the directional coupler. ① refers to this port of the directional coupler and the transmission efficiency towards the antenna is about 23 dB in a frequency range of 100 MHz..500 MHz<sup>7</sup>. The reflections of the resonator antenna are transferred partly ( $\approx 23 \text{ dB}$ ) back to this port. The rest is circulated to attenuators (40 dB) and quantified with the VNA at port ②. Measurements at this port are restricted by the circulator to the frequency range 135 MHz..175 MHz.

As an alternative, a power detector can be connected instead of the VNA. Doing so, the reflected power  $P_{\text{reflected}}$  from the resonator antenna is measured. The conversion of the measured voltage  $U$  reads  $P_{\text{reflected}} = 11.6 \text{ dBm} - U \cdot 40 \text{ dBm V}^{-1}$ , as the power is measured behind the 30 dB attenuator [Minb]. The directional coupler is removed for these measurements.

<sup>6</sup>The thermal conductivity of OFHC copper with RRR = 50 at  $T = 77 \text{ K}$  is  $\kappa_{\text{Cu}_{50}} = 515 \text{ W m}^{-1} \text{ K}^{-1}$  [Nat10].

<sup>7</sup>See figure A.5 in appendix A.5 for the frequency dependent S-parameters of the directional coupler.

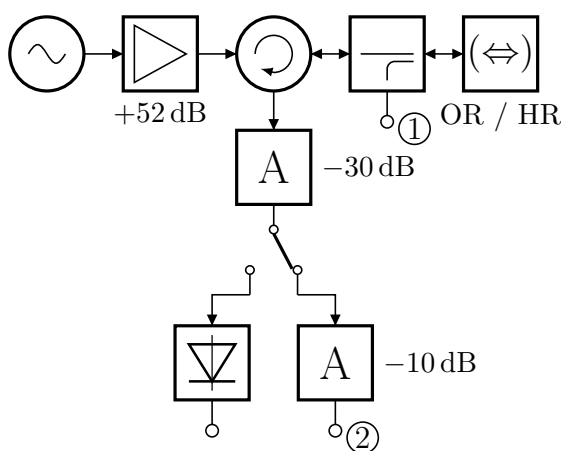


**Figure 6.8:** Sketch of the RF setup. The VCO (left) output is amplified ( $P_{\max} \approx 49 \text{ dBm}$ ) and fed into the resonator antenna (right) via circulator and a directional coupler. The reflected signal is circulated to a 30 dB and 10 dB attenuator. Port ① and ② are connected to a VNA. Alternatively, the directional coupler is removed and the reflected power quantified with a power detector.<sup>a</sup>

<sup>a</sup>Amplifier: *ZHL-100W-S+*, *Mini-Circuits*.

Circulator: *PE8426*, *Pasternack*.

Directional Coupler: *780-20*, *Sage Laboratories*.

Attenuator 30 dB: *RFS100G1A*, *RF-Lambda*.

Power Detector: *ZX47-40LN+*, *Mini-Circuits*.

## Helical Resonator

The resonance of the HR is discussed in subsection 6.1.2. However, the RF setup illustrated in figure 6.8 influences the signals, which is why the S-parameters  $|S_{11}|^2$  and  $|S_{21}|^2$  are illustrated in figure 6.9 without the driving RF and plasma as comparison. In addition, the S-parameter  $|S_{31}|^2$  is plotted, where ③ is the port of the pick-up coil inserted into the HR. All three S-parameter clearly show the resonance at 152.3 MHz. In the upper two subplots is the resonance seen as a dip, due to less reflections, while it is a peak in the lowest subplot, due to the increased field amplitudes within the HR.

The other two measurements are obtained with the driving RF on. The RF frequency  $f_{\text{RF}}$  is first tuned to resonance in order to ignite the plasma. Then,  $f_{\text{RF}}$  is shifted to around 159 MHz, since the VNA is not able to measure at frequencies close to the strong driving RF. The VNA has only two ports. Therefore, this procedure is done twice and  $f_{\text{RF}}$  is somewhat different in the lowest subplot. Even if the driving RF is so far from the resonant frequency, it can drive the plasma. After the measurement with plasma, the driving RF is switched off briefly. This causes the plasma to go out. When the RF is switched on again, the plasma does not ignite and so the measurement can be taken with the driving RF but without plasma.

The measurement with driving RF but without plasma shows similar results as the first measurement without both. The spikes are a consequence of the driving frequency, since it is about 70 dB stronger. The lower values of  $|S_{21}|^2$  are probably an artifact of the VNA in combination with the strong disturbance.

Comparing the measurement obtained with ignited plasma in the lowest subplot, the field amplitudes within the HR are lower at the resonance frequency. However, this is not the result of strong absorption of the plasma, as  $|S_{11}|^2$  and  $|S_{21}|^2$  demonstrate. While without plasma a dip is visible, the dip completely vanishes with plasma. Furthermore, the measured values are larger than before at resonance. Indeed, it is a continuous transition ramping the plasma intensity up. Therefore, the HR at its original resonance frequency becomes as reflective as at neighboring frequencies and this reflectivity is nearly 100 %. An influence of the plasma on the RF characteristic of the resonator is expected, since the plasma consists of free charged particles. Thus, it has its own spatially dependent

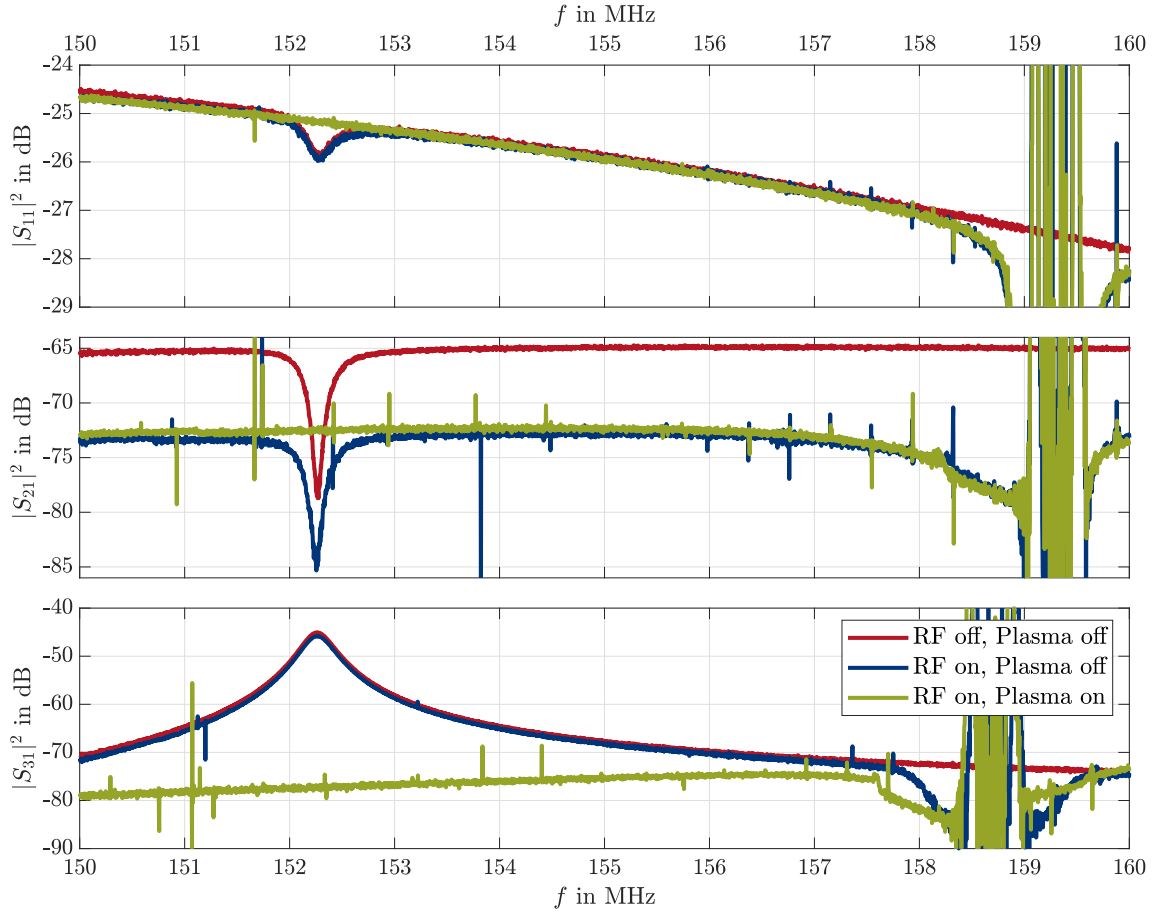


**Figure 6.9:** Measurement results of different S-parameters with the HR. The ports ① and ② are indicated in figure 6.8. ③ is the port of an additional pick-up coil inserted into the HR. The resonance frequency is at 152.3 MHz. While it is clearly visible without plasma, it vanishes with a strong plasma (green lines). Note that the RF frequency  $f_{RF}$  is tuned to about 159 MHz, since the VNA is not able to measure around this dominating frequency.  $f_{RF}$  is slightly different in the lower subplot, as these measurements have been performed separately.

impedance. Equation (6.5) gives the reflectance  $|S_{11}|^2$  for the unperturbed HR. The inductance, capacitance and resistance of the plasma couple with the HR resulting in the impedance  $Z_{rp}$  of resonator with plasma. Assuming that these three characteristics of the plasma change only slowly with frequency, allows to write the coupled impedance in the form

$$Z_{rp} = R_{rp} + i \left( \omega L_{rp} - \frac{1}{\omega C_{rp}} \right) = R_{rp} + i X_{rp}.$$

During the continuous disappearance of the resonance frequency with increasing plasma intensity, no shift of it is observed. Further, no new resonance frequency has been found in the range between 100 MHz and 500 MHz. Therefore, it is reasoned that the reactance stays unchanged and  $X = X_{rp}$ , as only the reactance depends on the frequency under these assumptions.

Using these considerations, the reflectance is given by  $|S_{11}|^2 = \Delta_{R_p}/2\bar{R}_p$  at resonance, where  $X = 0$ .  $R_{rp}$  must be larger than  $R_r$  of the unperturbed HR, because driving the

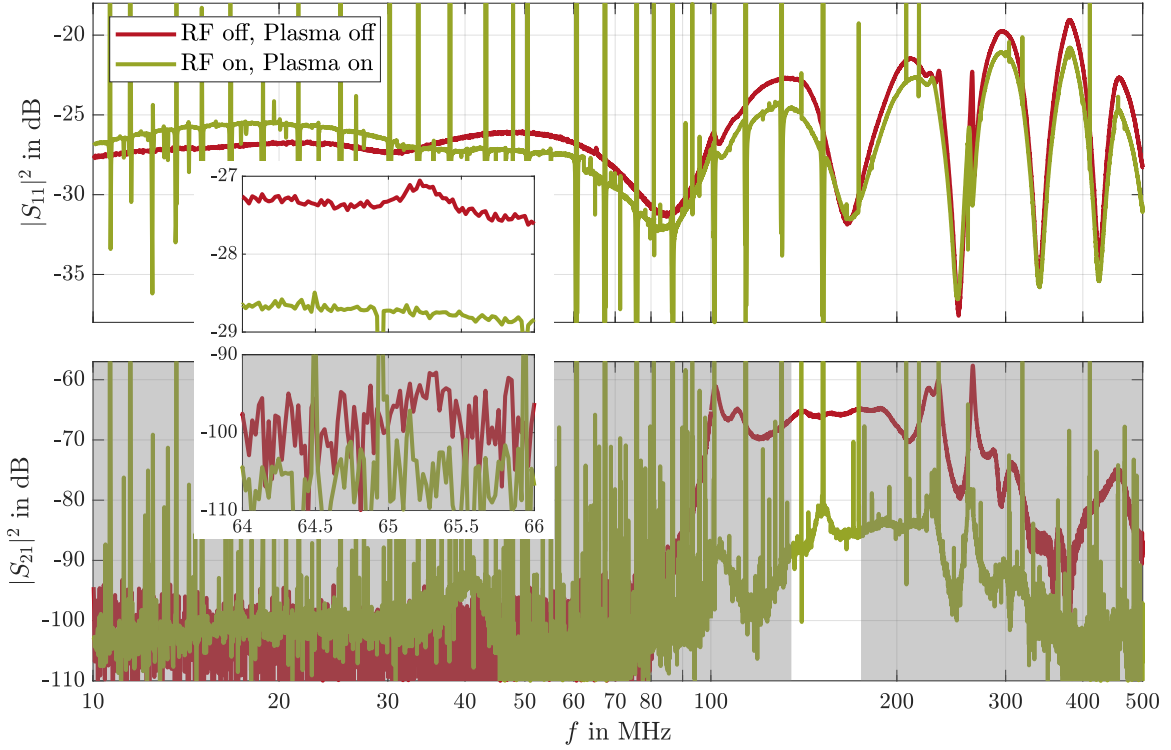


**Figure 6.10:** Measurement of different S-parameters with the OR as depicted in figure 6.8. The frequency range outside the specifications of the circulator is grayed out. The inset shows a magnification of the resonance frequency at 65.2 MHz (see figure 6.2). The driving RF frequency is  $f_{\text{RF}} = 152$  MHz. The characteristics of the measurement setup dominate the original signal from the OR. Even the resonance can only be guessed. Further, no significant change between both measurements is visible.

plasma converts electrical energy in thermal and potential in the form of e.g. metastable atoms. The mutual inductance  $M$  has probably changed as well, since the plasma was ignited. Thus, it is likely that  $\Delta_{R_p} \gg \Delta_R = 21.7(9)$  mΩ of the original system. However, the measurements itself indicate a value of  $\Delta_{R_p} \approx 2\bar{R}_p$  resulting in  $|S_{11}|^2 \approx 1$  for all frequencies. In general, the lumped circuit approximation fails describing a HR coupled with a plasma and the pattern as well as the speed of voltage propagation become important and non-trivial [Mar+21].

The HR, as presented in this work, is not capable of producing higher metastable quench fluxes than the OR. The highest observed quench flux is  $0.23\text{ }^{39}\text{Ar h}^{-1}$  at a source pressure of  $p_{\text{source}} \approx 2 \times 10^{-5}$  mbar. This value is around a factor of two lower than typical values of the OR. One reason may be the vanishing resonance frequency and the resulting high reflectance, since the networks are no longer matched. However, HR are widely used for plasma generation especially for fabrication of semiconductor devices. These HR operate conveniently at frequencies of 3 MHz..30 MHz [LL05; PK97]. The possibility of sustaining a plasma with low matching loss at low gas pressure is described in [LL05]. The RF input is often tapped to the HR helix instead of inductively coupled. However, this RF tap position influences the plasma profile [PLK00; PK97]. Therefore, further research is needed to find out the optimal parameters for a HR in the context of ArTTA. Possible

next steps and a classification of the literature helpful in this process are made in section 7.2.

## Open Resonator

The RF electronic characteristics of the OR are not well accessible by the methods used for the HR. Figure 6.10 shows the measured values for the frequency range of 10 MHz..500 MHz. However, the measurement setup dominates the signal of the bare OR. Even the resonance frequency can only be guessed with driving RF and plasma off. A measurement with driving RF but without plasma is not possible, since the plasma ignites over a wide frequency range. Inserting a pick-up coil once around the source tube showed a strong influence on the OR properties as well as on the plasma, while for some frequency ranges its own characteristic dominates. All in all, no significant and interpretable difference is visible between the measurements. Therefore, other ways have to be found in order to elucidate the RF characteristics of the OR with plasma. Particularly, RF devices for the frequency range around the resonance frequency may be helpful to test a driving RF at these frequencies in more detail.

## 6.4 Spatial Dependence of Metastable Argon Production

Mandaric [Man22] designed and build up a measurement tool in order to resolve the spatially dependent metastable argon production. The measurement setup and general outcomes are summarized in the following. For details it is referred to [Man22]. This technique is then used in conjunction with other measurements to provide further information on the sources of metastable atoms in section 6.5.

### Measurement Setup

The basic idea is to de-excite all metastable atoms up to a specific distance from the source exit. Therefore, only atoms excited to the metastable state behind this distance will be measured by the absolute metastable quench flux (see figure 6.11). This idea is implemented placing a “sheet of light” tuned to the quench transition at the desired position. The sheet of light is a laser beam with a width of about 1 mm in the direction of the atom beam and 18 mm perpendicular to it [Man22]. The bare flux is quantified blocking the laser beam. Afterwards, the laser beam is moved with a constant velocity of  $0.10 \text{ mm s}^{-1}$  from the source tube to the collimator rack and the remaining  $^{40}\text{Ar}$  metastable flux is time dependently measured. All other laser beams are switched off.

### Experimental Results

Figure 6.12(a) displays images of the RF-discharge plasma using the OR with  $\text{LN}_2$ -dewar cooling. The plasma mode and therefore efficiency is varied for these measurements by changing the settings of an impedance matching circuit. The corresponding measurement results are plotted in figure 6.12(b). The measured metastable  $^{40}\text{Ar}$  flux is normalized to the respective bare flux quantified before and after each measurement. The steep decrease at the beginning results from the finite width of the laser beam. After a distance of a little

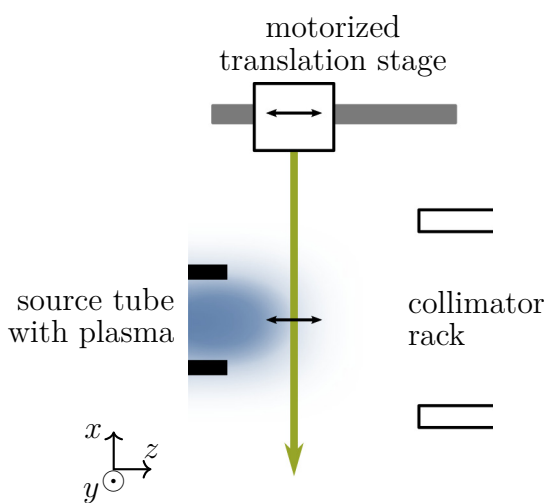


**Figure 6.11:** Sketch of the measurement setup to resolve the spatial excitation of  $^{40}\text{Ar}$  to the metastable state. A laser beam with a width in  $z$  and  $y$  directions of about 1.0 mm and 18 mm, respectively, is sent through the source chamber perpendicular to the atomic beam axis [Man22]. The laser frequency is tuned to the quench transition. Therefore, all metastable atoms, to the left of the laser beam, are quenched. Thus, only the atoms excited to the right of the laser beam are measured with the quench flux tool. The latter is traversed with a motorized translation in  $z$ -direction.

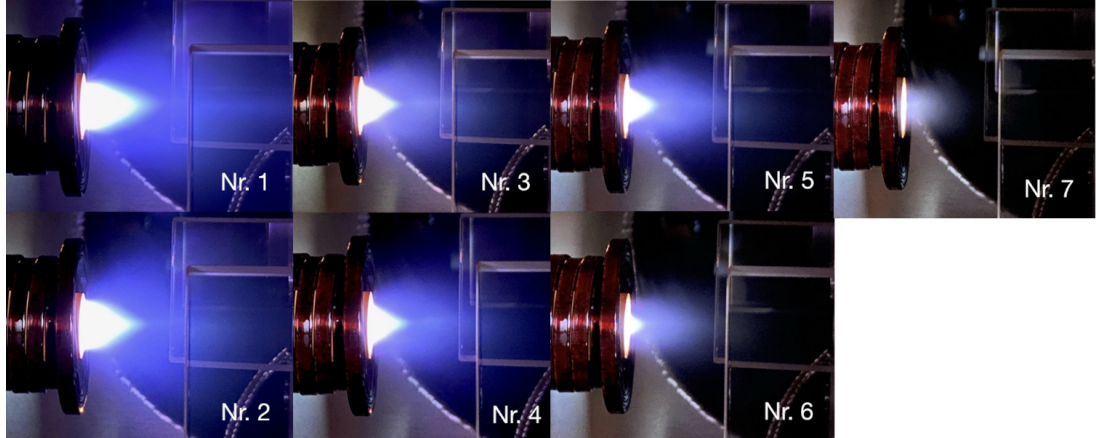
bit more than 1 mm, the width of the laser beam, the relative amount of metastable atoms being produced outside the source tube is visible. Up to 15 % of the metastable atoms get excited even behind a distance of 22 mm, where the first collimator mirror starts. Note that this is not necessarily the position of the first collimator laser beam. The course of the obtained distributions does not linearly scale with the measured overall flux. In general, intersecting courses have also been observed [Man22]. However, comparing the images with the measurements, a correlation between the plasma glowing and the spatial production is observed.

Furthermore, Mandaric showed that the longitudinal velocity distribution stayed unaffected de-exciting metastable atoms produced up to around 3 mm behind the source tube exit [Man22]. However, the transverse velocity distribution became somewhat narrower. The images in figure 6.12(a) illustrate that the plasma reaches the furthest out on the central axis. Atoms with vanishing transverse velocity stay on this axis, are excited and consequently result in a narrower transverse velocity distribution.

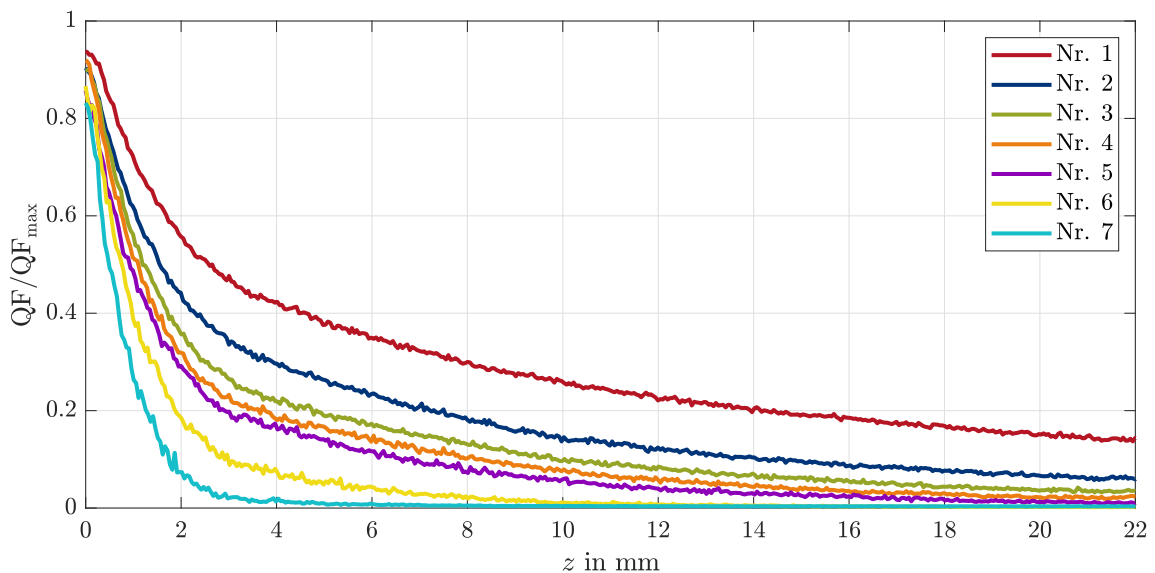
All in all, depending on the plasma mode, a relevant part of the metastable atoms is produced outside the source tube reaching values of up to 50 %. Atoms can be excited to the metastable state multiple millimeter behind the source exit. Without having this measurement setup at hand, the glowing of the plasma is a good indicator for the production volume. The relevant part of the velocity distribution is in good agreement independent of the metastable atom origin in  $z$ -direction.

## 6.5 Study of the Metastable Atom Sources

In this section, the influence of the RF power, RF frequency  $f_{\text{RF}}$ , the source pressure  $p_{\text{source}}$  and the plasma mode on the velocity distribution and spatial production is analyzed. The OR is used for all measurements, as the performance of the above described HR is not sufficient. Attention is paid to observed differences between LN<sub>2</sub>-can and LN<sub>2</sub>-dewar.



(a) Images of the source with plasma. The OR coil is visible on the left side of each image and two of the collimator mirrors are visible on the right side. This figure is taken from [Man22].



(b) Normalized cumulative distributions of the spatial  $^{40}\text{Ar}$  production for various plasma modes. The courses of the various distributions do not linearly scale with the overall flux. The bare flux is quantified before and after each measurement. The cumulative distribution does not start at one because the scattering of the laser beam hitting the source tube de-excites already some of the atoms. This figure is adapted from [Man22].

**Figure 6.12:** Measurement of the spatially dependent metastable  $^{40}\text{Ar}$  production.

The plasma mode is changed such that the overall metastable flux decreases with increasing number. The further the glowing of the plasma reaches into the chamber, the more metastable atoms are produced behind the source exit. The pressure in the source chamber is  $p_{\text{source}} \simeq 2.0 \times 10^{-5} \text{ mbar}$  [Man22].

In the following, the quench flux QF is always given including statistical errors and a systematic error of 26 % according to section 4.4. Plotted error bars illustrate statistical fluctuations. The source pressure  $p_{\text{source}}$  is quantified using a pressure gauge mounted on one edge of the source chamber. The standard conversion factor for air or nitrogen is applied.

The following figures illustrate both transverse and longitudinal velocity distributions. General information about the measurement setup, along with a basic discussion of the distributions, is given in Chapter 5. When applicable, a third subplot shows the spatial production of metastable atoms up to a distance of  $z = 54$  mm, since the collimator mirrors have been removed for these measurements. Basics about this measurement method can be found in the previous section 6.4. All three metrics are normalized for comparability of the trends. One measurement is shown in all following figures. Thus, it can be used as a guide to the eye for comparisons between the figures. This measurement has been obtained with LN<sub>2</sub>-dewar and OR at a source pressure of  $p_{\text{source}} = 1.92 \times 10^{-5}$  mbar, a RF frequency of  $f_{\text{RF}} = 166.4$  MHz, maximum RF power and resulted in a quench flux of  $\text{QF} = 0.50(13) \text{ } ^{39}\text{Ar h}^{-1}$ .

### 6.5.1 RF Power Dependence – first Comparison of LN<sub>2</sub>-Can and LN<sub>2</sub>-Dewar

The effect of different RF powers is measured using the LN<sub>2</sub>-can with the OR. The measurement results are plotted in figure 6.13. The RF input power increases with increasing quench flux QF as well as the reflected RF power. The latter is measured behind a 30 dB attenuator with a power detector (see figure 6.8). The resulting values of the reflected power are in increasing order 28 dBm, 34 dBm, 40 dBm, 43 dBm and 43 dBm. The maximum output of the RF amplifier is around 49 dBm. Thus, a relevant part of the RF power is reflected from the OR.

The width of the transverse velocity distribution increases with increasing RF power. At the same time, the longitudinal velocity distribution reports larger velocities. The most probable velocity is increased by about almost 100 m s<sup>-1</sup>. For comparison, the difference between the LN<sub>2</sub> cooled source and at ambient temperature is around 230 m s<sup>-1</sup> (see figure 5.4). The increase of transverse and longitudinal velocities indicates a warming of source and argon gas. This is reasonable, as the RF power and therefore the energy deposition in the source tube and the argon gas is increased. The discussion of the LN<sub>2</sub> cooling devices in section 6.2 revealed that the Al<sub>2</sub>O<sub>3</sub> tube is the bottleneck in heat transfer. Therefore, a larger cross-section and/or tubes made out of AlN may help to reduce both transverse and longitudinal velocities.

For comparison of both cooling methods, a measurement at maximum RF power and with the same source pressure is additionally plotted in figure 6.13 (yellow dotted line with circles). The obtained quench flux is slightly higher, while the velocities remained lower. A general statement that the LN<sub>2</sub>-dewar cools the atoms to lower temperatures is, up to now, difficult to make, since especially the plasma mode is not clearly characterizable. The plasma mode has also a strong influence on the velocity distributions, as will be seen later. Nevertheless, the combination of dewar and OR is able to produce comparable amounts of metastable argon atoms with a tendency towards better velocity distributions. This generally agrees with the results of the heat transfer discussion in section 6.2.

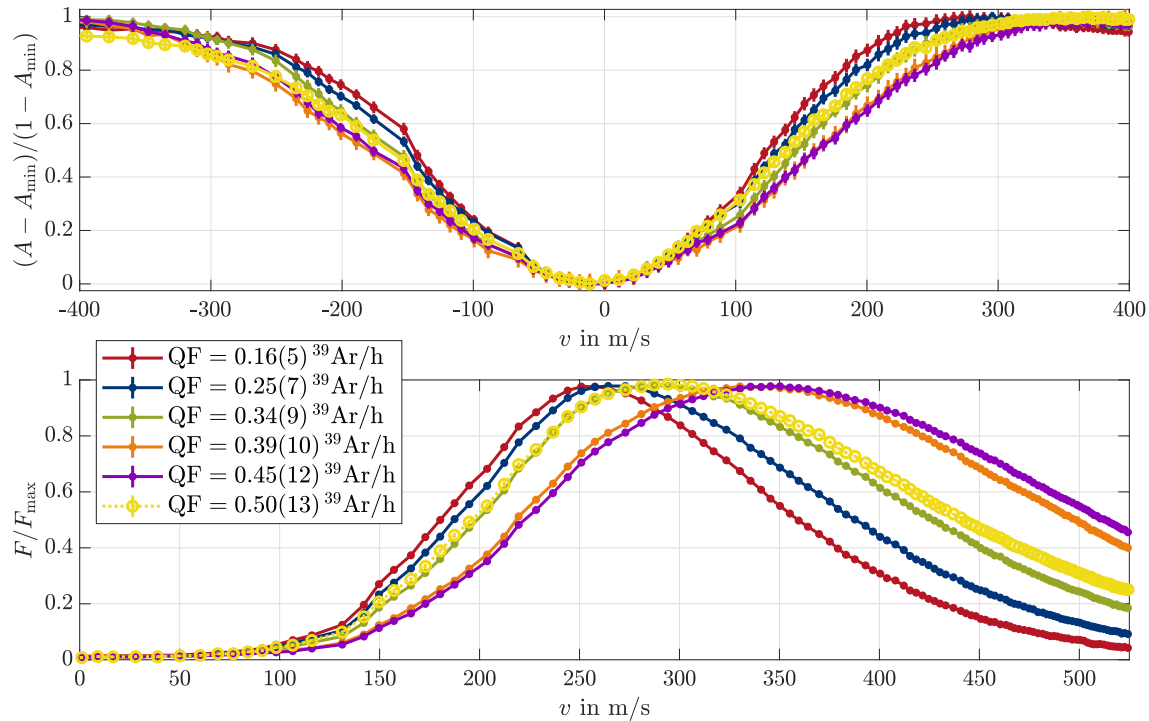


**Figure 6.13:** Measurement of the RF power dependence on both transverse and longitudinal velocity distributions of the metastable atoms. The RF power increases with increasing quench flux. The last measurement (yellow dotted line with circles) is performed with LN<sub>2</sub>-dewar and OR, while LN<sub>2</sub>-can and OR are used for the other ones. The transverse velocity distribution broadens with increasing RF power and the longitudinal one shifts to higher velocities. This indicates an increase of the source temperature. In contrast, the LN<sub>2</sub>-dewar obtained a slightly higher quench flux, while the velocity stayed narrower and slower. The RF frequencies are  $f_{\text{RF}} = 146.5$  MHz and  $f_{\text{RF}} = 166.4$  MHz using the can and dewar, respectively. The source pressure is close to  $2 \times 10^{-5}$  mbar.

### 6.5.2 Pressure Dependence

The pressure dependence is analyzed using both the LN<sub>2</sub>-can and LN<sub>2</sub>-dewar. Figure 6.14 displays the results obtained with the LN<sub>2</sub>-dewar. The three measurements at lower pressures are obtained with the same plasma mode. This means that the plasma changed continuously while the pressure is adjusted. The subplot at the bottom illustrates the relative spatial production of the metastable atoms. With increasing pressure, the production extends further out and the total quench flux  $QF_{\text{max}}$  rises.

The subplot at the top of figure 6.14 shows the transverse velocity distributions. Their width decreases with decreasing pressure. A possible explanation is the increase of the mean free path length with decreasing pressure. Therefore, it is more likely that an atom traveling along the beam axis leaves the source tube without being kicked into another direction. Thus, the source tube slightly collimates the atom beam. A lower temperature could be another possible explanation. However, this is refuted looking at the longitudinal velocity distributions in the middle subplot. The distribution of the lowest pressure is the

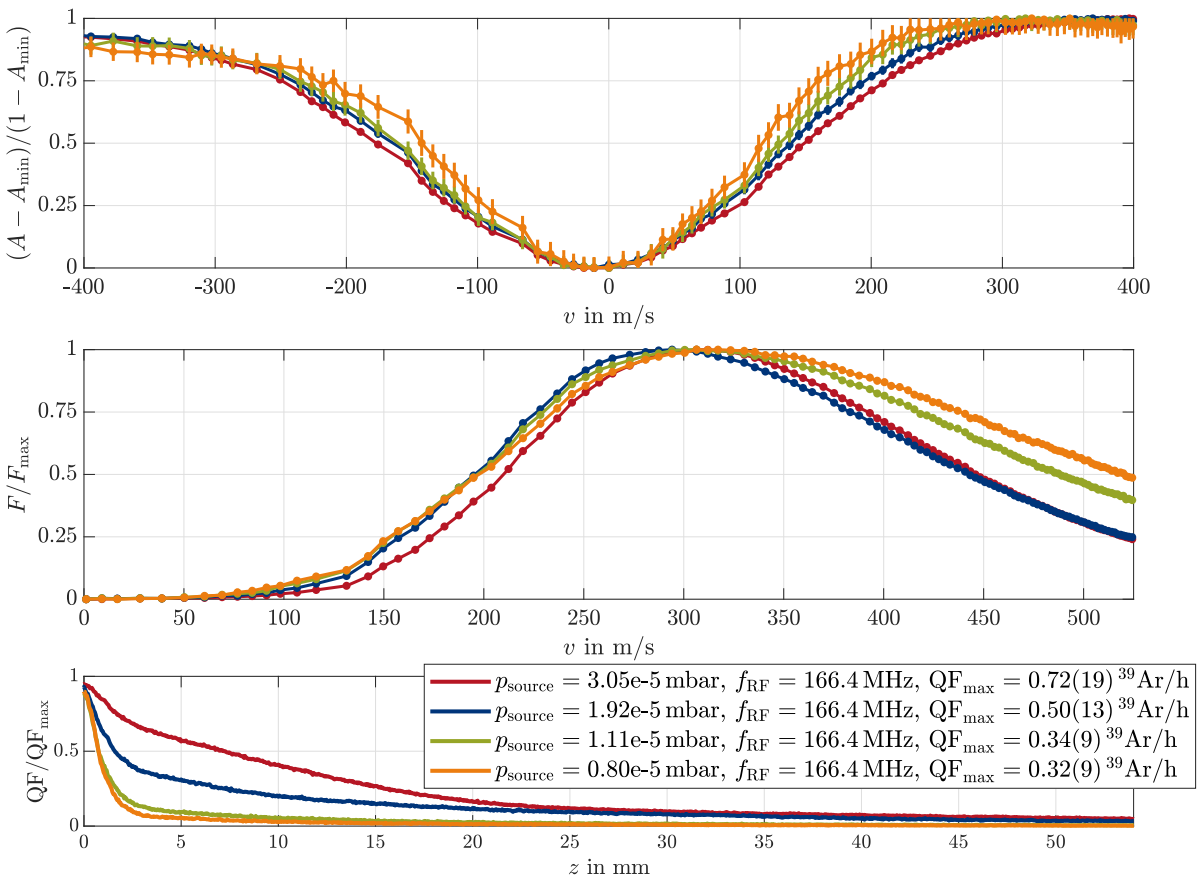


**Figure 6.14:** Measurement of the pressure dependence on both transverse and longitudinal velocity distributions of the metastable atoms as well as the spatial production. The three measurements at lower pressures are obtained with the same plasma mode. The transverse velocity distribution broadens with increasing pressure, while the average longitudinal velocity decreases. This decrease is primarily due to a steeper drop of velocities above the most likely.

broadest with the highest relative densities at large velocities. This contradicts a reduced temperature, as is substantiated in the following.

Referring back to the two longitudinal distribution models (5.6) and (5.7). Both contain the well-known Maxwell-Boltzmann distribution and an additional term regarding collisions with other atoms. Each collision is assumed to kick an atom out of the solid angle observed by the longitudinal velocity measurements. Both models have in common that collision mainly affect slower atoms. Therefore, the flatter rise of the relative density between  $100 \text{ m s}^{-1}$  and  $250 \text{ m s}^{-1}$  of the lowest pressure compared to the highest is expected. As less atoms are kicked out of the beam at lower pressures, the transverse distribution stays smaller. This effect is even more dominant than the broadening due to a higher temperature, which is hereby proven. Since the temperature is the second open parameter of the two models and it mainly affects the courses at higher velocities, it accounts for the larger tails at lower pressures. Thus, the temperature decreases with increasing pressure. One possible explanation is that less thermal energy is deposited due to the higher atomic density. This is because the mean free path length of the electrons also decreases and they

are thus accelerated over a shorter distance.

The observed behavior using LN<sub>2</sub>-can and OR differs. Figure A.6 in appendix A.5 reports the measurement results obtained with LN<sub>2</sub>-can. The measured transverse velocity distributions show the same behavior as described above. Also the general change of the courses of the longitudinal velocity distributions. However, they are shifted as a whole towards higher velocities with increasing pressure. A possible explanation is the difference of the source tubes dimensions. While the inner diameter is 12.0(6) mm in the case of the LN<sub>2</sub>-dewar, it is 10.0(5) mm in the case of the LN<sub>2</sub>-can. Therefore, the cross-section area of the dewar source tube is 44 % larger. Correspondingly, the pressure inside is lower as well as the overall forward velocity. This effect comes more and more into play increasing the pressure. Remember that the pressure within the source chamber is the reference value. While the measurements at  $p_{\text{source}} = 0.80 \times 10^{-5}$  mbar are equal within the errors, those at about  $2.0 \times 10^{-5}$  mbar differ. The most likely velocity of the LN<sub>2</sub>-can is about 50 m s<sup>-1</sup> larger and the distribution wider at this pressure.

All in all, higher pressures and larger cross-sections of the source tube result in larger quench fluxes as well as smaller and slower velocity distributions in the longitudinal direction. Thereby, the width of the transverse velocity distribution increases. However, this is not of importance, as they are not accessible outside a small range and the flux is already higher at zero transverse velocity.

### 6.5.3 Influence of the RF Frequency and the Plasma Mode

In this final subsection, the influence of the RF frequency  $f_{\text{RF}}$  and the plasma mode is discussed. Figure 6.15 shows the results of four measurements in chronological order. The first and third measurement (red and green) demonstrate the reproducibility of the “standard” plasma mode as various other settings and measurements have been performed in the meantime. The “standard” plasma mode is the mode that gives the highest quench flux at a given source pressure and frequency, using only the free parameters of the network matching circuit for optimization.

The second measurement (blue) is performed with a slightly higher RF frequency. The quench flux remained unchanged. However, the relative spatial production illustrates that more metastable atoms are exiting the source tube while less are generated outside. The transverse velocity distribution is slightly broadened and the observed velocities in the longitudinal direction are higher. Both points towards an increased temperature of the metastable atoms. Nevertheless, the effects are small and therefore neglectable. On the other hand, this does not mean that this holds for all RF frequencies.

The plasma mode is changed for the last measurement (orange) using the free parameter of the network matching circuit. The resulting quench flux is smaller and the relative spatial production is comparable to that at a higher RF frequency. The transverse velocity distribution is also comparable<sup>8</sup>. However, the longitudinal velocity distribution is stretched to higher velocities. No matter which of both longitudinal models (5.6) and (5.7) is applied, an increased temperature is the resulting reason. But this is not observed

---

<sup>8</sup>The deviation of the left side is mainly a scaling effect as there is always still some absorption at  $-400 \text{ m s}^{-1}$  for some reason.

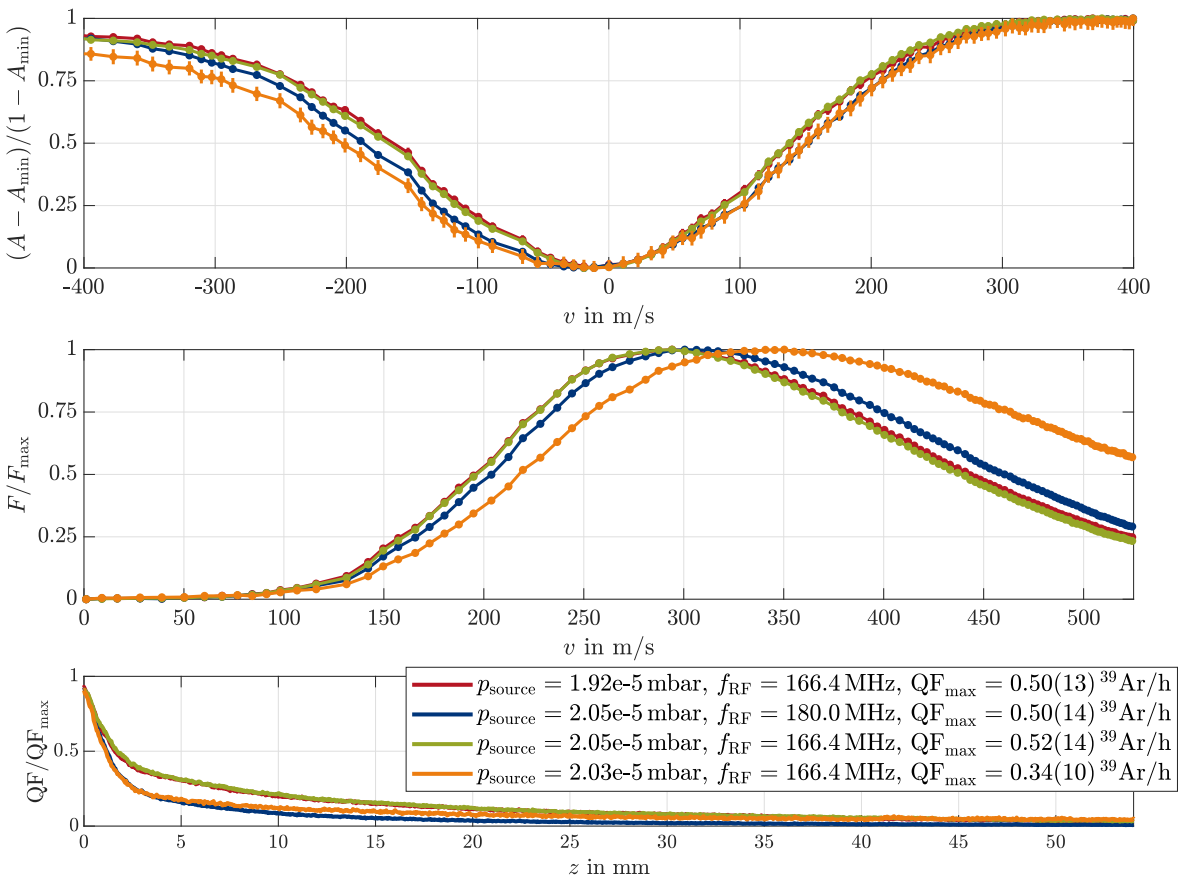


**Figure 6.15:** Measurement of the influence of the RF frequency and plasma mode on both transverse and longitudinal velocity distributions of the metastable atoms as well as the spatial production. The measurements are listed in timely consecutive order. The first and third measurement demonstrate the reproducibility of the “standard” plasma mode. The other two illustrate possible influences of the RF frequency and the plasma mode.

looking at the transverse velocity distribution. Therefore, improved models considering the plasma dynamics are necessary if one wants to understand the interactions in detail. Nevertheless, it becomes clear that the plasma mode itself has a strong influence especially on the longitudinal velocity distribution.

Compendious, the “standard” plasma has the narrowest and slowest longitudinal velocity distribution with the highest flux. No alternative setup was observed which could result in a higher metastable flux using additional techniques like the collimator.

## 6.6 Impact on ArTTA Performance – Conclusion

High metastable flux in the forward direction of the source is critical for counting and dating  $^{39}\text{Ar}$ . The above stated results are recapitulated in the following. Finally, conclusions are drawn with respect to the ZSL and an improved ArTTA performance.

Summarizing the findings of the previous sections, the LN<sub>2</sub>-dewar has a 90 % better thermal conductivity from the LN<sub>2</sub> to the source tube. However, the thermal conductivity of the current Al<sub>2</sub>O<sub>3</sub> tube is slightly lower compared to the LN<sub>2</sub>-can. Furthermore, in both cooling devices the current Al<sub>2</sub>O<sub>3</sub> tubes are the bottleneck in heat transfer. Therefore, a larger cross-section of the bulk material and/or tubes made out of AlN may help to reduce both transverse and longitudinal velocities. Comparing the velocity distributions, the LN<sub>2</sub>-dewar obtained slower longitudinal velocities for source pressures  $p_{\text{source}} > 10^{-5}$  mbar, while they are equal to those of the LN<sub>2</sub>-can at the current measurement pressure of  $p_{\text{source}} = 0.80 \times 10^{-5}$  mbar.

The spatial production analysis revealed that, depending on the plasma mode, a relevant fraction of metastable atoms is produced outside the source tube. Furthermore, metastable atoms generated outside the source tube have a narrower transverse velocity distribution [Man22]. Nevertheless, an early and fast deceleration in transverse direction is important. Thus, a reduction of the distance between the source exit and the first transverse deceleration laser beams is suggested.

The “standard” plasma mode, which is the mode currently used, has the narrowest and slowest longitudinal velocity distribution with the highest quench flux. A reduction of the RF power results in slower and narrower longitudinal velocity distributions. Therefore, a reduction is advantageous as long as the quench flux remains unchanged. Higher pressures and larger source tube cross-sections result in larger quench fluxes. Additionally, the reported longitudinal velocity distributions are smaller and slower. However, at higher pressures, follow-up studies are needed to elucidate the impact of increased collision losses. Therefore, a simultaneous measurement of the metastable <sup>40</sup>Ar quench flux and the <sup>38</sup>Ar loading rate with collimator and 2D-MOT depending on the source pressure is suggested. Note that a meanwhile outdated pressure dependent measurement of the loading rate indicated a local maximum, followed by the global one<sup>9</sup>. However, an issue may be a faster degeneration of the collimator mirrors at higher pressures.

A larger source pressure results in slower and narrower longitudinal velocities (see figure 6.14). However, the tail<sup>10</sup> still goes beyond the capture velocity of the current ZSL, which is  $v_c \approx 610 \text{ m s}^{-1}$  [Ebs18]. Therefore, not only the quench flux but also the amount of addressed atoms by the ZSL is increased. On the other hand, this amount can be kept constant by reducing the capture velocity and thus the length of the ZSL. For example, reducing the capture velocity by  $100 \text{ m s}^{-1}$  will result in a reduced ZSL length of about 30 %. This reduces collision losses and the transverse distance traveled due to a shorter cross-section. These considerations need to be deepened, especially in conjunction with the simultaneous measurements of quench flux and loading rate proposed above.

Compendious, the LN<sub>2</sub>-dewar with OR generates equal or better metastable atom distributions with respect to the ArTTA performance compared to the LN<sub>2</sub>-can. The gained knowledge indicates possible improvements of the ZSL, if higher source pressures will be used in the future. For example, a 50 % higher <sup>39</sup>Ar count rate is expected increasing the source pressure to  $2.0 \times 10^{-5}$  mbar and assuming that the collision losses and the increased fraction of atoms included by the ZSL cancel mutually. Furthermore, an exchange of the

---

<sup>9</sup>This measurement has not yet been published.

<sup>10</sup>Remember that the measured fluorescence  $F$  has to be multiplied with approximately  $v^{3/4}$  in order to get the actual velocity distribution.

source tube is recommended, as it may results in smaller and lower velocity distributions. On the one hand, the already discussed effects and possible improvements of the ZSL count again, on the other hand also an increased gain of the collimator is expected.



# 7 Conclusion and Outlook

The work presented in this thesis started with the ArTTA technology as a whole and continuously focuses on the metastable atom source. The focus is always on the impact on the  $^{39}\text{Ar}$  count rate and reliable routine measurements. Chapter 3 derived new alignment procedures for the quantum optical tools and provides a detailed description for the daily user. Additional support comes from the new monitoring software used uniformly at both facilities.

In chapter 4, a new device for absolute measurements of the metastable  $^{40}\text{Ar}$  flux is presented. Its application suggests a possible improvement of the ZSL. This was supported by the measured velocity distributions and a discussion of transverse diffusion during longitudinal deceleration.

Finally, emphasis was placed on the source of metastable atoms. Two different types of RF antennas and two  $\text{LN}_2$  cooling methods were presented. Their properties were analyzed with and without plasma before the influence of various other parameters on the metastable atom source was reported.

This final chapter concludes with a review of the key results and suggestions for future improvements. The first section deals with the second ArTTA facility, on which most of the work was performed. The second section focuses on the source of metastable atoms. Finally, the chapter ends with the ArTTA technology with which the thesis began.

## 7.1 Second ArTTA Facility

This section provides a conclusion and an outlook on the second facility itself. It refers to general experiences from daily work and addresses open issues.

The assembly of the second ArTTA facility is reported in detail in [Rin21; Fen18]. Currently, it is located in two custom designed ship containers. However, the reduced stability of the floor, the very sparse space and the fare distance between both ArTTA facilities are problematic. For example, simultaneously working with more than two persons in the container is not practical, and in some places there is only room for one. The far distance between the laboratories is mainly problematic with respect to stored items. The large distance costs time and hinders the work flow especially during larger vacuum or optic assemblies. Because not all items are available multiple times in each laboratory, one has to switch between the facilities several times.

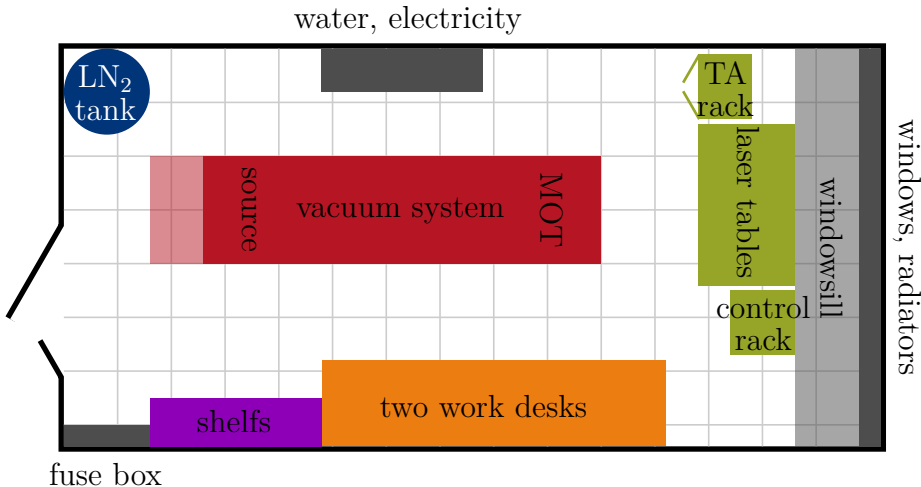


**Figure 7.1:** Possible arrangement of the second ArTTA facility in the adjacent to the first laboratory. The grid spacing is 0.5 m. The central part of the device, the vacuum system, is located in the middle and is accessible from all sides. The transparent area on the left is blocked when working on the collimator. The laser system is placed at the end of the room. This allows to separate this part of the room with a curtain. The two laser tables are positioned one above the other as before. The wide and deep windowsill can be used as a staging to work on the upper laser table.

Currently, the neighboring laboratory of the first facility is available. As the second apparatus is shut down and already partly disassembled, it is suggested to move it to this room if it is to be revived. This immediate vicinity would allow for exchanging laser light between both facilities, which can be helpful answering emerging question. Figure 7.1 illustrates a possible arrangement. The central part, the vacuum system, is located in the middle of the room. Accessibility from all sides is important, especially around the source chamber and the MOT. A hanging shelf above the vacuum system for electronic equipment, as already exists, is recommended.

The laser system is located at the end of the room. Two laser tables are stacked above each other, as space is still limited. However, this solution has proven its worth in the past and will be even more convenient with a higher ceiling and accessibility from two sides. Furthermore, the windowsill can be used as a staging to work on the upper laser table, or it should be removed. Storing the tapered amplifiers (TAs) in an own encapsulated rack has also been proven successful. It is recommended to copy this concept for the spectroscopy setups, as their current location is hardly accessible for alignment. However, they should be well separated from the TAs due to strong stray light and magnetic fields of the Faraday isolators.

In the course of this work, the fore-vacuum has been set up as a compact version of the redesign from Schmidt [Sch21]. With this, all physical parts necessary for  $^{39}\text{Ar}$  dating are at hand. However, a sufficient count rate has not been achieved yet. On the one hand, special emphasis was placed on an improved understanding of the ArTTA technique, being concluded in the following section. Therefore, the setup as a whole was no longer tuned towards higher count rates and single parts have even been removed in order to obtain other measurements. On the other hand, several issues in the basic setup have

been detected with time. Some of these deficiencies still need to be addressed, so they are listed below.

- The AOM paths have been set up in a very compact way<sup>1</sup>. This setup has not proven to be beneficial. Replacing them by established arrangements is suggested.
- While a redesign of the ZSL is generally proposed (see following section), the functionality of the upstream differential pumping stage in particular is questioned. To our current knowledge, it hinders the pumping of the ZSL vacuum pipe. Furthermore, the order of the differential pump stages is reversed in the second system, with unknown consequences.
- The optical setup of the 2D-MOT lacked the possibility of aligning the angle of the laser beams. However, this is crucial as it changes the appearing Doppler detuning. This issue is already partly addressed but not yet finished. The same free parameter is missing at the MOT laser beams.
- The radius of the MOT laser beams is smaller than the general radius of the atom beam. The optics have to be increased to a 2" system. The focal length of the collimating lens should be increased to the focal length of the first instrument, i.e. 150 mm. It has to be checked, if also the size of the stray light blocking lens tubes within the vacuum chamber has to be increased. The same accounts for the ZSL and Booster laser beams. See subsection 5.3.1 for theoretical considerations.
- One of the two atmosphere to ultrahigh vacuum fibers has to be replaced. The polarization maintenance is not sufficient, probably due to too strong pressing of the Teflon feedthrough. See appendix A.3 for assembling details.

All in all, the second apparatus helped gaining knowledge about the ArTTA technique. This knowledge resulted in several improvements of the first facility with respect to the count rate at that time. Possible next steps are suggested above. Either to continue using it as a research device or to measure the concentration of rare isotopes.

## 7.2 Metastable Atom Source

A detailed summary of the findings with respect to the metastable atom source is given in section 6.6. Conclusions regarding the ArTTA performance have been discussed and are therefore not repeated here. This section focuses on the RF antennas and the plasma itself, discussing relevant literature in the context of ArTTA.

Mixing argon with other gases has an influence on the metastable density. For example, an increase of a factor of around four is reported in an inductively coupled plasma using an argon oxygen mixture of  $\text{Ar} : \text{O}_2 = 9 : 1$  [Hay+09]. The increase is explained by a decrease of the electron number density and therefore a decrease of the electron-induced quenching (2.21). Though, these findings have been obtained by a pressure of 0.13 mbar, much higher as the pressures used in ArTTA. Some measurements of mixtures have also been performed in the scope of this work. However, the mixtures of argon with air, helium,

---

<sup>1</sup>A convex lens focuses the laser beam onto a concave mirror in the focal plane. The focal length of mirror and lens is equal. The AOM is near the mirror.

krypton or xenon resulted only in a decrease of the MOT loading rate<sup>2</sup>.

Regarding the antennas, an improved coupling with the plasma or increased RF power is suggested. The maximum metastable density has yet not been achieved, increasing the RF power. However, the existence of an optimum RF power is reported in the case of argon carrier gas mixtures in [RLM09]. The existence is also expected from the course of the electron induced excitation cross-sections [Loc+16]. Inductive discharges at low densities, such as those used in ArTTA, have been shown to operate in a capacitance-like mode, resulting in much lower density [LL05]. It is suggested to add a metal cylinder between coil and plasma, slotted along the axial direction. The electrostatic shielding reduces the capacitive coupling to a negligible value [LL05].

In general, the use of helical resonators (HRs) for plasma generation is extensively described in literature, e.g. [Mar+21; LL05; PLK00; PK97; Nia+94; LLF90]. The version used in this work and proposed externally has not proved successful. Therefore, it is suggested to build a new HR, based on the reported knowledge in the literature. Conveniently, HR for plasma generation are operated at frequencies of 3 MHz..30 MHz, with 13.56 MHz being a typical value [LL05; PK97]. The RF input is directly tapped to the inner helix. However, the tap position determines the impedance matching and influences the plasma profile [LL05; PLK00; PK97]. For example, a higher plasma density in the open-circuit section of the HR is achievable by placing the tap position at an even multiple of  $\lambda/4$  from the short-circuited end [PLK00]. This section can then be placed at the source exit, where the metastable atoms are able to leave the source without collisions. In general, Lieberman and Lichtenberg [LL05] give an broad overview over plasma discharges and Martines et al. [Mar+21] particularly over the HR. The advantage of a HR compared to the nowadays used open resonator (OR) is a larger distance between the helix turns. Therefore, no isolation is necessary, probably reducing the mirror degeneration. Additionally, no voltage breakthrough can appear, which results in a longer life time.

Modeling of the argon plasma and the metastable production will further elucidate how to change the source design towards increased usable metastable argon densities. Bogaerts and Gijbels [BG95], for example, provide a model for a current glow discharge or Rauf and Kushner [RK97] for a RF discharge. Hebner and Miller [HM00] discuss a model coupling the metastable state with its three nearby states. Both can be used as a starting point with the additional literature provided. Nevertheless, the generation of RF discharges and the processes within the plasma are non-trivial. As plasma physics is an own and wide research field, it is proposed to look for a cooperation with a research group in the field of low density and low temperature plasma.

### 7.3 ArTTA Technology

In this final section, the central results for the ArTTA technology are addressed and performance-enhancing adaptations are proposed.

A new monitoring system including hard- and software has been established. As all crucial parts are documented and version controlled using GitLab, all necessary information are at

---

<sup>2</sup>These measurements are not reported in detail in this thesis.

hand for further developments. Nevertheless, it depends on future generations to keep the documentation up to date. Some steps have to be done at the first facility towards using the full capability of the current ATTAsystem. These are mainly improved measurements of the several laser powers using pick-up plates. Another point is the integration of pressure sensors, as they are read out differently as at the second facility.

A new instrument for the determination of the absolute metastable  $^{40}\text{Ar}$  flux was successfully developed and put into operation in both laboratories. The findings of the theoretical description are important to be considered with respect to accuracy and comparability between the apparatuses. This mainly refers to the strength of the magnetic field within the quench chamber and the necessity that the ZSL solenoid and the downstream solenoid of the 2D-MOT should enhance each other.

The new device has already been used successfully in the course of the metastable atom source characterization. Furthermore, measurements of the  $^{40}\text{Ar}$  metastable flux using the collimator obtained values being three to five times higher as the current equivalent  $^{39}\text{Ar}$  count rate. This suggests and motivates, among other findings, a redesign of the ZSL, since this is the part where atoms may be lost.

In the redesign process of the ZSL, emphasis should be placed on balancing capture range, deceleration losses, and loss amplification with increasing length of the ZSL. An additional 2D-MOT within the ZSL at moderate velocities is also thinkable by changing to a spinflip slower design. Some of these aspects are discussed in section 5.3 and further considerations will soon be published in the master thesis of Oehmke.

The ( $^{38}\text{Ar}$ ) MOT loading rate has been established as a routine characterization tool before and after each  $^{39}\text{Ar}$  measurement. Additionally, it is also used for alignment purposes or fundamental research questions. One benefit compared to the previously used  $^{40}\text{Ar}$  beam imaging is the inclusion of ZSL and MOT itself. Another reason is the greater sensitivity to small atomic currents. This is mainly important as it has been demonstrated that the collimator is not optimal adjusted for  $^{39}\text{Ar}$  using  $^{40}\text{Ar}$  for the alignment. Therefore, the collimator is now finally aligned on the  $^{38}\text{Ar}$  loading rate. However, the loading rate has its difficulties measuring large metastable fluxes, like it is the case using in addition collimator and 2D-MOT. The reason are metastable-metastable losses due to the high resulting density. A solution may be a combination with the quench method. De-exciting the atoms at the center of the MOT will keep densities lower and enables reliable absolute measurements detecting again the decay photons.

The new collimator alignment procedure resulted in an 1.5 times higher  $^{39}\text{Ar}$  count rate [Mei22]. Furthermore, an increased distance between the collimator results in higher  $^{39}\text{Ar}$  count rates, based on theoretical considerations and simulations [Rit13]. This has been substantiated by measurements of the collimator gain of the absolute metastable  $^{40}\text{Ar}$  flux. Based on these results, the mirror spacing was recently increased in the first system as well. Furthermore, as expected from a theoretical point of view, Kundy recently reported an increase in the  $^{38}\text{Ar}$  loading rate by introducing an additional one-dimensional optical molasses into the gap between the source tube exit and the collimator [Kun23]. This gap has now been closed in the course of extending the mirror distance. First results with respect to the  $^{39}\text{Ar}$  count rate will be available soon.

The latest results on the metastable atomic source shed light on its properties. The  $\text{LN}_2$ -dewar has been designed and analyzed in detail. It needs three to five times less  $\text{LN}_2$ , saving

time and money. Thereby, the metastable atoms leave the source with equal velocities and a slightly higher flux. Increasing the source pressure to  $2.0 \times 10^{-5}$  mbar resulted in a 50 % higher quench flux. Additionally, the velocity distribution in longitudinal direction slows down. This enables further optimizations of the ZSL. The impact of increased collision losses downstream of the quench chamber have to be elucidated in following studies. First suggestions focusing on this issue are stated in section 6.6. Furthermore, a switch to source tubes with a larger bulk cross-section and/or made out of aluminum nitride (AlN) is highly recommended, as the current tubes are the bottleneck in heat transfer.

Compendious, the knowledge about the ArTTA technology has been increased and substantial improvements towards reliable as well as continuous routine  $^{39}\text{Ar}$  measurements have been achieved. Crucial features haven been analyzed and the set of characterization tools as well as their application refined. Together with the ArTTA group, the amount of measured samples has been increased to 94 samples within 2021 and 2022 (see figure B.1 in appendix B). Future and motivated improvements will soon result in an increased count rate of  $^{39}\text{Ar}$  along with further improvements of the sample throughput. This will contribute to understanding environmental systems and addressing current problems for our society.

# A Appendix

## A.1 Radiation Pattern of Different Optical Transitions

The emission of a photon is a consequence of the non-vanishing dipole moment  $\vec{\mu}_{eg} = -e \langle e | \vec{r} | g \rangle$  [Fox06]<sup>1</sup>, where  $|g\rangle$  is the ground and  $|e\rangle$  the excited state. The elementary charge is denoted by  $e$ . The radiation pattern of the far field can now be derived by analyzing the directional energy flux of a classical dipole moment  $\vec{d} \propto \vec{\mu}_{ge}$ . This flux is given by the Poynting vector [PS84; Gri99]

$$\begin{aligned}\vec{S} &= \frac{1}{\mu_0} \vec{E} \times \vec{B} \\ &\propto \frac{1}{r^2} ((\hat{r} \times \vec{d}) \times \hat{r}) \times (\hat{r} \times \vec{d}) \\ &= (|\vec{d}|^2 - (\vec{d}^\top \cdot \hat{r})^2) \frac{\hat{r}}{r^2} \\ &\propto \varrho(\vec{r}) \hat{r},\end{aligned}\tag{A.1}$$

with  $\varrho(\vec{r})$  being the normalized radiation pattern. Inserting the dipole moment

$$\vec{d} = d_0 \begin{pmatrix} \cos(\omega t) \\ \sin(\omega t) \\ 0 \end{pmatrix}$$

of a rotating electric dipole in the  $x, y$ -plane and the radial unit vector

$$\hat{r} = \begin{pmatrix} \cos \varphi \sin \theta \\ \sin \varphi \sin \theta \\ \cos \theta \end{pmatrix}$$

into equation (A.1) gives the corresponding radiation pattern

$$\varrho(\vec{r}) = \frac{3}{4} \frac{2 - \sin^2 \theta}{4\pi r^2}.\tag{A.2}$$

Note that the temporal oscillation of the dipole moment averages out the polar angle  $\varphi$ .

The radiation pattern for linear dipole moments is given in table 5.1 in section 5.3.

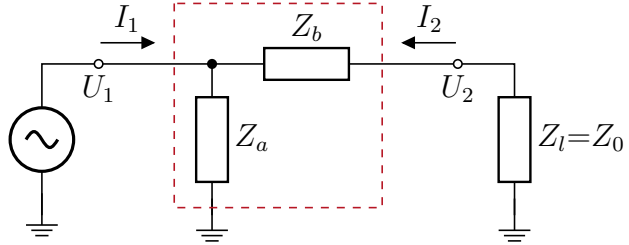
---

<sup>1</sup>Note that not all superpositions have a nonzero dipole moment. This fact is considered in the selection rules for dipole transitions (see subsection 2.2.4).

## A.2 S-Parameter Calculation of a Two-Port Network

A useful tool designing RF circuits is the determination of the S-parameter. In the following it is determined for the two-port network in figure A.1, constructed with the two impedances  $Z_a$  and  $Z_b$ .

**Figure A.1:** Network to determine the  $S_{11}$  and  $S_{21}$  parameter of an example two-port network within the red dashed rectangle. Port 1 is on the left and port 2 on the right hand side. This figure is adapted from [Hag09].



The reflection coefficient  $S_{11}$  is derived looking into port 1 of the two-port network. Port 2 has to be terminated with the reference impedance  $Z_0$ , which is normally  $50\Omega$ . Accordingly no signal is entering port 2 resulting in  $U_{1\text{out}} = S_{11}U_{1\text{in}}$  (compare figure 2.10). Kirchhoff's law implies for the voltage as well as the current through port 1:

$$U_1 = U_{1\text{in}} + U_{1\text{out}}, \quad I_1 = I_{1\text{in}} - I_{1\text{out}}. \quad (\text{A.3})$$

$Z_1$  is the impedance looking into port 1. It ensures that  $U_1 = I_1Z_1$  while  $Z_0$  defines the ratio between the incoming and outgoing waves:  $U_{1\text{in}} = I_{1\text{in}}Z_0$ , respectively  $U_{1\text{out}} = I_{1\text{out}}Z_0$ . Summing everything up, one derives the equation for the reflection coefficient

$$\Gamma = S_{11} = \frac{U_{1\text{out}}}{U_{1\text{in}}} = \frac{U_1 - I_1Z_0}{U_1 + I_1Z_0} = \frac{Z_1 - Z_0}{Z_1 + Z_0}. \quad (\text{A.4})$$

$S_{11}$  depends on  $Z_0$ , as the former is always defined compared to a reference impedance corresponding to a reference potential of the electrical wave.

Using the rules for impedances built in series and in parallel (2.26) one derives

$$Z_1 = \frac{1}{Z_a^{-1} + (Z_b + Z_0)^{-1}}. \quad (\text{A.5})$$

Inserting this into equation (A.4) for the reflection coefficient results in

$$S_{11} = \frac{Z_aZ_b - Z_bZ_0 - Z_0^2}{Z_aZ_b + 2Z_aZ_0 + Z_bZ_0 + Z_0^2}.$$

The transmission coefficient from port 1 to 2  $S_{21}$  is derived using the same conditions as before. At port 2 the voltage is  $U_2 = U_{2\text{out}} = -I_2Z_0$ , as there is still no reflection from the termination. The current through port 2 is given by the remainder of  $I_1$  not flowing through  $Z_a$ :  $I_2 = -I_1 + U_1/Z_a$ . Combining the latter with equations (A.3), (A.5) and  $U_1 = I_1Z_1$  as well as the definition of  $S_{21}$  one ends up with

$$S_{21} = \frac{U_{2\text{out}}}{U_{1\text{in}}} = 2 \frac{I_1Z_0 - U_1\frac{Z_0}{Z_a}}{U_1 + I_1Z_0} = 2 \frac{Z_1^{-1} - Z_a^{-1}}{Z_0^{-1} + Z_1^{-1}} = \frac{2Z_0Z_a}{2Z_0Z_a + Z_0Z_b + Z_aZ_b + Z_0^2}.$$

Due to the applicability of the reciprocity theorem it follows that  $S_{21} = S_{12}$ . The latter is also derived in [Hag09]. The  $S_{22}$  parameter can be determined with the same approach as  $S_{11}$ .

### A.3 Atmosphere to Ultrahigh Vacuum Fiber

The whole collimator in the source chamber is mounted on a kinematic mount. Moving the setup without changing the path of the laser beams between the pairs of mirrors is preferable. This allows the output direction of the collimator to be set independently of other parameters. However, one has to attach the end of the fiber that provides the laser light to the setup within the vacuum. Bought fiber feedthroughs had transmission efficiencies well below 50 %. Therefore, they were replaced by self-assembled fibers that go directly into the ultrahigh vacuum. The way of construction is published in [AC98]. Figure A.2 shows the single parts and the final fiber.

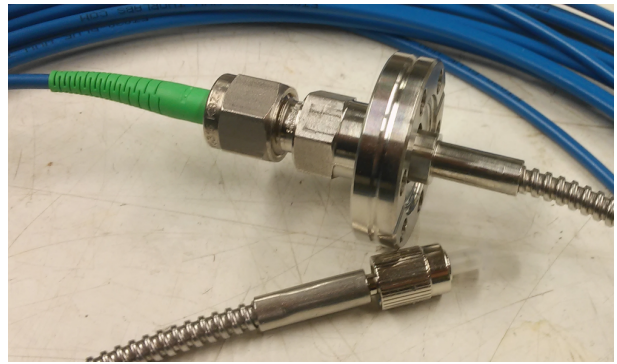
A bare fiber of type *PM780-HP* from *Thorlabs* is used. The feedthrough is made out of a *Swagelok* tube fitting adapter. The standard ferrule is removed and replaced by a Teflon taper and a press disk. The fiber is feed through a 250  $\mu\text{m}$  diameter bore hole in the taper. During assembly, the fiber must be free of dust particles and other impurities.



(a) Image of the feedthrough components. From left to right: CF40 to Swagelok adapter with clamping hull for a metal hose on the left, Teflon feedthrough, press disk with bend protection extension, nut, bend protection.



(b) Metal and plastic fiber protection hose. The metal hose is used within the vacuum and slotted for evacuation.



(c) Final assembled fiber with a length of approximately 10 m.

**Figure A.2:** Images of the single parts of the feedthrough and the final fiber.

It is important that the nut is tightened until the feedthrough is leak tight but not further. Otherwise it may happen that the polarization maintenance is distorted. Within the vacuum a slotted metal hose is used for protection. Outside a typical plastic tube with strain relief. At the ends are standard FP/APC connectors mounted.

## A.4 DDM: Supplementary Information

Figure A.3 and A.4 show results obtained with the DDM in section 4.3. The experimental parameter are explained in subsection 4.3.1. A detailed comparison with measurements and results for further experimental settings can be found in subsection 4.3.3.

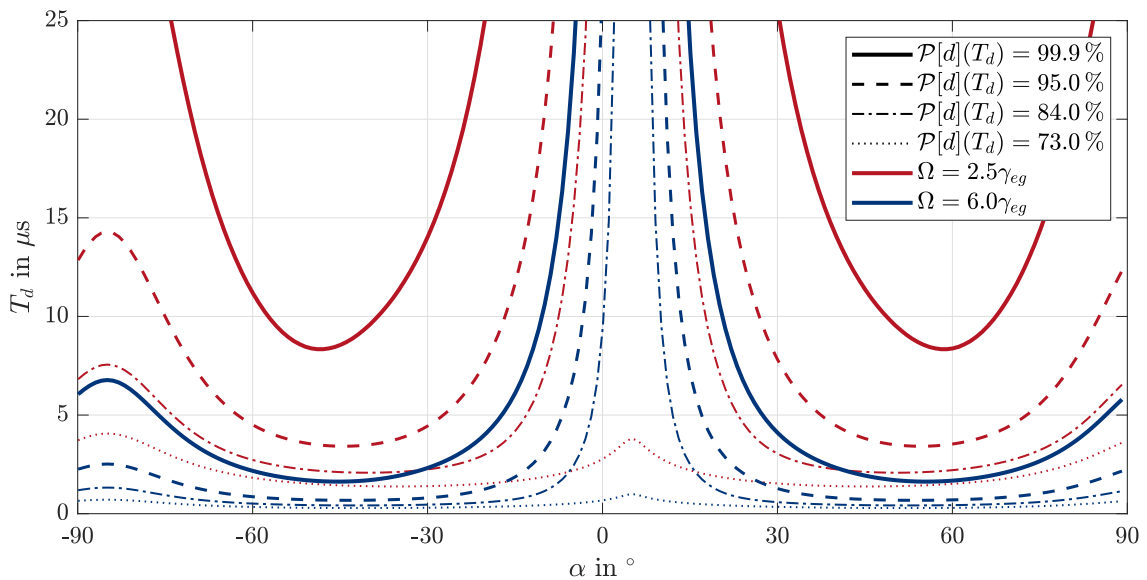
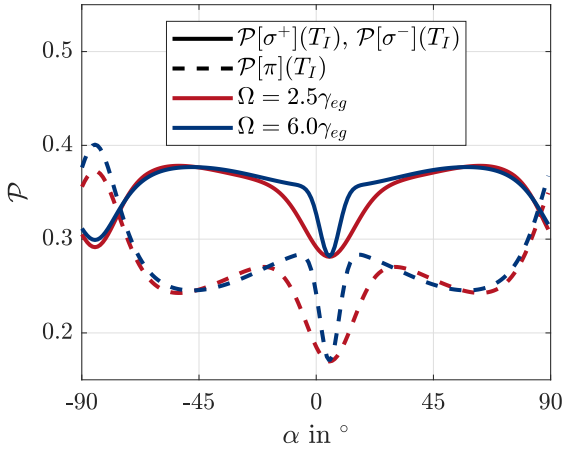


**Figure A.3:** Plot of the decay time  $T_d$  until 99.9 %, 95.0 %, 84.0 % and 73.0 % of the atoms decayed. Most of the atoms decay within the first 10  $\mu\text{s}$ . However, for laser polarizations of  $\alpha \sim \theta \approx 0^\circ$  the coupling of the  $m_J = 0$  ground state gets very weak and the decay time strongly increases for the final atoms. For  $\alpha - \theta \sim \pm 90^\circ$  is the excitation of the  $m_J = \pm J$  ground states softened, as mainly  $\sigma^\pm$  transition with a large Zeeman shift are driven. The magnetic field is  $\vec{B} \approx (0.03, 0.32 - 3.6)^\top \text{G}$ .

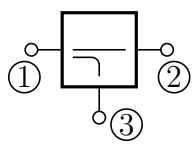
## A.5 Metastable Atom Sources: Supplementary Information

Figure A.5 reports the S-parameters of the directional coupler used for the RF electronic analysis of the metastable atom sources in section 6.3.

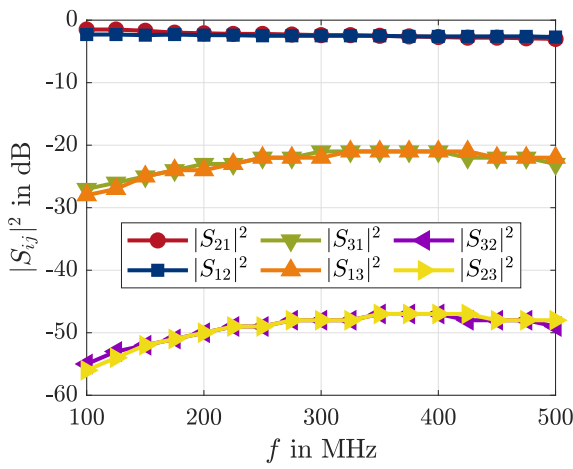
Figure A.6 illustrates further measurements discussed in section 6.5. There, the pressure dependence on the velocity distributions is analyzed. The figure shown here contains measurements obtained with the LN<sub>2</sub>-can instead of the LN<sub>2</sub>-dewar, as in figure 6.14.



**Figure A.4:** Graph of the decay photon polarization probability  $\mathcal{P}$  depending on the laser polarization  $\alpha$ . The evolution time is  $T_I = 15\text{ }\mu\text{s}$ . The results are shown for two laser intensities. Note that the probability includes whether an atom decayed at all. Especially around  $\alpha - \theta \sim 0^\circ$  not all atoms have emitted a decay photon. The magnetic field is  $\vec{B} \approx (0.03, 0.32 - 3.6)^\top \text{G}$ .



(a) Port definition of the directional coupler.



(b) Measured S-parameters of the directional coupler.

**Figure A.5:** The measured S-parameters of the directional coupler 780-20 from *Sage Laboratories* are reported in (b), while the definition of the ports is illustrated in (a).

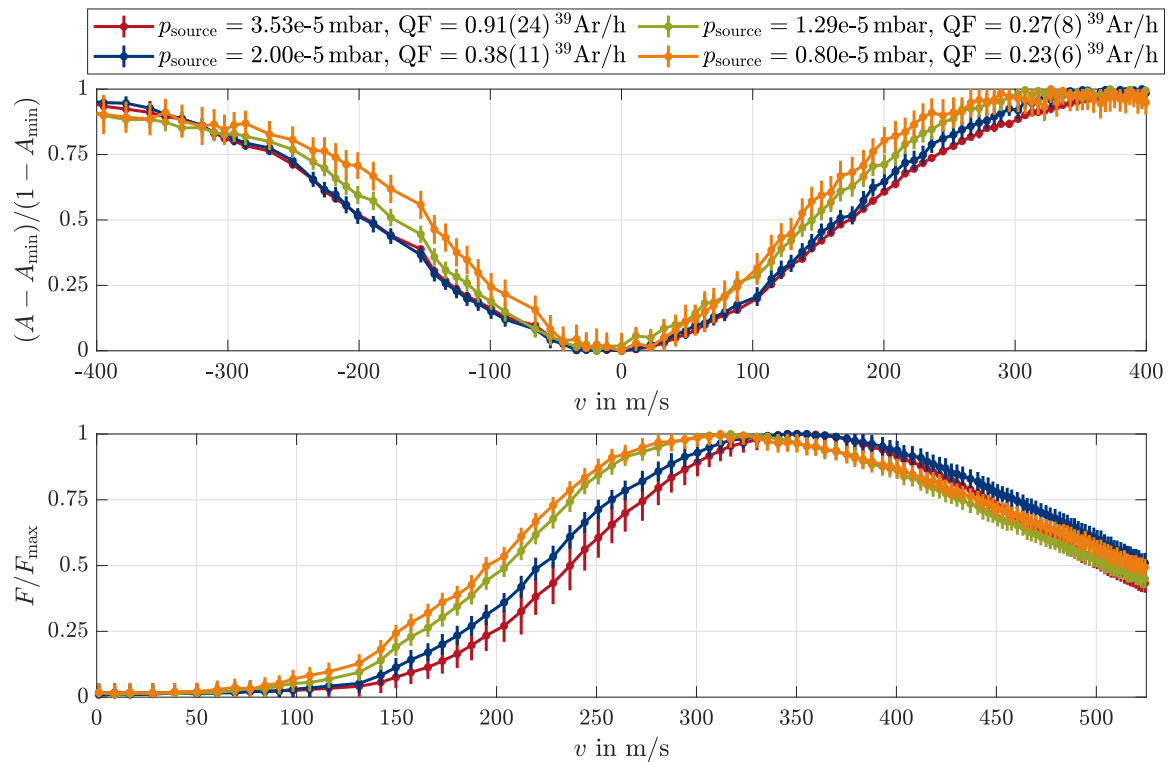


**Figure A.6:** Measurements of the pressure dependence of both transverse and longitudinal velocity distributions of the metastable atoms using the  $\text{LN}_2$ -can and the OR. The transverse velocity distribution broadens with increasing pressure, while the average longitudinal velocity increases. This increase is primarily due to a shift to larger velocities below the most likely. However, a slightly steeper drop at velocities above the most likely is visible. This is similar compared to the results obtained with the  $\text{LN}_2$ -dewar in figure 6.14, while, on the other hand, the whole distributions are pressure dependent shifted.

## B Environmental $^{39}\text{Ar}$ Dating Projects

An overview of conducted environmental  $^{39}\text{Ar}$  projects by the ArTTA collaboration during the time span of this work is given in the following. Some are discussed in more depth in the subsequent segments.

A timeline of the single  $^{39}\text{Ar}$  measurements is illustrated in B.1. They are grouped by their corresponding type. The upper subplot shows the measured count rate  $r$ . The contamination acceleration  $a$  in the middle subplot is derived from a measurement of nearly  $^{39}\text{Ar}$  free samples (dead), their surrounding references and further metrics [Ebs18]. The final concentration  $c$  of a single measurement of a sample is displayed in the lower subplot. Remarkable are measured concentrations well above the atmospheric value of  $1\text{R}_\text{A}$ . Such values have been obtained in the course of Lake Kivu or permafrost from Svalbard, for example.

### Leupa Ice Cave in the Julian Alps

The Leupa Ice Cave in the Canin-Kanin massive in the Julian Alps is located at an altitude of 2285 m above sea level (asl) [CG19]. It is a natural and dynamically active ice cave. However, the altitude of the mean annual 0 °C isotherm is estimated at 2370(90) m asl in the vicinity [Col+16]. Appropriately, the –2 °C isotherm, defining the boundary where environments are dominated by frost action, is even higher[CG19]. Its altitude is estimated to 2665(90) m asl, approximately 400m above the Leupa Ice Cave entrance [Col+16]. Therefore, a degradation of permafrost has been observed and is expected to further increase with ongoing climate change [CG19]. The formed and stored ice sheet in the Leupa Ice Cave provides various information and serves as a paleoclimatic archive. Dating the ice is critical to using the combined information for further research. Some taxon “*Zea mays*” pollen have been found in the deepest analyzed layer [Sch21]. As these are introduced from the American continent to Europe after 1492, an upper age limit can be defined. However, the  $^{39}\text{Ar}$  dating confines the ice sheet formation to the time period between 117 y and 54 y before 2018. Further details can be found in [Sch21].

### Lake Kivu on the border between Rwanda and DRC

Lake Kivu is a meromictic gas-rich lake [Sch21]. It is located on the border between the countries Rwanda and Democratic Republic of the Congo (DRC). The lake is strongly stratified mainly due to its vertical salinity profile (see figure B.2). Distortions of the stratification are discussed to cause limnic eruptions comparable to the disasters at Lake Nyos and Lake Monoun in Cameroun in 1986 and 1984, respectively. A limnic eruption

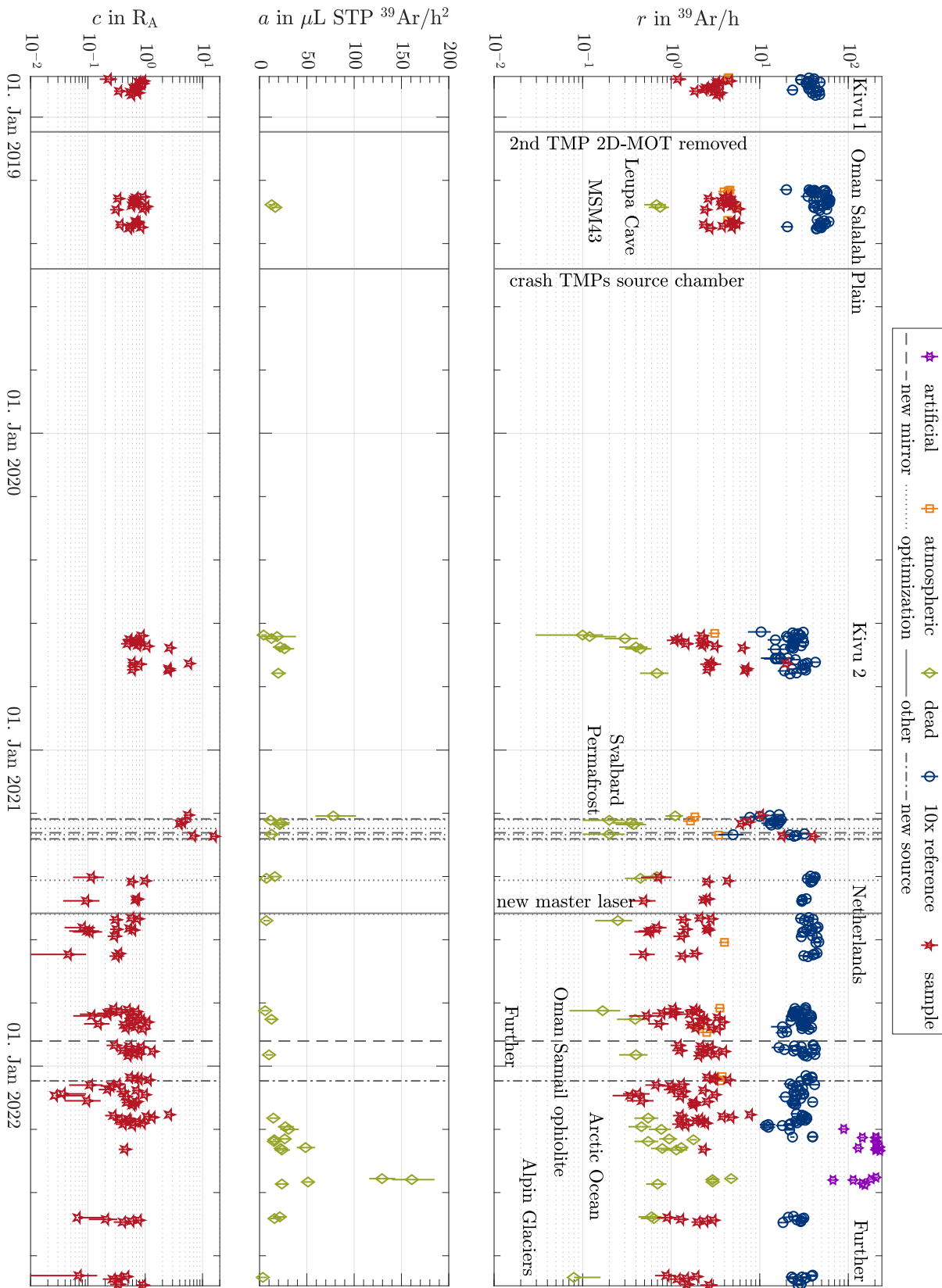


**Figure B.1:** Timeline of  $^{39}\text{Ar}$  measurements for various environmental projects conducted by the ArTTA collaboration. The upper subplot illustrates the measured count rate  $r$ , while the middle one elucidates the contamination acceleration  $a$ . The resulting sample concentrations  $c$  are shown at the lower subplot. Lines indicate some of the maintenance work.

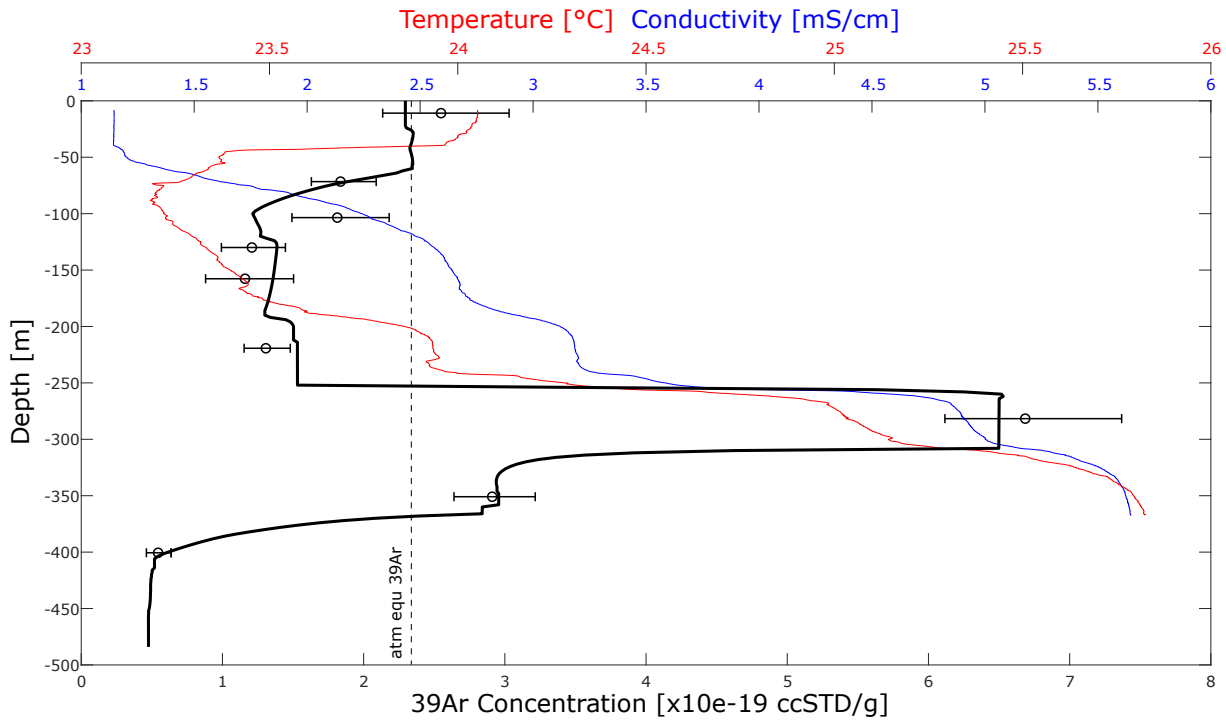


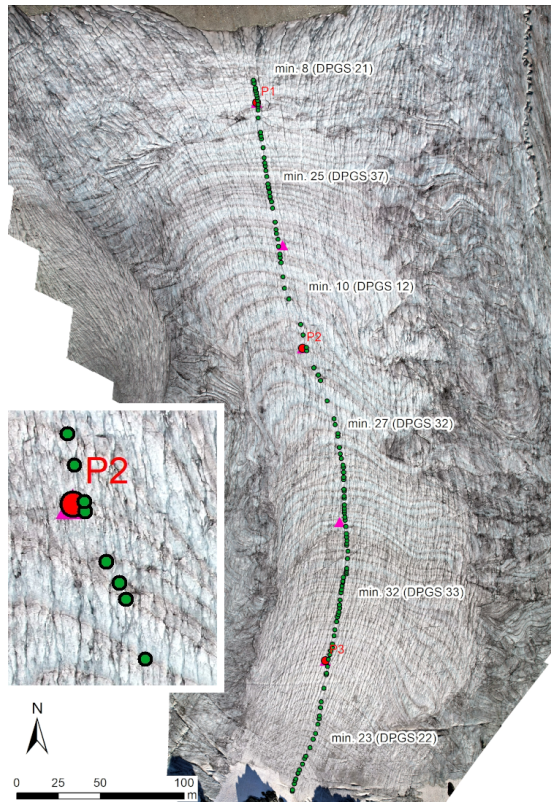
**Figure B.2:** Vertical profile of the  $^{39}\text{Ar}$  concentration results. The conductivity of the lake water and its temperature is a guide to the eye with respect to the stratification. The black line is the resulting concentration of the Simstrat simulation. This figure is provided by Schmidt.

is the release of most of the gas stored in the lake within a short time and consequently the oxygen concentration in the vicinity of the lake can drop causing suffocation and death to its residents. Therefore, understanding hydrodynamics is not only of interest for limnological research. The question of how old the water of the individual layers in the lake is was evident.

The research project, mainly conducted by Schmidt [Sch21], included two sampling campaigns. One in March 2018 and a second in June 2019. Water samples have been taken above the gas-rich zone and gas samples below a depth of 250 m. Surprisingly high  $^{39}\text{Ar}$  abundances of up to  $5.9_{-0.5}^{+0.6} \text{ R}_\text{A}$  are measured (see figure B.2). These concentrations far above atmospheric can be explained by groundwater intrusions with high  $^{39}\text{Ar}$  concentrations due to geogenically generated  $^{39}\text{Ar}$  [And+89; LLB89; Yok+13]. Lake Kivu is mainly fed by groundwater, which comes amongst others from the vicinity of the Nyiragongo volcano [Ros+15]. Its bedrock provides the necessary elements uranium, thorium and potassium for  $^{39}\text{Ar}$  production [Šrá+17; WG92; Cha+09; Sah73]. It was possible to determine the  $^{39}\text{Ar}$  concentrations of the groundwater intrusions using the one-dimensional hydrodynamic lake model Simstrat adapted to Lake Kivu including its known sublacustrine groundwater intrusions by Bärenbold, Kipfer, and Schmid [Bär20; BKS22]. Adapting the isotopic argon concentrations in order to reproduce the measured profile allowed to identify two multiple enriched aquifers [Sch21].

All in all, the ArTTA method has been successfully introduced for limnological research. New knowledge was gained about the water column of Lake Kivu and the volcanic groundwater system. A paper about the whole project containing the final results will be

**Figure B.3:** Bird's eye view of the Jamtalferner in Austria, near the border with Switzerland. The glacier surface is at an elevation of 2790 m at P3 (red dot) in the south and of 2708 m at P1 in the north. The well preserved stratification of this part of the glacier is clearly visible. The inset shows a magnification of the layers, which are tagged by green dots. The red dots indicate the position of level rods for mass loss discrimination. The purple triangles illustrate ice bloc sampling locations. The  $^{39}\text{Ar}$  age of these blocs is compared with the amount of layers between them. The height reference is GT Austria. The position of P2 is 190 874 m north and -12 911 m east with respect to MGII Austria GK West (EPSG: 31254).



submitted soon.

### Oman Salalah Plain Groundwater

The study in the Oman Salalah plain, mainly conducted by Rädle, focused on the application of multi-tracer groundwater dating and its analyses. Both models used suggest a composition of the groundwater with a very young component below 30 y and a very old component beyond 1000 y [Räd+22]. The reported findings are important estimating the groundwater renewal rate because freshwater is scarce there.

### Samail Ophiolite in the Sultanate of Oman

In the northeast of the Sultanate of Oman is the Samail ophiolite (or Al Hajar Mountains). In the face of climate change, ophiolites are possible carbon storage compartments. They are parts of the ocean crust tectonically exposed to land. The large amount of peridotite within the Samail ophiolite makes it interesting for carbon capture and storage (CCS) techniques, as it can theoretically store up to  $3 \times 10^4$  Gt of CO<sub>2</sub> if fully carbonated [KM08]. This corresponds to about 750 years of man made emissions. However, even if a full carbonization is unlikely, more realistic estimates of storing several thousand Gt of CO<sub>2</sub> [KM08] could still contribute to a significant change of the human aspect of global warming.

The  $^{39}\text{Ar}$  dating, mainly conducted by Meienburg [Mei22], of this collaborative project, focuses on the natural low temperature ( $\leq 150^\circ\text{C}$ ) peridotite alteration timescale. Therefore, water samples from several wells were analyzed. A characteristic  $^{39}\text{Ar}$  timescale of  $159^{+45}_{-29}$  y was found for the low temperature peridotite alteration [Mei22].

---

“This suggests that carbon storage via mineralization within the Samail ophiolite could be utilized to create a carbon sink able to significantly change the human aspect of climate change. [...] As the reaction rates seem to be sufficient to form a significant sink for CO<sub>2</sub> even at natural temperatures. This would therefore allow CCS storage in the Samail ophilite on a timescales which is necessary in order to meet the goals of the Paris Agreement.” [Mei22]

## Alpine Glacier Ice

Since the application of ArTTA on alpine glacier ice has been successfully demonstrated [Fen+19], further questions are currently being addressed as part of a collaborative project. Therefore, a first field trip has been performed to Austria in September 2021. Ice blocs of the Jamtalferner have been collected. Preliminary results verify the obtained <sup>39</sup>Ar age by comparison to the well-established annual layer counting (see figure B.3). However, this is only a first part of this project, mainly conducted by Wachs at the ArTTA side. Results on the diffusion of argon in ice as well as glaciological findings will be published soon.



# Acknowledgements

Many thanks to all who have contributed in any way to this thesis. I have learned a lot in this period. But above all, I don't want to miss the many new friends I made during this time.

I want to sincerely thank Markus Oberthaler for the opportunity to participate in this unique and multifaceted project. Thank you for the valuable discussions and the opportunity to deepen my knowledge and experience in so many areas.

Werner Aeschbach, thank you very much for being my second supervisor and the inspiring discussions about environmental physics. It was always a pleasure to attend one of your meetings.

Thank you, Selim Jochim, for taking the time to review this work.

A huge thank you goes out to the ArTTA team! It was, is and will be great to work with you on this in many ways special experiment. An overwhelming thank you goes to Lisa Ringena! She introduced me to the fascinating and quite complex world of ArTTA. I do not want to miss the first two years I worked with you in the container. It was a great time and yes, you definitely broadened my musical experience. Dear Maximilian Schmidt, the conversations with you were always a pleasure. Thank you so much for giving me all the different insights into Lake Kivu and much more. I like to think back to the one or other action in the lab or the unique running dinner. I hope we will meet again soon outside the virtual space. David Wachs, thank you for the discussions and support, especially in the final stages of my work. It is always a welcome distraction to explore with you the current problems in the lab. Our previous mountain trips in snow and ice have been a pleasure. I hope they were not the last. A big thank you for the profound proofreading. I thank Yannis Arck for the support in stressful times, his lectures about weather forecast models and the great stories about his expedition to the Arctic Ocean. Your proofreading was very helpful. The most traveled thank you goes to Florian Meienburg. It was always a wonderful time hanging around with you. You are a very thorough proof-reader. Thank you for organizing the first retreat and the passion you put into everything you do. Lasse Kundy, thank you for all the proofreading and the discussions about various topics. Thanks also to Niclas Mandaric for building the setup for the spatial production measurement and all the other support in the laboratory. Thank you Verena Oehmke for setting up the longitudinal velocity measurement. Thanks also to all the other students I had the opportunity to mentor! It was a lot of fun Sophie, Nicco, Magda and Mio. Last but not least a thank you to all students of the Institute for Environmental Physics for the great exchange!

## *Acknowledgements*

---

Andrea Fischer, Pascal Bohleber and Martin Stocker-Waldhuber, thank you very much for the informative and cool field trip to Jamtalferner and that you shared all your knowledge about glaciology!

To the fantastic crowd of Matterwave/SYNQS students: you can always be counted on. In lab questions, energetic and moral support, physics topics, celebrating breakfast, hanging around, celebrations of any kind and for any occasion.... Especially to Stefan Lannig, Maurus Hans and Yannick Deller for the physics discussions while writing this paper. Thank you Stefan for proofreading the one or other part.

Vielen, vielen Dank an die mechanische Werkstatt. Allen voran David Jansen für die vielen spannenden Gespräche, die Unterstützung beim Entwurf vom Dewar so wie vielem weiteren. Ebenfalls ein großes Dankeschön an Julia Bing und Christian Herdt, dass auf euch jederzeit Verlass ist.

Danke an alle Mitarbeitenden aus der elektronischen Werkstatt, welche in zahlreichen Gesprächen zur Entwicklung der ein oder anderen Platine beigetragen haben. Vielen Dank, dass ihr die meisten defekten Geräte wieder zum Laufen gebracht habt.

Vielen Dank an Christiane und Dagmar für euer offenes Ohr und die administrative Unterstützung in allen Fragen.

Vielen Dank an all die tollen Menschen, die ich während und durch meine Promotion in Heidelberg neu als Freunde kennen gelernt und gewonnen habe. Ich freue mich sehr darauf, mich nun wieder mehr Zeit euch und weniger dem Schreibtisch zu widmen. Vielen Dank hierbei vor allem an Franzi für das kurzfristige Korrekturlesen von Preface und Introduction.

Liebe Familie, ich bin sehr dankbar euch immer als stärkende Kraft in meinem Rücken zu wissen. Vielen Dank dafür, für die schöne Zeit, wenn wir uns sehen und einfach dafür, dass es euch gibt.

Liebe Jessie, unendlichen Dank für deine wunderbare Liebe, die viele Kraft und Unterstützung. Ohne dich hätte mich mein Weg vermutlich nie nach Heidelberg geführt. Thank you!

# Bibliography

## List of own publications

The following publication is used in this thesis.

- [Räd+22] Viola Rädle et al. “Multi-Tracer Groundwater Dating in Southern Oman Using Bayesian Modeling”. In: *Water Resources Research* 58.6 (2022). DOI: 10.1029/2021WR031776.

The following publications are not part of this work.

- [Dur+19] Aleksandar Duric et al. “Characterization of optical properties of aerosols for fire detection”. In: *EUSAS European Conference on Aerosols in the scope of fire detection*. Langenhagen, Germany, Feb. 2019.
- [Kel+20] Georgios A. Kelesidis et al. “Light scattering from nanoparticle agglomerates”. In: *Powder Technology* 365 (2020). SI: In honor of LS Fan, pp. 52–59. ISSN: 0032-5910. DOI: 10.1016/j.powtec.2019.02.003.
- [Rob+17] Julian Robertz et al. “Portable instrument for online investigations of optical properties of airborne particles”. In: *16th International Conference on Automatic Fire Detection AUBE’17 & 2017 Suppression, Detection, and Signaling Research and Applications Conference, SUPDET 2017*. Vol. 16. Hyattsville, MD, USA, Sept. 2017.

## References

- [AC98] Eric R.I. Abraham and Eric A. Cornell. “Teflon feedthrough for coupling optical fibers into ultrahigh vacuum systems”. In: *Appl. Opt.* 37.10 (Apr. 1998), pp. 1762–1763. DOI: 10.1364/AO.37.001762.
- [AG72] G C Angel and R A Giles. “The velocity distribution of atoms issuing from a multi-channel glass capillary array and its implication on the measurement of atomic beam scattering cross sections”. In: *Journal of Physics B: Atomic and Molecular Physics* 5.1 (Jan. 1972), p. 80. DOI: 10.1088/0022-3700/5/1/018.
- [All19] Allied Vision Technologies. *Mako G-223B NIR - EMVA1288 Data*. Stadtroda, Germany: Allied Vision Technologies, 2019.

- [All22] Allied Vision Technologies. *Mako G-223B NIR - DataSheet*. V1.0.1. Stadtroda, Germany: Allied Vision Technologies, Aug. 2022.
- [And+89] J.N Andrews et al. “The in situ production of radioisotopes in rock matrices with particular reference to the Stripa granite”. In: *Geochimica et Cosmochimica Acta* 53.8 (1989), pp. 1803–1815. ISSN: 0016-7037. DOI: 10.1016/0016-7037(89)90301-3.
- [AVV72] Yu. G. Abashev, G. F. Voronin, and R. A. Valitov. “Velocity distribution in an atomic beam”. In: *Measurement Techniques* 15 (Nov. 1972), pp. 1679–1681. DOI: 10.1007/BF00813391.
- [Bär20] Fabian Bärenbold. “Managing Lake Kivu: moving from a steady-state to a dynamic modelling approach”. PhD thesis. Zurich, Switzerland: Swiss Federal Institute Technology ETHZ, 2020.
- [Bee52] August Beer. “Bestimmung der Absorption des rothen Lichts in farbigen Flüssigkeiten”. In: *Annalen der Physik* 162.5 (1852), pp. 78–88. DOI: 10.1002/andp.18521620505.
- [Bel+09] Sergey G. Belostotskiy et al. “Spatially Resolved Measurements of Argon Metastable ( $1s_5$ ) Density in a High Pressure Microdischarge Using Diode Laser Absorption Spectroscopy”. In: *IEEE Transactions on Plasma Science* 37.6 (2009), pp. 852–858. DOI: 10.1109/TPS.2009.2015949.
- [Ben+08] Michael L. Bender et al. “The contemporary degassing rate of  $^{40}\text{Ar}$  from the solid Earth”. In: *Proceedings of the National Academy of Sciences* 105.24 (2008), pp. 8232–8237. DOI: 10.1073/pnas.0711679105.
- [BG95] A. Bogaerts and R. Gijbels. “Modeling of metastable argon atoms in a direct-current glow discharge”. In: *Phys. Rev. A* 52 (5 Nov. 1995), pp. 3743–3751. DOI: 10.1103/PhysRevA.52.3743.
- [BKS22] Fabian Bärenbold, Rolf Kipfer, and Martin Schmid. “Dynamic modelling provides new insights into development and maintenance of Lake Kivu’s density stratification”. In: *Environmental Modelling & Software* 147 (2022), p. 105251. ISSN: 1364-8152. DOI: 10.1016/j.envsoft.2021.105251.
- [BP07] Heinz-Peter Breuer and Francesco Petruccione. *The Theory of Open Quantum Systems*. Oxford University Press, Jan. 2007. ISBN: 9780199213900. DOI: 10.1093/acprof:oso/9780199213900.001.0001.
- [Bra99] J. R. Brandenberger. “Landé  $g_J$  values in atomic argon: A measurement of the ratio  $g_J(2p_9)/g_J(1s_5)$  by saturation spectroscopy”. In: *Phys. Rev. A* 60 (2 Aug. 1999), pp. 1336–1340. DOI: 10.1103/PhysRevA.60.1336.
- [Cal+22] Lauren K. Callahan et al. “Initial tests of Accelerator Mass Spectrometry with the Argonne Gas-Filled Analyzer and the commissioning of the MONICA detector”. In: *Nuclear Instruments and Methods in Physics Research Section B: Beam Interactions with Materials and Atoms* 532 (2022), pp. 7–12. ISSN: 0168-583X. DOI: 10.1016/j.nimb.2022.09.009.
- [Car+17] Ian Cartwright et al. “A review of radioactive isotopes and other residence time tracers in understanding groundwater recharge: Possibilities, challenges, and limitations”. In: *Journal of Hydrology* 555 (2017), pp. 797–811. ISSN: 0022-1694. DOI: 10.1016/j.jhydrol.2017.10.053.

- 
- [CC81] A. Chutjian and D. C. Cartwright. “Electron-impact excitation of electronic states in argon at incident energies between 16 and 100 eV”. In: *Phys. Rev. A* 23 (5 May 1981), pp. 2178–2193. DOI: [10.1103/PhysRevA.23.2178](https://doi.org/10.1103/PhysRevA.23.2178).
- [CG02] D. Crecraft and S. Gergely. *Analog Electronics: Circuits, Systems and Signal Processing*. Elsevier Science, 2002. ISBN: 9780080475837.
- [CG19] Renato R. Colucci and Mauro Guglielmin. “Climate change and rapid ice melt: Suggestions from abrupt permafrost degradation and ice melting in an alpine ice cave”. In: *Progress in Physical Geography: Earth and Environment* 43.4 (2019), pp. 561–573. DOI: [10.1177/0309133319846056](https://doi.org/10.1177/0309133319846056).
- [Cha+09] Ramananda Chakrabarti et al. “Isotopic and geochemical evidence for a heterogeneous mantle plume origin of the Virunga volcanics, Western rift, East African Rift system”. In: *Chemical Geology* 259.3 (2009), pp. 273–289. ISSN: 0009-2541. DOI: [10.1016/j.chemgeo.2008.11.010](https://doi.org/10.1016/j.chemgeo.2008.11.010).
- [Che+20] Zhe Cheng et al. “Experimental observation of high intrinsic thermal conductivity of AlN”. In: *Phys. Rev. Mater.* 4 (4 Apr. 2020), p. 044602. DOI: [10.1103/PhysRevMaterials.4.044602](https://doi.org/10.1103/PhysRevMaterials.4.044602).
- [Che+99] C. Y. Chen et al. “Ultrasensitive Isotope Trace Analyses with a Magneto-Optical Trap”. In: *Science* 286.5442 (1999), pp. 1139–1141. DOI: [10.1126/science.286.5442.1139](https://doi.org/10.1126/science.286.5442.1139).
- [Che18] J. Chen. “Nuclear Data Sheets for A=39”. In: *Nuclear Data Sheets* 149 (2018), pp. 1–251. ISSN: 0090-3752. DOI: [10.1016/j.nds.2018.03.001](https://doi.org/10.1016/j.nds.2018.03.001).
- [Chu+22] Y.-Q. Chu et al. “Optically enhanced discharge excitation and trapping of  $^{39}\text{Ar}$ ”. In: *Phys. Rev. A* 105 (6 June 2022), p. 063108. DOI: [10.1103/PhysRevA.105.063108](https://doi.org/10.1103/PhysRevA.105.063108).
- [Col+04] Ph Collon et al. “Development of an AMS method to study oceanic circulation characteristics using cosmogenic  $^{39}\text{Ar}$ ”. In: *Nuclear Instruments and Methods in Physics Research Section B: Beam Interactions with Materials and Atoms* 223-224 (2004). Proceedings of the Ninth International Conference on Accelerator Mass Spectrometry, pp. 428–434. ISSN: 0168-583X. DOI: [10.1016/j.nimb.2004.04.081](https://doi.org/10.1016/j.nimb.2004.04.081).
- [Col+16] R.R. Colucci et al. “Rock glaciers, protalus ramparts and pronival ramparts in the south-eastern Alps”. In: *Geomorphology* 269 (2016), pp. 112–121. ISSN: 0169-555X. DOI: [10.1016/j.geomorph.2016.06.039](https://doi.org/10.1016/j.geomorph.2016.06.039).
- [DBG99] Arati Dasgupta, M. Blaha, and J. L. Giuliani. “Electron-impact excitation from the ground and the metastable levels of Ar I”. In: *Phys. Rev. A* 61 (1 Dec. 1999), p. 012703. DOI: [10.1103/PhysRevA.61.012703](https://doi.org/10.1103/PhysRevA.61.012703).
- [Den+14] K. Deng et al. “A modified model of helical resonator with predictable loaded resonant frequency and Q-factor”. In: *Review of Scientific Instruments* 85.10 (2014), p. 104706. DOI: [10.1063/1.4897478](https://doi.org/10.1063/1.4897478).
- [DPS99] G. D’Amico, G. Pesce, and A. Sasso. “Field shift analysis of visible and near-infrared argon transitions”. In: *J. Opt. Soc. Am. B* 16.7 (July 1999), pp. 1033–1038. DOI: [10.1364/JOSAB.16.001033](https://doi.org/10.1364/JOSAB.16.001033).

- [Dra69] H. W. Drawin. “Influence of atom-atom collisions on the collisional-radiative ionization and recombination coefficients of hydrogen plasmas”. In: *Zeitschrift für Physik A Hadrons and nuclei* 225 (5 Oct. 1969), pp. 483–493. DOI: 10.1007/BF01392775.
- [Du+03] X. Du et al. “A new method of measuring  $^{81}\text{Kr}$  and  $^{85}\text{Kr}$  abundances in environmental samples”. In: *Geophysical Research Letters* 30.20 (2003). DOI: 10.1029/2003GL018293.
- [Ebs+18] Sven Ebser et al. “ $^{39}\text{Ar}$  dating with small samples provides new key constraints on ocean ventilation”. In: *Nature Communications* 9.1 (Nov. 2018), p. 5046. ISSN: 2041-1723. DOI: 10.1038/s41467-018-07465-7.
- [Ebs12] Sven Ebser. “Optimierung und Stabilisierung von  $^{39}\text{Ar}$ -ATTA bis hin zur erstmaligen Anwendung auf die Datierung natürlicher Wasserproben”. Diplom Thesis. Heidelberg, Germany: Ruperto-Carola University of Heidelberg, 2012.
- [Ebs18] Sven C. Ebser. “Dating of Ice and Ocean Samples with Atom Trap Trace Analysis of  $^{39}\text{Ar}$ ”. PhD thesis. Heidelberg, Germany: Ruperto-Carola University of Heidelberg, 2018.
- [Ein05] A. Einstein. “Über die von der molekularkinetischen Theorie der Wärme geforderte Bewegung von in ruhenden Flüssigkeiten suspendierten Teilchen”. In: *Annalen der Physik* 322.8 (1905), pp. 549–560. DOI: 10.1002/andp.19053220806.
- [ESS47] I. Estermann, O. C. Simpson, and O. Stern. “The Free Fall of Atoms and the Measurement of the Velocity Distribution in a Molecular Beam of Cesium Atoms”. In: *Phys. Rev.* 71 (4 Feb. 1947), pp. 238–249. DOI: 10.1103/PhysRev.71.238.
- [Fen+17] Z. Feng et al. “Bichromatic force on metastable argon for atom-trap trace analysis”. In: *Phys. Rev. A* 96 (1 July 2017), p. 013424. DOI: 10.1103/PhysRevA.96.013424.
- [Fen+19] Zhongyi Feng et al. “Dating glacier ice of the last millennium by quantum technology”. In: *Proceedings of the National Academy of Sciences* 116.18 (2019), pp. 8781–8786. DOI: 10.1073/pnas.1816468116.
- [Fen12] Zhongyi Feng. “Implementierung einer Atomflussüberwachung für  $^{39}\text{Ar}$  ATTA”. Bachelor Thesis. Heidelberg, Germany: Ruperto-Carola University of Heidelberg, 2012.
- [Fen18] Zhongyi Feng. “Quantum technological dating of glacier ice from the last millennium and a new self-contained facility for routine measurements”. PhD thesis. Heidelberg, Germany: Ruperto-Carola University of Heidelberg, 2018.
- [FK67] Robert S. Freund and William Klemperer. “Molecular Beam Time-of-Flight Measurements for the Study of Metastable and Repulsive Electronic States”. In: *The Journal of Chemical Physics* 47.8 (1967), pp. 2897–2904. DOI: 10.1063/1.1712313.
- [FLR85] C. M. Ferreira, J. Loureiro, and A. Ricard. “Populations in the metastable and the resonance levels of argon and stepwise ionization effects in a low-pressure argon positive column”. In: *Journal of Applied Physics* 57.1 (1985), pp. 82–90. DOI: 10.1063/1.335400.

- 
- [Fox06] M. Fox. *Quantum Optics: An Introduction*. Oxford Master Series in Physics. OUP Oxford, 2006. ISBN: 9780198566731.
- [FR83] C. M. Ferreira and A. Ricard. “Modelling of the low-pressure argon positive column”. In: *Journal of Applied Physics* 54.5 (1983), pp. 2261–2271. DOI: 10.1063/1.332380.
- [Frö15] Anika Frölian. “Optisches Pumpen über das transiente  $2p^6$ -Niveau zur Erhöhung der Dichte von metastabilem Argon in einer RF-Gasentladung”. Bachelor Thesis. Heidelberg, Germany: Ruperto-Carola University of Heidelberg, 2015.
- [Gre15] Andrei Grebennikov. *RF and Microwave Power Amplifier Design*. McGraw-Hill professional engineering. McGraw-Hill Education, 2015. ISBN: 978-0-07-182863-5.
- [Gri99] D. J. Griffiths. *Introduction to Electrodynamics*. Pearson international edition. Prentice Hall, 1999. ISBN: 9780139199608.
- [Gu+21] Ji-Qiang Gu et al. “Reconstruction of the atmospheric  $^{39}\text{Ar}/\text{Ar}$  history”. In: *Chemical Geology* 583 (2021), p. 120480. ISSN: 0009-2541. DOI: 10.1016/j.chemgeo.2021.120480.
- [Gu+22] Ji-Qiang Gu et al. “Estimation of the Ventilation Transit Time Distribution at the Yap-Mariana Junction Using  $^{39}\text{Ar}$ ,  $^{85}\text{Kr}$  and  $^{14}\text{C}$  Tracers”. In: *Journal of Geophysical Research: Oceans* 127.7 (2022), e2022JC018417. DOI: 10.1029/2022JC018417.
- [Hag09] Jon B. Hagen. *Radio-Frequency Electronics: Circuits and Applications*. 2nd ed. Cambridge University Press, 2009. DOI: 10.1017/CBO9780511626951.
- [Han14] Maurus Hans. “Optisches Pumpen zur Erhöhung der Dichte von metastabilem Argon in einer RF-Gasentladung”. Bachelor Thesis. Heidelberg, Germany: Ruperto-Carola University of Heidelberg, 2014.
- [Hay+09] Y Hayashi et al. “Argon metastable state densities in inductively coupled plasma in mixtures of Ar and O<sub>2</sub>”. In: *Journal of Physics D: Applied Physics* 42.14 (July 2009), p. 145206. DOI: 10.1088/0022-3727/42/14/145206.
- [HM00] G. A. Hebner and P. A. Miller. “Behavior of excited argon atoms in inductively driven plasmas”. In: *Journal of Applied Physics* 87.12 (2000), pp. 8304–8315. DOI: 10.1063/1.373542.
- [IAE22] IAEA - Nuclear Data Section. *LiveChart of Nuclides*. 2022. URL: <https://www-nds.iaea.org/relnsd/vcharthtml/VChartHTML.html> (visited on 11/27/2022).
- [Jia+11] W. Jiang et al. “ $^{39}\text{Ar}$  Detection at the  $10^{-16}$  Isotopic Abundance Level with Atom Trap Trace Analysis”. In: *Phys. Rev. Lett.* 106 (10 Mar. 2011), p. 103001. DOI: 10.1103/PhysRevLett.106.103001.
- [Jia+12] W. Jiang et al. “An atom counter for measuring  $^{81}\text{Kr}$  and  $^{85}\text{Kr}$  in environmental samples”. In: *Geochimica et Cosmochimica Acta* 91 (2012), pp. 1–6. ISSN: 0016-7037. DOI: 10.1016/j.gca.2012.05.019.
- [Jia+20] Z. H. Jia et al. “An electromagnetic separation system for the enrichment of  $^{39}\text{Ar}$ ”. In: *Review of Scientific Instruments* 91.3 (2020), p. 033309. DOI: 10.1063/1.5128697.

- [Kau11] Christoph Kaup. *Single-Atom Detection of  $^{39}\text{Ar}$* . Diplom Thesis. Heidelberg, Germany, 2011.
- [Kir45] Gustav R. Kirchhoff. “Ueber den Durchgang eines elektrischen Stromes durch eine Ebene, insbesondere durch eine kreisförmige”. In: *Annalen der Physik* 140.4 (1845), pp. 497–514. DOI: [doi.org/10.1002/andp.18451400402](https://doi.org/10.1002/andp.18451400402).
- [KM08] Peter B. Kelemen and Jürg Matter. “In situ carbonation of peridotite for CO<sub>2</sub> storage”. In: *Proceedings of the National Academy of Sciences* 105.45 (2008), pp. 17295–17300. DOI: [10.1073/pnas.0805794105](https://doi.org/10.1073/pnas.0805794105).
- [Kra+22] A. Kramida et al. *NIST Atomic Spectra Database*. 2022. DOI: [10.18434/T4W30F](https://doi.org/10.18434/T4W30F). (Visited on 11/25/2022).
- [KS93] Hidetoshi Katori and Fujio Shimizu. “Lifetime measurement of the  $1s_5$  metastable state of argon and krypton with a magneto-optical trap”. In: *Phys. Rev. Lett.* 70 (23 June 1993), pp. 3545–3548. DOI: [10.1103/PhysRevLett.70.3545](https://doi.org/10.1103/PhysRevLett.70.3545).
- [Kun23] Lasse Kundy. “Working Title: Argon Trap Trace Analysis – Investigation of Repumper Frequencies and Improved Transverse Laser Cooling”. unpublished Master Thesis. Heidelberg, Germany: Ruperto-Carola University of Heidelberg, 2023.
- [Lee+06] Jee-Yon Lee et al. “A redetermination of the isotopic abundances of atmospheric Ar”. In: *Geochimica et Cosmochimica Acta* 70.17 (2006), pp. 4507–4512. ISSN: 0016-7037. DOI: [10.1016/j.gca.2006.06.1563](https://doi.org/10.1016/j.gca.2006.06.1563).
- [LL05] Michael A. Lieberman and Allan J. Lichtenberg. *Principles of Plasma Discharges and Materials Processing*. John Wiley & Sons, Ltd, 2005. ISBN: 9780471724254. DOI: [10.1002/0471724254](https://doi.org/10.1002/0471724254).
- [LLB89] H.H. Loosli, B.E. Lehmann, and W. Balderer. “Argon-39, argon-37 and krypton-85 isotopes in Stripa groundwaters”. In: *Geochimica et Cosmochimica Acta* 53.8 (1989), pp. 1825–1829. ISSN: 0016-7037. DOI: [10.1016/0016-7037\(89\)90303-7](https://doi.org/10.1016/0016-7037(89)90303-7).
- [LLF90] Michael A. Lieberman, Allan J. Lichtenberg, and D.L. Flamm. *Theory of a Helical Resonator Plasma Source*. Tech. rep. UCB/ERL M90/10. EECS Department, University of California, Berkeley, Feb. 1990.
- [LM81] V. S. Letokhov and V. G. Minogin. “Laser radiation pressure on free atoms”. In: *Physics Reports* 73.1 (1981), pp. 1–65. ISSN: 0370-1573. DOI: [10.1016/0370-1573\(81\)90116-2](https://doi.org/10.1016/0370-1573(81)90116-2).
- [LO68] H.H. Loosli and H. Oeschger. “Detection of  $^{39}\text{Ar}$  in atmospheric argon”. In: *Earth and Planetary Science Letters* 5 (1968), pp. 191–198. ISSN: 0012-821X. DOI: [10.1016/S0012-821X\(68\)80039-1](https://doi.org/10.1016/S0012-821X(68)80039-1).
- [Loc+16] E. H. Lock et al. “Electron beam-generated Ar/N<sub>2</sub> plasmas: The effect of nitrogen addition on the brightest argon emission lines”. In: *Physics of Plasmas* 23.4 (2016), p. 043518. DOI: [10.1063/1.4946880](https://doi.org/10.1063/1.4946880).
- [Loo83] H.H. Loosli. “A dating method with  $^{39}\text{Ar}$ ”. In: *Earth and Planetary Science Letters* 63.1 (1983), pp. 51–62. ISSN: 0012-821X. DOI: [10.1016/0012-821X\(83\)90021-3](https://doi.org/10.1016/0012-821X(83)90021-3).

- 
- [Man22] Niclas V. Mandaric. “Characterization of the spatially dependent metastable argon production in a RF-discharge source”. Bachelor Thesis. Heidelberg, Germany: Ruperto-Carola University of Heidelberg, 2022.
- [Mar+21] Emilio Martines et al. “The Helical Resonator: A Scheme for Radio Frequency Plasma Generation”. In: *Applied Sciences* 11.16 (2021). ISSN: 2076-3417. DOI: 10.3390/app11167444.
- [Mei22] Florian Meienburg. “<sup>39</sup>Ar groundwater study in the Samail ophiolite, Oman in the context of carbon sequestration”. Master Thesis. Heidelberg, Germany: Ruperto-Carola University of Heidelberg, 2022.
- [Mes10] Dieter Meschede. *Gerthsen Physik*. 24th ed. Springer Berlin, Heidelberg, Sept. 2010. ISBN: 978-3-642-12894-3. DOI: 10.1007/978-3-642-12894-3.
- [Met] Metoxit AG. *Oxidkeramik mit Leidenschaft*. Thayngen, Switzerland: Metoxit AG. URL: <https://metoxit.com/assets/Uploads/Metoxit-Materialubersicht-de.pdf> (visited on 11/16/2022).
- [MI 18] M&I Materials Ltd. *Apiezon N Grease, Cryogenic High Vacuum Grease*. Manchester, United Kingdom: M&I Materials Ltd., Jan. 2018. URL: [https://static.mimaterials.com/apiezon/DocumentLibrary/TechnicalDatasheets/Apiezon\\_N\\_Cryogenic\\_High\\_Vacuum\\_Grease\\_Datasheet.pdf](https://static.mimaterials.com/apiezon/DocumentLibrary/TechnicalDatasheets/Apiezon_N_Cryogenic_High_Vacuum_Grease_Datasheet.pdf) (visited on 06/05/2019).
- [Mina] Mini-Circuits. *Coaxial High Power Amplifier ZHL-100W-52-S+*. Brooklyn, New York, United States: Mini-Circuits. URL: <https://www.minicircuits.com/pdfs/ZHL-100W-52-S+.pdf> (visited on 08/08/2022).
- [Minb] Mini-Circuits. *Coaxial Power Detector ZX47-40+ and ZX47-40LN+*. Brooklyn, New York, United States: Mini-Circuits. URL: <https://www.minicircuits.com/pdfs/ZX47-40+.pdf> (visited on 08/08/2022).
- [Moo+04] I. D. Moore et al. “Counting Individual <sup>41</sup>Ca Atoms with a Magneto-Optical Trap”. In: *Phys. Rev. Lett.* 92 (15 Apr. 2004), p. 153002. DOI: 10.1103/PhysRevLett.92.153002.
- [MS59] W. W. Macalpine and R. O. Schildknecht. “Coaxial Resonators with Helical Inner Conductor”. In: *Proceedings of the IRE* 47.12 (1959), pp. 2099–2105. DOI: 10.1109/JRPROC.1959.287128.
- [MS99] Harold J. Metcalf and Peter Straten. *Laser Cooling and Trapping*. Graduate Texts in Contemporary Physics. Springer New York, 1999. ISBN: 978-0-387-98747-7. DOI: 10.1007/978-1-4612-1470-0.
- [Nat] National Institute of Standards and Technology. *Material Properties: 304 Stainless (UNS S30400)*. URL: [https://trc.nist.gov/cryogenics/materials/304Stainless/304Stainless\\_rev.htm](https://trc.nist.gov/cryogenics/materials/304Stainless/304Stainless_rev.htm) (visited on 06/05/2019).
- [Nat10] National Institute of Standards and Technology. *Material Properties: OFHC Copper (UNS C10100/C10200)*. 2010. URL: [https://trc.nist.gov/cryogenics/materials/OFHC%20Copper/OFHC\\_Copper\\_rev1.htm](https://trc.nist.gov/cryogenics/materials/OFHC%20Copper/OFHC_Copper_rev1.htm) (visited on 06/05/2019).
- [Nia+94] K Niazi et al. “Operation of a helical resonator plasma source”. In: *Plasma Sources Science and Technology* 3.4 (Nov. 1994), p. 482. DOI: 10.1088/0963-0252/3/4/005.

- [NSH85] T. Nemoto, S. Sasaki, and Y. Hakuraku. “Thermal conductivity of alumina and silicon carbide ceramics at low temperatures”. In: *Cryogenics* 25.9 (1985), pp. 531–532. ISSN: 0011-2275. DOI: 10.1016/0011-2275(85)90080-3.
- [Olv+10] F.W.J. Olver et al. *NIST Handbook of Mathematical Functions Hardback and CD-ROM*. Cambridge University Press, 2010. ISBN: 9780521192255.
- [Oxe20] Jonathan Oxer. *Datalogging with MQTT, Node-RED, InfluxDB, and Grafana*. 2020. URL: [https://youtu.be/ffg3\\_1AgtyA](https://youtu.be/ffg3_1AgtyA) (visited on 04/13/2022).
- [Ped+18] Laura Pedrosa-Rodriguez et al. “Design, development and testing of a helical resonator for trapping Sr<sup>+</sup> ions for frequency standards and sensing applications”. In: *Measurement* 125 (2018), pp. 156–162. ISSN: 0263-2241. DOI: 10.1016/j.measurement.2018.04.086.
- [PK97] Jong-Chul Park and Bongkoo Kang. “Impedance model of helical resonator discharge”. In: *IEEE Transactions on Plasma Science* 25.6 (1997), pp. 1398–1405. DOI: 10.1109/27.650909.
- [PLK00] Jong-Chul Park, Jae Koo Lee, and Bongkoo Kang. “Properties of inductively coupled plasma source with helical coil”. In: *IEEE Transactions on Plasma Science* 28.2 (2000), pp. 403–413. DOI: 10.1109/27.848099.
- [PS84] J. H. Poynting and John William Strutt. “XV. On the transfer of energy in the electromagnetic field”. In: *Philosophical Transactions of the Royal Society of London* 175 (1884), pp. 343–361. DOI: 10.1098/rstl.1884.0016.
- [PWT62] R. W. Powell, Margaret J. Woodman, and R. P. Tye. “The thermal conductivity and electrical resistivity of indium, *Philosophical Magazine*”. In: *Philosophical Magazine*. Philosophical Magazine 7.79 (1962), pp. 1183–1186. ISSN: 0031-8086. DOI: 10.1080/14786436208209118.
- [Räd+22] Viola Rädle et al. “Multi-Tracer Groundwater Dating in Southern Oman Using Bayesian Modeling”. In: *Water Resources Research* 58.6 (2022). DOI: 10.1029/2021WR031776.
- [Ram85] Norman F. Ramsey. *Molecular Beams*. International series of monographs on physics. OUP Oxford, 1985. ISBN: 0198520212.
- [RDS74] R. D. Rundel, F. B. Dunning, and R. F. Stebbings. “Velocity distributions in metastable atom beams produced by coaxial electron impact”. In: *Review of Scientific Instruments* 45.1 (1974), pp. 116–119. DOI: 10.1063/1.1686422.
- [Rin16] Lisa Ringena. “Optimization of <sup>39</sup>Ar-ATTA with new Laser System and a Double-Frequency Magneto-Optical Trap”. Master Thesis. Heidelberg, Germany: Ruperto-Carola University of Heidelberg, 2016.
- [Rin21] Lisa E. Ringena. “Demonstration of a Dual Atom Trap Trace Analysis Setup for <sup>39</sup>Ar and <sup>85</sup>Kr”. PhD thesis. Heidelberg, Germany: Ruperto-Carola University of Heidelberg, 2021.
- [Rit+14] F. Ritterbusch et al. “Groundwater dating with Atom Trap Trace Analysis of <sup>39</sup>Ar”. In: *Geophysical Research Letters* 41.19 (2014), pp. 6758–6764. DOI: 10.1002/2014GL061120.
- [Rit+22] Florian Ritterbusch et al. “A Tibetan ice core covering the past 1,300 years radiometrically dated with <sup>39</sup>Ar”. In: *Proceedings of the National Academy of Sciences* 119.40 (2022), e2200835119. DOI: 10.1073/pnas.2200835119.

- 
- [Rit09] Florian Ritterbusch. *Dating of groundwater with Atom Trap Trace Analysis of  $^{39}\text{Ar}$* . Diplom Thesis. Heidelberg, Germany, 2009.
- [Rit13] Florian Ritterbusch. “Dating of groundwater with Atom Trap Trace Analysis of  $^{39}\text{Ar}$ ”. PhD thesis. Heidelberg, Germany: Ruperto-Carola University of Heidelberg, 2013.
- [RK97] Shahid Rauf and Mark J. Kushner. “Argon metastable densities in radio frequency Ar, Ar/O<sub>2</sub> and Ar/CF<sub>4</sub> electrical discharges”. In: *Journal of Applied Physics* 82.6 (1997), pp. 2805–2813. DOI: 10.1063/1.366111.
- [RLM09] Kenneth Rudinger, Zheng-Tian Lu, and Peter Mueller. “The role of carrier gases in the production of metastable argon atoms in a rf discharge”. In: *Review of Scientific Instruments* 80.3 (2009), p. 036105. DOI: 10.1063/1.3105722.
- [Ros+15] Kelly Ann Ross et al. “Characterisation of the Subaqueous Groundwater Discharge That Maintains the Permanent Stratification within Lake Kivu; East Africa”. In: *PLOS ONE* 10 (Mar. 2015), pp. 1–21. DOI: 10.1371/journal.pone.0121217.
- [Sah73] Th. G. Sahama. “Evolution of the Nyiragongo Magma”. In: *Journal of Petrology* 14.1 (Feb. 1973), pp. 33–48. ISSN: 0022-3530. DOI: 10.1093/petrology/14.1.33.
- [Sch+85] Reiner Schlitzer et al. “A meridional  $^{14}\text{C}$  and  $^{39}\text{Ar}$  section in northeast Atlantic deep water”. In: *Journal of Geophysical Research: Oceans* 90.C4 (1985), pp. 6945–6952. DOI: 10.1029/JC090iC04p06945.
- [Sch02] R. Schmitt. *Electromagnetics Explained: A Handbook for Wireless/ RF, EMC, and High-Speed Electronics*. EDN Series for Design Engineers. Elsevier Science, 2002. ISBN: 9780080505237.
- [Sch21] Maximilian Schmidt. “Investigations of Lake Kivu with  $^{39}\text{Ar}$  Atom Trap Trace Analysis”. PhD thesis. Heidelberg, Germany: Ruperto-Carola University of Heidelberg, 2021.
- [Sch22] Sophie Schwenzler. “Composition and Characterisation of an Absolute Metastable  $^{40}\text{Ar}$  Flux Measurement”. Bachelor Thesis. Heidelberg, Germany: Ruperto-Carola University of Heidelberg, 2022.
- [Sem] Semrock, Inc. *830 nm RazorEdge® ultrasteep long-pass edge filter*. URL: <https://www.semrock.com/filterdetails.aspx?id=lp02-830ru-25> (visited on 06/24/2021).
- [SGH81] H Abu Safia, J P Grandin, and X Husson. “g factor measurements for Ne, Ar and Kr”. In: *Journal of Physics B: Atomic and Molecular Physics* 14.18 (Sept. 1981), p. 3363. DOI: 10.1088/0022-3700/14/18/008.
- [Siv+12] J. D. Sivers et al. “On the application of radio frequency voltages to ion traps via helical resonators”. In: *Applied Physics B* 107 (2012), pp. 921–934. DOI: 10.1007/s00340-011-4837-0.
- [Spr+19] Matthias Sprenger et al. “The Demographics of Water: A Review of Water Ages in the Critical Zone”. In: *Reviews of Geophysics* 57.3 (2019), pp. 800–834. DOI: 10.1029/2018RG000633.

- [Šrá+17] Ondřej Šrámek et al. “Subterranean production of neutrons,  $^{39}\text{Ar}$  and  $^{21}\text{Ne}$ : Rates and uncertainties”. In: *Geochimica et Cosmochimica Acta* 196 (2017), pp. 370–387. ISSN: 0016-7037. DOI: 10.1016/j.gca.2016.09.040.
- [SSK65] R. W. Stoenner, O. A. Schaeffer, and S. Katcoff. “Half-Lives of Argon-37, Argon-39, and Argon-42”. In: *Science* 148.3675 (1965), pp. 1325–1328. DOI: 10.1126/science.148.3675.1325.
- [Ten+22] Jonathan Tennyson et al. “The 2021 release of the Quantemol database (QDB) of plasma chemistries and reactions”. In: *Plasma Sources Science and Technology* 31.9 (Dec. 2022), p. 095020. DOI: 10.1088/1361-6595/ac907e.
- [Ter43] Frederick Emmons Terman. *Radio Engineers’ Handbook*. McGraw-Hill Book Company, Inc., 1943.
- [Tho21] Thorlabs, Inc. *Right-Angle Kinematic Mirror Mounts for 30 mm Cage Systems*. Newton, New Jersey, United States: Thorlabs, Inc., Nov. 2021. URL: [https://www.thorlabs.de/newgroupage9.cfm?objectgroup\\_id=6813](https://www.thorlabs.de/newgroupage9.cfm?objectgroup_id=6813) (visited on 11/15/2021).
- [Ton+21] Amin L. Tong et al. “An atom trap system for  $^{39}\text{Ar}$  dating with improved precision”. In: *Review of Scientific Instruments* 92.6 (2021), p. 063204. DOI: 10.1063/5.0050620. eprint: <https://doi.org/10.1063/5.0050620>.
- [Wei+99] John Weiner et al. “Experiments and theory in cold and ultracold collisions”. In: *Rev. Mod. Phys.* 71 (1 Jan. 1999), pp. 1–85. DOI: 10.1103/RevModPhys.71.1.
- [Wel+09] J. Welte et al. “Hyperfine spectroscopy of the  $1\text{s}_5$ - $2\text{p}_9$  transition of  $^{39}\text{Ar}$ ”. In: *Review of Scientific Instruments* 80.11 (2009), p. 113109. DOI: 10.1063/1.3257691.
- [Wel+10] J Welte et al. “Towards the realization of atom trap trace analysis for  $^{39}\text{Ar}$ ”. In: *New Journal of Physics* 12.6 (June 2010), p. 065031. DOI: 10.1088/1367-2630/12/6/065031.
- [Wel11] Joachim Welte. “Atom Trap Trace Analysis of  $^{39}\text{Ar}$ ”. PhD thesis. Heidelberg, Germany: Ruperto-Carola University of Heidelberg, 2011.
- [WG92] R. W. Williams and J. B. Gill. “TH isotope and U-series disequilibria in some alkali basalts”. In: *Geophysical Research Letters* 19.2 (1992), pp. 139–142. DOI: 10.1029/91GL02864.
- [Whe28] H.A. Wheeler. “Simple Inductance Formulas for Radio Coils”. In: *Proceedings of the Institute of Radio Engineers* 16.10 (1928), pp. 1398–1400. DOI: 10.1109/JRPROC.1928.221309.
- [Wie+89] W. L. Wiese et al. “Unified set of atomic transition probabilities for neutral argon”. In: *Phys. Rev. A* 39 (5 Mar. 1989), pp. 2461–2471. DOI: 10.1103/PhysRevA.39.2461.
- [Wil13] Klaus Wille. *Vorlesung Elektronik*. lecture notes. 2013. URL: [https://web.archive.org/web/20140124060707/http://www.delta.tu-dortmund.de/cms/Medienpool/ELEKTRONIK\\_2013/ELEKTRONIK\\_2013\\_KAPITEL\\_04.pdf](https://web.archive.org/web/20140124060707/http://www.delta.tu-dortmund.de/cms/Medienpool/ELEKTRONIK_2013/ELEKTRONIK_2013_KAPITEL_04.pdf) (visited on 10/25/2022).

- 
- [Yok+13] R. Yokochi et al. “Noble gas radionuclides in Yellowstone geothermal gas emissions: A reconnaissance”. In: *Chemical Geology* 339 (2013). Frontiers in Gas Geochemistry, pp. 43–51. ISSN: 0009-2541. DOI: [10.1016/j.chemgeo.2012.09.037](https://doi.org/10.1016/j.chemgeo.2012.09.037).
- [Zha+15] Grace H. Zhang et al. “Note: Fast compact laser shutter using a direct current motor and three-dimensional printing”. In: *Review of Scientific Instruments* 86.12 (2015), p. 126105. DOI: [10.1063/1.4937614](https://doi.org/10.1063/1.4937614).
- [ZWB14] Oleg Zatsarinny, Yang Wang, and Klaus Bartschat. “Electron-impact excitation of argon at intermediate energies”. In: *Phys. Rev. A* 89 (2 Feb. 2014), p. 022706. DOI: [10.1103/PhysRevA.89.022706](https://doi.org/10.1103/PhysRevA.89.022706).